THESIS APPROVAL

GRADUATE SCHOOL, KASETSART UNIVERSITY

Doctor of Philosophy (Chemistry)
DEGREE

Chemistry	Chemistry
FIELD	**DEPARTMENT**

TITLE: (Photo)Electrochemical Studies of Nanoporous TiO_2 and Ce-doped TiO_2 Film Electrodes Prepared by the Sol-Gel Method

NAME: Miss Sutasinee Kityakarn

THIS THESIS HAS BEEN ACCEPTED BY

THESIS ADVISOR
(Associate Professor Attera Worayingyong, Ph.D.)

THESIS CO-ADVISOR
(Assistant Professor Marisa Arunchaiya, Ph.D.)

THESIS CO-ADVISOR
(Assistant Professor Prayoon Songsiriritthigul, Ph.D.)

DEPARTMENT HEAD
(Assistant Professor Noojaree Prasitpan, Ph.D.)

APPROVED BY THE GRADUATE SCHOOL ON

DEAN
(Associate Professor Gunjana Theeragool, D.Agr.)

THESIS

(PHOTO)ELECTROCHEMICAL STUDIES OF NANOPOROUS TiO_2 AND Ce-DOPED TiO_2 FILM ELECTRODES PREPARED BY THE SOL-GEL METHOD

SUTASINEE KITYAKARN

A Thesis Submitted in Partial Fulfillment of
the Requirements for the Degree of
Doctor of Philosophy (Chemistry)
Graduate School, Kasetsart University
2009

Sutasinee Kityakarn 2009: (Photo)Electrochemical Studies of Nanoporous TiO_2 and Ce-doped TiO_2 Film Electrodes Prepared by the Sol-Gel Method. Doctor of Philosophy (Chemistry), Major Field: Chemistry, Department of Chemistry. Thesis Advisor: Associate Professor Attera Worayingyong, Ph.D. 207 pages.

Nanoporous undoped TiO_2 and Ce-doped TiO_2 film electrodes were successfully prepared by a sol-gel method using high water content (a high ratio of water to alkoxide precursor of 200:1). Mixture phases of anatase and rutile were investigated by x-ray diffraction (XRD). Extended x-ray absorption fine structure (EXAFS) technique was also used to determine the mixture phases of anatase and rutile in undoped TiO_2 and Ce-doped TiO_2 powder together with the position of Ce ions in the TiO_2 structure. Results from scanning electron microscopic technique (SEM) showed that the undoped TiO_2 and Ce-doped TiO_2 electrodes were relatively compact films whereas a commercial TiO_2-P25 formed an agglomerated fine particle electrode. Electrochemical properties and photo-electrochemical properties of TiO_2 electrodes were studied by cyclic voltammetry (CV) and electrochemical impedance spectroscopy (EIS). The Ce-doped TiO_2 electrode showed a higher current in the dark compared with the undoped TiO_2 electrode due to a higher number of hydrated Ti(III) sites resulting from Ce(III) on the surface. Under irradiation, the overall impedance of the undoped TiO_2 showed a smaller value than that of the Ce doped-TiO_2 electrode, which meant that the undoped TiO_2 had higher conductivity due to fewer grain boundaries of the mixture phases of anatase and rutile. The EIS results were simulated using a transmission line model for porous film electrodes. Charge transfer processes and recombination reactions were taken into account for the simulation of irradiated EIS results. The enhancement of photocurrents depended on anodic potential, photon flux and electrolyte solution. The limitation of the overall reaction resulted from the charge transfer and recombination reactions.

Student's signature	Thesis Advisor's signature	___ / ___ / ___

ACKNOWLEDGEMENT

I wish to express my sincere appreciation to Assoc. Prof. Dr. Attera Worayingyong, my research director, for her generous guidance and expert advice throughout all the stages of this research. I would also like to thank Dr. Michael Wörner for his special advice about the electrochemical impedance technique and his advice for electrochemical research in Karlsruhe, Germany. I wish to thank Prof. André M. Braun and Prof. Hans Schulz for their suggestions during my stay in Karlsruhe, Germany. Appreciation is also extended to Assist. Prof. Marisa Arunchaiya for her valuable assistance.

Special thanks are also due to Assist. Prof. Dr. Prayoon Songsiriritthigul, Prof. Dr. Sukit Limpijumnong, Dr. Wantana Klysubun and Dr. Mike F. Smith at the Synchrotron Light Research Institute (SLRI), Nakhon Ratchasima, for their advice in x-ray absorption spectroscopy.

I wish to acknowledge the Synchrotron Light Research Institute (SLRI) and the Faculty of Science, Kasetsart University for the financial support.

Last but not least, my thanks go to my parents, my sister, and many good friends in the department, for their moral support, encouragement and concern. Their love has been an essential source of strength to me during my study.

Sutasinee Kityakarn
May 2009

TABLE OF CONTENTS

LIST OF TABLES

Table **Page**

LIST OF TABLES (Continued)

LIST OF TABLES (Continued)

Appendix A Table

LIST OF FIGURES

Figure **Page**

LIST OF FIGURES (Continued)

LIST OF FIGURES (Continued)

LIST OF FIGURES (Continued)

LIST OF FIGURES (Continued)

LIST OF FIGURES (Continued)

LIST OF FIGURES (Continued)

LIST OF FIGURES (Continued)

LISTS OF ABBREVIATIONS

CB = Conduction band
CV = Cyclic voltammetry
E_{fb} = Flat band potential
E_g = Band gap energy
EIS = Electrochemical impedance spectroscopy
EXAFS = Extended x-ray absorption fine structure spectroscopy
JCPDS = Joint Committee on Powder Diffraction Standards
PEC = Photoelectrochemical
SEM = Scanning electron microscopy
VB = Valence band
XANES = X-ray absorption near edge spectroscopy
XAS = X-ray absorption spectroscopy
XPS = X-ray photoelectron spectroscopy
XRD = X-ray diffraction

(PHOTO)ELECTROCHEMICAL STUDIES OF NANOPOROUS TiO_2 AND Ce-DOPED TiO_2 FILM ELECTRODES PREPARED BY THE SOL-GEL METHOD

INTRODUCTION

Heterogeneous photocatalysis is an emerging technique valuable for water and air purification and remediation. The effective utilization of clean, safe and abundant solar energy will lead to promising solutions not only for energy issues but for many problems caused by environmental pollution. A number of reports have dealt with the use of supported photocatalysts, especially the use of semiconductor materials that allow one to improve the efficiency by bias potential in a photoelectrochemical (PEC) cell (Litter, 1999 and Linsegibler *et al.*, 1995). Semiconductor can be excited by light with equal or greater energy than band gap to generate electron-hole (e^-/h^+) pairs. The photogenerated electrons transfer to a back contact completing a circuit while the photogenerated holes transfer to surface to oxidize adsorbed molecules. All processes occur interiorly and at surface called photoinduced processes.

TiO_2 is so far the most useful material for photocatalytic purposes, owing to its exceptional optical and electronic properties, chemical stability, non-toxicity and low cost. TiO_2 photocatalysis has been demonstrated as an alternative route for conventional water treatment because it can decompose and even mineralize pollutants and/or undesirable compounds in wastewater. TiO_2 exists in two useful crystallographic forms, anatase and rutile. The energy band gaps of anatase (3.23 eV, 384 nm) and rutile (3.02 eV, 411 nm) combine with the valence band positions to generate highly energetic holes at the interface, giving rise to easy oxidation reactions (Diebold, 2003). TiO_2 is exposed to the light of energy more than the band gap energy, and electron-hole pairs are generated. The photogenerated holes are involved in the oxidation of organic substrates, either directly or via the OH radical formed by the reaction with OH^- and/or adsorbed water, while the photogenerated electrons must be removed from the particles by transferring to a suitable electron acceptor and/or through the external electrical circuit to the counter electrode producing the photocurrent (Hagfeldt and Grätzel, 1995 and Mills and Hunte, 1997). The commercial TiO_2 (P25), a mixture of anatase and rutile, is used as the standard for comparison with the prepared photocatalysts. The mixtured-phase of TiO_2 shows high photocatalytic activity due to the interconnection between anatase and rutile (Sun *et al.*, 2003). Modified TiO_2, with an additional metal ion such as cerium, is considered to enhance the charge separation (Li *et al.*, 2006) and modify the band gap of TiO_2 as a visible-light system (Li *et al.*, 2005).

The sol-gel method is the most successful technique to prepare the homogeneous metal oxide, mixture of metal oxides at low temperature, nanosized metal oxide and especially coating metal oxide on substrate (Nerendar and Messing, 1997, Sakka, n.d. and Gonzalez *et al.*, 1997). The method consists of hydrolysis and condensation of metal alkoxide, $M(OR)_n$. The properties of material can be controlled by pH, solvent, hydrolysis rate, temperature, calcination temperature and atmosphere of calcination. It is used to prepare thin film electrode by coating sol on substrate. The other influence to thin film preparation is substrate cleaning method, which is important because more adhesive contaminations such as oil, grease, inorganic or organic adhesive molecule on surface will affect film coating quality (Pullker, 1984). Oxygen plasma and chemical cleaning are considered to be effective cleaning surface in this regard.

In order to understand the mechanism of a photoelectrochemical catalytic reaction, charge transfer in a well prepared film electrode should be carefully investigated. The powerful technique for investigating the charge transfer and the mass transfer occurring at the interfacial electrode is the promising electrochemical impedance spectroscopy (EIS). Interpretation of impedance data requires equations governing kinetics of an electrochemical reaction or a model involving the network of electrical elements, called *equivalent circuit* (Krause, 2003).

To explain the charge transfer clearly, the mixture of anatase and rutile phases in TiO_2 together with the position and state of the cerium ion in the TiO_2 should be determined. X-ray diffraction (XRD) is normally used for phase characterization. X-ray absorption spectroscopy (XAS) especially, extended X-ray absorption fine structure (EXAFS), is emerged as a powerful technique for local atomic structure determination.

In this study, nanoporous film electrodes of TiO_2 and Ce-doped TiO_2 were prepared by the sol-gel method. It aimed to reach the same mixture of anatase and rutile as that of the commercial TiO_2-P25. The method would produce a higher quality of nanoporous TiO_2 film than the particulate film of TiO_2-P25. The film morphologies which resulted from different coating methods were observed by a scanning electron microscopy (SEM). The mixture phase of anatase and rutile was quantified by both XRD and XAS (i.e. EXAFS). The local structure of the cerium ion in the TiO_2 structure was investigated by XAS (i.e. EXAFS). The (Photo)electrochemical properties of TiO_2 film electrodes were investigated by cyclic voltammetry (CV) and EIS. The EIS technique was used to explain the charge transfer reaction and recombination of TiO_2 film electrode by modification equivalent circuits to observed data.

OBJECTIVES

1. To prepare a nanoporous film electrode of TiO_2 reaching the mixture phase of anatase to rutile of the commercial TiO_2-P25.
2. To prepare a nanoporous film electrode of Ce-doped TiO_2 enhancing the charge separation on the film electrode.
3. To develop a method for a high quality film electrode by examining different cleaning methods together with the sol-gel preparation condition.
4. To modify equivalent circuits of electrochemical impedance spectroscopy (EIS) for the prepared TiO_2 film electrode.
5. To explain the charge transfer and recombination of the TiO_2 film electrode.

LITERATURE REVIEW

1. Photo(electro)chemical Catalysis

Photochemical catalysis is the acceleration of a photoreaction in the presence of a catalyst where the photoreaction occurs on the surface of a catalyst (Mills and Hunte, 1997) A semiconductor can be excited by light with equal or higher energy than the band gap to generate electron-hole pairs (e^-/h^+). The electrical conductivity of material is explained by the different band energies between a conduction band (CB) and a valence band (VB), called the band gap energy (E_g). The overlap of CB and VB is the highest electrical conductivity material, called metal. The small E_g is a semiconductor in which electrons in VB can diffuse/migrate to CB under ambient conditions. An insulator has the highest band gap energy allowing electrons in VB to diffuse/migrate to CB only under a thermal condition or an electric field. The photo-induced phenomenon is a process in which the semiconductor is excited by light (Carp *et al.*, 2004). The generated electrons and/or holes can be used electrically as a solar cell, chemically as photochemical catalysts and to change the surface itself as superhydrophilicity. All photoinduced processes take into account surface bound redox reaction. The inset of Figure 1 shows the excitation of electron in the occupied valence band of the semiconductor to the unoccupied conduction band by a photo-induced process (Mitter and Ko, 1999 and Linsebigler *et al.*, 1995). The photogenerated electrons transfer to the semiconductor surface to reduce the adsorbed molecule (usually oxygen in solution, acceptor species, A), (1), while the generated holes can migrate to the surface where an electron from donor species can combine with the surface hole oxidizing the donor species, D (usually an organic molecule or adsorbed water), (2). The competition reaction of charge transfer is a recombination process, (3) surface recombination and (4) volume recombination.

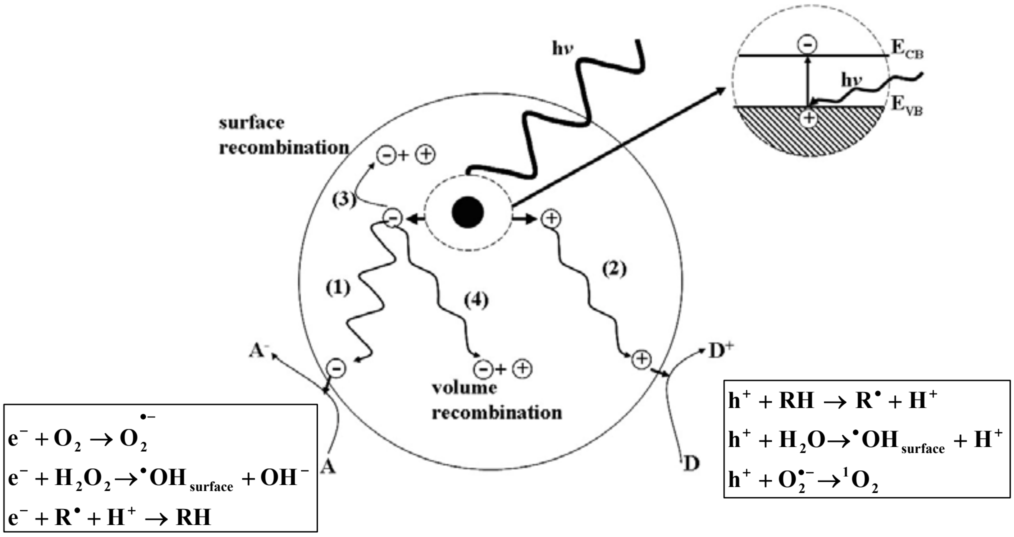

Figure 1 Schematic representation of photoinduced in semiconductor particles.

Adapted from: Linsebigler *et al.* (1995) and Fujishima *et al.* (2008).

1.1 Photocatalyst

1.2.1. Titanium oxide (TiO_2)

The semiconductor TiO_2 has three phases which are brookite, rutile and anatase. The two latter phases are commonly used as photocatalysts with anatase showing a higher photocatalytic activity (Yu *et al.* 2001, Jiang *et al.*, 2006 and Sokmen *et al.*, 2001). The unit cell of TiO_2 consists of TiO_6 octahedral variously connected by edges or corners. The basic unit cell of the octahedral in solution can join together to form oligomers which are the growth units leading to both anatase and rutile phases (Yanqing *et al.*, 2001). The joining of the basic octahedral units takes place at the opposite edges giving a growth unit for the rutile phase. However, it takes place at the non-opposite edges giving a growth unit for anatase phase, as shown in Figure 2. Anatase has no corners connected but has four edges shared per octahedron. It can be viewed as a zigzag chain of octahedral. In the rutile phase, octahedral are shared by edges or corner to form a linear chain along [001] and each chain is connected to the other with a corner connection. The octahedron in rutile is not regular, showing a slight orthorhombic distortion. The octahedron in anatase is significantly distorted so that its symmetry is lower than orthorhombic.

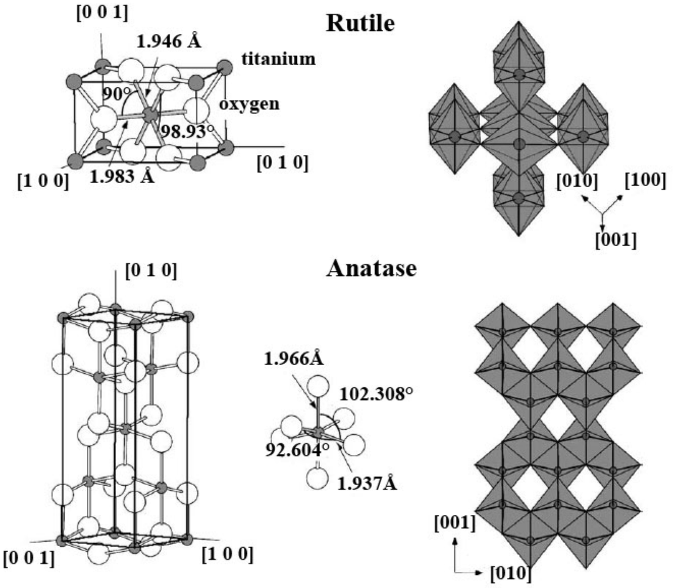

Figure 2 Bulk structures of rutile and anatase.

Adapted from: Diebold (2003).

Table 1 The properties of TiO_2.

Properties/Crystalline phase	Anatase	Rutile
System and Space group	Tetragonal/ D_{4h}^{19}-I4_1/amd	Tetragonal/ D_{4h}^{14}-P4_2/mnm
Ti-Ti distance (Å)	a = 3.79, c = 3.04	a = 3.57, c = 2.96
Ti-O distance (Å)	1.980	1.949 and 1.980
Density (kg/m^3)	3830	4240
Reflextive Index	2.5688	2.9467
Band gap (eV)	3.2	3.0

Source: Diebold (2003)

The difference in lattice structures causes different mass densities and electronic band structures between the two forms of TiO_2. The properties of TiO_2

are shown in Table 1 (Diebold, 2003). The most interesting photochemical catalyst is TiO_2 semiconductor reflected by the number of publications that include both theoretical aspects and practical applications (Carp *et al.*, 2004). The most active field of TiO_2 photocatalysis is the degradation of organic compounds in environments including photocatalysts for viruses, bacteria, fungi, algae and cancer cells. This performance is attributed to highly oxidizing holes and hydroxyl radicals ($OH^\bullet$) that are oxidizing agents.

Marci *et al.* investigated the two different types of commercial polycrystalline TiO_2 (pure anatase, Merck) and P25 (mixture phase of 75% anatase and 25% rutile, Degussa), using them as photocatalysts in gas-solid and liquid- solid regimes of toluene degradation (Marci *et al.*, 2003). The different regimes showed different intermediates due to the key role played by the interfaces. The main intermediates found in significant amounts were *p*-cresol and bezaldehyde in the liquid-solid regime but only benzaldehyde in the gas-solid one by using both types of catalysts. Moreover, benzoic acid, hydorquinone and *trans*, *trans*-muconic acid were detected only with TiO_2 pure anatase. These suggested the occurrence of different photodegradation pathways not only depending on the interfaces but also on the kind of photocatalyst. Einaga *et al.* proposed the formation of carbon deposits on TiO_2 that was the key step for catalyst deactivation (Einaga *et al.*, 2002). They studied the photocatalytic decompositions of benzene, toluene, cyclohexane and cyclohexene over commercial TiO_2. These performances strongly depend on the structures of hydrocarbons comparing the alkane, alkene and aromatic compounds. The hydroxyl radicals ($OH^\bullet$) add to the aromatic rings of benzene, toluene and unsaturated C=C bonds of cyclohexene. The radicals also attract the H atoms from the methyl groups of toluene and saturate C-H bonds of cyclohexane and cyclohexene resulting different intermediate radicals formation. The intermediate radicals are subsequently oxidized by molecular O_2 and decompose to CO_2 and CO via the subsequent oxidation processes or polymerize to give carbon deposits. The decomposition of carbon deposit on TiO_2 in photoirradiated under humidified air regenerated the catalysts resulting the increasing the photooxidation rate of toluene and cyclohexene. Sokmen *et al.* studied the degradation mechanism of 2-methylthiophene in TiO_2 anatase suspensions (Sokmen *et al.*, 2001). The 2-methylthiophene decomposed to thiophene-2-aldehyde, 2-methyl-5-(2-thienylmethyl)thiophene, 2-hydroxymethylthiophene and 5-methyl-(5H)thiophene-2-one. The first three products were observed in the photolysis of 2-methylthiophene in the dichloromethane/water system. The formation of dimeric and trimeric structures suggests that the products observed might be formed via a radical route. The photooxidation process is a developing new technique but it seems ineffective for complete oxidative conversion of the relatively concentrated solution studied.

Moreover, the commercial nanostructure TiO_2, as Degussa P25, has superior photocatalytic activity and has been widely used as a gold standard for the comparison of reactivity (Sun *et al.*, 2003, Li *et al.*, 2007 and Sun and Paragiotis, 2003). Degussa P25 is produced through high-temperature flame hydrolysis of $TiCl_4$ in the presence of hydrogen and oxygen. The final product in powder form is a mixture phase of approximately 75% anatase and 25% rutile. The key to the high photocatalytic activity of P25 is the interconnected anatase and rutile phases. The band gap of anatase and rutile are 3.2 V and 3.0 V, respectively, otherwise the Fermi level of them is in the middle between the conduction band and the valence band, Figure 3 (a). The band bending happens in both anatase and rutile through Fermi level lineup when they contact each other, see Figure 3 (b). In the case of irradiation, the e^-/h^+ pairs are generated and photogenerated holes transfer from the valence band of the anatase phase to the rutile phase through the valence band bending. These concepts can explain the highest photocatalytic activity of P25 conceding the e^-/h^+ separation. There are more promoted electrons in the anatase than the rutile. The reaction on the anatase surface is a reduction while the oxidation occurs on the rutile surface.

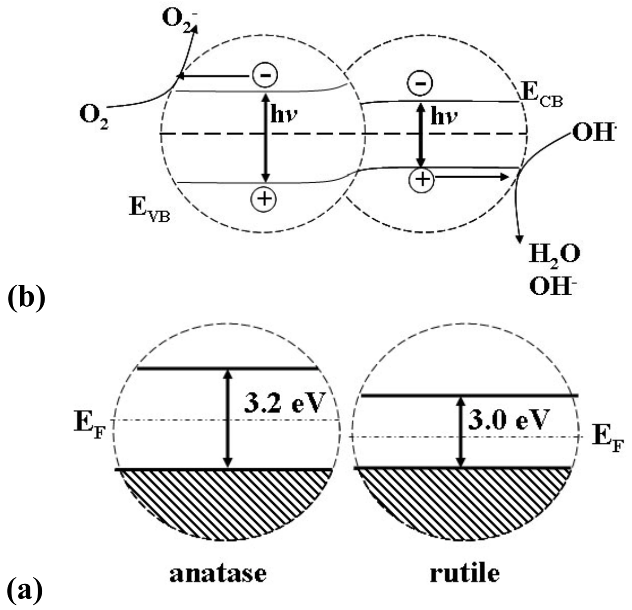

Figure 3 Proposed mechanism of electron-hole separation in P25 during photocatalysis; (a) before each particle is connected and (b) after particle is connected.

Adapted from: Sun *et al.* (2003).

Sun *et al.* studied the photoxidation of phenol in aqueous suspension of Pt doped TiO_2 anatase and P25 (Sun *et al.*, 2003). They proposed two different mechanisms of suppressing electron-hole recombination for the different TiO_2 phases (Einaga *et al.*, 2002 and Sun *et al.*, 2003). A Pt doped pure anatase could suppress electron-hole recombination due to decreased carrier densities in TiO_2 particles and the recombination rate decreased because the rate depended on the carrier densities in TiO_2. The Pt particles deposited on TiO_2 change the original equilibrium by drawing the electrons out of the TiO_2 particle through the Pt-TiO_2 contact. This performance can decrease the carrier densities in TiO_2 bulk. Alternatively, the suppressing recombination of Pt doped on a mixture anatase and rutile occurs via the interconnected anatase and rutile. Increased conduction band energy of anatase stops electrons going from anatase to rutile but the holes in anatase can be transferred to rutile through the valence band because of the band bending. These processes decrease the electron-hole recombination. Thevenet *et al.* studied the totally degradation of alkyne and acetylene in synthetic air and static conditions into CO_2 and H_2O by using irradiated TiO_2 powder and coated on various supports (Thevenet *et al.*, 2005). The irradiated TiO_2 could degrade C_2H_2 into CO_2 and H_2O in gas phase and no organic intermediates. The P25 was more efficient in terms of photocatalytical material than the pure anatase phase. The chemical nature of the fibre support did not influence the photodegradation while the adsorbing additive showed significant photocatalytic activity. In addition, Kosanić investigated the photocatalytic degradation of oxalic acid in aqueous suspensions of P25 and the formation of CO_2 under UV irradiation (Kasanić, 1998). The maximum amount of CO_2 evolved increased with the increasing oxalic acid concentration. The amount of CO_2 was independent of the initial oxalic acid concentration but the overall rate of reaction increased as the oxalic acid concentration increased. This effect could be explained by assuming that at low substrate concentrations the number of catalytic sites was not a limiting factor of the degradation rate that is proportional to the substrate concentration. Otherwise, Vinodpal *et al.* prepared the particulate film electrode of P25 for investigation of 4-chlorophenol degradation (Vinodpal *et al.*, 1993). They found that the rate of 4-chlorophenol photocatalytic degradation increase under UV illumination and external anodic bias. These results indicated that the charge separation in the TiO_2 particulate film can be controlled by an externally applied bias. They observed that ability of TiO_2 particulate film electrode to degradation 4-chlorophenol was similar to that of suspended TiO_2 particles in slurries. These revealed that immobilized photocatalysts has advantage of utilizing an anodic bias for enhance charge separation.

1.2.2. Lanthanide ions doped TiO_2

Photocatalytic efficiency of TiO_2 depends upon the relative degree of branching of the reactive e^-/h^+ pairs into interfacial charge transfer reaction (Choi *et al.*, 1994). In order to enhance interfacial charge transfer reactions, the properties of TiO_2 particles and electrodes have been modified by platinization, selective metal ion doping of the crystalline TiO_2 matrix. Metal ion dopants influence the photoreactivity of TiO_2 by acting as electron (or hole) traps and by altering the e^-/h^+ pair recombination rate through the following process.

$$M^{n+} + e_{CB}^- \rightarrow M^{(n-1)+} \qquad \text{electron trap}$$

$$M^{n+} + h_{VB}^+ \rightarrow M^{(n+1)+} \qquad \text{hole trap}$$

where the energy level for $M^{n+}/M^{(n-1)+}$ lies below the conduction band edge (E_{CB}) and the energy level for $M^{n+}/M^{(n+1)+}$ lies above the valence band edge (E_{VB}). These reactions prevent electron-hole recombination and result in an increased rate of formation of $^\bullet$OH radical (Nagaveni *et al.*, 2004). During the photocatalytic process, the recombination of photogenerated electrons and holes is one of the most significant factors that determine the photocatalytic activity of the TiO_2. A presence of metal ions in titania does not modify the position of the valence band edge of anatase but introduces new energy levels of the transition metal ions into the band gap of TiO_2. A metal particle deposited on TiO_2 enhances the photocatalytic activity because it enhances the separation of the e^-/h^+ pairs. He *et al.* found the deposited nano Pt could significantly improve the photocatalytic activity of TiO_2 film (He *et al.*, 2006). The improvement was considerably dependent on its deposition method. In addition, Sun *et al.* studied the photooxidation of phenol on Pt deposited on TiO_2 (Sun *et al.*, 2003). The Pt deposited on anatase resulted in an acceleration of phenol photocatalytic oxidation when Pt content was up to 1 wt%; further increase of Pt content did not increase the photocatalytic activity. The charge separation was displayed by limited Pt deposition. This should be an optimal Pt amount for Pt deposition on anatase. The photooxidation of phenol with P25 was not accelerated by modifying P25 with Pt but it was due to the interconnected anatase and rutile explained above.

However, a metal ion substituted TiO_2 shows a different behavior metal to doped TiO_2 due to the solubility of metal ion (e.g. transition metal ion) in TiO_2 and the position of metal *d* levels within the band gap energy of TiO_2. Therefore, transition metal ions substituted for Ti^{4+} in TiO_2 do not enhance photocatalytic activity even with an extension of absorption in the visible region. Yamashita *et al.*

studied the degradation of propanol diluted in water under visible light using metal (V^+, Mn^+ and Fe^+) ion-implanted TiO_2 (Yamashita *et al.*, 2002). The metal ion-implanted TiO_2 resulted a definite shift in the absorption spectra toward to visible regions. XAFS studies had revealed that the metal ion was located at the lattice position of Ti^{4+}. These showed that the modified TiO_2 was able to absorb visible light and operated as a photocatalyst under visible light. Also, Ohno *et al.* reported the expansion of the effective wavelength of TiO_2 photocatalyts into the visible region, for Ru doped TiO_2 (Ohno *et al.*, 1999). The oxygen evolution reaction occurred by irradiation of visible light at more 440 nm using iron (III) ions as the electron acceptor. The activity of the Ru doped TiO_2 powder for the photooxidation of water was dependent on the doping concentration and was the highest at about 0.007 wt% Ru. For the photocatalysts doped with a large amount of Ru, the activity was lowered probably by the formation of recombination centers at high concentration.

Cerium oxide (CeO_2) is one of the most reactive rare earth metal oxides that are a broad range application in various fields (Fang *et al.*, 2007). It is frequently incorporated into ‘catalysts’ due to its considersable performance for the catalytic combustion of hydrocarbons. It has been reported that CeO_2 has the properties of stabilizing the active phase and the high activity for aromatic destruction (Worayingyong *et al.*, 2004). It not only increases the surface area of catalysts but also inhibits the collapse of unit cells (Xiao *et al.*, 2006) and the anatase-to-rutile phase transformation (Ohno *et al.*, 1999 and Fang *et al.*, 2007). However, there are only a few reports on the photocatalytic activity of cerium doped materials. Xiao *et al.* studied the photocatalytic activities for mineralization of Rhodamine B (RB) in air using undoped and Ce doped TiO_2 (Xiao *et al.*, 2006). The undoped and Ce doped nanoparticles showed higher photocatalytic activities than photocatalyst P25 but the maximum degradation of RB rate corresponded to the undoped. The negative effect of cerium incorporation to the titania samples on the photocatytic performance may be ascribed to the partial blockage of surface sites available for RB photodegradation. Moreover, Nagaveni *et al.* proposed that the lower photocatalytic activity of M doped was due to the new energy level in the band gap of TiO_2 and acted as the electron (or hole) recombination center (Nagaveni *et al.*, 2004). They found that the solid solution formation of metal ions with TiO_2 was restricted to a very narrow range of doped ion concentrations. The lesser amount of surface hydroxyl groups was observed in cases of metal doped TiO_2 compared to the undoped TiO_2. This could be one of the reasons for the lower activity of metal doped TiO_2.

The effect of ceria on the separation of e^-/h^+ pairs under visible light irradiation was also investigated (Li *et al.*, 2005). Li *et al.* and Xie and Yuan proposed that the Ce *4f* level played an important role in an interfacial charge transfer and elimination of electron-hole recombination (Li *et al.*, 2005 and Xie and Yuan, 2003). The exited electrons might be more easily transferred to O_2 on the surface of catalysts because of the formation of labile oxygen vacancies and particularly the relatively high mobility of bulk oxygen. Also, the higher content Ti^{3+} on Ln-TiO_2 (Ln: lanthanide metal ions) surface accelerated the interfacial charge transfer and enhanced the photocatalytic activity but the content should have an optimal range. The Ti^{3+} content increased with increasing Ce content. These created more recombination centers of e^-/h^+ pairs and led to the decrease of photocatalytic activity. The introduction of structure defect (Ce *4f* level) into the TiO_2 crystal lattice led to the optical absorption band between 400 and 500 nm because the excited electrons were expanded from the UV light of anatase TiO_2 to visible light (Ce *4f* level).

Li *et al.* studied the different effects of cerium ions doped on properties of anatase and rutile (Li *et al.*, 2006). The photocatalytic efficiency of the rutile samples doped with an appropriate amount of Ce^{4+} was enhanced while all Ce^{4+} doped anatase samples showed a much lower activity than pure anatase. The doping increased the percentage of the hydroxylated surface and led to a better photocatalytic activity for the rutile phase. Ce^{4+} could also acts as an electron trap to enhance the e^-/h^+ pair recombination but it could become a recombination center with more doping. The decreasing photocatalytic activity of Ce^{4+} doped anatase might be because of i) the decreasing hydroxyl surface, ii) more CeO_2 was on the surface of the Ce^{4+} doped anatase which would reduce the contact between dye and photocatalyst and iii), the agglomeration caused by Ce^{4+} doping also resulted in the further reduction of the photocatalytic efficiency.

1.2 Photoelectrochemical catalysts/ Photoelectrodes

A particle film of P25 on conducting glass performed a photo-electrochemical catalyst for oxidation of organics such as chlorinated phenol and was first reported by Vinodpal *et al.* and Datye *et al.* (Vinodpal *et al.*, 1993 and Datye *et al.*, 1995). Unlike conventional semiconductor electrodes, particulate electrodes cannot sustain the development of a space charge layer and, consequently, the energy bands are almost flat (Jiang *et al.*, 2003). For these reasons, the applied potential plays a quite different role in the particulate and the conventional semiconductor electrodes. With a conventional semiconductor electrode, the main function of the applied potential is to regulate the band bending across the space charge region in order to, typically, minimize electron-hole recombination processes. In addition, where necessary, the applied potential bias can accelerate the interfacial electron transfer process. In the case of a particulate semiconductor electrode, the spatial separation of photogenerated e^-/h^+ pairs can be achieved only by removal of photogenerated holes through interfacial reactions since there are no band bending. The applied potential serves the function of collecting the free electrons made available by the interfacial reactions. In other words, the applied potential simply assists in the removal of the free electrons. It can not serve the purpose of controlling the interfacial reaction, and instead the interfacial reaction rate controls the free electron concentration in the film.

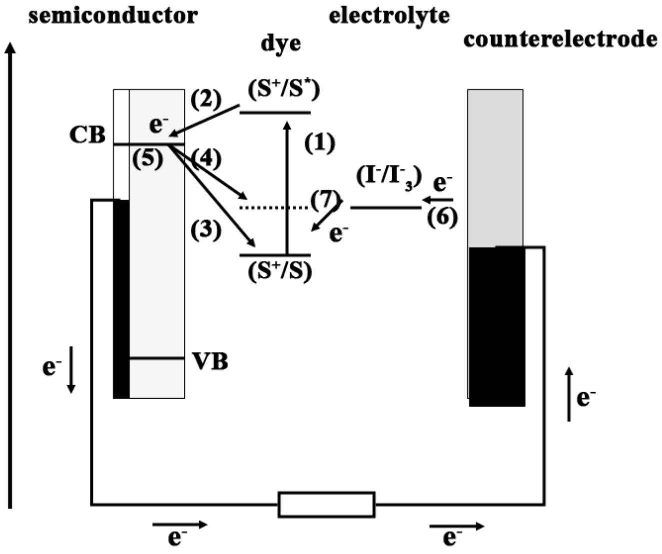

(b)

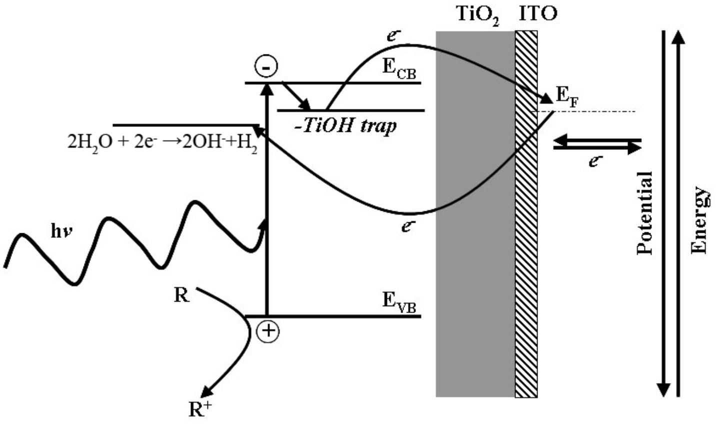

(a)

Figure 4 (a) Schematic representation of the relative energetics of a particulate film electrode on ITO conducting glass under an applied potential and (b) Schematic representation of the electron-hole pair separation and recombination in dye-sensitized nanocrystalline TiO_2 photoelectrochemical cell.

Adapted from: Jiang *et al.* (2003), Hagfeldt and Grätzel (1995) and Mills and Hunte (1997).

The energy level diagram for the system can be represented schematically as shown in Figure 4 (a). Jiang *et al.* proposed that the Fermi level of the conducting ITO substrate was controlled by the applied potential (Jiang *et al.*, 2003). As the potential is lower than the water reduction potential (H_2O/OH^-, E^0_{red}=-0.8277 at 298 K), the pure electrochemical reduction takes place at the underlying ITO substrate, generating a cathodic current. Upon illumination, photoelectrons are generated and are subsequently trapped by the TiO_2 surface groups. Once the applied potential is positive of the electron trap potential, a flow of electrons from the trap band to the conducting substrate occurs and an anodic photocurrent is generated. The carrier concentration in the film is extremely low when there is no UV illumination; therefore, no anodic photocurrent can be generated even when the electrode potential is much more positive than the trap band potential.

Under UV illumination, when the potential is above the zero current potential or trap band potential and the photoholes are removed by the interfacial reactions, surface photoelectrons flow through the film to the conducting ITO substrate. Meanwhile, at the bare/exposed ITO sites the direct electrochemical reduction reaction still occurs, and as a result, the total current obtained is the sum of the reduction and oxidation processes.

For a thin TiO_2 film of about 1 μm which is close to the UV light penetrating range the conductance can be greatly increased under illumination (Jiang *et al.*, 2003). The film resistance under illumination is dramatically decreased as long as there are enough photogenerated hole scavengers at the TiO_2 surface. Due to the great difference in mobility between ions in pores and the free electrons in film, the screening effect can be neglected and an electric field can be established inside the film. The main application area for TiO_2 particulate film electrodes to date has been in dye sensitized solar cell developments (Hirano *et al.*, 2000, Moon *et al.*, 2003 and Ngamsinlapasathian *et al.*, 2005), where considerable attention has been given to electron transport mechanisms within the film. The kinetics for dye sensitized solar cell e.g. Ru complex photosensitized TiO_2 photovoltaic cell are showed in Figure 4 (b) (Hagfeldt and Grätzel, 1995 and Mills and Hunte, 1997). The photoabsorbed dye is electronically excited and the electrons can transfer into conduction band of semiconductor, (1) and (2) in Figure 4 (b) (in the picosecond range). The recombination processes include the reduction of oxidized form of dye sensitized (S^+), i.e. in microsecond, and the reduction of triiodide by conduction band electrons, (3) and (4) in Figure 4 (b). The electron movement in the TiO_2 semiconductor to the back contact (5) is significantly slower that in the single crystal TiO_2 (in millisecond to second ragne). The reduction of triiodide at counter electrode and the reduction of oxidized dye by triiodide are showed (6) and (7) in Figure 4 (b), respectively. Many believe the driving force for electron transport in the TiO_2 film is the electron concentration gradient in the film. For dye sensitized TiO_2 porous film, this may be true because the electrons typically exist as free electrons in the film due to the extremely high electron injection rate compared with the relatively slow electron-hole recombination process (Hagfeldt and Grätzel, 1995 and Cahen *et al.*, 2000). As a result, even though there is no external applied electric field, the free electrons can still diffuse to the collecting electrodes with little chance for recombination to occur.

1.3 Photoelectrochemical cells (Mills and Hunte, 1997, Rajeshwar, 2002, Fujishima *et al.*, 2000)

The semiconductor in the solid state area has adopted the electron energy in a vacuum as referenced, whereas electrochemists have traditionally used the standard hydrogen electrode (SHE), appearing to lie at -4.5 eV with respect to the vacuum level. When the semiconductor is immersed in the redox electrolyte, the electrochemical potential (Fermi level) is disparate across the interface, see Figure 5. Equilibrium of this interface thus necessitates the flow of charge form one phase to the other and a *band bending* ensure within the semiconductor phase.

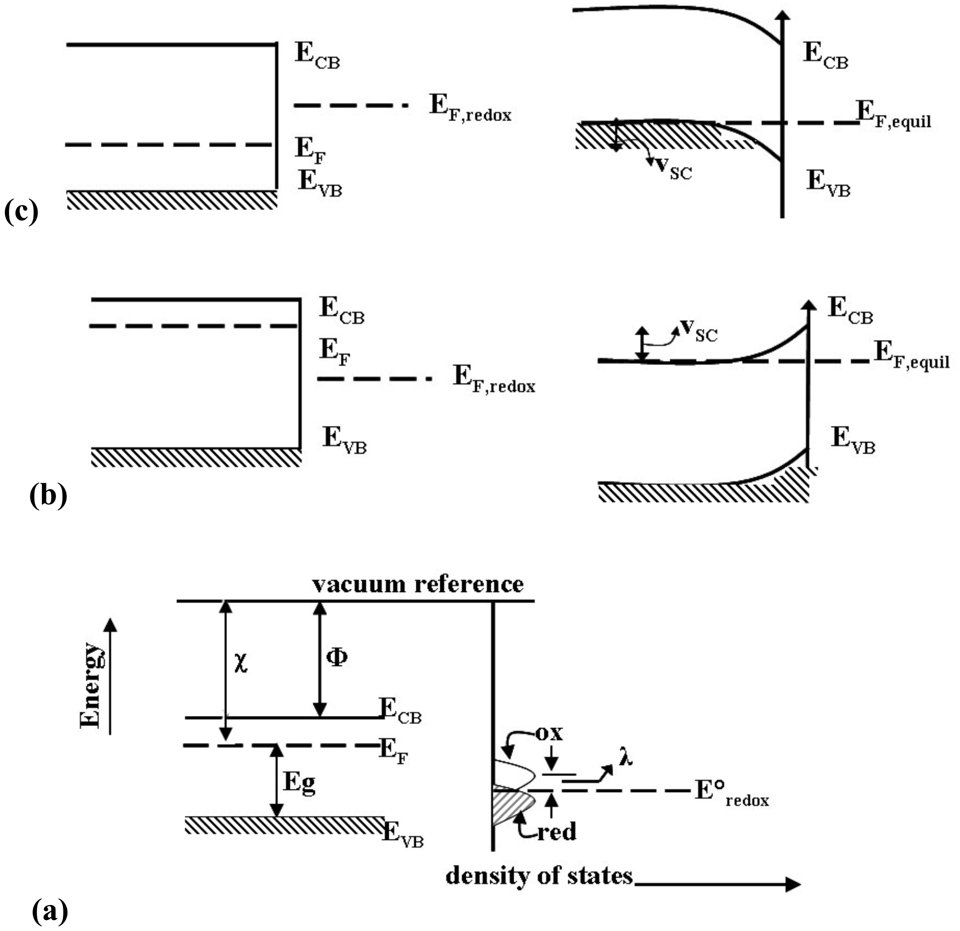

Figure 5 Energy levels in a semiconductor (left-hand side) and a redox electrolyte (right-hand side) shown on a common vacuum reference scale. χ and ϕ are the semiconductor electron affinity and work function, respectively (a), The semiconductor-electrolyte interface before and after equilibration (i.e. contact of the two phases) shown for a *n*-type (b) and for a *p*-type (c).

Adapted from: Rajeshwar (2002).

In *n*-type semiconductor, the electronic charge needed for Fermi level equilibration from the semiconductor phase originates from the donor impurities. Thus the depletion layer that arises as a consequence within the semiconductor contains positive charges from these ionized donors. The situation before and after contact of the two phases for *n*-type and *p*-type semiconductor are illustrated in Figure 5 (b) and (c), respectively. The Fermi level at equilibrium is $E_F = E_{F,Redox}$ and the build in voltage (V_{SC}) drops within spontaneously electrical field of the semiconductor phase.

In *n*-type semiconductors, the photogenerated electrons move into the bulk of the semiconductor to the back contact (Ohmic contact) producing the photocurrent, as a consequence, it can transferred to the non-photoactive electrode (Pt electrode) or surface, where there is an electron acceptor (A), and be reduced, $A + e^- \rightarrow A^-$. While the photogenerated holes under the influenced electrical field can diffuse/migrate to the surface of the semiconductor to oxidize a suitable electron donor (D), $D + h^+ \rightarrow D^+$. The reverse process takes place at a *p*-type semiconductor electrode. In *p*-type semiconductor, the photogenerated holes penetrate deeper than depletion layer will vanish and photocurrent will flow into the external circuit (Vanmaekelbergh and Cardon, 1986). From the thermodynamic considerations, adsorbed coupled can be reduced photocatalytically by electron in conduction band. If they have more positive redox potentials than flat band potential (E_{fb}), located the energy of charge carries at the semiconductor, and it can be oxidized by the valence band holes if they have more negative redox potentials than the E_{fb} of the valence band, see Figure 6.

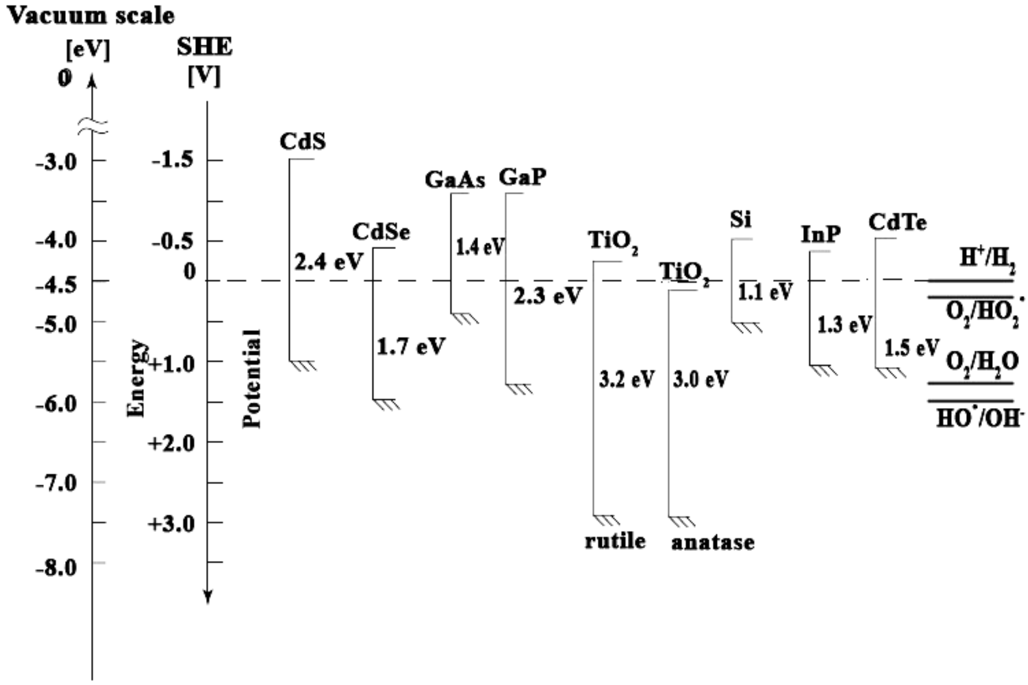

Figure 6. Various semiconductor band edge positions shown both on the vacuum scale and with respect to the standard hydrogen electrode (SHE) reference.

Adapted from: Rajeshwar (2002).

The ability of the electrons and holes for redox can be controlled by changes in the pH. The E_{fb} values follow a Nernstain pH dependence, decreasing 59 mV per pH unit, as equation.

$$E_{fb} = E_{fb}(pH0) - 0.059VpH \qquad (1)$$

The first photoelectrochemical cell for water splitting was studied by using a rutile TiO_2 photoanode and Pt counter electrode reported by Fujishima and Honda in 1972. They observed the oxidation of water (oxygen evolution) at TiO_2 photoanode and the reduction of water (hydrogen evolution) at Pt black electrode, as shown following:

$$TiO_2 + 2h\nu \rightarrow 2e^- + 2h^+$$

At the TiO_2 film electrode: $H_2O + 2h^+ \rightarrow (1/2)O_2 + 2H^+$

At the Pt flat electrode: $2H^+ + 2e^- \rightarrow H_2$

The overall reaction is $H_2O + 2h\nu \rightarrow (1/2)O_2 + H_2$

The E_{CB} of rutile is approximately 0.2 V more positive than E (H^+/H_2) (Mills and Hunte, 1997). At the Pt electrode, it may be the reduction of dissolved oxygen and/or some electrolyte impurity, alternatively. They circumvented by using an anolyte and catholyte with different pH values (Ngamsinlapasathian *et al.*, 2005). Wrighton *et al.* and Watanabe *et al.* also found that $SrTiO_3$, which E_{CB} is negative than E (H^+/H_2), was able to photoelectrolyze water without an additional voltage (Wrighton, 1979 and Watanabe *et al.*, 1976). However, the other n-type oxide semiconductors can be used as a photoanode for the photoelectrolysis of water, where the E_{CB} is in a more negative position than E (H^+/H_2), but there is less efficient solar photoelectrolysis. p-type semiconductors, which are unusually with a small band gap, are much rarer in nature and consequently rarely used in semiconductor photolysis. The photoelectrochemical cell is not only useful for photocatalyst but also for electrical production, see Figure 7. The photogenerated hole migrates to oxidize A^- to A and consequently the photogenerated electron must move through an electrical circuit to the counter electrode, reducing A to A^-.

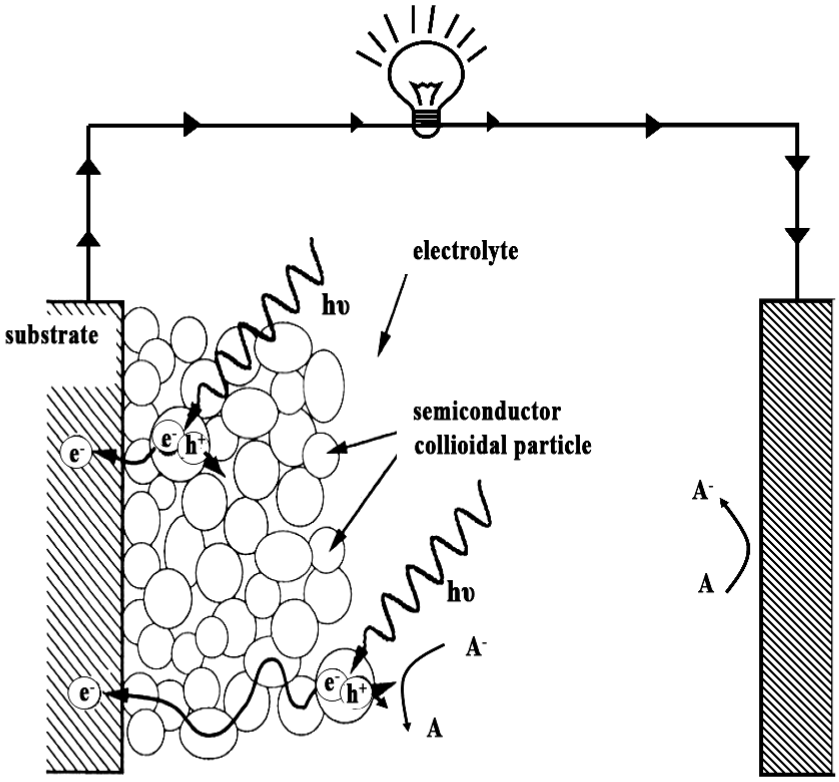

Figure 7 Schematic principle of dye-sensitized solar cell.

Adapted from: Carp *et al.* (2004).

2. Preparation and Characterization of Film Electrodes

2.1 Sol-Gel Preparation Method (Nerendar and Messing, 1997, Sakka, n.d. and Gonzalez *et al.*, 1997)

The sol-gel technique started around 1970 with the purpose to make bulk glasses from bulk gels at low temperature. The metalorganic precursors, which bond alkyl group to a central metal atom through an oxygen atom, are mixed with metal precursors to form a homogeneous solution. The metalorganic precursors are hydrolyzed through the addition of water or organic solvent which carefully controls the pH and the reaction temperature. As hydrolysis and polymerization occur, colloidal particles or micells with an approximate diameter of 10 nm are formed (sol). These particles continue to increase in size until a metal oxide gel forms. The solvent can be eliminated by heat treatment under air resulting in “Xerogel”, while under supercritical condition in autoclave resulting in “Aerogel”. The crystallization of metal oxide forms by heating dried gel to decompose organic and skeleted densification. The properties of material are controlled by pH, hydrolysis rate, temperature, calcination temperature and atmosphere of calcination.

2.1.1. Hydrolysis effect (H_2O/precursor ratio)

The alkoxide based gel $[M(OR)_n]_n$ is a synthesis from metal alkoxide (MOR) or a mixture of metal salts and metal alkoxides (Nerender and Messing, 1997 and Gonzalez *et al.*, 1997). The precursors hydrolyze readily with water (or organic solvent) forming hydrolyzed monomer. Partially hydrolyzed monomers condense via alcohol by alcoxolation or via water by oxolation forming (RO-M-OR), or olation forming (M-OH-M) to form oligomer as an initiator of gelation (polymerization). In the case of substoichiometric quantities (low water content), the hydrolysis of the alkoxide is not complete and linear oligomers as opposed to branched ones were obtained (Scheme I). When the H_2O/alkoxide ratio is excess of that required for stoichiometry, hydrolysis is observed to approach completion. This increase in the extent of hydrolysis is observed to lead to highly branched polymeric products, see scheme II.

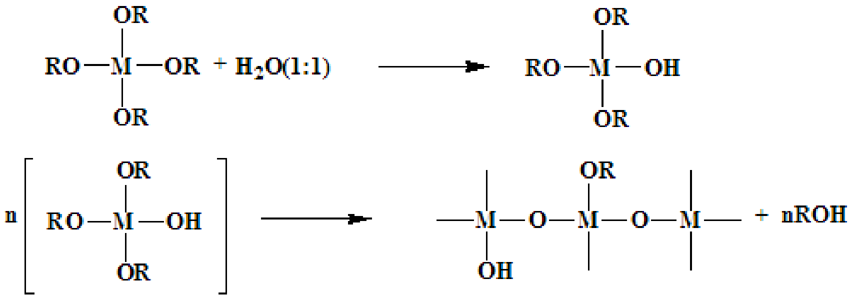

Scheme I

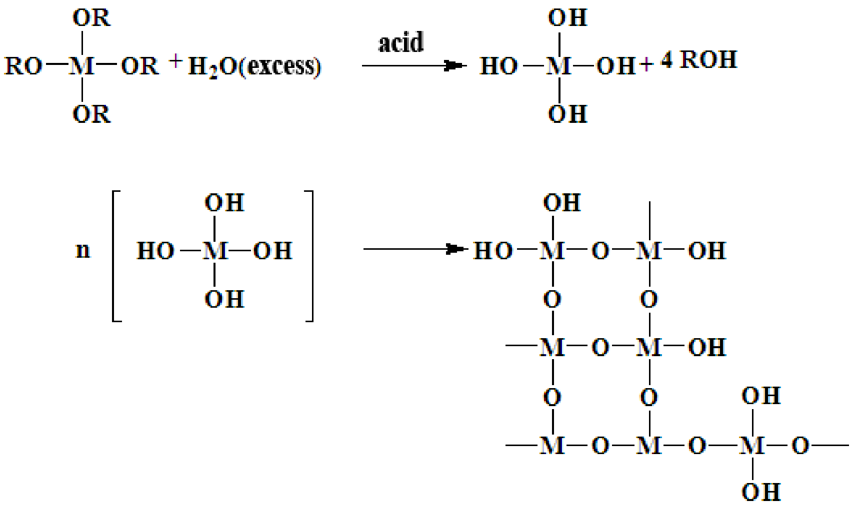

Scheme II

There are many publications investigating the effect of water content. Yu *et al.* investigated a critical value for H_2O/alkoxides molar ratio (h) in all pH conditions to give the higher specific surface areas and pore volumes of the specimens (Yu *et al.*, 2000). The H_2O/alkoxide molar ratio affects the nucleophilic reaction between H_2O and alkoxide producing a different initial monomer. They proposed that the monomers react with each other to form a cross-link structure, 3D structure and particle-like structure depending on the h value then the calcined particles give the different specific surface areas. The highest specific surface area is the 3D structure polymer due to residual voids in the network structure. Several researchers reported the influence of water on the hydrolysis process producing the nanoparticle TiO_2. Soloviev *et al.* attempted to answer the particle growth proceeded by a hydrolyzed monomer or nuclei association (Soloviev *et al.*, 2001). The experimental results showed that the hydrolysis/condensation reaction takes place during the mixing of the reagents (water and 2-propanol solution) and that it was complete at a low hydrolysis rate. The complete transformation of alkoxide into titanium oxide needs the theoretical hydrolysis ratio (h=2). They proposed that the first hydrolysis of titanium tetraisopropoxide begins a fast nucleation process resulting in nanosized titanium-oxo alkoxoclusters and then the subsequent powder particle growth proceeds by the aggregation of nucleus. The second hydrolysis of the particle surface OR group seems to be responsible for this growth and needs a hydrolysis ratio higher than critical hydrolysis ratio (1.1 ± 0.1) to appear. Also, Oskam *et al.* reported the growth kinetic of TiO_2 nanoparticles synthesized from aqueous solution using titanium (IV) isopropoxide as a precursor (Oskam *et al.*, 2003). The high H_2O to titanium mole ratio is very fast and nucleation and growth are completed within seconds. The TiO_2 particles formed are unstable and a white suspension is immediately formed due to the precipitation of large aggregates. Peptization at elevated temperature in the presence of chloride or nitrate can be used to break up the aggregates into very small aggregates (<20 nm) and primary particles. After this step, the TiO_2 primary particles are crystalline and consist mainly of anatase. The anatase to rutile transformation depends on the growth time. The average size of primary particles was dependent on coarsening. Parameters that influence coarsening include time, temperature, and solution chemistry. The growth kinetics of both primary and secondary particles can be further modified using different anions, solvents, pH or concentration, since these parameters may affect the equilibrium solubility, the viscosity, the particle shape as well as the energy gain for oriented attachment. Hsu and Nacu studied the influenced parameters for nanosized TiO_2 preparation using sol gel method (Hsu and Nacu, 2003). They found the effect of water and acid concentrations was the main factors influencing both particle size and the standard deviation of size distribution and the temperature and feed rate were the followed influence parameters. The strong hydrogen bond between the increased number of nuclei leads to their agglomeration and a larger particle size and a wider size distribution. In addition, an increase acid concentration has the effect of decreasing not only the particle size but also the standard deviation of the size distribution. The presence of acid promoted the hydrolysis rate, acts as a catalyst, and prevented the particle agglomeration through eletrostatic repulsions. Otherwise, Yu *et al.* found that the highest ethanol/titanium precursor showed the weak intensities of anatase peaks and meanwhile the brookite phase disappeared because of the suppressed titanium alkoxide hydrolysis and rapid crystallization of the TiO_2 particles (Yu *et al.*, 2002). Usually, a stronger nucleophilic reaction between H_2O and alkoxide molecules will occur and more alkoxyl groups in the alkoxide will be substituted by hydroxyl group of H_2O (Yu *et al.*, 2000). Therefore, the decrease of the quantity of unhydrolyzed alkyls in precursors results in a reduction in steric hindrance by the residual alkyls preventing crystallization to crystalline anatase. From the influence of hydrolysis rate, Baiju *et al.* found the photocatalytic activity of the sol-gel derived nanocrystalline TiO_2 is observed to be a function of the both h and the calcination temperature, which are effective in controlling the powder morphology, the average nanocrystalline size the surface area, and the crystallinity (Baiju *et al.*, 2007). The photocatalytic activity of the sol-gel derived nanocrystalline TiO_2 powder under UV irradiation showed the maximum photocatalytic activity with highest H_2O/titanium precursor (h = 60) and intermediate calcination (673 K).

2.1.2. pH effect (Wrighton, 1979 and Nerender Messing, 1997)

The hydrolysis rate not only depends on water content but also depends on the pH of the solution. Under acidic condition, the hydrolysis rate is very rapid and gel formation time is increased. In the opposite way, the hydrolysis rate and gelation time decrease with increasing pH of solution.

Hu *et al.* prepared nanosized TiO_2 powders using sol-gel method under various pH values (Hu *et al.*, 2003). Brookite formed at low synthesized pH value. It transformed to anatase at low temperature and to rutile at high temperature. Concerning, the *a* and *c* parameters of the TiO_2 unit cell, the *c* parameter increased and *a* parameter slightly decreased with increasing pH value. It was found that the *c* parameter increased with the decrease of the volume fraction of brookite. It seems that the variation in the lattice parameter of anatase is ascribed to the presence of brookite. The attachment of brookite on anatase has been recently reported and possibly results in the microstrain in anatase. For example, Lee and Yang studied the influence of reaction parameters on morphology and change of phase content in crystalline TiO_2 particles (Lee and Yang, 2005). The TiO_2 was prepared by hydrolysis of $TiCl_4$ catalyzed by HCl. Reaction temperature, reaction time and HCl concentration in the solution are the influent factors in determining phase content in

TiO_2 particles. The molar ration of Cl^{-}_{total} to Ti^{4+} for brookite formation ranged between 6.4 and 33. The maximum volume fraction of brookite in the as-prepared TiO_2 particles was obtained when oxidation of Ti^{4+} to TiO_2 was completed and it gradually decreased with increases in reaction time due to transformation of brookite to rutile after completion of oxidation. The heat treatment for TiO_2 particles, a mixture of brookite and rutile phases, showed that brookite phase transformed to anatase, which was finally transformed to the stable structure of rutile phase with increase in heat treatment temperature. Su *et al.* studied the TiO_2 formation and phase transformation using X-ray diffraction (XRD) and transmission electron microscopy (TEM) (Su *et al.*, 2004). The titanium (IV) *n*-butoxide in *iso*-propyl alcohol was used as precursor. They found that the initial state of TiO_2 with elliptical shape showed characteristics of octahedral configuration with two pointed sharp ends. Under acidic condition, the surface hydroxyl group of TiO_2 octahedral can be protronated to form $Ti\text{-}H_2^{+}$, which then combines readily with another Ti-OH to form a Ti-O-Ti oxygen bridge by eliminating a water molecule and simultaneously releasing one proton ion. The slow nucleation in the crystal growth and the irregular surfaces of final TiO_2 particles arose due to the poor nucleophilicity of the nitrate anion. The water condensation process may occur between faces of TiO_2 octahedral (face sharing mechanism), leading to the formation of the anatase phase, or between edges of TiO_2 octahedra (edge sharing mechanism), leading to the formation of the rutile phase. Otherwise, an anion in the acidic solution affects the TiO_2 phase transformation. Kanna and Wongnawa studied the effect of anion in acidic solution to anatase to rutile transformation (Kanna and Wongnawa, 2008). They used the different acid solution and found that H_2SO_4 and H_3PO_4 acids produced an amorphous and only anatase phase. The attraction forces between a Ti^{4+} ion and SO_4^{2-} or PO_4^{3-} are strong so these anions will be bonded to Ti basic unit easily. The bondings of SO_4^{2-} in multidentate modes occupy one full face of an octahedral and inhibit the growth of chains along the opposite edges and hence inhibit the formation of rutile.

2.2. Cleaning methods of conducting glass (Pullker, 1984)

To prepare a photoelectrode for the photoelectrochemical catalysis or experiment, a thin film of semiconductor on a conducting glass has to be accomplished. The surface contamination can be gaseous, liquid or solid in the physical state and may be as film or particulate form. The cleaning of the substrate is very important because the film will not adhere well or may not adhere. Pure water or hot water with detergent may be effective for small adhesive particulate on the surface. It is less effective to the more adhesive contamination as water containing oxidic polishing residues, inorganic or organic dust particles or film consisting of oil and grease. Cleaning surfaces can be classified into two categories; atomically clean surfaces are required for special scientific work and can be realized in ultra high vacuum and technologically clean surfaces are performed under atmosphere. The heating operation and/or particle bombardment are used for cleaning in vacuum. The cleaning under atmosphere can perform with solvents. The various cleaning fluids are used depending on the nature of the contaminations.

a) Rubbing and immersion cleaning

The simplest method is rubbing the surface with cotton wool dipped in the mixture solvent to remove superficial dirt from the substrate. Otherwise, the often used cleaning technique is immersion or dipping into the various solvents such as acidic solution. The lipids and fatty contaminations get off by the bases to soaps. These techniques are easy to construct, they mildly attack the substrate material and are inexpensive techniques. In this study, the ITO substrate was immersed in boiling acetone and then immersed in nitric acid. Finally, it was immersed in distilled water to clean the ITO.

b) Vapour degreasing

This process is useful for removing grease and oil films from surfaces. The apparatus consists with an open-tank with a heating element at the bottom and water-cooling running around the top. The cleaning fluids may be isopropyl alcohol or halogenated hydrocarbon solution. The method shows static electrification thus the charge elimination must be performed by ionized cleaning. This technique is an excellent way to obtain highly clean surfaces but it is complicated and difficult to construct.

c) Ultrasonic cleaning

The strong adherent contamination can be removed by this technique. Inorganic acidic or basic solution is used as well as organic solvents. The transducer in a sonicator converts an oscillating electrical input into a vibratory mechanical output, sound waves. This gives rise to cavitation being prime mechanism cleaning in such a system at the glass surface/ cleaning liquid interface. This technique is used to remove pitch and polishing-agent residues from optically worked glass. For example, Kikkawa *et al.* cleaned the substrate with detergent and acetone in a sonicator (Kikkawa *et al.*, 1991).

d) Plasma cleaning

The plasma is a partially ionized gas, i.e. oxygen, argon or a mixture gas. The ionized particles are accelerated under an applied radio frequency to the surface. The absorbed molecules on the surface will be oxidized for oxygen plasma while the particulate deposits will be scrubbed in argon plasma to clean the substrate surface. For example, Kim *et al.* cleaned the ITO surface by oxygen plasma to improve the stability of organic light emitting diodes (Kim *et al.,* 2002).

2.3. Preparation of thin film electrodes

Thin films technology is recently created interest due to more applications becoming evident such as electrochromic device (Vlachopoulos *et al.*, 2008 and Sun, 2005), corrosion protection, solar cell (Li *et al.*, 2006, Jiang *et al.*, 2003, Hirano *et al.*, 2000, Moon *et al.*, 2003 and Ngamsinlapadathian *et al.*, 2005), photoelectrocatalysts (Xiao *et al.*, 2006, Li *et al.* 2005 and Xie *et al.*, 2003), etc. The properties of thin film material are different from particulate material (bulk material). The films formation grows in two dimensions while bulk material formation grows in zero dimension. The geometry and properties of both forms are different (Soloviev, 2001).

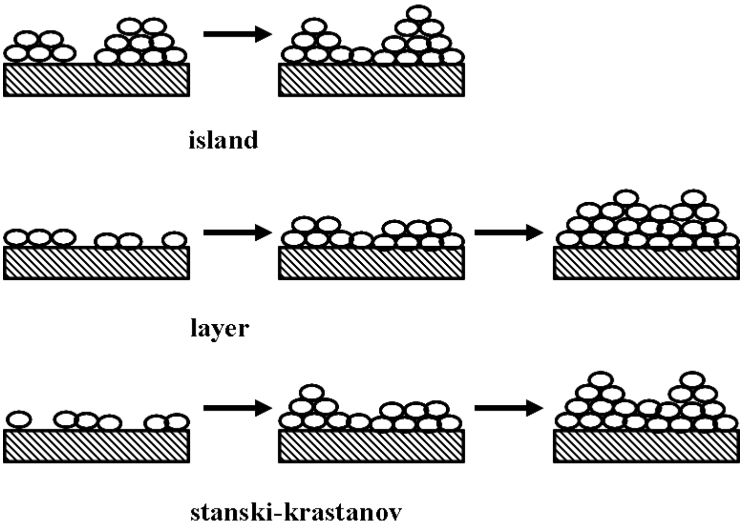

Figure 8 Thin film formation model.

Adapted from: Ohring (1992).

The thin film growth bases on three models (Ohring, 1992): i) island (or Volmer-Weber), ii) layer (or Frank-van der Merwe) and iii) Stranski-Krastanov, which schematically present in Figure 8. The island model is atoms or molecules on the substrate which are more strongly bound to each other than to the substrate such as metals on insulators, alkali halide crystals, on graphite and mica substrates. The layer model; the atoms are strongly bound to the substrate so that the others form a stable two dimensions of planar sheet. The extension layer occurs from the binding of layer by layer. The combination of island and layer models is the Stranski-Krastanov growth mechanism. This model is the one or more monolayer forming become unfavorable forming and island form depends on many parameters as film-substrate lattice mismatch, strain energy accumulates in the growing film.

The sol-gel method is used to prepare film material and bulk material. Several factors distinguish structural evolution of films from that of bulk gel (Brinker *et al.*, 1988): i) during deposition the rapid increase in concentration (18-36 fold), resulting from evaporation, forces the precursors into close proximity with each other, significantly increasing the reaction rate. From this point, further evaporation generates porosity within the film. By comparison, in bulk systems the concentration remains constant during gelation and increases only during the drying step. ii) Concentration-induced gelation imposes a time scale for the sequential stages of film formation which depends on the evaporation rate of the solvent. Compared to the bulk systems, aggregation, gelation and drying occur much more rapidly: in seconds rather that days or months. iii) Fluid flow due to gravity, evaporation, or angular acceleration, combined with attachment of the precursor species to the substrate, imposes a shear stress within the film during deposition. After gelation, shrinkage due to removal of solvent and continued condensation creates a tensile stress within the film. Such stresses are not present in bulk gels. The methods used to prepare the film material include: dip coating, vapor condensation, spin coating. But in our experiment, the dip coating method will be of interest.

a) Dip coating method (Brinker, 1988 and Schmidt and Mennig, n.d.)

The dip coating is a process where the substrate is coated. It is immersed in a liquid and then withdrawn with a well-defined withdrawal speed under controlled temperature and atmospheric conditions. The coating thickness is mainly defined by the withdrawal speed, by the solid content and the viscosity of the liquid. The dipping process and schematically dipping are represented in Figure 9.

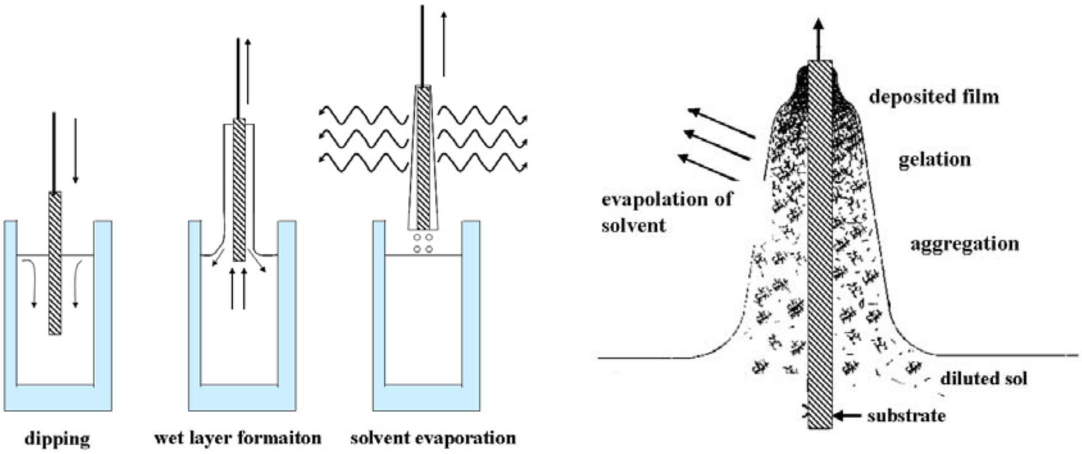

(a)

(b)

Figure 9 (a) Dipping process and (b) Schematically dipping.

Adapted from: Brinker (1988) and Schmidt and Menning (n.d.).

The atmosphere controls the evaporation of the solvent and the subsequent destabilization of the sols by solvent evaporation leads to a gelation process and the formation of a transparent film due to the small particle size in the sols. The gelation process can be explained by the approach to the charged particle to distances below the repulsion potential. Then the repulsion is changed to an attraction leading to a very fast gelation. The resulting gel then has to be calcinated by thermal treatment and the calcination temperature is dependent on the composition. In most cases a remarkably reduced calcination temperature compared to the bulk system is observed.

2.4. Characterizations

2.4.1. X-ray powder diffraction spectroscopy (XRD) (Anthony, 1999 and Niemantsverdriet, 2000)

X-ray diffraction has been used for the fingerprint characterization of crystalline materials and for determination of their structure. X-rays are produced when high energy charged particles, e.g. electrons accelerated through 30 kV, bombard matter. They have two components which are white radiation and monochromatic wavelengths. The wavelengths of X-ray in the angstrom range (Å) are sufficiently energetic to penetrate solids and are well suited to probe their internal structure. The X-ray wavelength commonly employed is the characteristic Kα radiation, $\lambda = 1.5418$ Å, emitted by Cu. When crystals diffract X-rays, the atom or ions act as secondary point sources and scatter the X-rays; in the optical grating, the lines scratched or ruled on the glass surface cause scattering. The Bragg's law (eq. 2) is much simpler and is used almost universally.

$$2d\sin\theta = n\lambda \tag{2}$$

The diffraction of X-ray by an ordered lattice interface allows one to derive lattice spacing by using the Bragg relation and the simple diagram of an X-ray diffraction experiment shown in Figure 10.

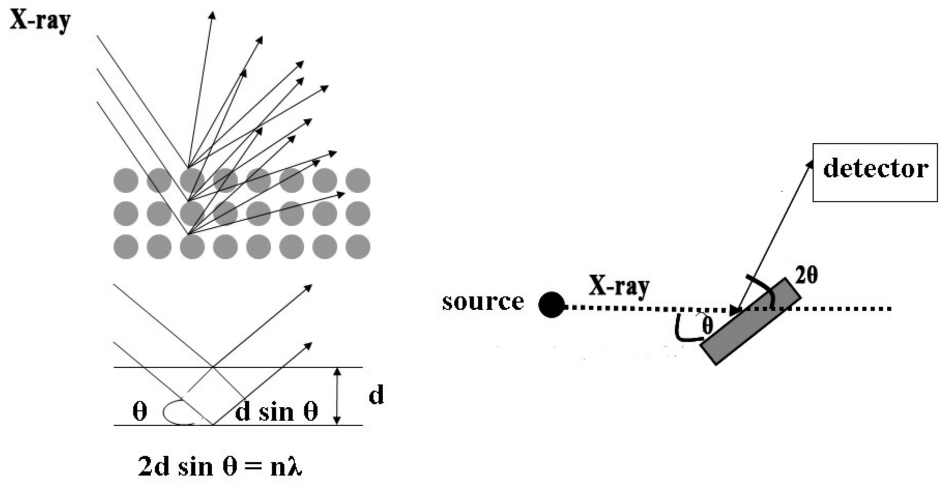

Figure 10 Derivation of Bragg’s Law and a simple diagram of an X-ray spectrometer.

Adapted from: Anthony (1999).

The XRD pattern of a powdered sample is measured with scintillation or Geiger counter detector which scans the intensity of the diffracted radiation as a function of angle 2θ between the incoming and the diffracted beams. Usually, the range 10 to 80° 2θ is sufficient to cover the most useful part of the powder pattern. Each crystalline phase has a characteristic pattern which can be used as a fingerprint for identification purposes. The two variables in a powder pattern are peak position, i.e. 2θ, which can be measured very accurately and intensity which can be measured either qualitatively or quantitatively. The two materials have one or more common 2θ, calculated to d-spacing using Bragg’s law, but when comparing the whole patterns which may contain between 5 and >100 observed peaks, the two are found to be quite different. For the identification of unknown crystalline materials, an invaluable reference source is the Powder Diffraction File (International Centre for Diffraction Data, USA.), known as the ASTM or Joint Committee on Powder Diffraction Standards (JCPDS) files. In the search indices, materials are classified either according to their most intense peaks or according to the first eight peaks in the powder pattern.

2.4.2. Scanning electron microscopy (SEM) (Anthony, 1999, Niemantsverdriet, 2000 and Douglas *et al.*, 2007)

Electron microscopy is extremely useful for providing structural information over a wide range of magnification. At one extreme, SEM complements optical microscopy for studying the texture, topography and surface features of powders or solid pieces. The resulting picture has a definite 3D quality because of the depth of focus of the SEM instrument. Electrons have characteristic wavelengths of less than an Å and come close to seeing atomic detail. The electron microscopes operate in either transmission or reflection. In reflection mode, sample thickness is not a problem. It is usually necessary to coat the sample with a thin layer of metal such as Au sputtering, to prevent the build-up of charge on the surface. The main instrument (SEM) covers the magnification range between ~1μm (the lower resolution limit of optical microscope) and ~ 0.1μm (the upper practical working limit of transmission electron microscopy, TEM) although SEM can be used to study structure over a much wider range, from ~ 10^{-2} to ~ 10^{2}μm.

To obtain a SEM image, a finely focused electron beam impinges on the surface sample. The electron beam form electron gun is scanned across the sample in a raster scan by scan coils (the two pairs of electromagnetic coils, one pair deflects the beam in the x direction, and other pair deflects in the y direction), see Figure 11 (a). The resulting raster scanning pattern is similar to that used in the cathode-ray-tube (CRT) of a television in which the electron beam is swept across the surface linearly in the x direction, returned to its starting position and shifted downward in the y direction. This process is repeated until a desired area of the surface has been scanned. In SEM, backscattered and secondary electrons [see in Figure 11 (b)] are detected and used to construct the image. The backscattered electrons form deeper regions and carry information on the composition of the sample. The secondary electrons have mostly low energies (in the range ~ 5-50 eV) and originate from the surface sample region. Contrast is caused by the orientation, parts of the surface facing the detector appearing brighter than the parts of the surface with their surface normal pointing away from the detector.

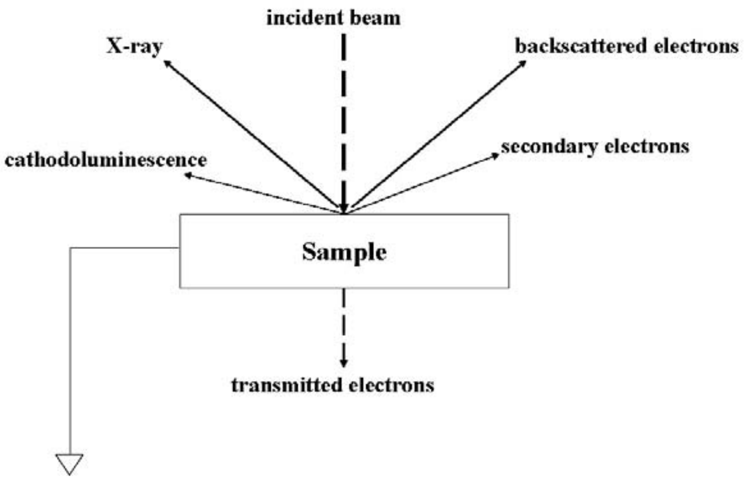

(b)

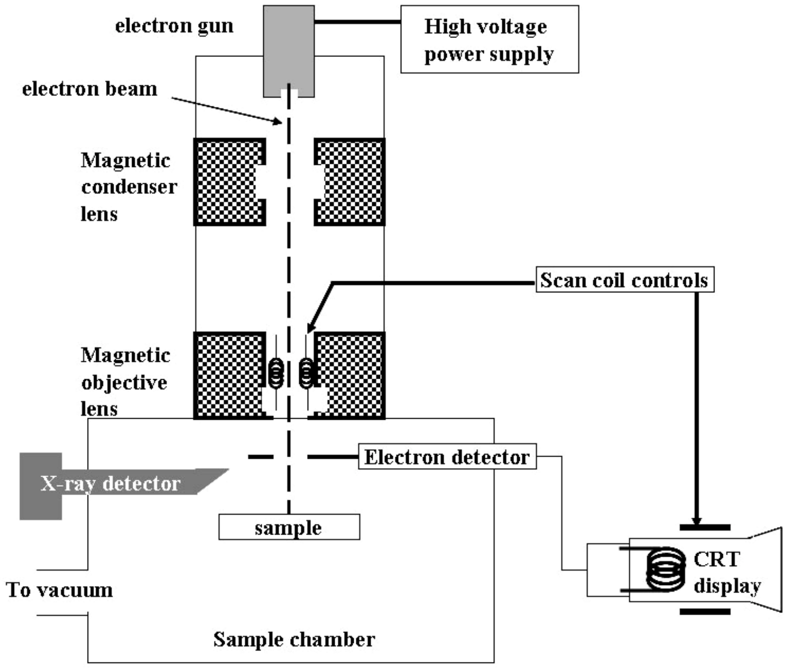

(a)

Figure 11 (a) Diagram of SEM instrument and (b) Interaction of electron beam.

Adapted from: Niemantsverdriet (2000).

2.4.3. X-ray absorption spectroscopy (XAS) (Anthony, 1999, Niemantsverdriet, 2000 and Douglas *et al.*, 2007)

X-ray absorption technique gives detailed local structure information. The main techniques are absorption edge fine structure, also called *X-ray absorption near edge structure (XANES)* and *extended X-ray absorption fine structure (EXAFS)*, both of which monitor the absorption spectra in the region of absorption edges. They are based on the absorption of X-ray and the creation of photoelectrons, which are scattered by nearby atoms in a lattice. The X-ray absorption phenomenon and X-ray absorption spectra are shown in Figure 12.

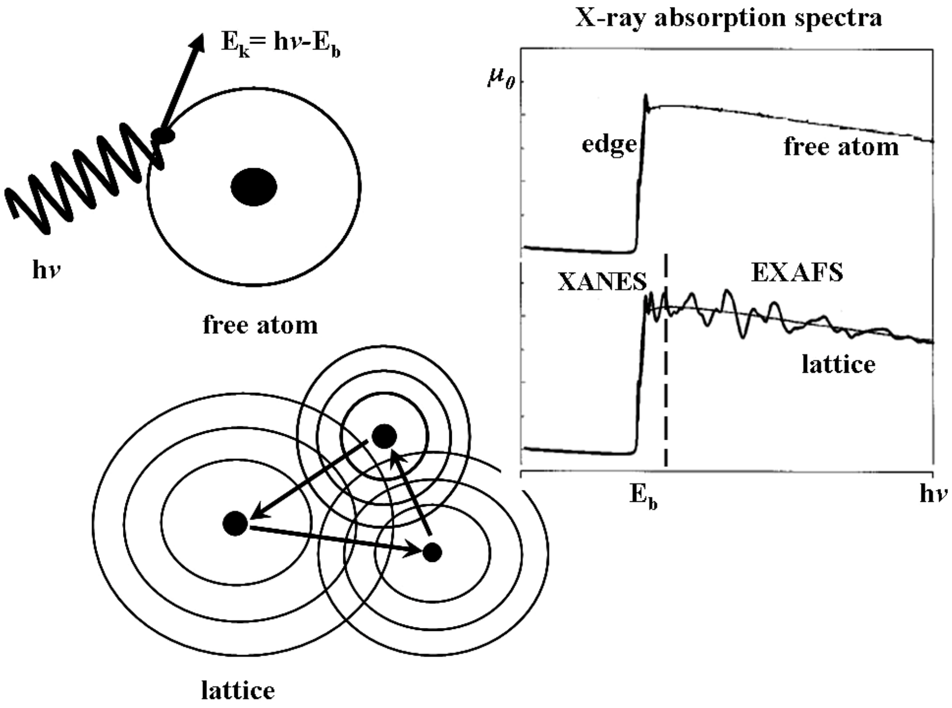

Figure 12 Absorption of X-ray as a function of photon energy E=hv by a free atom and lattice. The fine structure represents the X-ray absorption spectra.

Adapted from: Douglas *et al.* (2007).

A free atom has an electron with binding energy E_b. If the atom is irradiated with X-ray of energy, hv, absorption takes place when h$v \geq E_b$ and the electron leaves with a kinetic energy $E_k = h\nu - E_b$. The X-ray absorption spectrum including XANES and EXAFS regions shows a series of edge corresponding to the binding energies of all electrons present in the atom. Fine structure arises if there are neighbors surrounding the absorbing atom. In this case the photoelectron, which has both particle and wave character, can be scattered back from a neighbor's atom. The outgoing interferes by the backscattered electrons. Depending on the wavelength of the electron, the distance between the emitting and scattering atoms, and the phase shift caused by the scattering event, the two waves enhance or destroy each other. As a result, the cross section of X-ray absorption is modulated by the interference between the photoelectron waves, such that it is enhanced at energies where constructive interference occurs. Interference effects are visible in the X-ray absorption spectrum and give detailed information on the distance, number and type of neighbors of the absorbing atom. The wavelengths at which absorption edge occur depend on the relative separation of the atomic energy levels in atoms. This technique has had to wait before it could be exploited as an analytical tool until the bright, tunable sources of X-ray at synchrotrons became available. The synchrotron radiation is produced when electrons are accelerated in a magnetic field. It is a very intense spectrum of continuous X-ray wavelengths. The much higher sensitivity is achieved and more information can be obtained from the absorption spectra.

2.4.3.1. X-ray absorption near edge structure (XANES)

In the region of an absorption edge, a fine structure associated with inner shell transition is often seen, e.g. the K edge refer to transition of excited the innermost 1*s* electron to the unoccupied state. (Bare, 2005 and Ruiz-Lopez and Munoz-Páez, 1991). The exact peak positions depend on details of oxidation state, site symmetry, surrounding ligands and the nature of the bonding. The pre-edge peak arises from transitions of electrons to bound excited electronic states, but this electronic excitation is strongly modulated by the surrounding atoms in the short to medium range (< 100 absorbing atoms) (Choi *et al.*, 2005). Therefore the pre-edge region contains much potentially useful structural and electronic information, and is frequently used to elucidate the structure of TiO_2 powders in the Ti K-edge XANES spectrum.

2.4.3.2. Extended x-ray absorption fine structure (EXAFS) (Choi *et al.*, 2005 and Rehr and Albers, 2000)

Whereas XANES examines at high resolution the fine structure in the region of absorption edge, EXAFS examines the variation of absorption with energy (or wavelength) over a much wider range, extending out from the absorption edge to higher energies by up to ~1keV (Choi *et al.*, 2005 and Rehr and Alber, 2000). It is a powerful technique for the local structural analysis of short-range ordered compounds because it is very sensitive to the local atomic environment and does not depend on long-range order.

In order to separate the structural information from the energy dependence of the absorption cross sections, the normalized EXAFS spectrum χ is usually defined as the normalized oscillatory part of X-ray absorption coefficient, μ, as $\chi(E) = \{\mu(E) - \mu_0(E)\} / \Delta\mu_0(E)$ (Rehr and Alber, 2000). Conventionally, χ is often defined with respect to photoelectron momentum index, $k = \sqrt{h\omega - |E_c|}$, as measured from threshold, i.e., one defines $\chi(k)$ rather than $\chi(E)$ on an absolute energy scale. The validity of the Kronig short-range-order theory was largely substantiated by Sayers, who developed a quantitative parameterization of EXAFS that has become the standard for much current work (Sayer and Stern, 1971):

$$\chi(k) = \sum_R S_0^2 N_R \frac{|f(k)|}{kR^2} \times sin(2kR + 2\delta_c + \phi) e^{-2R/\lambda(k)} e^{-2\sigma^2 k^2} \qquad (3)$$

Here the structural parameters are the interatomic distances R, the coordination number (or number of equivalent scatters) N_R, and the temperature-dependent rms fluctuation in bond length σ, which should also include effects due to structural disorder. The $f(k) = |f(k)|e^{i\phi(k)}$ is the backscattering amplitude, ϕ is phase factor reflecting the quantum-mechanical wavelike nature of backscattering, δ_c is central-atom partial-wave phase shift of the final state, and $\lambda(k)$ is the energy-dependent EXAFS mean free path (not to be confused with the de Broglie wavelength). Although the overall amplitude factor S_0^2 did not appear in the original formula, Rehr and Alber had added it here for completeness, since the resulting equation can be obtained from a more detailed many-body theory (Rehr and Alber, 2000). A Fourier transform of the EXAFS with respect to k corresponds to an effective radial distribution function, which peak near the first few near neighbor distances. This important observation paved the way for using EXAFS as a general probe of microscopic structural information in molecules and solids. This technique is especially important in noncrystalline materials, where lattice methods like X-ray diffraction cannot be applied.

3. Electrochemical and Photoelectrochemical Characterizations

3.1. Cyclic voltammetry

3.1.1 Basic concepts

Cyclic voltammetry is often the first experiment performed in an electrochemical study (Wang, 2000). It consists of scanning linearly the potential of a stationary working electrode using triangular potential waveform. During the potential sweep, the potentiostat measures the current resulting from the applied potential. The resulting plot of current versus potential is termed a cyclic voltammogram, in Figure 13.

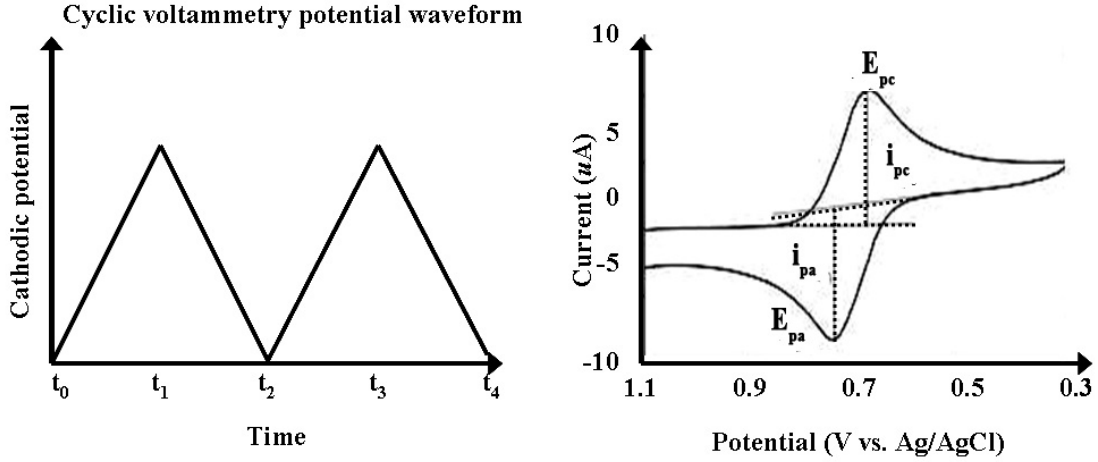

Figure 13 (a) Cyclic voltammetry potential wave form and (b) Cyclic voltammogram.

Adapted from: Wang (2000).

The reversible redox couple is assumed only the oxidized form Ox presenting initially ($Ox + e^- \rightleftharpoons R$). As the applied potential approaches the characteristic E^o for the reduction process, a cathodic current (i_{pc}) begins to increase, until a peak is reached (cathodic potential, E_{pc}). After traversing the potential region in which the reduction process takes place, the direction of the potential sweep is reversed. During the reverse scan, R molecules are reoxidized back to Ox ($R \rightarrow Ox + e^-$) and an anodic peak (i_{pa}) results at anodic potential (E_{pa}). The magnitude of the observed faradaic current can provide information on the overall rate of the many processes occurring at the working electrode surface. For a multi-step process, the overall rate is determined by the slowest step. The rate determining steps of the redox reaction at the working electrode may be any of the following individual steps depending on the system: i) rate of mass transport of the electro-active species, ii) rate of adsorption or desorption at the electrode surface, iii) rate of the electron transfer between the electro-active species and the electrode, or iv) rate of the individual chemical reactions which are part of the overall reaction.

Dark/Irradiation conditions

The electrochemistry of a porous electrode has been widely investigated for several years (Fabergat-Santiago *et al.*, 2003). A crucial characteristic of a nanoporous semiconductor electrode permeated with a conductive phase is the ability to accumulate a large number of injected electron charges in the solid matrix. The displacement of the Fermi level toward the semiconductor conducting band produces a homogeneous increases hugely with the potential. A similar feature can be found in other types of electroactive films, such as ion insertion materials, redox and electronically conducting polymers and super-capacitors, all of which show a large capacitance associated with charging a solid matrix. In some of these systems, anodic and cathodic CV peaks are basically related to the exhaustion of available sites for the injected or adsorbed species (redox capacitance or pseudocapacitance).

The charge transfer process of semiconductors in the dark condition can be described by considering only (majority carrier) processes involving CB (illustrative purposes a n-type semiconductor), see Figure 14 (Rajeshwar, 2002). There are two principle charge transfer routes involving surface state. The forward current (or cathodic current at potential < 0) can involve direct exchange of electrons between the semiconductor CB and Ox states in solution (1) or can be mediated by surface states (2). The other route involves holes injection into the semiconductor VB again from Ox states in solution [(3) and (4)]. The energy states of the redox system now overlap with the VB of the semiconductor such that hole (h^+) injection in the dark is possible. The injected holes remain at the surface with large band bending and attack the semiconductor itself causing the latter to undergo corrosion. If the bias potential is such that the band bending is modest and the holes recombine with electrons, a cathodic current flows being carried by the majority carrier in the bulk.

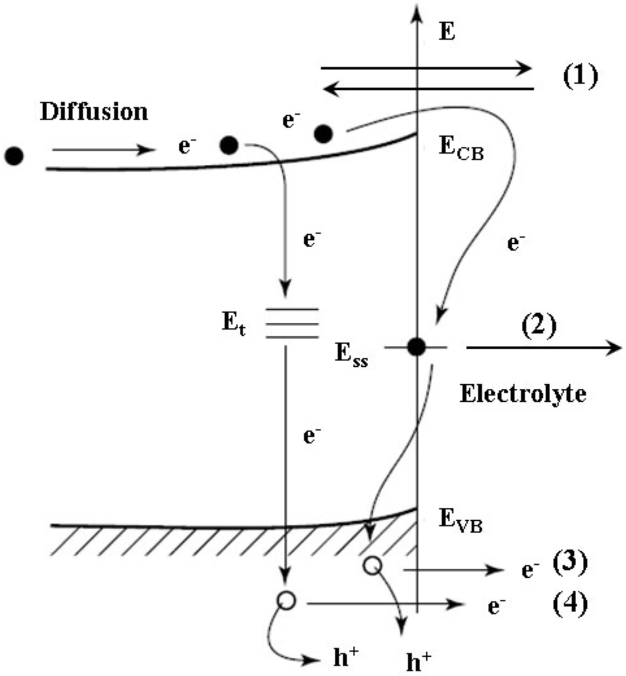

Figure 14 Charge transfer process in the dark condition.

Adapted from: Rajeshwar (2002).

Under the photoinduced process, the measured current is called photocurrent (Rajeshwar, 2002 and Hagfeldt and Grätzel, 1995). The photocurrent generation in the film electrode is presented in Figure 15. During illumination, light absorption in any individual colloidal particle will generate e^-/h^+ pairs. The charge separation process of the photoexited e^-/h^+ pair occurs then in the electric filed. The minority carriers (i.e. holes) are swept to the surface and the electrons can create a gradient in the electrochemical potential between the particle and the ohmic contact. In this gradient the electrons can be transported through the interconnected colloidal particles to the ohmic contact, when they are withdrawn as a current (i.e. photocurrent).

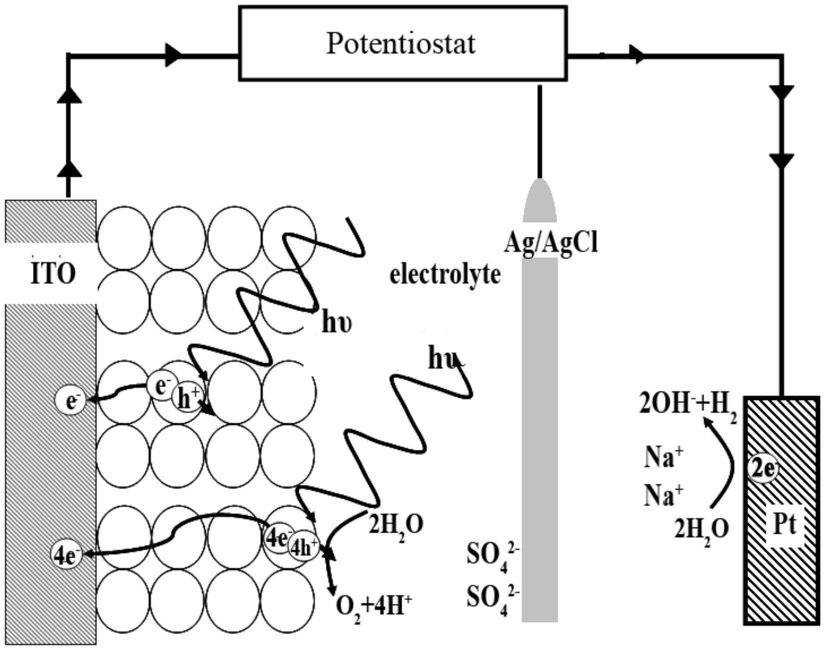

Figure 15 Scheme of photocurrent measurement.

Adapted from: Hagfeldt and Grätzel (1995).

3.2. Electrochemical impedance spectroscopy (EIS)

3.2.1. Basic concepts

The impedance spectroscopy is the powerful electrochemical technique for investigating the properties of electronic material and electrochemical systems. It lies in the fact that they are essentially equilibrium or steady-state techniques that are capable of accessing relaxation phenomena where relaxation times vary over many orders of magnitude (Macdonald *et al.*, 1997 and Krause, 2003). In contrast, linear sweep or potential step techniques usually drive electrodes to a condition far from equilibrium. The steady-state character allows the use of signal averaging within a single experiment to gain a high level of precision. Furthermore, the wide frequency band width (10^{6}-10^{-4} Hz), that is available using transfer function analyzers, permits a wide range of interfacial processes connected with time constants ranging from minutes down to microseconds to be investigated. An additional advantage is that the methods of analysis are very well developed from electrical engineering and that many of the concepts used in the analysis of electrical circuits can be applied which consists of resistor, capacitor, inductor and specialized distributed element to extract data (Agarwal *et al.*, 1992).

The EIS can be applied to any material and any system whose two-pole-arrangement reacts to temporal alteration of the electric voltage between the poles (potential alteration) with characteristic alterations of the current (Zahner Manual). The most important applications are measurements on electrochemical systems. The connection is represented by the first pole as a metal or a semiconductor which is surrounded by a conductive liquid (electrolyte). The second pole often is the electrolyte itself (impedance of a single electrode = electrode-impedance) or a 2'nd conductive electrode in the solution (cell-impedance)

The electrochemical impedance is a well-developed branch of AC theory that describes the response of an AC current or voltage as a function of frequency (Anonymous, n.d., Application note). In DC theory, where the frequency is zero, the resistance is defined by Ohm's law:

$$R = \frac{E}{I} \tag{4}$$

In AC theory, where the frequency is non-zero, the resistance analogues to Ohm's law:

$$Z = \frac{E}{I} \tag{5}$$

where E and I are defined as potential and current, respectively. Z is defined as impedance. The impedance values are also measured in Ohm (Ω). In addition to resistors, capacitors and inductors impede the flow of electrons in an AC circuit. In electrochemical cells, slow electrode kinetics, slow preceding chemical reactions, and diffusion can all impede electron flow and can be considered analogous to the resistors, capacitors and inductors.

The electrochemical impedance is based on perturbation of the electrochemical cell with an alternating signal of small magnitude (Anonymous, Gammy). The perturbation can be of a wide range of parameters such as the applied potential, the applied current and the convection rate at hydrodynamic electrodes or light intensity. The main advantage of this technique is that the response can be regarded as approximately linear as long as the perturbation is sufficiently small. In a linear (or pseudo-linear) system, the current (I) response to a sinusoidal potential (E) will be at the same frequency but shifted in phase, see Figure 16.

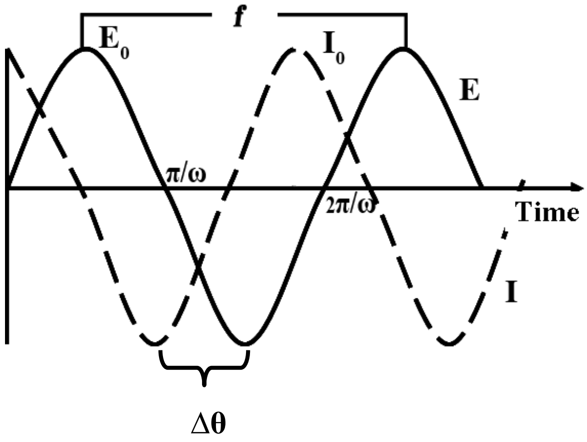

Figure 16 AC waveforms for an applied potential and a resulting current; solid line represents potential while dash line represents current.

Adapted from: Anonymous (n.d.).

For simplification, the sinusoidal perturbations of the applied voltage are only considered (Anonymous, n.d., Application note):

$$E(t) = E_0 \cos(\omega t) \tag{6}$$

E(t) is the potential at time t, E_0 is the amplitude of the voltage E(t), and ω is the radial frequency (in rad/s). The relationship between radial frequency and frequency *f* (in Hz) is $\omega = 2\pi f$. The current response, I (t), is shifted in phase (θ) and I_0 is the amplitude of the current I(t):

$$I(t) = I_0 \cos(\omega t - \theta) \tag{7}$$

Where I(t) is the current at time, t, I_0 is the current amplitude and θ is phase shift by which the voltage lags the current, see Figure 16. An analogous to Ohm's law allows calculating the impedance of the system as:

$$Z = \frac{E}{I} = \frac{E_0 \cos(\omega t)}{I_0 \cos(\omega t - \theta)} = Z_0 \frac{\cos(\omega t)}{\cos(\omega t - \theta)} \tag{8}$$

The impedance is therefore expressed in terms of a magnitude, Z_0, and a phase shift, θ. The impedance vector was calculated as the quotient of the voltage and current vectors (Anonymous, n.d., Application note):

$$Z_{total} = \frac{E'+E''j}{I'+I''i} = Z'+Z''j \tag{9}$$

Where the superscript' and " are as real and imaginary component of voltage, current and impedance. The absolute magnitude of the impedance can be expressed as:

$$|Z| = \sqrt{Z'^2 + Z''^2} \tag{10}$$

Also the phase angle can be defined as: $\tan\theta = Z'/Z''$

The impedance is a vector quantity and as such can be expressed either in terms of real and imaginary parts or in terms of magnitude and phase. From these two forms of mathematical expression, the two most common forms of data presentation can be derived. The complex plane or Nyquist plot, which plots the imaginary impedance component (Z") against the real impedance component (Z') at each frequency, is shown in Figure 17 (a).

The low frequency data are on the right side of the semicircle and high frequency data are on the left. It has several advantages. The primary one is that the plot format makes it easy to see the effects of the ohmic resistance. It is easy to extrapolate the semicircle toward the left, down to the x axis to read the ohmic resistance (R_Ω). The semicircle shape does not depend on the ohmic resistance. However, some disadvantages are a non-readable frequency and the capacitance can be calculated only after the frequency information is known. The frequency corresponding to the top of semicircle ($\omega_{\theta\max}$) can be used to calculate the capacitance if R_p is known.

Another form of data presentation is the Bode plot. Most commonly, it shows a plot of the absolute impedance, $|Z|$, as calculated from eq.10, and the phase shift, θ, of the impedance, each as a function of frequency, see Figure 17 (b). It has advantages over the Nyquist plot in that the frequency appears as one of the axes; it's easy to understand from the plot how the impedance depends on the frequency. The log $|Z|$ vs. log ω curve can yield values of R_p and R_Ω. Extrapolating this line to the log $|Z|$ axis at $\omega = 1$ yield the value of C_{dl} from the relationship, $|Z| = 1/C_{dl}$. In addition, the phase angle against the log ω appeared in the Bode plot and the double layer capacitance, C_{dl}, can be calculated from:

$$\omega_{(\theta\max)} = \sqrt{(1/C_{dl}R_p)(1 + R_p/R_\Omega)} \qquad (11)$$

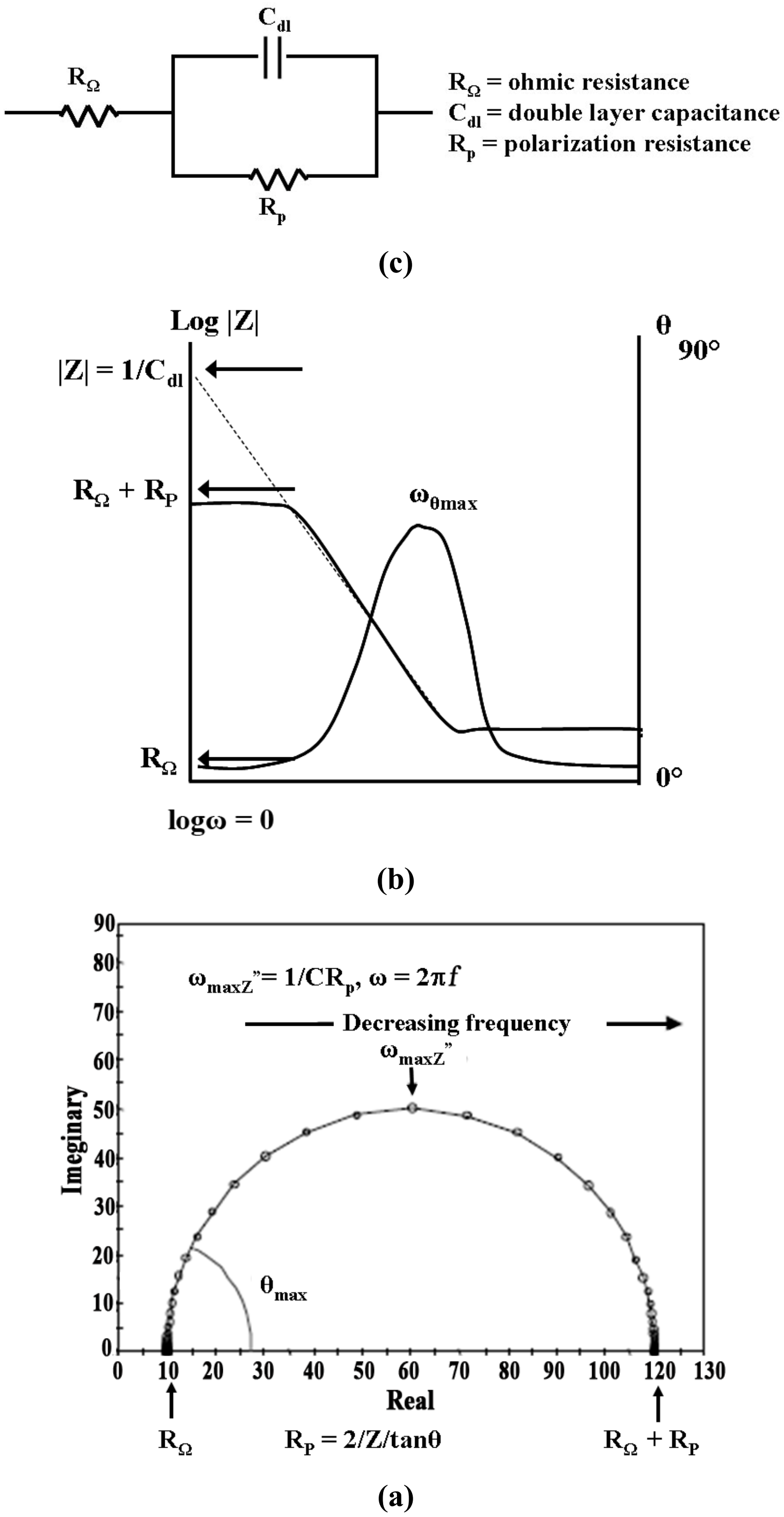

(a)

Figure 17 (a) Nyquist plot, (b) Bode plot and (c) Randles cell.

Adapted from: Anonymous, Application note.

The Bode plot is desirable when the data scatter prevent adequate fitting of the Nyquist semicircle. In general, the Bode plot provides a clearer description of the electrochemical system frequency dependant behavior than the Nyquist plot. On some electrochemical processes, there is more than one rate determining step. Each step represents a system impedance component and contributes to the overall reaction rate constant. The electrochemical impedance experiment can often distinguish between these steps and provide information on their respective rates or relaxation time.

3.2.2. Equivalent circuit

The transfer function for a given system should be derived from the equations governing the kinetics of the electrochemical reaction involved (Krause, 2003). A second method for modeling electrochemical processes involves the use of networks of electrical circuit elements, so called, *equivalent circuit*, which can be selected on the basis of an perceptive understanding of the electrochemical system. Selection of an appropriate model can be time consuming. The lack of complete agreement between the data and a model could be attributed to the error structure (or noise) of the experimental data, to nonstationary process, or to the use of an inadequate or incomplete model (Agarwal *et al.*, 1992). Whether based on electrical circuit analogous or on solution of conservation equations, models for impedance spectra are sufficiently constrained that they cannot provide a framework for determining the noise in the data. A model is built sequentially until all features of the data are represented. Interpretation of the resulting regressed circuit components in terms of physical process may be difficult because several electrical-circuit models could be used to model a given impedance spectrum.

In order to express a simple three electrode electrochemical cell in terms of an equivalent circuit, at least three quantities need to be taken into account. One of them is the resistance of the electrolyte solution between the reference and the working electrodes, another is the electrochemical double layer that can be expressed as the double layer capacitance and finally the impedance of the charge-transfer process also called faradaic impedance. The most commonly used model is an electrical circuit analogue consisting of resistors, capacitors, inductors and specialized distributed elements. For example, the Randles cell is a well-known simple equivalent circuit model, see Figure 17 (c). It includes an ohmic or uncompensated resistance of solution between the working and reference electrodes, a double layer capacitance and a charge transfer or polarization resistance. The Randles cell is often the starting point for other more complex models. The double layer capacitance is in parallel with the impedance due to the charge transfer reaction.

In all real systems, some deviation from ideal behavior can be observed. If a potential is applied to a macroscopic system, the total current is the sum of a large number of microscopic current filaments, which originate and end at the electrode. If the electrode surface is rough, one or more of the dielectric materials in the system is inhomogeneous, then all these microscopic current filaments would be different. A response to a small amplitude excitation signal would lead to frequency-dependent effects that can often be modeled with simple distributed circuit elements

a) Constant phase element (CPE) (Krause, 2003 and Tomkiewicz, 1990)

The CPE can be used to describe inhomogeneous diffusion. It has also been interpreted as a distribution of relaxation times due to inhomogeneous dielectric materials, i.e. materials that can pass an alternating current but not a DC current. It can include contributions from static disorder such as porosity, random mixture of conductor and insulator that can be described by the effective medium approximation at percolation or an interface that can be described by fractal geometry. The CPE is defined as:

$$Z_{CPE} = A_0 (j\omega)^{-\alpha} \tag{12}$$

where A_0 and α are frequency-independent parameters and $0 \leq \alpha \leq 1$. In the complex plane diagram, a CPE would appear as a straight line at a constant phase angle of $\theta = -(\alpha \times 90^\circ)$. For $\alpha = 0$, the CPE describes an ideal resistor and for $\alpha = 1$, it describes an ideal capacitor. The main problem associated with the CPE is that it is only valid over a limited frequency range. It usually needs to be modified at both ends of the frequency spectrum.

b) Warburg impedance (W) (Krause, 2003 and Zahner manual)

The rate of an electrochemical reaction can be strongly influenced by the diffusion of a reactant towards or a product away from the electrode surface. This is often the case when a solution species must diffuse through a film on the electrode surface. This situation can exist when the electrode is covered with reaction products, adsorbed solution components, or a prepared coating. Whenever diffusion effects completely dominate the electrochemical reaction mechanism, the impedance is the Warburg impedance.

$$Z_W = \sigma\omega(1-j)^{-1/2} \tag{13}$$

On Nyquist plot the infinite Warburg impedance appears as a diagonal line with a slope of 0.5. On Bode plot, the Warburg impedance exhibits a phase shift of 45°. In eq. 13 (Krause, 2003), σ is the Warburg coefficient defined as $\sigma = \frac{RT}{n^2F^2A\sqrt{2}}\left(\frac{1}{C_0^*\sqrt{D_0}} + \frac{1}{C_R^*\sqrt{D_R}}\right)$, where F is radial frequency, D_0 and D_R are diffusion coefficients of oxidation and reduction species, A is the surface area of the electrode and n is the number of electrons transferred. C^* is the bulk concentration of the diffusing species in unit moles/cm^3 (i.e. subscript O is oxidation species and R is reduction species). This equation 13 is only valid if the diffusion layer has an infinite thickness. If the diffusion layer is bounded, the impedance at lower frequencies no longer obeys the equation above and will obey the equation 14 instead (Krause, 2003).

$$Z_W = \sigma\omega(1 - j)^{-1/2} \tan\left(\delta\left(\frac{j\omega}{D}\right)^{1/2}\right) \tag{14}$$

Where δ is Nernst diffusion layer thickness and D is an average value of the diffusion coefficients of the diffusing species.

c) Transmission line mode for porous electrodes (Levie, 1963, Bisquert *et al.*, 2000 and Göhr, 1997)

Porous electrodes operate in contact with an electrolyte by simultaneous transport of electronic and ionic species in the solid and liquid phase, respectively. Owing to the small scale of the constituents of the porous network, charge carriers in transit are always close to the surface, implying that transport and heterogeneous transfer processes are strongly coupled in these systems. Advanced models are required for the impedance measurements of porous electrodes to be properly described and understood, due to the complexity of both the structure and the processes involved. Levie was the first to develop a transmission line model to describe the frequency dispersion in a porous electrode (Levie, 1963). He supposed the electrode surface to consist essentially of circular cylinders of uniform diameter and of semi-infinite length. In order to put the matter in a general perspective, a comparison follows of the features expected in a homogeneous electrode with those of a porous electrode in which two phases, liquid and solid, become mixed inside the electrode region. A homogeneous electrode with a macroscopically flat surface is shown schematically in Figure 18 (a). The equivalent circuit modeling the cell impedance is a series connection of elements, describing the division of the applied small-signal AC voltage in three parts: one at the bulk of the layer (Z_{bulk}), another at the solid/liquid interface (Z_{if}), and finally another one including the potential drop at bulk electrolyte and metal contacts (R_S).

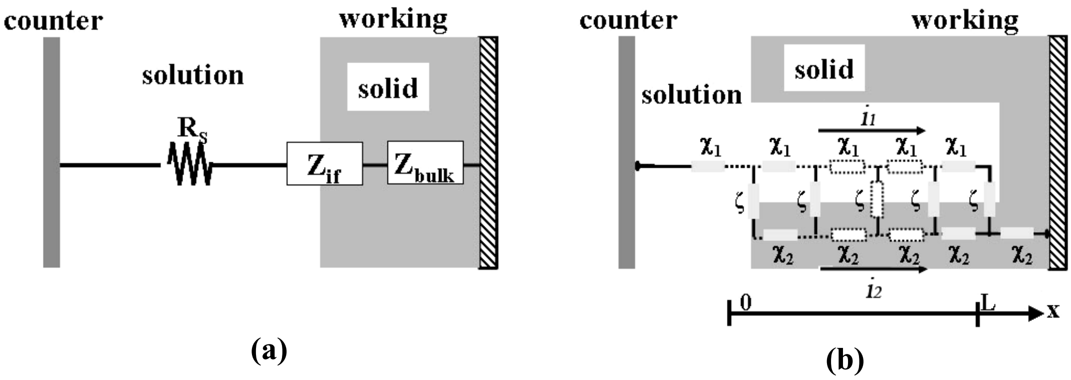

(a) (b)

Figure 18 (a) Scheme of a compact electrode with a macroscopically flat surface and (b) Scheme of a porous electrode.

Adapted from: Bisquert *et al.* (2000).

As is well-known from studies of the interfacial impedance Z_{if} of planar semiconductor electrodes, several effects occur at the semiconductor/liquid contact including the capacitance and resistance of the space-charge region, the effect of surface states, the capacity and charge transfer resistance across the Helmholtz layer (see Appendix A1) and the diffusion of reacting species. Therefore, the form of Z_{if} may become quite complex, but nonetheless the various processes involved in Z_{if} are "localized" in the sense that the potential difference driving these processes obeys two conditions: i) it resides essentially at the semiconductor/electrolyte interface, and ii) it is essentially independent of position on the surface. Another way, the flux of carriers is always normal to the plane of the surface, and the current density is the same at any point on the surface. Consequently, Z_{if} can be described by the series and/or parallel combinations of resistive and capacitive components. In Figure 18 (b), a schematic illustration is provided of those cases where the two phases are closely mixed in space because the layer is porous at a small scale. Both media are considered as effectively homogeneous and continuously connection. A standard equivalent circuit model is represented in Figure 18 (b) that describes the essential features of electrical transport along each phase and the exchange of charge through the inner surface. This model assumes that the dominant contribution to the current is electrical field driven rather than diffusive. Now the porous structure gives rise to the spread of electrical current in various directions. First, electrical charge can flow along each medium (electrolyte and bulk material); the resulting AC currents are termed here i_1 and i_2 (the subscripts 1 and 2 denote the liquid and solid phase, respectively) and they follow the x direction in the scheme of Figure 18 (b), i.e., both i_1 and i_2 are *parallel* to the inner surface.

Moreover, current can flow to the inner surface due to electrochemical reactions and/or capacitive charging. Therefore, at a given location, i_1 may decrease (increase) with a corresponding increase (decrease) of i_2, the constraint being obeyed that $i_T = i_1 + i_2$ (the total current flowing through the external circuit) is independent of position. In accordance with the description of electrical current distribution, the elements χ_1 and χ_2 describe a local ohmic drop at each point of the transport channels, depending on media conductivity and more generally on transport properties, whereas the element ξ describes an exchange of electrical charge at the interface owing to faradaic currents and polarization at the pore surface. The branching in the equivalent circuit model is intended to occur in a continuous pattern. The quantities χ_1 and χ_2 are impedances per unit length ($\Omega \cdot m^{-1}$) corresponding to the whole electrode area (A) and ξ is an impedance length ($\Omega \cdot m$). The overall impedance is isomorphous to that of a transmission line.

MATERIALS AND METHODS

Materials

1. Chemicals and Materials

- Titanium(IV)bis(ethyl acetoacetato)diisopropoxide [[$CH_3C(O-)=CHCO_2C_2H_5]_2Ti[OCH(CH_3)_2]_2$, Aldrich, technical grade]
- Cerium(III)nitrate hexahydrate [$Ce(NO_3)_3.6H_2O$, Fluka, 99.0%]
- Sodium sulfate decahydrate [$Na_2SO_4\bullet 10HO_2$, Fluka, 98%]
- Nitric acid [HNO_3 , Aldrich, 65% w/w]
- Cerium oxide [CeO_2, Aldrich, 99.9%]
- Titanium oxide (P25) [TiO_2, Degussa, 99.9%]
- Methanol [CH_3OH, Aldrich, >98%]
- Acetone [CH_3COCH_3, Aldrich, 98%]
- Indium doped tin oxide [ITO 2 x 3 cm^2 , PGO, <10 Ω/cm^2]
- Platinum-flat electrode [flat, 1 x 1 cm^2, Metrohm]
- Silver/silvercholride electrode [Ag/AgCl 3 M KCl, Metrohm]

2. Equipment

- All prepared powder samples were calcined in a Thermolyne 2100 tube furnace using a quartz tube.
- All prepared film electrodes were calcined in Heraeus furnace.
- The structural morphology was characterized by a Philips X' Pert-MPD X-ray diffractometer using Cu Kα radiation (λ 1.54 Å). The identification of crystalline phase was accomplished by JCPDS files.
- The morphology of electrode was analyzed by Scanning Electron Microscope with Energy dispersive spectrometer (SEM, Philips 525, Institute for Microstruture Technology (IMT), Forschungzentrum Karlsruhe, Karlsruhe, Germany). The others were measured by the Field Emission Scanning Electron Microscope (SEM Philips XL30).

- Ti K-edge and Ce L_3-edge X-ray absorption spectra were recorded using the beam line 8 at the Synchrotron Light Research Institute (SLRI), Nakhon Rachasrima, Thailand with a ring current of 100-50 mA at 1.2 GeV. A Si (111) monochromator crystal was used to eliminate high-order harmonics. Data were collected in transmission mode using gas-filled ionization chambers as detectors. N_2 gas was used to fill into ionization chamber. Energy calibration was carried out for all measurements using Ti foil for Ti K-edge absorption calibration, assigning the first inflection point to 4966 eV. For, CeO_2 were used for calibration of Ce L_3-edge absorption at 5731.5 eV.
- Cyclic voltammograms (CV) and Electrochemical impedance spectra (EIS) were obtained with an IM6 Electrochemical Workstation (Zahner Elektrik, Germany) equipped with a frequency analyzer module.
- A UV meter (PH series, Gentec) was used to measure the intensity of incident light.
- A halogen lamp (250 W, 5025AF-S, Braun, Germany) and a halogen cold light source equipped with fiber optic light guide (250 W, KL 2500, Schott, Germany) were used as light sources.

Methods

1. Preparation and Characterization of TiO_2 Powder

1.1. Sol-gel preparation

1.1.1. Hydrolysis effect (H_2O/precursor ratio, h)

(a) High water content (h =100 and 200)

Titanium(IV)bis(ethyl acetoacetato)diisopropoxide 4.2435 g was added dropwise into 36.00 cm^3 of distilled water which was acidified with concentrated nitric acid to reach pH 1. The suspension was then stirred at 358 K for 90 min and dried at 383 K for 24 h. The dried sample was calcined at 823 K (the heating rate of 1.7 K/min) in flowing N_2/O_2 (70/30) with a total flow rate of 100 cm^3/min for 4 h to obtain the sample TiO_2-HW (Table 2).

(b) Low water content (h = 4)

Titanium(IV)bis(ethyl acetoacetato)diisopropoxide 4.2435 g was mixed with acetylacetone 0.7150 g and ethylene glycol 4.50 cm^3 and stirred to reach homogeneous mixture. Distilled water 0.71 g was added and stirred until the solution was clear. The solution was allowed to rest in an oven at 348 K to form gel and dried at 383 K for 24 h to solidification. The dried sample was calcined at 823 K with the heating rate 1.7 K/min by flowing N_2/O_2 (70/30) with the total flow rate of 100 cm^3/min for 4 h to obtain the sample TiO_2-LW (Table 2).

Table 2 Sample codes for the prepared powder with percentage weight for each component, H_2O/precursor ratio and characterization method.

Sample code	Preparation method	Ti (%w/w)	Ce (%w/w)	H_2O/precursor ratio by mole (h)	Characterization Method
TiO_2-P25	Degussa	100.00	-	-	XRD/EXAFS
TiO_2-LW004	Sol-gel preparation	100.00	-	4	XRD
TiO_2-HW100	Sol-gel preparation	100.00	-	100	XRD/EXAFS
TiO_2-HW200	Sol-gel preparation	100.00	-	200	XRD/EXAFS
8%CeTiO_2-LW004	Sol-gel preparation	91.99	8.01	4	XRD/EXAFS
8%CeTiO_2-HW200	Sol-gel preparation	91.91	8.09	200	XRD

1.2. Characterizations

1.2.1. Powder x-ray diffraction (XRD)

The crystalline phase was identified by XRD. The XRD experiments were performed on a Phillips X' pert x-ray diffractometer using Cu K_α radiation (λ = 1.54 Å) and a curved graphite monochromator. The x-ray tube was operated at 40 kV and 30 mA. X-ray powder diffraction patterns were recorded at step size of 0.02^o with 0.5 s count accumulation per step in the range between 10 and 80 degree. The diffraction pattern has been indexed by comparison with the JCPDS files (Joint Committee on Powder Diffraction Standards).

1.2.2. Extended x-ray absorption fine structure spectroscopy (EXAFS)

(a) Ti K-edge absorption

X-ray absorption spectra at the Ti K-edge were measured in transmission mode of the beam line 8 at SLRI. The synchrotron radiation was monochromatized using a Si (111) double-crystal monochromator. The Ti foil was used to calibrate the K-edge absorption peak at 4966 eV. The operating pressure of chamber was 63 KPa N_2. The absorption measurement was in the range of 4900-5490 eV.

Analysis method

(i) Ti K-edge absorption

The EXAFS spectra [Figure 19 (a)] were recorded from XASAvg (MATLAB modified by Dr. Watana Kylsubun) and data consisted of 7 columns. First, the preceding converted the 7 columns data file into .ave file that can be accessed by PROCESS for data analysis. This conversion worked by running a session of PROCESS and entering a sequence of keystrokes that were listed in prepave.keystroke. The prepave.keystroke file was saved into the folder which was as same as the data file and was modified by a text editor, see Appendix A2.

Second, the EXAFSPAK software was used to extract raw EXAFS data (George and Pickering, 2000). The measured X-ray absorption spectra below the pre-edge region were fitted to a straight line,μ_{spline} (E), was fitted to a polynomial function [Figure 19 (b)]. The polynomials were extrapolated over the entire energy region and subtracted from the total absorption spectra. The absorption spectra with the subtracted background were normailized for the above-edge energy region, $\chi(E)=\{\mu_{\mathrm{expt}}(E)-\mu_{spline}(E)\}/\mu_{vic}(E)$ where the denominator is the Victoreen polynomial that describes absorption by free atoms [Figure 19 (c)]. The normalized k^3-weighted EXAFS spectra [Figure 20 (a)], $k^3\chi(k)$ [or k^3chi(k)], were Fourier transformed to reveal the contribution of neighboring atoms, acting as scatterers, to the Fourier transform (FT) signal, see Figure 20 (b).

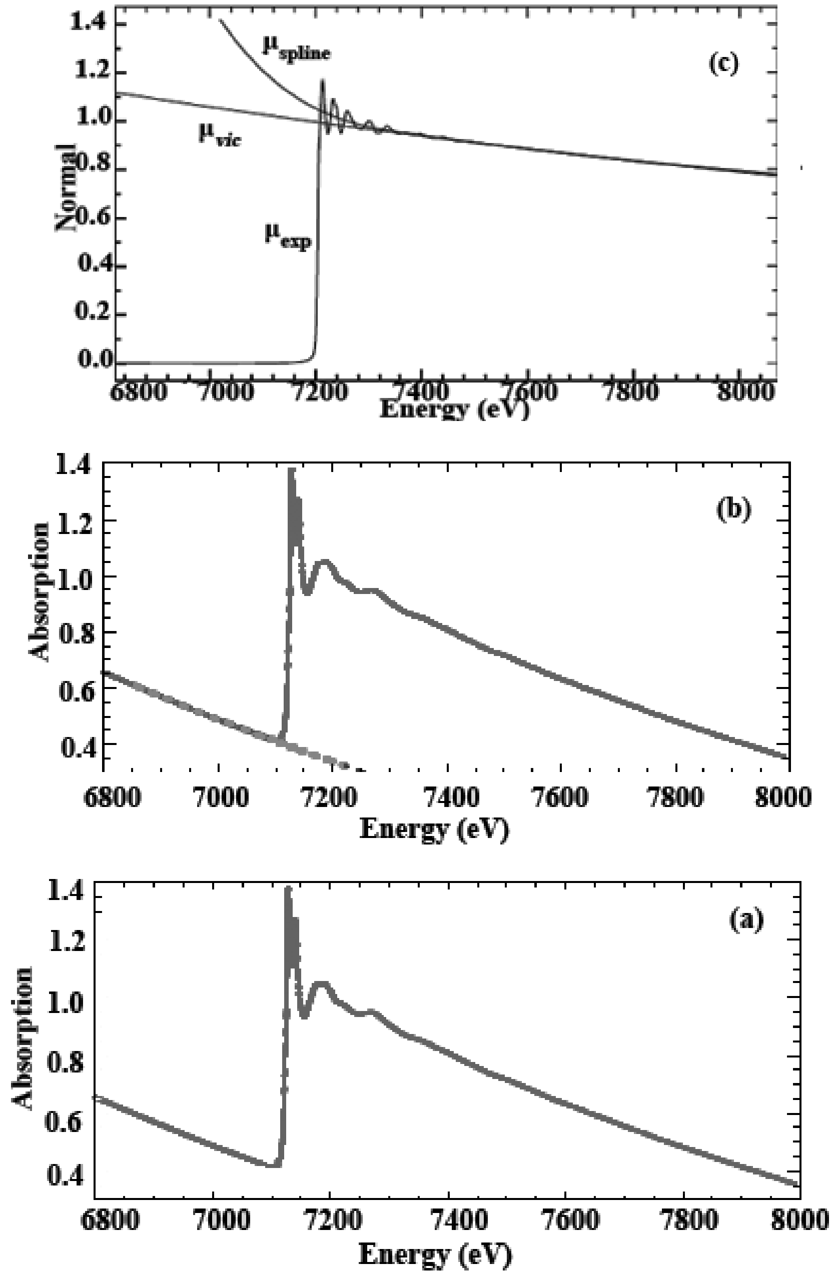

Figure 19 Example of EXAFS data analysis (a) X-ray absorption spectrum, (b) Pre-edge subtraction and (c) Normailization.

Adapted source: George and Pickering (2002).

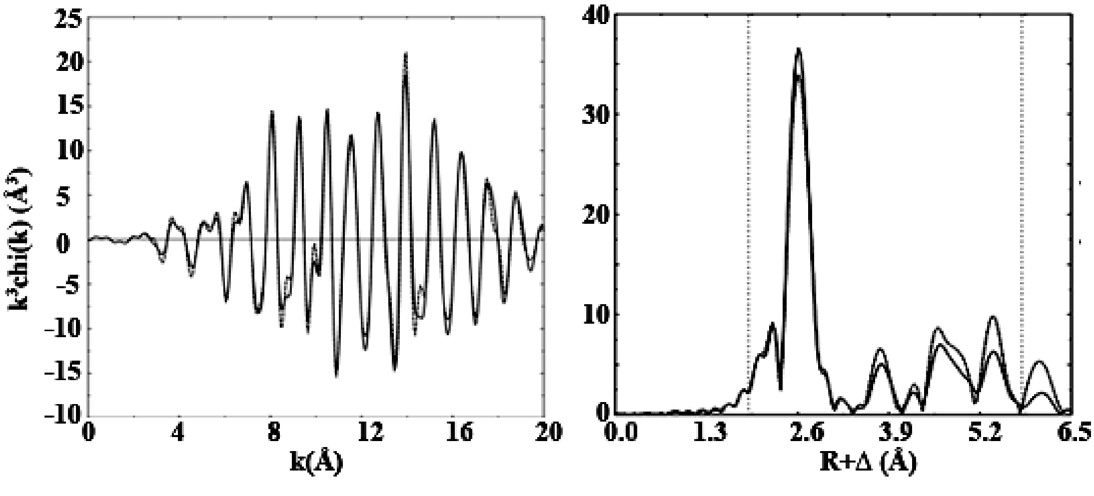

(a) (b)

Figure 20 Example of (a) k^3-weighted EXAFS spectrum and (b) Fourier transformation spectrum.

Adapted source: George and Pickering (2002).

Third, the FEFF7 (not part of EXAFSPAK) was used, for single and multiple scattering analysis, to simulate the theoretical EXAFS spectra, i.e. the criteria for path selection was taken to be the anatase and rutile structure, see Figure 21 (Smith *et al.*, 2009). The ratio anatase and rutile theoretical EXAFS spectra was use a weight average of 14 paths of anatase and 11 paths of rutile included atoms within a 5.5 Å radius from the Ti absorber. All processes could refer to the FEFF7 manual and the example of anatase EXFAS spectrum simulation is shown in Appendix A3.

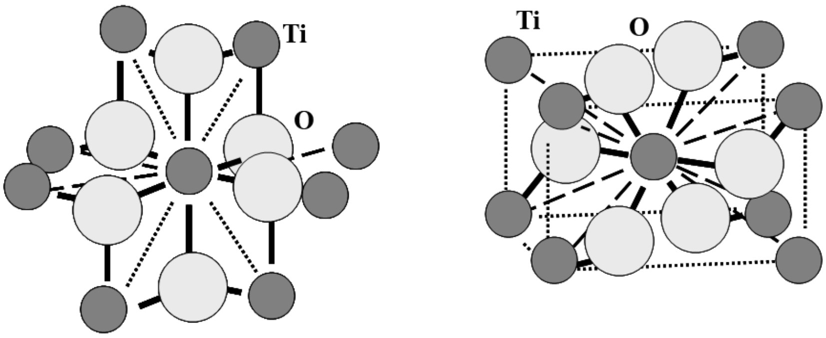

(a) (b)

Figure 21 Structure of (a) anatase and (b) rutile.

Adapted source: Smith *et al.* (2009).

OPT (i.e. a part of EXAFSPAK software) is used for curve fitting EXAFS data to obtain structural information. The EXAFS equation is used by OPT. Each parameter in equation is described in Literature review chapter.

$$\chi(k) \approx S_0^2 \sum_{i=1}^{n} \frac{N_i S_i(k,R_i) F_i(k,R_i)}{kR^2} \exp\left(\frac{-2R_i}{\lambda(k,R_i)}\right) \exp(-2\sigma_i^2 k_i^2) \sin[2kR_i + \phi_i(k,R_i) + \phi_c(k)] \qquad (15)$$

2. Preparation and Characterization of Ce doped TiO_2 Powder

2.1. Sol-gel preparation

2.1.1. Hydrolysis effect (H_2O/precursor ratio, h)

(a) High water content (h = 200)

Titanium(IV)bis(ethyl acetoacetato)diisopropoxide 4.2435 g was added dropwise into a mixture of 36.00 cm^3 H_2O and cerium(III)nitrate hexahrydrate which acidized with concentrated nitric acid to pH 1. The next step was the same as the TiO_2 preparation [1.1.1, (a)] to obtain 8%Ce TiO_2-HW (Table 2).

(b) Low water content (h = 4)

Titanium(IV)bis(ethyl acetoacetato)diisopropoxide 4.2435 g was mixed with acetylacetone 0.715 g and ethylene glycol 4.50 cm^3 and was followed by the addition of cerium(III)nitrate hexahydrate 0.1230 g, 8%Ce and stirred to a homogeneous mixture. 0.71 g of water was added and stirred until the solution was clear. The next step was the same as TiO_2 preparation [1.1.1, (b)] to obtain 8%Ce (Table 2)

2.2. Characterizations

2.2.1. Powder x-ray diffraction (XRD)

The XRD measurement of Ce doped TiO_2 was performed in the same way as TiO_2 characterization, see 1.2.1.

2.2.2. Extended x-ray absorption fine structure spectroscopy (EXAFS)

(a) Ti K-edge absorption

X-ray absorption Ti K-edge and data analysis were performed in the same way as section 1.2.2 (a).

(b) Ce L_3-edge absorption

X-ray absorption spectra at the Ce L_3-edge were measured in transmission mode of the beam line 8 at SLRI. The synchrotron radiation was monochromatized using a Si (111) double-crystal monochromator. The CeO_2 was used to calibrate the L_3-edge absorption peak at 5731.5 eV. The operating pressure of chamber was 87 KPa N_2. The absorption measurement was in rage 5660-5840 eV.

Analysis method

(i) Ti K-edge absorption

The X-ray absorption analysis was fitted following 1.2.2 (i). The anatase structure was calculated using FEFF7.

(ii) Ce L_3-edge absorption

The FEFF7 was used to simulate the theoretical EXAFS spectra with the criteria for path selection taken to be the Ce interstitial in anatase structure and the Ce substitute Ti atom in anatase structure. A FEFF file was modified considering the position of Ce (interstitial and substitute) in anatase structure. The percentage of Ce substitute (interstitial) in anatase structure can be calculated by:

$$\%\text{ by weight (m)} = \frac{M_{Ce}N_{Ce}}{M_{Ce}N_{Ce} + M_{Ti}N_{Ti} + 2M_O N_O} \tag{16}$$

$$\%\text{ by atom (N)} = \frac{N_{Ce}}{N_{Ce} + N_{Ti}} \tag{17}$$

$$\%\text{ Ce by numbers of atom} = \frac{N_{Ce}}{N} = x \quad ; N_{Ce} = Nx \tag{18}$$

Where N = numbers of atom in unit cell = $N_{Ti} + N_{Ce}$

M = atomic weight

<u>Substitute</u>
$$x = \frac{-m(M_{Ti} + 2M_O)}{(mM_{Ce} + mM_{Ti} - M_{Ce})} \tag{19}$$

<u>Interstitial</u>
$$x = \frac{-m(M_{Ti} + 2M_O)}{(m-1)M_{Ce}} \tag{20}$$

3. Preparation and Characterization of Thin Film Electrodes

3.1. Cleaning methods

3.1.1. Conventional cleaning

The indium tin oxide conductive glass (ITO) was rinsed with acetone and then washed with distilled water.

3.1.2. Chemical cleaning

The ITO was treated by boiling acetone (348 K) for 10 min, immersed in 30% v/v HNO_3 for 30 min and followed by distilled water for 1 h.

3.1.3. Oxygen plasma cleaning

Microwave inducted oxygen plasma (PDC-32 G, Harrick) was used with operating pressure of 47 Pa. The DC voltage and current was 700 V and 15 mA, respectively. The operating time was 10 min. The oxygen plasma was accelerated under radio frequency to bombard the absorbed impurities on ITO.

3.2. Preparation of TiO_2 film electrode for cleaning investigation

3.2.1. Dip coating method

(a) TiO_2-SG film electrode

The Titanium(IV)bis(ethyl acetoacetato)diispropoxide 4.2435 g. was added dropwise into the solution of 36.00 cm^3, pH 1 HNO_3. The suspension was stirred at 358 K for 100 min and rested to room temperature. A treated ITO conducting glass was used as a support. An area of 2 x 2 cm^2 of the ITO glass was dipped into the prepared sol for 2 min and heated at 473 K for 10 min. This procedure was repeated 20 times to increase the thickness of TiO_2. Finally, the coating electrode was calcined at 823 K (the heating rate of 1.7 K/min) by flowing N_2/O_2 (70/30) with a total flow rate of 100 cm^3/min for 4 h.

(b) 2%Ce TiO_2-SG film electrode

The 2%CeTiO_2-SG was prepared by the sol-gel method described in section 3.2.1 (a), with the addition of the titanium alkoxide precursor into cerium nitrate acidic solution of 36.00 cm^3. The number of layer was 15 layers.

3.2.2. Suspension method

(a) TiO_2-P25 particulate film electrode

A method described by Vonodpal *et al.* has been modified [Vonodpal *et al.,* 1993]. An aqueous suspension, 300 μl, of TiO_2-P25 (Degussa, 1.00 g) in 50.00 cm3 of H_2O and methanol (1:4 v:v) was applied on an ITO conducting glass plate. The solvent was evaporated at 308 K for 2 h. This process was repeated 5 times to increase the number of layers, followed by calcination at 723 K (the heating rate of 1.7 K/min) by flowing N_2/O_2 (70/30) with a total flow rate of 100 cm^3/min for 4 h.

3.3. Preparation of TiO_2 film electrode on cleaned ITO by conventional method for electrochemical and photoelectrochemical characterizations.

3.3.1. Dip coating method

(a) TiO_2-SG film electrodes

The preparation of TiO_2-SG electrodes were described in section 3.2.1 (a), and ITO substrates were cleaned by conventional method. The thickness of TiO_2-SG film was increased by repeating the dipping process. Sample codes were assigned according to Table 3.

(b) 2%Ce TiO_2-SG film electrodes

The preparation of 2%Ce TiO_2-SG electrodes were described in section 3.2.1 (b) and ITO substrates were cleaned by conventional method. The thickness of 2%Ce TiO_2-SG film was increased by repeating the dipping process. Sample codes were assigned according to Table 3.

Table 3 Sample codes for the electrodes studied with cleaning method, preparation method, number of layers, weight of material, percentage weight for each component.

Sample code	Cleaning method	Preparation method	Number of layers	Weight (g)	Ti (%w/w)	Ce (%w/w)
TiO_2-SG	conventional /chemical	Sol-gel dip coating	10	0.0061	100.00	-
	,,	,,	15	0.0101	100.00	-
	,,	,,	20	0.0136	100.00	-
	,,	,,	25	0.0177	100.00	-
2%CeTiO_2-SG	conventional /chemical	Sol-gel dip coating	10	0.0058	97.69	2.31
	,,	,,	15	0.0120	97.69	2.31
	,,	,,	20	0.0153	97.69	2.31
	,,	,,	25	0.0194	97.69	2.31
TiO_2-P25	conventional /chemical	Particulate drop coating	1	0.0010	100.00	-
	,,	,,	3	0.0026	100.00	-
	,,	,,	5	0.0043	100.00	-
	,,	,,	8	0.0089	100.00	-

3.3.2. Suspension method

(a) TiO_2-P25 particulate film electrode

The TiO_2-P25 particulate film electrodes were prepared as in the same way of section 3.2.2 (a) and ITO substrates were cleaned by conventional method. The number of layers was increased by repeating the dropping process. The sample code of TiO_2-P25 electrodes were listed in Table 3.

3.4. Preparation of TiO_2 film electrode on cleaned ITO by chemical cleaning method for development of experimental set up.

3.4.1. Dip coating method

(a) TiO_2-SG film electrodes

The preparation of TiO_2-SG electrodes were described in section 3.2.1 (a) and ITO substrates were cleaned by chemical cleaning method. Sample codes were assigned according to Table 3.

(b) 2%Ce TiO_2-SG film electrodes

The preparation of 2%Ce TiO_2-SG electrodes were described in section 3.2.1 (b) and ITO substrates were cleaned by chemical cleaning method. Sample codes were assigned according to Table 3.

3.4.2. Suspension method

(a) TiO_2-P25 particulate film electrode

The TiO_2-P25 particulate film electrodes were prepared as in the same way of section 3.2.2 (a) and ITO substrates were cleaned by chemical cleaning method. Sample codes were assigned according to Table 3.

3.5. Characterizations

3.5.1. Powder x-ray diffraction (XRD)

The XRD of TiO_2-SG, 2Ce%TiO_2-SG and TiO_2-P25 electrodes were performed in the same way as TiO_2 power characterization, see 1.2.1.

3.5.2. Scanning electron microscopy with energy dispersive spectroscopy (SEM and EDS)

The morphology of the prepared electrodes was analysed by Scanning electron microscope and the Energy dispersive X-ray spectrometer (SEM, Philips 525) was used for chemical qualitative analysis. Scanning electron microscope was operated at 10-13 kV and specimens were sputtered with Au.

4. Electrochemical and Photoelectrochemical Characterizations

4.1. Cyclic voltammetry (CV)

4.1.1. Dark condition

The Cyclic voltammograms (CV) were carried out in a three-electrode configuration with a Pt flat (1 x 1 cm^2) as a counter electrode and Ag/AgCl/3 M KCl as a reference electrode and thin film electrodes (TiO_2-SG or 2%Ce TiO_2-SG or TiO_2-P25 electrodes, shown in Table 3) as a working electrode recorded with an IM6 Electrochemical Workstation (Zahner Elektrik, Germany). The CV experiments were carried out at the scan rate of 100 mV/s and in the potential range -1.1 to 1.3 V vs. Ag/AgCl. Sodium sulfate (Na_2SO_4, 0.50 M, pH 6.3) was employed as a supporting electrolyte and purged with Ar gas. The cylindrical electrochemical cell was used.

Experimental effects on CV under dark condition were studied in term of film thickness and pH of electrolyte solution as follows:

(a) Film thickness

The CV experiments under dark condition were performed as that described in section 4.1.1. The different thickness of TiO_2 film (TiO_2-SG, 2%Ce TiO_2-SG and TiO_2-P25) electrodes were used, as listed in Table 3.

(b) pH of electrolyte solution

The CV experiments under dark condition were performed as described in section 4.1.1. The 20 layers of TiO_2-SG, 15 layers of 2%Ce TiO_2-SG and 5 layers of TiO_2-P25 were used as working electrodes. Sulfuric acid (H_2SO_4, 50µl) was added to 0.50 M Na_2SO_4 to obtain a pH 2.9 electrolyte solution.

4.1.2. Irradiation condition

The CV experiments under chopped irradiation were performed in the same way as in the dark condition, section 4.1.1 but the scan rate was modified to 25 mV/s and the potential range was -0.4 to 1.2 V vs. Ag/AgCl. The electrochemical set up I, a halogen lamp (250 W, 5025AF-S, Braun) as light source and a cylindrical electrochemical cell, was used.

Experimental effects on CV under irradiation condition were studied in term of film thickness, effect of photon flux and effect of methanol addition as follows:

(a) Film thickness

The CV experiments were described in section 4.1.2. The different thickness of TiO_2-SG, 2%Ce TiO_2-SG and TiO_2P25 electrodes, shown in Table 3, were used as working electrodes. The CV measurements were performed at 100% of photon flux.

(b) Effect of photon flux

The CV experiments were described in section 4.1.2. A 20 layers of TiO_2-SG electrode was used as a working electrode. The percentages of incident light were various distance between the light source and the working electrode (6, 11, 16 and 26) and the different power of light source (two powers; high and low), listed in Table 4. The photocurrents of various distance and power were measured by UV meter (PH, Gentec).

Table 4 The various percentages of incident light.

Distance (cm)	**Power (high and low)**	**Photocurrent (mW)**	**Percentage of incident light (%)**
26	Low	70	10
16	Low	154	22
11	High	324	46
6	Low	513	74
6	High	697	100

(c) Effect of methanol addition

The CV experiments were described in section 4.1.2. The 20 layers of TiO_2-SG was used as working electrode. 2.5 M methanol was added to 0.5 M Na_2SO_4, used as an electrolyte solution. The CV measurements were performed at 100% of photon flux.

4.2. Electrochemical impedance spectroscopy (EIS)

4.2.1. Dark condition

The three electrodes technique was used as that described in 4.1.1. The impedance spectra were recorded with an IM6 Electrochemical Workstation. A 5 mV AC perturbation was applied ranging between 20 mHz to 100 KHz. The setting parameters were listed in Table 5. Sodium sulfate (Na_2SO_4, 0.5 M) was used as electrolyte solution.

Table 5 The setting parameters of EIS measurement

Setting parameter	**Detail**
Mode	Potentiostat
DC voltage	0.6-0.0 V
AC frequency	1 KHz
AC potential amplitude	5 mV
Numbers of counts	1 count
Scan mode	Sweep mode
• lower limit	20 mHz
• start	10 Hz
• upper limit	100 KHz
Step per decade (<66 Hz, > 66 Hz)	3,7

Experimental effects on EIS under dark condition were studied in term of indium tin oxide, porous TiO_2-SG and 2%Ce TiO_2-SG electrodes, Mott-Schottky plot of thin film electrode and TiO_2-P25 particulate film electrode as follows:

(a) Indium tin oxide (ITO), substrate

The EIS experiments were performed in the same way as section 4.2.1 and in the potential range 0.6 to 0.0 V vs. Ag/AgCl. A calcined ITO (823 K) and a non calcined ITO were used as working electrodes.

(b) Porous TiO_2-SG and 2%Ce TiO_2-SG film electrodes

The EIS experiments were performed in the same way as section 4.2.1 and in the potential range 0.6 to 0.0 V. The 20 layers of TiO_2-SG and 15 layers of 2%Ce TiO_2-SG were used as working electrodes.

(c) Mott-Schottky plot of thin film electrode

The EIS experiments were performed in the same way as section 4.2.1 and in the potential range 0.5 to 0.0 V. The 20 layers of TiO_2-SG was used as a working electrode.

(d) TiO_2-P25 particulate film

The EIS experiments were performed in the same way as section 4.2.1 and in the potential range 0.6 to 0.0 V. The 5 layers of TiO_2-P25 was used as a working electrode.

4.2.2. Irradiation condition

The three electrodes technique was used following 4.1.1. The impedance spectra were recorded in the same way as dark condition, section 4.2.1. The electrochemical set up I, the halogen lamp (250 W, 5025AF-S, Braun) and the cylindrical electrochemical cell, was used.

Experimental effects on EIS under irradiation condition were studied in term of indium tin oxide, porous TiO_2-SG and 2%Ce TiO_2-SG film electrode, film thickness and effect of photon flux as follows:

(a) Indium tin oxide (ITO), substrate

The EIS experiments were performed in the same way as section 4.2.2 and in the potential range 0.6 to 0.0 V vs. Ag/AgCl. A calcined ITO was used as a working electrode.

(b) Porous TiO_2-SG and 2%Ce TiO_2 film electrodes

The EIS experiments were performed in the same way as section 4.2.2 and in the potential range 0.6 to 0.0 V vs. Ag/AgCl. The 20 layers of TiO_2-SG and 15 layers of 2%Ce TiO_2-SG were used as working electrodes.

(c) Film thickness

The EIS experiments were performed in the same way as section 4.2.2 and at the potential 0.3 V vs. Ag/AgCl. The 15, 20 and 25 layers of TiO_2-SG electrodes were used as working electrodes.

(d) Effect of photon flux

The EIS experiments were performed in the same way as section 4.2.2 and at the potential 0.3 V vs. Ag/AgCl. A 20 layers of TiO_2-SG electrode was used as a working electrode. The percentages of photon flux, listed in Table 4, were operated.

4.3. Development of the experimental set up

To improve the irradiation process, the halogen light source and the electrochemical cell in the previous irradiation reaction have been changed. The set up I which has been used for the experiment section 4.1.2 and 4.2.2, is as follows: a halogen lamp as an irradiation source (250 W, 5025AF-S, Braun) and a cylindrical electrochemical cell [Figure 22 (a)]. The light source has been changed to a cold halogen lamp with optical fiber light guide (250 W, KL 2500 LCD, Schott) and the electrochemical cell has been changed to a rectangular electrochemical cell. The developed set up was called “set up II” as shown in Figure 22 (b).

(a) (b)

Figure 22 The electrochemical set up; (a) set up I and (b) set up II.

The (photo)electrochemical experiments with the set up II were tested under irradiation as follows:

4.3.1. Cyclic voltammetry (CV)

(a) TiO_2-P25 particulate film electrode

The CV were carried out in a three-electrode configuration with a Pt flat (1 x 1 cm^2) as a counter electrode and Ag/AgCl/3 M KCl as a reference electrode and a TiO_2-P25 electrodes as a working electrode recorded with an IM6 Electrochemical Workstation, see Figure 22. The CV experiments under chopped irradiation were carried out at the scan rate of 25 mV/s and in the potential range –0.4

to 1.2 V vs. Ag/AgCl. Sodium sulfate (Na_2SO_4, 0.50 M, pH 6.3) was employed as a supporting electrolyte and purged with Ar gas. The electrochemical set up I and set up II [Figure 22 (a) and (b)] were used to investigate the influence of the light source and the shape of the electrochemical cell.

(b) TiO_2-SG film electrode

The CV experiments under irradiation were performed as same as in section 4.3.1 (a). A 20 layers of TiO_2-SG electrode was used as a working electrode. The set up II, i.e. the rectangular electrochemical cell and the halogen cold light source, were used [see Figure 22 (b)]. The light source was irradiated from the front side (EE, electrolyte/electrode interface) and the back side (SE, substrate/electrode interface).

4.3.2. Electrochemical impedance spectroscopy (EIS)

(a) TiO_2-SG film electrodes

(i) The direction of illumination

The EIS were carried out in a three-electrode configuration with a Pt flat (1 x 1 cm^2) as a counter electrode and Ag/AgCl/3 M KCl as a reference electrode and a 20 layers of TiO_2-SG electrodes as a working electrode recorded with an IM6 electrochemical workstation. A 5 mV AC perturbation was applied ranging between 20 mHz to 100 KHz. The setting parameters were set as those listed in Table 6. The direction of illumination was assigned front side (EE, electrolyte/electrode interface) and back side (SE, substrate/electrode interface), using the electrochemical set up II [Figure 22 (b)].

Table 6 The setting parameters of EIS measurement

Setting parameter	**Detail**
Mode	Potentiostat
DC voltage	0.6-0.0 V
AC frequency	1 KHz
AC potential amplitude	5 mV
Numbers of counts	1 count
Scan mode	Sweep mode
• lower limit	20 mHz
• start	10 Hz
• upper limit	100 KHz
Step per decade (<66 Hz, > 66 Hz)	3,7

(ii) Effect of applied potential

The three electrodes system was set up in the same way as that described in section 4.3.2 (i) with the setting parameters in Table 6. A 20 layers of TiO_2-SG electrode was used as a working electrode. The DC voltage was varied from 0.6 to 0.0 V vs. Ag/AgCl.

(iii) Effect of methanol addition

The three electrodes system was set up in the same way as that described in section 4.3.2 (i) with the setting parameters in Table 6. A 20 layers of TiO_2-SG electrode was used as a working electrode. 2.5 M methanol was added to 0.5 M Na_2SO_4 being an electrolyte solution. The DC voltage was at 0.3 V vs. Ag/AgCl and the fraction of photon flux was performed.

(b) TiO_2-P25 particulate film electrodes

The three electrodes system was set up in the same way as that described in section 4.3.2 (i). A 5 layers of TiO_2-P25 electrode was used as a working electrode. The DC voltage was performed at 0.6 V vs. Ag/AgCl. The important setting parameters were set as those listed in Table 7.

Table 7 The setting parameters of EIS measurement

Setting parameter	**Detail**
Mode	Potentiostat
DC voltage	0.6 V
AC frequency	100 Hz (or 1 KHz or 5 KHz)
AC potential amplitude	5 mV (or 10 mV)
Numbers of counts	1 count
Scan mode	Sweep mode
• lower limit	20 mHz (or 100 mHz)
• start	10 Hz
• upper limit	100 KHz
Step per decade (<66 Hz, > 66 Hz)	(3,7) [or (5,7)]

RESULTS AND DISCUSSIONS

1 Preparation and Characterization of TiO_2 Powder

1.1 Sol-gel preparation

1.1.1 Hydrolysis effect (H_2O/precursor ratio, h)

(a) High water content (h=100 and 200)

The sol-gel method consists of hydrolysis and polycondensation of alkoxide metal. The important parameter to control the structure of metal oxide is water content. The water content relates to the hydrolysis rate. When the water content is in excess of the hydrolysis that is required for stoichiometry, hydrolysis is observed to approach completion (Niltharach, n.d.). The increase in the hydrolysis rate is observed to lead to highly branched polymeric products, see Scheme I. Rutile has two opposite edges of each (TiO_6^{2-}) sharing to form a linear chain along the 001 direction while anatase has no four edges shared per octahedron. Anatase can be viewed as zigzag chains and each chain can link through edge sharing (Yanqing *et al.*, 2001). The increase in cross linking as a result of the increase in the extent of the hydrolysis at high water content produces more rutile with high density mixed with low density anatase at low temperature.

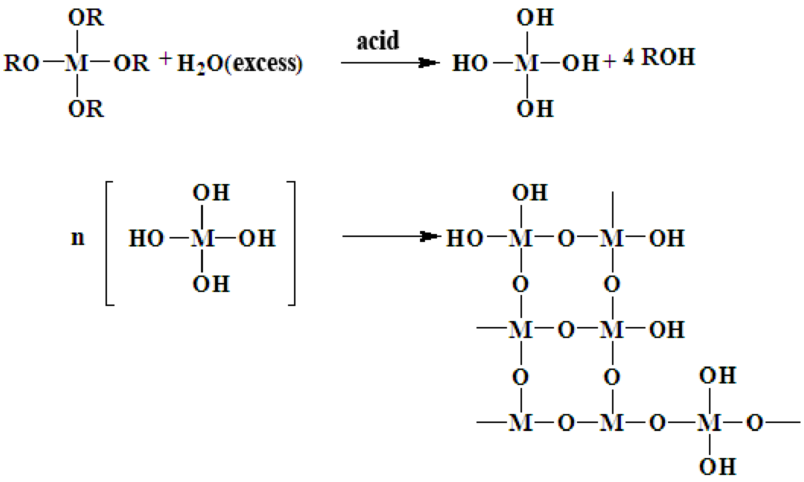

Scheme I

(b) Low water content (h=4)

In the case of the (sub)stoichiometry quantities of water, the hydrolysis of the alkoxide is not complete, and linear oligomers, as opposed to branched ones, see Scheme II (Niltharach, n.d.). Alkyl group (R) of Titanium(IV)bis(ethyl acetoacetato)diisopropoxide is rigid and has a steric effect on condensation (Scheme III). Although, the hydrolysis rate of this case is less than high water content. This result decreases cross linking producing more low density structure, i.e. anatase phase, than high density structure, i.e. rutile phase. This implies that the low hydrolysis rate produces more low density structure.

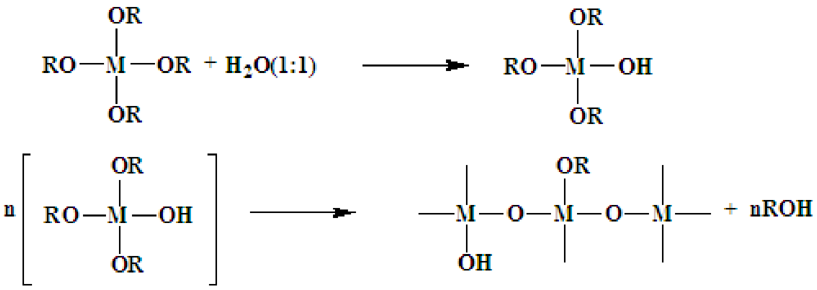

Scheme II

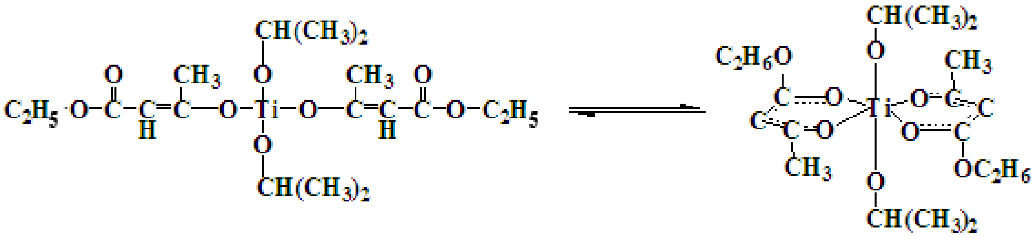

Scheme III

1.2 Charaterization

1.2.1 Powder x-ray diffraction (XRD)

The hydrolysis effect of prepared TiO_2 powder with different water to Ti-precursor ratio was investigated by the XRD. The XRD patterns of TiO_2-P25, TiO_2-LW004, TiO_2-HW100 and TiO_2-HW200 calcined at 823 K for 4 h are shown by overlay XRD patterns in Figure 23. The XRD pattern of TiO_2-P25 [Figure 23 (a)] shows mainly the anatase phase at 2θ 25.33˚, 48.10˚ and 55.10˚ (JCPDS PDF No. 83-2243) with some indication of the rutile phase at 2θ 27.51˚, 54.46˚ and 36.16˚ (JCPDS PDF No. 78-1510). The XRD patterns of the TiO_2 powder prepared with different water to Ti-precursor (TiO_2-LW004, TiO_2-HW100 and TiO_2-HW200) show the mixture phase of the anatase and the rutile phases but the anatase phase is the majority phase of TiO_2-LW004 and TiO_2-HW100 powder [Figure 23 (b) and (c)]. In contrast with TiO_2-HW200, the rutile phase is the majority phase in the XRD pattern [Figure 23 (d)].

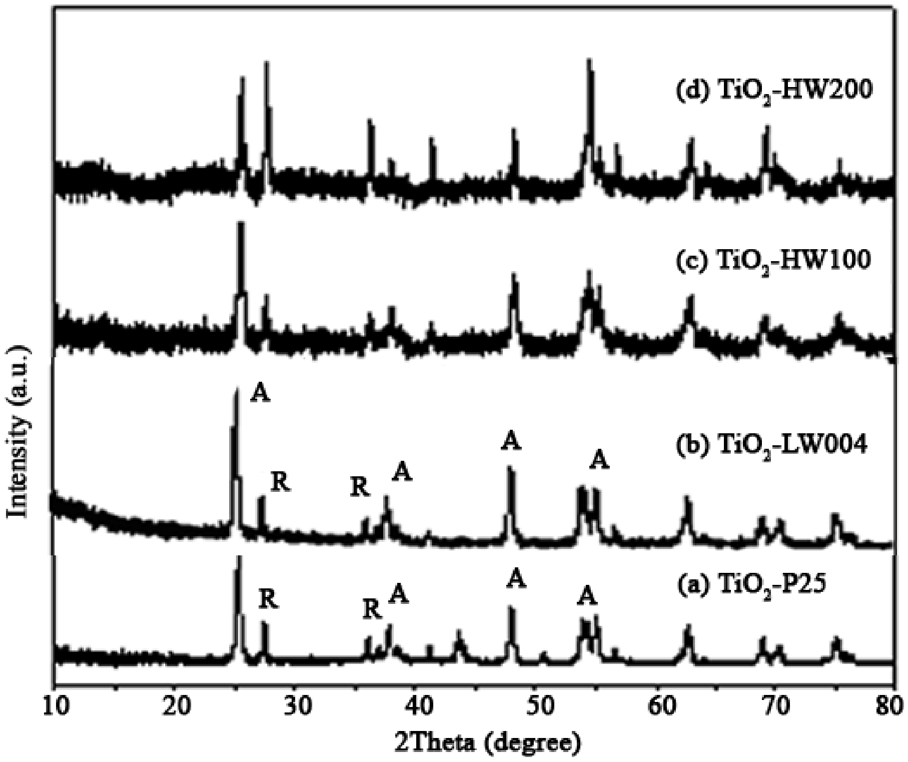

Figure 23 XRD patterns of (a) TiO_2-P25 (b) TiO_2- LW004, (c) TiO_2-HW100 and (d) TiO_2-HW200; A= anatase and R=rutile.

The molar ratio of the anatase and the rutile were determined by taking the ratio of the two most intense peaks of the anatase I_A (101) and rutile I_R (110) phase according to Spurr and Myer's method (Spurr and Myer, 1975).

$$W_R = 1/[1+0.8(I_A/I_R)], \qquad (21)$$

$$W_A = 1 - W_R, \qquad (22)$$

Where W_A and W_R are the mole fractions of the anatase and the rutile, I_A and I_R are the peak intensities of anatase 101 refraction and that of rutile 110 refraction. Table 8 shows the relative percentages of anatase and rutile in the samples.

Example The molar ratio of the anatase and rutile calculation

Sample : TiO_2-HW200

I_R = 1273 counts/sec at 27.67°

I_A = 1203 counts/sec at 25.05 °

$$
\begin{aligned}
W_R &= 1/[1+0.8(I_A/I_R)] \\
&= 1/[1+0.8(1203/1273)] \\
&= 1/[1+0.8(0.94)] \\
&= 1/[1+0.75] \\
&= 0.57
\end{aligned}
$$

$$
\begin{aligned}
W_A &= 1-W_R \\
&= 1-0.57 \\
&= 0.43
\end{aligned}
$$

then percentage of W_R is 57% and that of W_A is 43%

Table 8 The relative percentages of anatase and rutile phase of TiO_2-P25, TiO_2-LW004, TiO_2-HW100 and TiO_2-HW200.

Sample name	**XRD**	
	% anatase	**% rutile**
TiO_2P25	76	24
TiO_2-LW004	74	26
TiO_2-HW100	57	43
TiO_2-HW200	43	57

1.2.2 Extended x-ray absorption fine structure spectroscopy (EXAFS)

(a) Ti K-edge absorption

The Ti K-edge absorption spectra of TiO_2-P25, TiO_2-HW100 and TiO_2-HW200 are shown in Figure 24 (a). The Ti K-edge region approximately 4975 eV is assigned to the well understood dipole-allowed 1s → np ($n \geq 4$) transitions. The raw data was subtracted pre-edge and normalized using the EXAFSPAK software to extract the EXAFS data (George and Pickering, 1993). Figure 24 (b) shows the overlay Fourier transform spectra of the TiO_2-P25, TiO_2-HW100 and TiO_2-HW200. The peak at ~ 1.95 Å is a single scattering path of Ti-O by six coordinated oxygen nearest neighbors around the Ti atom. On the other hand, the two peaks in the range 3-5 Å are a single and a multiple scattering paths of Ti-Ti and Ti-O by neighboring Ti atoms. The single scattering is reflected by neighboring atom (i.e. oxygen) going back directly to an absorber atom (i.e. titanium), (Rehr and Albers, 2000). The multiple scattering is the electron waves of absorber atom onto other atoms which reflects off of still other atoms, see Figure 25. The fitting of TiO_2-HW200 EXFAS spectrum based on single scattering and both single and multiple scattering are shown in Figures 26 (a) and (b). The fitting based on the single scattering disappears along the distance of electron wave reflection while one based on both the single and the multiple scattering shows both short and long distance of electron wave reflection. These indicate that the fitting based on both the single and the multiple scattering is appropriate to apply for the fitting process, see Figure 26 (b).

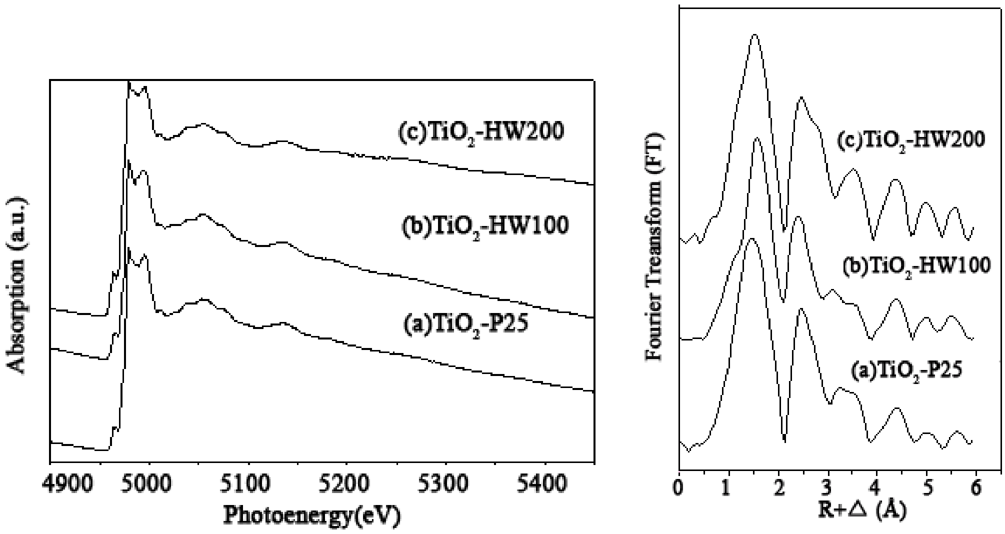

(a) **(b)**

Figure 24 (a) Ti K-edge absorption spectra of TiO$_2$-P25, TiO$_2$-HW100 and TiO$_2$-HW200 and (b) Fourier transform spectra of TiO$_2$-P25, TiO$_2$-HW100 and TiO$_2$-HW200.

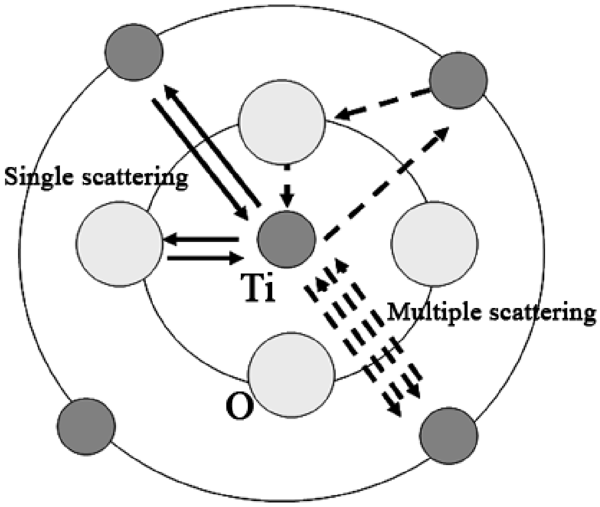

Figure 25 Schematic representation of the single scattering (solid arrow) and the multiple scattering (dash arrow).

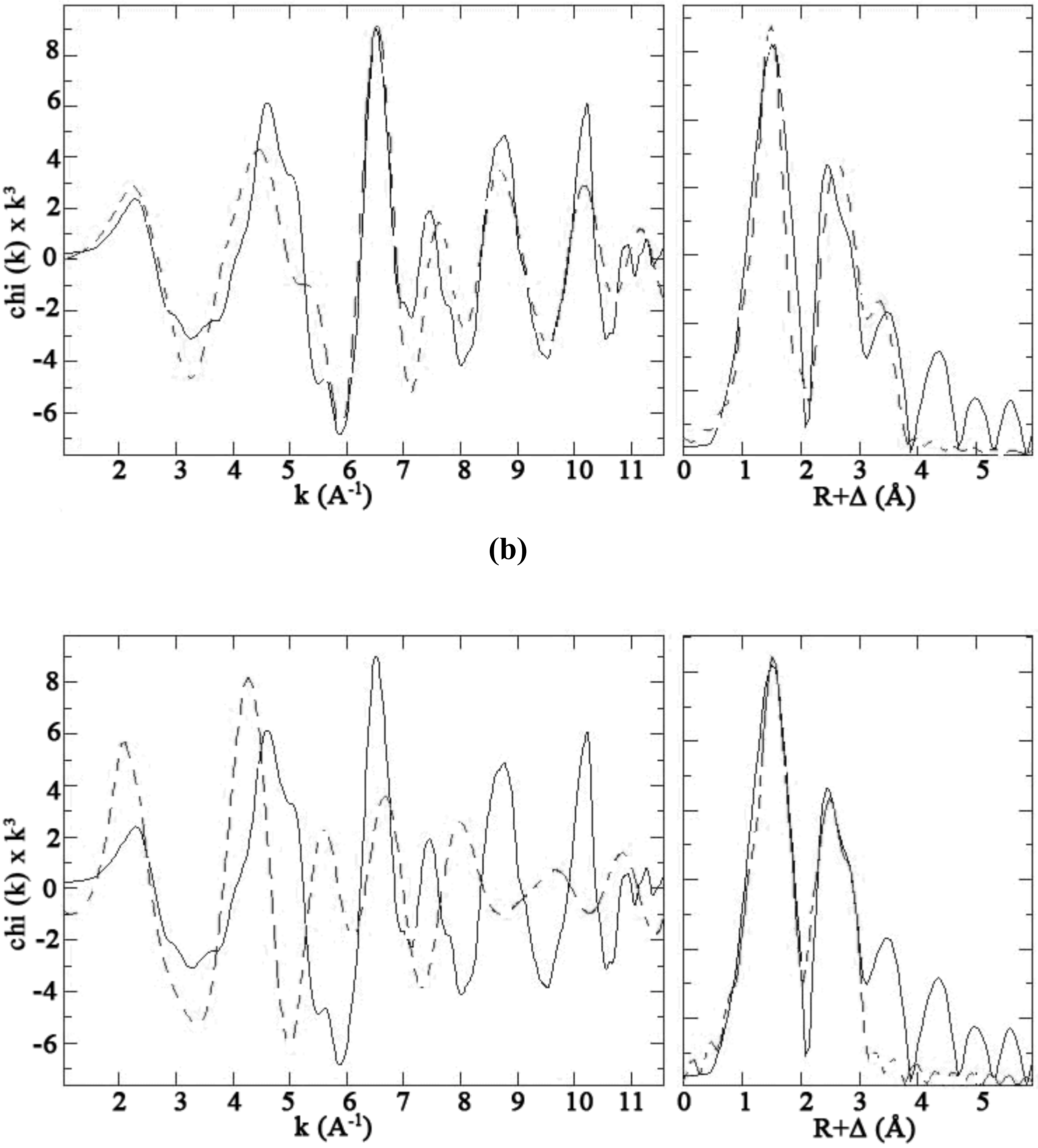

(b)

(a)

Figure 26 The fitting of experiment EXAFS (solid line) and simulation EXAFS (dash line) of TiO_2-HW200 (a) fitting based on the single scattering and (b) based on the single and the multiple scattering.

The anatase is a tetragonal structure (space group $I4_1/amd$) containing 12 atoms per unit cell with lattice parameters a = 3.784 Å and c = 9.514 Å. The Ti^{+4} ions are surrounded by six O^{2-}(4x Ti-O = 1.9338 Å, 2x Ti-O = 1.9790Å, from FEFF). The rutile is a tetragonal structure (space group $P4_2/mnm$) containing 8 atoms per unit cell with lattice parameters a = 4.5845 Å and c = 2.9533 Å (Wyckoff, 1948). The Ti^{+4} ions are surrounded by six O^{2-}(4x Ti-O = 1.9230 Å, 2x Ti-O = 2.0099 Å, from FEFF). The first-shell of neighbors of the Ti atom is thus nearly identical for the two crystal structures. The small difference between the Ti-O bond lengths cannot be resolved by the EXAFS measurement and the differences between the anatase and the rutile EXAFS spectra are due to the effect of higher shells, i.e. more distant neighbors. Nevertheless, the differences are sufficient to give a reasonably good measure of the fraction of anatase and rutile in the samples.

The investigation of the relative percentage of anatase and rutile ratio was done comparing the experiment data and simulation EXAFS spectra based on the known atom position in the anatase and rutile structures. The FEFF7 was used to simulate the EXAFS spectra based on both the single and the multiple scattering due to the accurate calculations. It was modified by weight average of the 14 and 11 most important paths, i.e. both the single and the multiple scattering paths, of anatase and rutile, respectively. The weighted averages of anatase and rutile were produced with the weights taken to be proportional to the relative percentages. The OPT [i.e. part of EXAFS and base on EXAFS eq. (23)] was used to fit between experiment data and simulation data to obtain the anatase to rutile ratio. The only free parameters in the fit were the two constant energy shifts E_0 (one for anatase and another for rutile, the values turned out to be very similar) and the percentage of anatase in the sample. All other parameters were fixed at the theoretical values calculated by FEFF7 (including the Debye-Waller factors σ^2, for which the theoretical values are only rough approximations).

$$\chi(k) \approx S_0^2 \sum_{i=1}^{n} \frac{N_i S_i(k,R_i) F_i(k,R_i)}{kR^2} \exp\left(\frac{-2R_i}{\lambda(k,R_i)}\right) \exp(-2\sigma_i^2 k_i^2) \sin[2kR_i + \phi_i(k,R_i) + \phi_c(k)] \qquad (23)$$

The fitting of experiment EXAFS and simulation EXAFS of TiO_2-P25 is shown in Figure 27. The percentages of anatase and rutile that gave the best fit to the data are shown in Table 9, corresponded to XRD results.

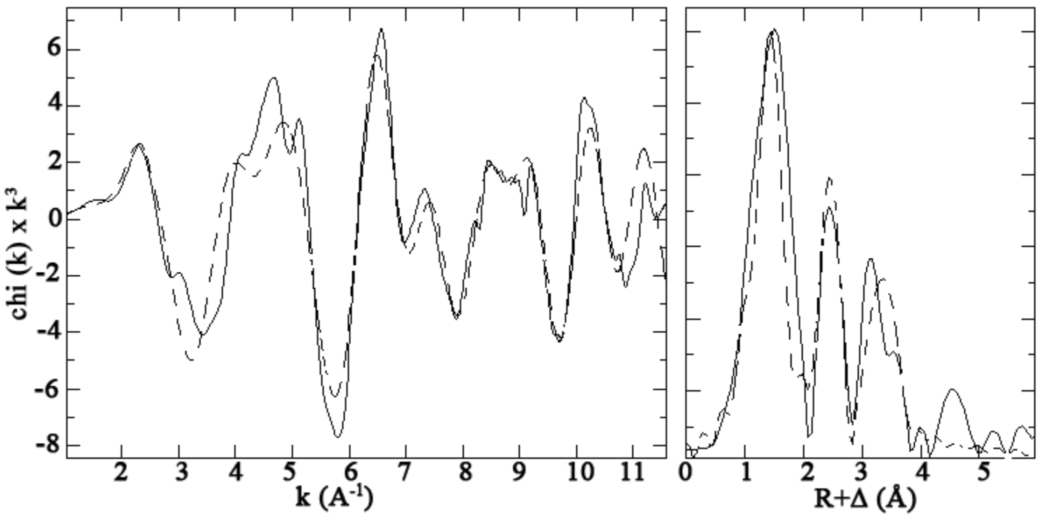

Figure 27 The fitting of experiment EXAFS (solid line) and simulation EXAFS (dash line) of TiO_2-P25.

Table 9 The relative percentages of anatase and rutile phase of TiO_2-P25, TiO_2-anatase, TiO_2-HW100 and TiO_2-HW200.

Sample name	XRD		EXAFS	
	% anatase	% rutile	% anatase	% rutile
TiO_2-P25	76	24	78	22
TiO_2-anatase	99	1	88	12
TiO_2-HW100	57	43	56	44
TiO_2-HW200	43	57	48	52

2 Preparation and Characterization of Ce doped TiO_2 Powder

2.1 Sol-gel preparation

Ce ions were doped into the TiO_2 structure. $Ce(NO_3)_3$ was used as a Ce source. The position of Ce ions in the TiO_2 structure was considered upon possibility; interstitial and substituted in the TiO_2 structure, see Figure 28. Both possible Ce positions in the TiO_2 structure affect TiO_2 formation because Ce ions may prevent the condensation producing the low density phase of TiO_2 (anatase).

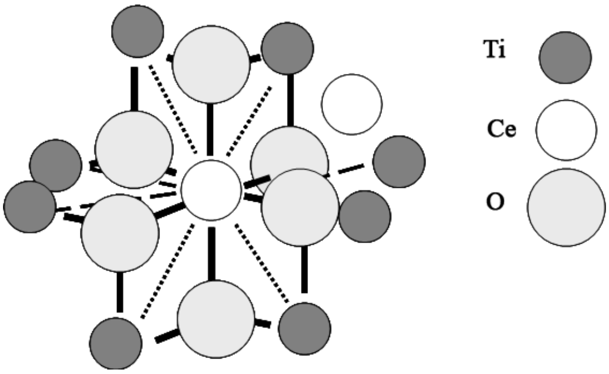

Figure 28 The proposed Ce ion position in the TiO_2 structure including the interstitial and substitute.

2.2 Characterization

2.2.1 Powder x-ray diffraction (XRD)

The TiO_2-SG powder and 8%Ce TiO_2-SG powder were prepared by sol-gel method and calcined at 823 K. The investigated phase behaviors of TiO_2 with different water content and effect of Ce doped in the TiO_2 structure were studied by XRD, see Figure 29. The XRD pattern of TiO_2 resulting from low water to Ti-complex ratio (TiO_2-LW004) shows mainly the anatase phase and some of the rutile phase [Figure 29 (a)]. The XRD pattern of the higher one [TiO_2-HW200, see

Figure 29(b)] shows mainly the rutile phase with some of the anatase phase. These results show that the high hydrolysis rate, i.e. the high water content, which accelerates highly cross linking producing high density phase (rutile). The diffraction patterns of 8%Ce TiO_2-SG (8%Ce TiO_2-LW004 and 8%Ce TiO_2-HW200, see Figure 29 (c) and (d), respectively) show only the anatase phase. These results indicate that the cerium doped in the TiO_2 structure prevents the rutile formation. Ce ions in the TiO_2 structure can stabilize the anatase phase by surrounding cerium atom through the formation of a Ti-O-Ce bond (Worayingyong *et al.*, 2004). The detailed information of Ce ions position will be discussed in the next section.

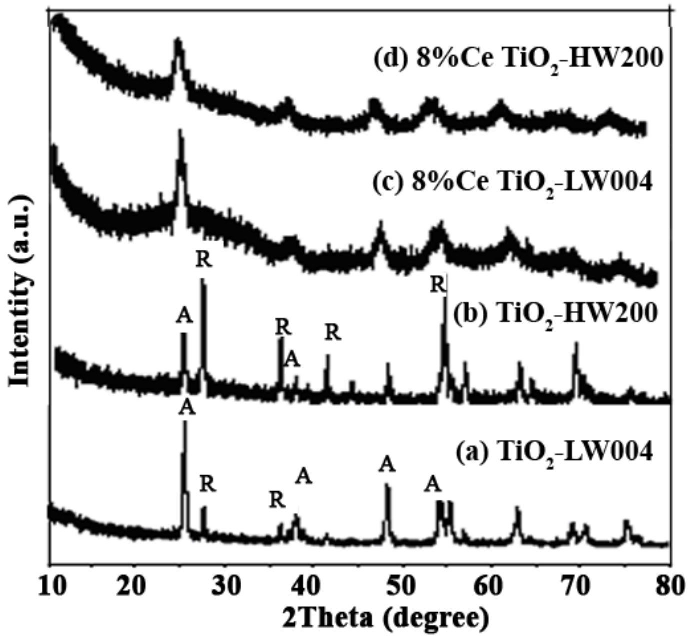

Figure 29 XRD patterns of undoped and doped Ce TiO_2-SG calcined at 823 K , (a) TiO_2-LW004, (b) TiO_2-HW200, (c) 8%Ce TiO_2-LW004 and (d) 8%Ce TiO_2-HW200; A= anatase and R=rutile.

2.2.2 Extended x-ray absorption fine structure spectroscopy (EXAFS)

The possible Ce ions position in the anatase structure is interstitial and substituted but the XRD technique cannot explain a Ce ions position in the TiO_2 structure. An EXAFS is a powerful technique for studying the local structure. The two possible sites of occupying are i) the Ti site (Ce-for-Ti substitution) and ii) the interstitial site located in the center of the square formed by neighboring Ti atoms that is normal the applied c-axis, see Figure 28.

The EXAFS spectra of Ce doped TiO_2-SG using both a) Ti K-edge absorption and b) Ce L_3-edge absorption are shown in Figure 30 (a) and (b), respectively. The former data is good quality and the EXAFS signal is easy to extract. However, these data depend only weakly on the presence of Ce (i.e. the data closely resemble that obtained for undoped samples). The latter data probing the Ce environment directly is very noisy. The aim is to use both measurements to complement one another in elucidating the structure of the Ce-doped samples.

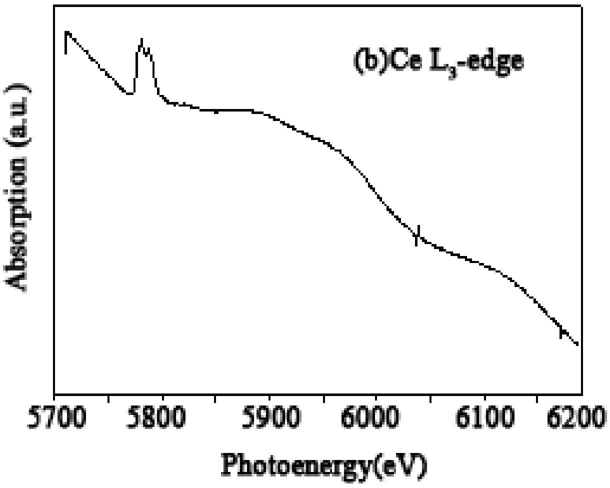

(b)

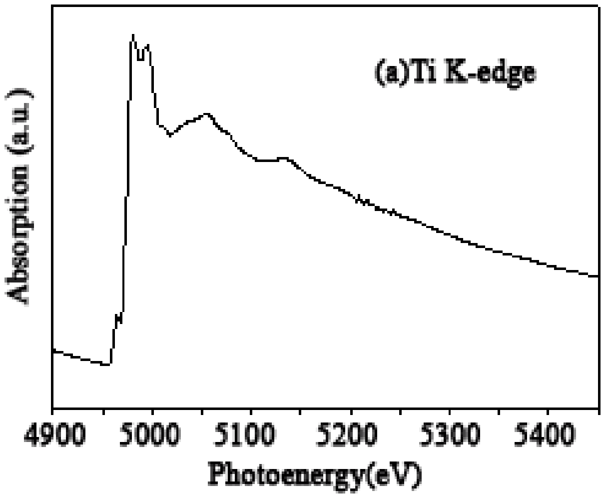

(a)

Figure 30 (a) Ti K-edge absorption spectrum and (b) Ce L_3-edge absorption spectrum of 8%Ce TiO_2-LW004.

(a) Ti K-edge absorption

The Ti K-edge absorption spectrum was analyzed following section 1.2.2 (i) of Materials and Methods chapter using EXAFSPAK software. The EXFAS spectra comparing between the Ti K-edge EXAFS spectrum of TiO_2-anatase

(99.8%, Aldrich) and 8%Ce TiO_2-LW004 are shown in Figure 31. The experimental spectra are obviously similar. The experimental data was fitted to a simulation by varying percentage of anatase and found ~88% anatase of TiO_2-anatase and ~ 77% anatase of 8%Ce TiO_2-LW004. The small effect that Ce has on the EXAFS spectrum was used to learn about the structure of the doped samples. The effects of Ce doping could have on the EXAFS spectrum as directly and indirectly. For Ce-for-Ti substitution, direct effects are changes in the EXAFS spectrum that are caused by the fact that a Ce ion scatters electrons differently than a Ti ion at the same location. For Ce interstitial-occupying, direct effects are features in the EXAFS spectrum that are due to the presence of additional Ce atoms in interstitial sites. Indirect effects of Ce may be due to changes in the lattice parameters of the anatase TiO_2 system (e.g. changes in Ti-O and Ti-Ti bond lengths) or due to phase changes induced by Ce impurities, such as the introduction of domains that have the rutile crystal structure. The presence of Ce is expected to have both direct and indirect effects on the spectrum. Separate consideration was performed by comparison of the experiment and simulation data.

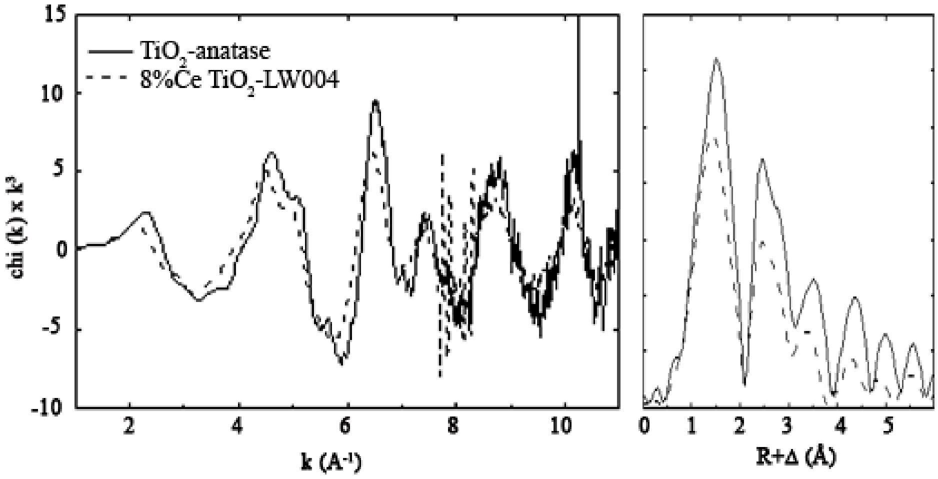

Figure 31 EXAFS spectra of TiO_2-anatase (solid line) and 8%Ce TiO_2-LW004 (dash line).

Figure 32 shows Fourier transform spectra of EXAFS simulations for both Ce occupation sites in the anatase lattice [i.e. interstitial [Figure

32 (a)] and substitute [Figure 32 (b)]]. This shows the expected direct effect of Ce on the Ti-absorption spectra. The Ce substitutes Ti position in TiO_2 structure have a much larger effect on the Ti spectra, which is not surprising. The height of the peak at ~ 2.5 Å (Ce-O) in the Fourier transform spectra increases with the amount of Ce ions.

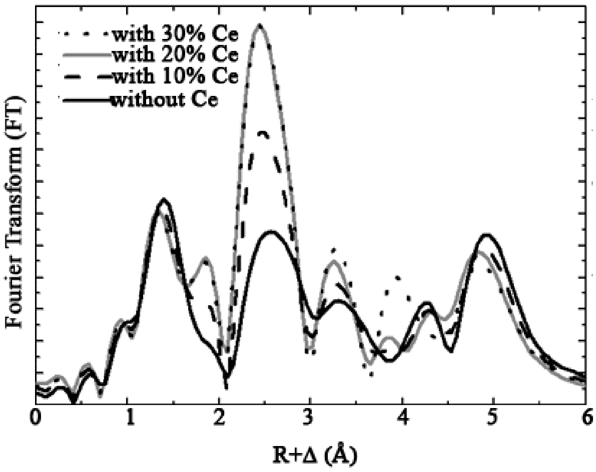

(b)

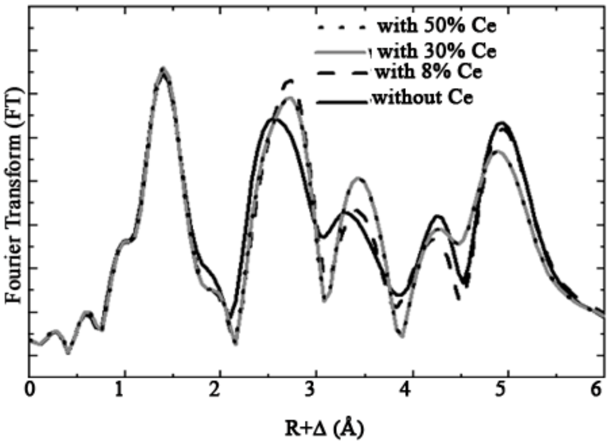

(a)

Figure 32 Fourier transform spectra of (a) interstitial of Ce in the TiO_2 structure and (b) substitute Ce on Ti position in the TiO_2 structure.

The fitted data with simulations found interstitial of Ce in the TiO_2 structure, anatase structure (with 10% Ce), which is consistent with our data, as shown in Figure 33 (F-factor = 0.7190E+03 and Weight F-factor = 48.03%).

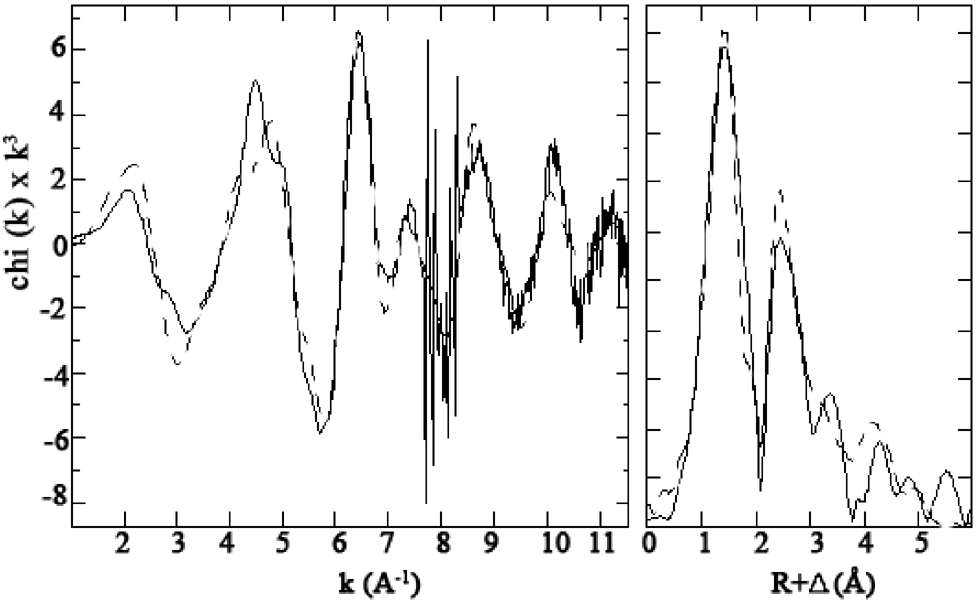

Figure 33 Ti EXAFS and Fourier transform spectra of 8%Ce TiO_2-LW004 (solid line) compared with the simulation of interstitial of 10%Ce in the TiO_2 structure (dash line).

(b) Ce L_3-edge absorption

The Ce absorption spectra for low percentages of Ce has small edge jump that affect the EXAFS $\chi(k)$, [or chi (k)], calculated by $\chi(k) = (\mu_{exp} - \mu_{spline})/\mu_{vic}$ where μ_{exp} is the experimental absorption (pre-edge result), μ_{spline} is the spline fit and μ_{vic} is Victoreen coefficients, shown Figure 34. The 8%Ce TiO_2-LW004 has a small edge jump and shows large spurious features at high energy that are likely due to background absorption. Thus, the data was restricted to a small energy range above the edge for data extraction (5660-5885 eV).

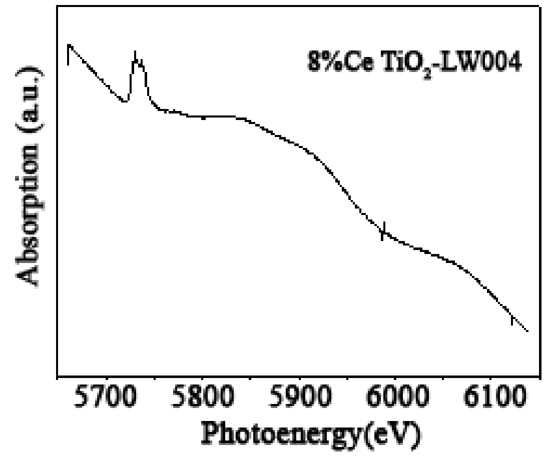

Figure 34 Ce L$_3$-edge absorption spectrum of 8%Ce TiO$_2$-LW004.

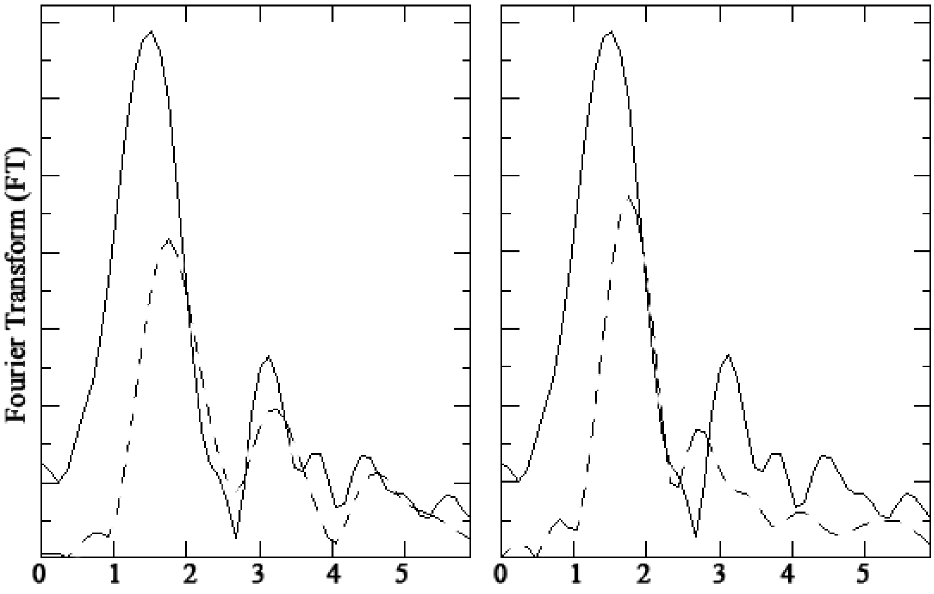

(a) (b)

Figure 35 Ce L$_3$-edge EXAFS of 8%CeATi-LW004 fitting with interstitial (a) and substitute occupation (b), experiment data (solid line) and simulation data (dash line).

From Figure 35, the fits of the data over this energy range were used to simulate each site of occupation. The simulated EXAFS for Ce-for-Ti substitution has two peaks at low radius (R). The second peak, occurring at ~ 2.5Å in the spectra is due to the neighboring Ti atoms (note that as well as theoretical curves have not been phase corrected, so the peak in the Fourier transform occurs at a smaller distance than the actual Ti-Ti distance in anatase, which is 3.03 Å). In the interstitial simulations, only one peak is seen. This is because the neighboring O atoms and Ti atoms are at distances from the absorbing Ce that are sufficiently similar to the corresponding peaks which cannot be resolved, and rather merge into one broad peak. The experimental data shows only a single peak and not any evidence of a feature at 2.5 Å. This would suggest interstitial occupation. However, because the data is limited to a narrow energy range, the presence (or lack thereof) of the 2.5 Å peak might not depend on the manner of background subtraction. The graphical program PySpline (see Appendix A4) was used to investigate the dependence of the spectra on background subtraction and a peak appeared a 2.5 Å. This analysis is not yet complete. One must also make sure that the local structural relaxation around the Ce impurity is not drastic enough to significantly alter the expected EXAFS signal from that determined assuming the bulk anatase structure. This effect is currently being investigated via first principle simulations done at SLRI. The actual distances between the Ce atom and the neighboring O and Ti atoms were being determined by ab initio calculations.

The preliminary evidence indicates interstitial occupation but the analysis of the Ce absorption data is not yet complete. Also, because of the difficulties in background subtraction noted above, the more experimental information about the background absorption in the conditions of the measurement would be useful. This would be provided by further measurements of 8% Ce TiO_2-SG samples. For example, it would be relatively easy to determine that one sample of 8% Ce-doped anatase titania has Ce in the interstitial site. This could be done by comparing the spectra, which would have very similar background absorption, and showing that one spectrum shows the 2.5 Å peak. On the other hand, an absolute determination that Ce is in the interstitial site, using the EXAFS spectrum of a single 8% doped sample, is more difficult because of the effect of the background and, indeed, whether the 2.5 Å peak is expected to be observable given the noisiness of experimental data.

The Ce L_3-edge absorption spectra have an interesting double-peak XANES feature near the edge. The double-peak shape of the edge is due to two transitions: the lower-energy peak is assigned to the $2p \rightarrow 5d$ transition with $4f^1$ L configuration, the higher-energy peak to the $2p \rightarrow 5d$ transition with $4f^0$ L configuration (Fonda *et al.* 1999). The occurrence of both peaks gives information about the valence state of the Ce ion. This information is independent of the EXAFS signal, which occurs after the edge jump. This process of further studying the significance of double-peak structure will be the other consideration.

3 Preparation and Characterization of Thin Film Electrodes

3.1 Preparation and characterization of thin film electrodes for cleaning investigation

3.1.1 Powder x-ray diffraction (XRD)

(a) Indium tin oxide (ITO), substrate

The cleaning of the indium tin oxide (ITO) substrate was considered to prepare the deposited TiO_2 film electrode. Comparing the different cleaning methods, the XRD patterns of bare ITO conducting glass cleaned by the conventional cleaning, the chemical cleaning and the oxygen plasma cleaning are shown Figure 36. The XRD patterns of bare ITO electrodes show only peaks of characteristic In_2O_3 as coating on borosilicate glass (JCPDS PDF No.06-0416) for a conventional cleaning [Figure 36 (a)], a chemical cleaning [Figure 36 (b)] and an oxygen plasma cleaning [Figure 36 (c)]. These indicate that the ITO electrodes are not damaged by the cleaning method.

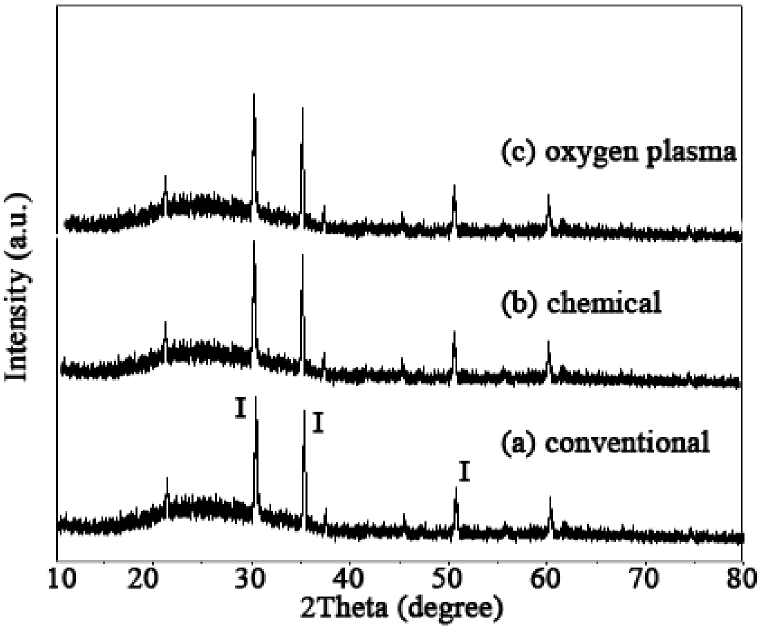

Figure 36 XRD patterns of ITO conducting glass cleaned by different cleaning methods; (a) conventional cleaning, (b) chemical cleaning and (c) oxygen plasma cleaning; I= In_2O_3.

(b) TiO_2-SG film electrode

The XRD pattern of TiO_2-SG on cleaned ITO by the conventional cleaning method shows mainly the anatase phase at 2θ 25.33°, 48.10° and 55.10° (JCPDS PDF No. 83-2243) with some indication of the rutile phase at 2θ 27.51°, 54.46° and 36.16° (JCPDS PDF No. 78-1510) [Figure 37 (a)]. The XRD patterns of TiO_2-SG on cleaned ITO by the chemical cleaning and the oxygen plasma cleaning show the characteristic peaks of mixture phases of anatase and rutile including characteristic peaks of In_2O_3 [Figure 37 (b) and (c)]. The TiO_2-SG was prepared with a high water content (HW200), adjusted pH 1 to show the mixture phase anatase and rutile as P25 (i.e. a mixture of 75%anatase and 25%rutile). The ITO substrates, cleaned by using the different cleaning methods were immersed in the

TiO_2-SG sol. Consequently, they were heated to obtain TiO_2 deposited on treated ITO, called the TiO_2-SG film electrodes. These XRD results show that the cleaning method have not effect on TiO_2 formation.

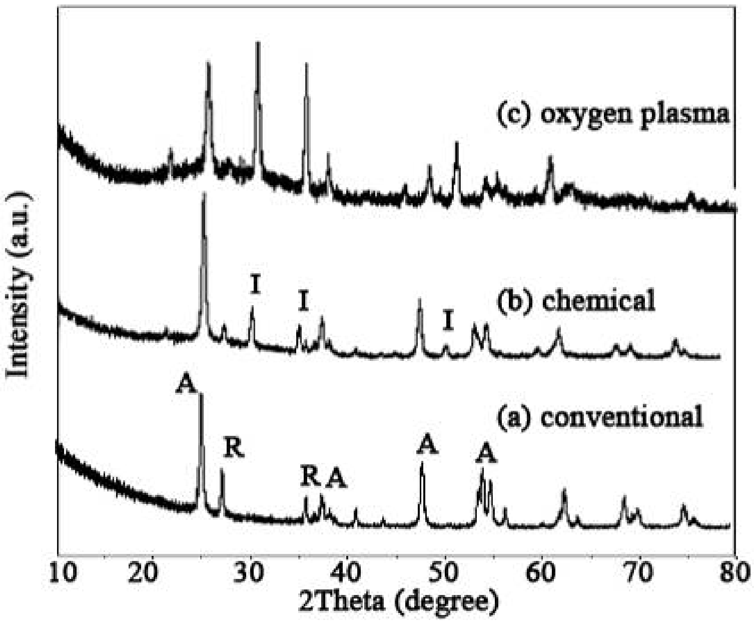

Figure 37 XRD patterns of TiO_2-SG on cleaned ITO by different cleaning methods; (a) conventional cleaning, (b) chemical cleaning and (c) oxygen plasma cleaning; A= anatase, R= rutile and I= In_2O_3.

(c) 2%Ce TiO_2-SG film electrode

The XRD patterns of 2%Ce TiO_2-SG on cleaned ITO by a conventional and a chemical cleaning method show only characteristic peaks of anatase phase at 2θ 25.33°, 48.10° and 55.10° (JCPDS PDF No. 83-2243), see Figure 38 (a) and (b), respectively. The XRD pattern of 2%Ce TiO_2-SG on cleaned ITO by an oxygen plasma cleaning shows characteristic peaks of anatase including characteristic peaks of In_2O_3 [Figure 38 (c)]. These XRD results indicate that Ce ions prevent the rutile formation, comparing TiO_2-SG film electrode (Figure 37).

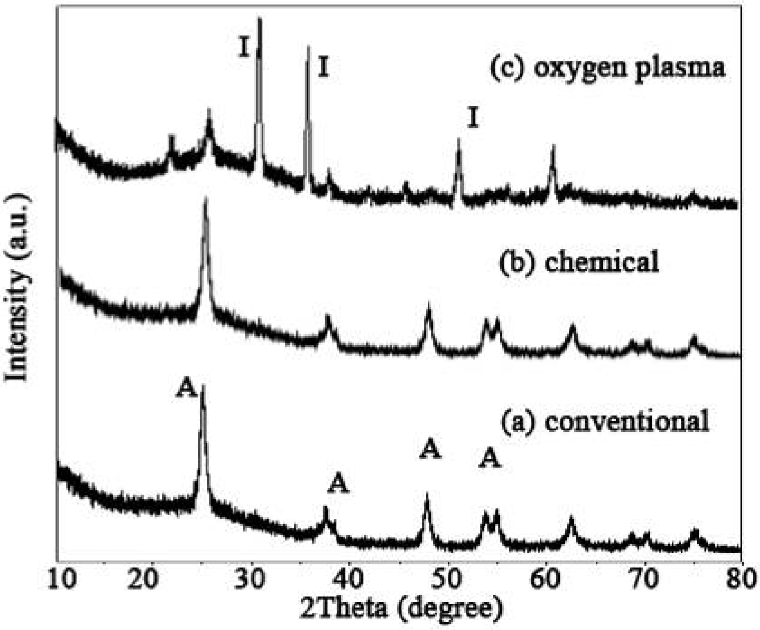

Figure 38 XRD patterns of 2%Ce TiO_2-SG on cleaned ITO by different cleaning methods; (a) conventional cleaning, (b) chemical cleaning and (c) oxygen plasma cleaning; A= anatase, R= rutile and I= In_2O_3.

(d) TiO_2-P25 particulate film electrode

The XRD patterns of TiO_2-P25 on cleaned ITO by a conventional cleaning method shows mainly the anatase phase at 2θ 25.33°, 48.10° and 55.10° (JCPDS PDF No. 83-2243) with some indication of the rutile phase at 2θ 27.51°, 54.46° and 36.16° (JCPDS PDF No. 78-1510) because of P25 is a mixture phase of 75% anatase and 25% rutile [Figure 39 (a)]. The XRD patterns of TiO_2-P25 on cleaned ITO by a chemical cleaning and oxygen plasma cleaning show characteristic peaks of mixture phases of anatase and rutile including characteristic peak of In_2O_3 [Figure 39 (b) and (c)]. The TiO_2-P25 film electrode was prepared by the dropping the suspension of mixed P25 and methanol to a cleaned ITO substrate. Consequently, they were heated to obtain TiO_2-P25 depositing on treated ITO, called the TiO_2-P25 film electrodes. These results reveal that the cleaning method have not effect to phase of P25. For oxygen plasma cleaning method, the XRD patterns of different TiO_2 electrode show the characteristic peaks of deposited TiO_2 including the characteristic peaks of In_2O_3. These may be the thickness of sample is very thin.

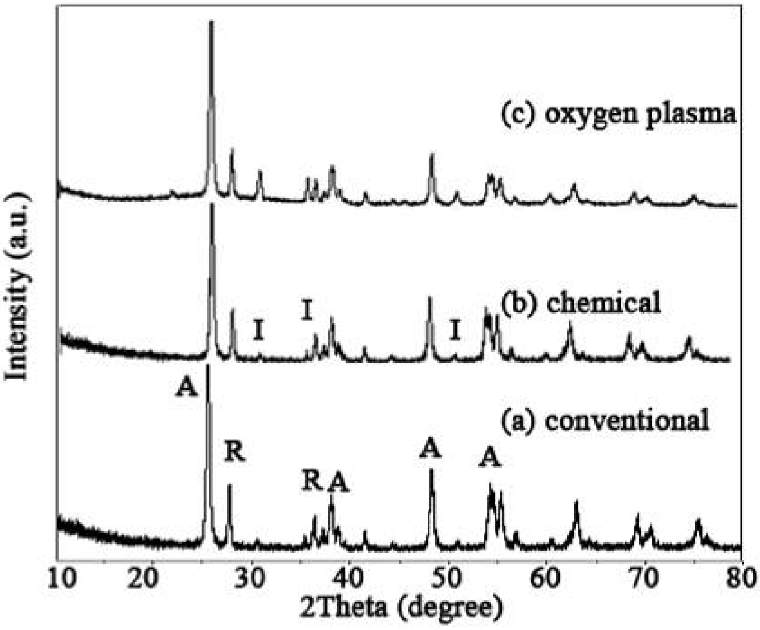

Figure 39 XRD patterns of TiO_2-P25 on cleaned ITO by different cleaning methods**;** (a) conventional cleaning, (b) chemical cleaning and (c) oxygen plasma cleaning; A= anatase, R= rutile and I= In_2O_3.

3.1.2 Scanning electron microscopy with energy dispersive spectroscopy (SEM and EDS)

(a) Conventional cleaning

Form 3.1.1, the XRD patterns of the different cleaning method are similar. To study the morphology of material surface, the bare ITO and prepared TiO_2 film electrodes were studied using SEM technique. The surface of the TiO_2-SG electrode shows island of TiO_2-SG on ITO due to these were prepared by sol-gel method with high water content [Figure 40 (a)]. In additional, the SEM of 2%Ce TiO_2-SG shows similar to TiO_2-SG electrode [Figure 40 (b)]. The sol TiO_2 (2%Ce

TiO_2) was aged at 358 K to form colloidal gel and then ITO was dipped in gel. The dip-coated TiO_2 electrode was dried at 473 K and calcined at 823 K. The dip-coated TiO_2 (2%Ce TiO_2) gel electrode lost water and organic ligand with increasing calcination temperature to transform to porous TiO_2 (2%Ce TiO_2) cover on ITO.

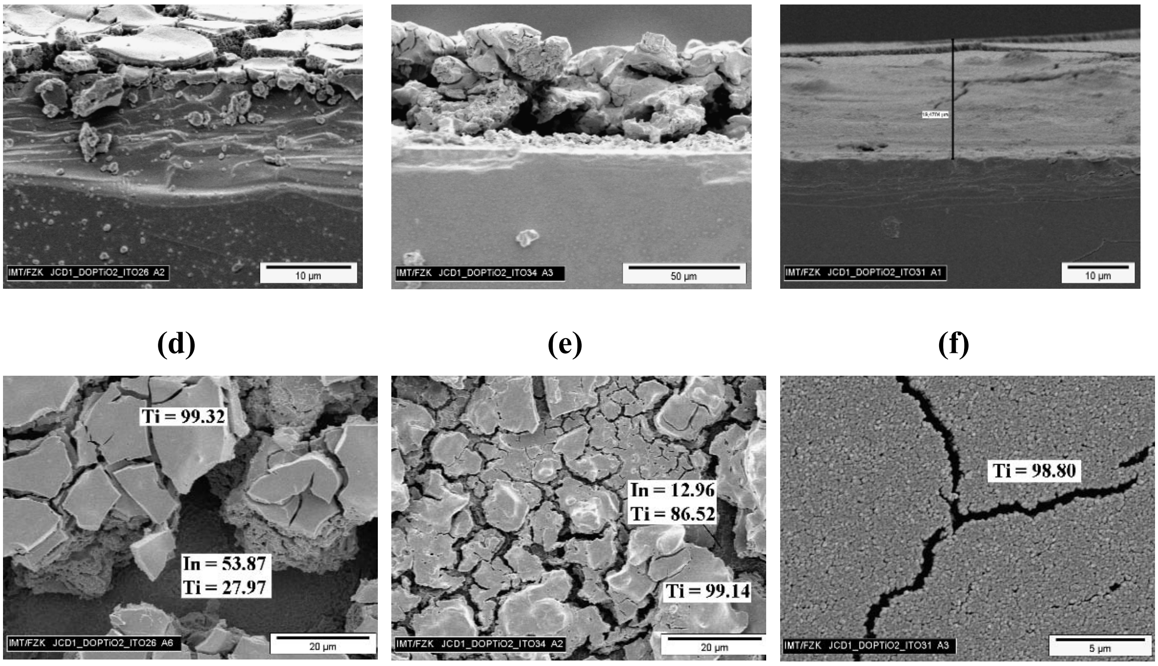

(d) **(e)** **(f)**

(a) **(b)** **(c)**

Figure 40 SEM of TiO_2-SG film electrodes with top view (a) and side view (d), SEM of 2%Ce TiO_2-SG film electrodes with top view (b) and side view (e) and SEM of TiO_2-P25 particulate film electrodes with top view (c) and side view (f).

In contrast, The SEM of the TiO_2-P25 electrode shows agglomerated fine particles on the substrate because the TiO_2-P25 electrode was prepared from P25 suspension and the solvent of suspension was eliminated by calcination at 723 K [Figure 40 (c)]. The thicknesses of different electrodes are 13, 56, and 13 μm. for TiO_2-SG, 2%Ce TiO_2-SG and TiO_2-P25, see Figure 40 (d), (e) and (f), respectively. The element percentage of electrodes is shown onset in Figure 40 (a), (b) and (c) and shown that ITO conducting glass coated with thin film TiO_2 at the cracking area. These SEM results indicate that cleaning method is important parameter to prepare the smoothly film electrode.

(b) Chemical cleaning and oxygen plasma cleaning

The SEM of 1 layer of non-calcined and calcined TiO_2-SG on cleaned ITO by the chemical and oxygen plasma cleaning methods are shown in Figure 41.

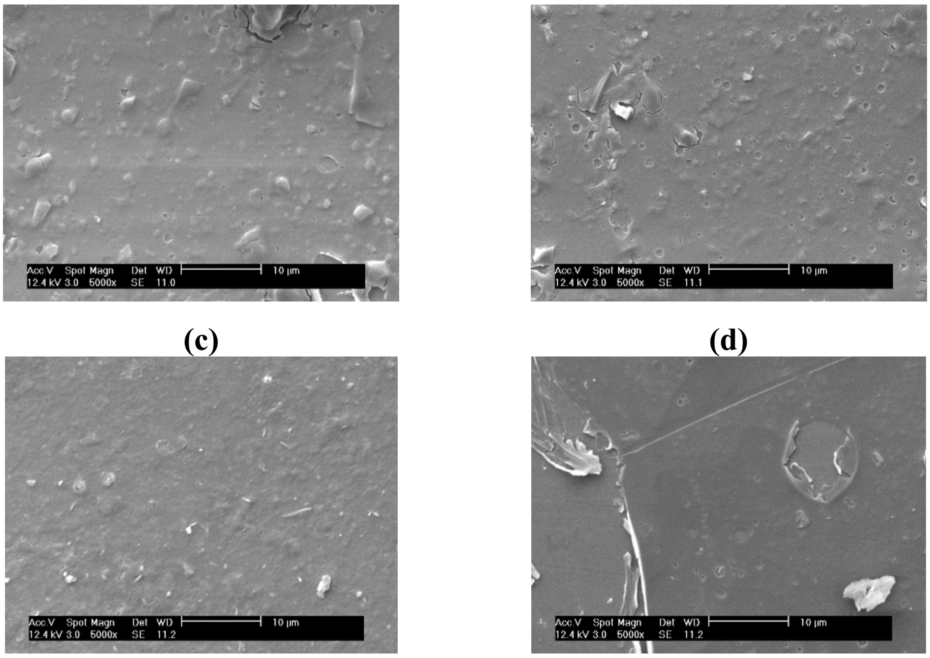

(c) **(d)**

(a) **(b)**

Figure 41 SEM of 1 layer of TiO_2-SG film electrodes (a) non-calcined and (b) calcined of 1 layer of TiO_2-SG film electrodes on cleaned ITO by chemical cleaning and (c) non-calcined and (d) calcined of 1 layer of TiO_2-SG electrodes on cleaned ITO by oxygen plasma cleaning.

Both cleaning methods show the smoothly first layer of non-calcined and calcined TiO_2 surface. These reveal thin film TiO_2 without cracking on

ITO electrodes comparing section 3.1.2 (a). Theses results indicate the cleaning process is an important method before coating TiO_2 on ITO.

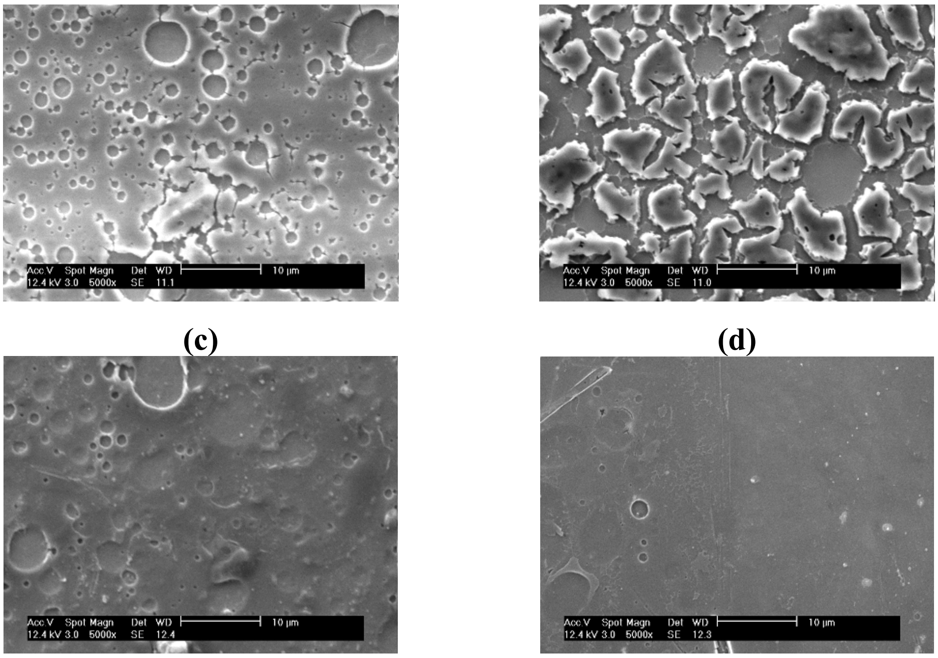

(c) (d)

(a) (b)

Figure 42 SEM of 5 layer of TiO_2-SG film electrodes (a) non-calcined and (b) calcined of 5 layer of TiO_2-SG film electrodes on cleaned ITO by chemical cleaning and (c) non-calcined and (d) calcined of 5 layer of TiO_2-SG electrodes on cleaned ITO by oxygen plasma cleaning.

Figure 42 shows the 5 layers of deposited TiO_2-SG on cleaned ITO by the chemical and oxygen plasma cleaning methods. Comparing the difference thickness of TiO_2-SG, see Figure 41 and Figure 42. A higher number of layers show more cracking area for TiO_2 electrode on cleaned ITO by an oxygen plasma method while chemical cleaning shows a small cracking area of deposited TiO_2-SG electrode. However, the ITO covered with TiO_2-SG 1 layer showed smooth surface (Figure 41). These imply that the surface become incoherently surface for oxygen plasma so the TiO_2-SG gel difficultly deposits on the second layer of TiO_2-SG. The chemical cleaning method was used for preparing the film electrode because it is more comfortable and cheaper compared to the oxygen plasma method.

The SEM photographs of different TiO_2 film electrodes on cleaned ITO by chemical cleaning method are shown in Figure 43. The low magnification SEM of different TiO_2 film electrodes show significantly different. The SEM of undoped and doped TiO_2-SG are the film TiO_2 deposited on ITO photographs [Figure 43 (a) and (b)] while the SEM of TiO_2-P25 is an accumulating particulates P25 photograph [Figure 43 (c)]. When increase the magnification of SEM, the particle size of undoped and doped TiO_2 are in range 20-30 nm [Figure 43 (d) and (e)] while the particle sizes of TiO_2-P25 is about 50 nm, see Figure 43 (f). These results indicate that the sol-gel method can produce the nanoparticles of TiO_2 and smaller TiO_2 particle than P25 particle.

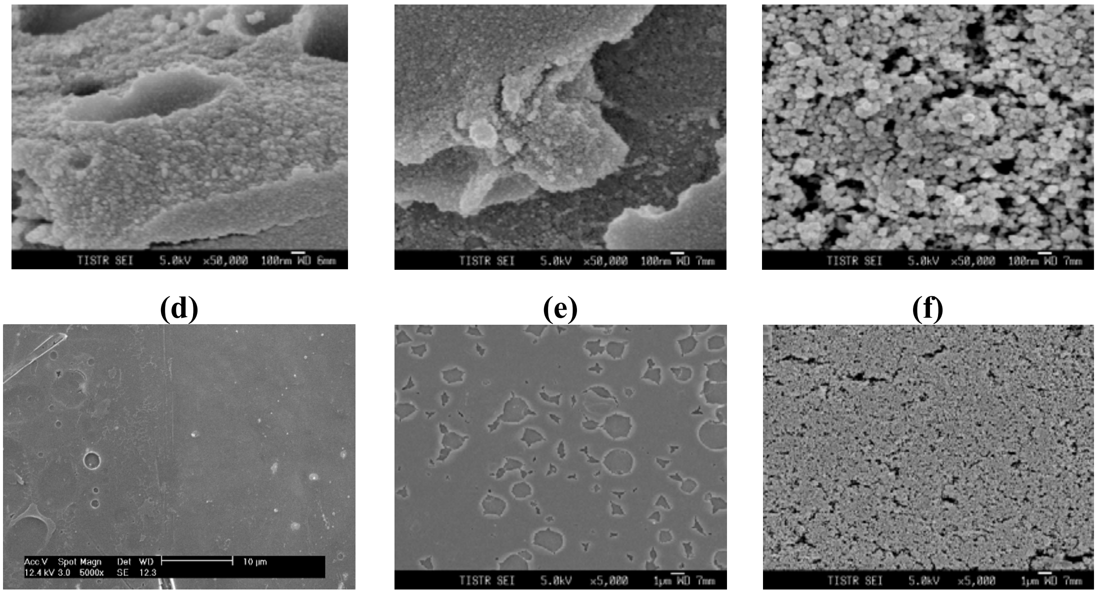

(d) **(e)** **(f)**

(a) **(b)** **(c)**

Figure 43 SEM of TiO_2-SG film electrodes with low (a) and high magnification (d), SEM of 2%Ce TiO_2-SG film electrodes with low (b) and high magnification (e) and SEM of TiO_2-P25 particulate film electrodes with low (c) and high magnification (f).

3.2 Preparation and characterization of TiO_2 film electrode for electrochemical and photoelectrochemical characterizations.

3.2.1 Powder x-ray diffraction (XRD)

The XRD spectra of bare ITO and TiO_2 film electrodes are shown in Figure 44. The XRD pattern of ITO shows only peaks of characteristic In_2O_3 as coating on borosilicate glass and the XRD pattern of TiO_2-P25 shows a mixture phase of anatase and rutile, see Figure 44 (a) and (b), respectively. The as-prepared TiO_2 i.e. non calcined TiO_2 deposited on ITO shows only broadly peaks of anatase phase [Figure 44 (c)]. The anatase peak is markedly observed with increasing the calcination temperature due to the dependent calcination temperature crystallization, see Figure 44 (d) (Diebold *et al.*, 1997, Su *et al.*, 2004 and Mitter and Ko, 1997). The desired mixture phase of anatase and rutile shows at the highest calcination temperature [Figure 44 (e)]. The TiO_2-SG was prepared with a high content of water assuming more Ti(OH)x with no steric effect on condensation. The high water concentration accelerates the cross-linking process leading to a macromolecule network with lower interconnectivity, i.e. low density phase, rutile (Mitter and Ko, 1997). These results indicated that the mixture phase of anatase and rutile was prepared by sol-gel method at 823 K. The 2%Ce TiO_2-SG electrode shows only anatase phase indicating Ce ion prevents the rutile formation [Figure 44 (f)]. In addition, the observed oxidation state of cerium ion in 8%Ce TiO_2-SG electrode was Ce^{3+} and Ce^{4+}, which was determined by x-ray photoemission spectroscopy (XPS) and x-ray absorption near edge spectroscopy (XANES) experiment of 8%Ce TiO_2-SG powder indicated mainly Ce^{4+} (Poo-arporn, 2008 and Nitharat, MS). These results indicated that the cerium species on the electrode surface are Ce^{3+} and Ce^{4+}, where the species in the bulk are mainly Ce^{4+}.

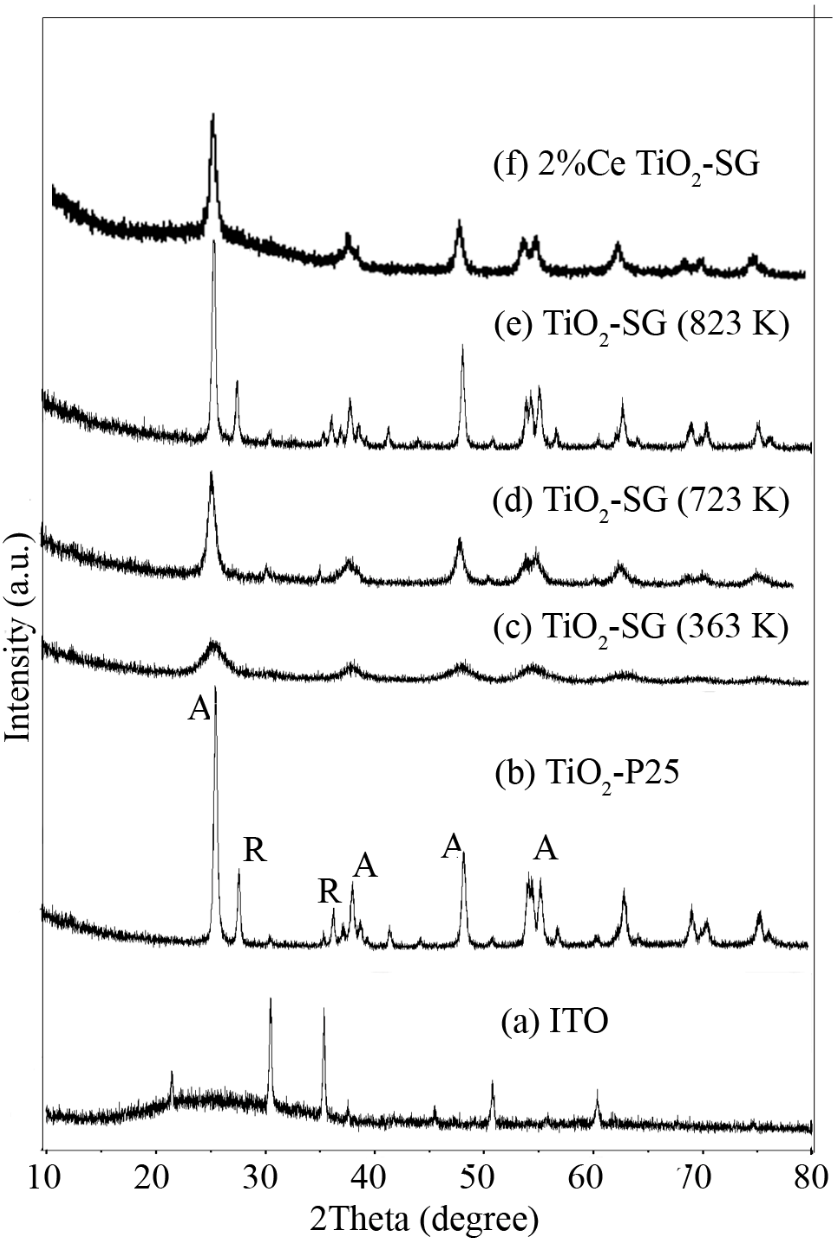

Figure 44 XRD patterns of (a) ITO conducting glass, (b) TiO_2-P25, (c) non calcined TiO_2-SG, (d) calcined TiO_2-SG at 723 K, (e) calcined TiO_2-SG at 823 K and (f) 2%Ce TiO_2-SG; A=anatase and R=rutile.

3.2.2 Scanning electron microscopy with energy dispersive spectroscopy (SEM and EDS)

Form 3.2.1, the XRD patterns of the different TiO_2 film electrode have not effect by cleaning of ITO by a conventional method. The SEM of the TiO_2-SG electrode shows island of TiO_2-SG film electrode [Figure 40 (a)] and the SEM of 2%Ce TiO_2-SG shows similar to TiO_2-SG film electrode [Figure 40 (b)]. The SEM of the TiO_2-P25 electrode shows agglomerated fine particles electrode [Figure 40 (c)]. The thicknesses of different electrodes are 13, 56, and 13 µm. for, 20 layers of TiO_2-SG, 15 layers of 2%Ce TiO_2-SG and 5 layers of TiO_2-P25, see Figure 40 (d), (e) and (f), respectively.

4 Electrochemical and Photoelectrochemical Characterizations

4.1 Cyclic voltammetry (CV)

4.1.1 Dark condition

(a) Film thickness

The voltammetric measurements of a bare ITO and TiO_2-SG electrodes in 0.5 M Na_2SO_4 (pH 6.3) were investigated. The bare ITO electrode reveals only double layer charging (no faradaic reaction) in the potential range -1.1 to 1.3 V vs. Ag/AgCl, see Figure 45. The TiO_2-SG electrodes with different thicknesses (10, 15, 20 and 25 layers) show clearly cathodic current starting at about -0.3 V vs. Ag/AgCl and anodic peaks are observed after the return voltage has been reached.

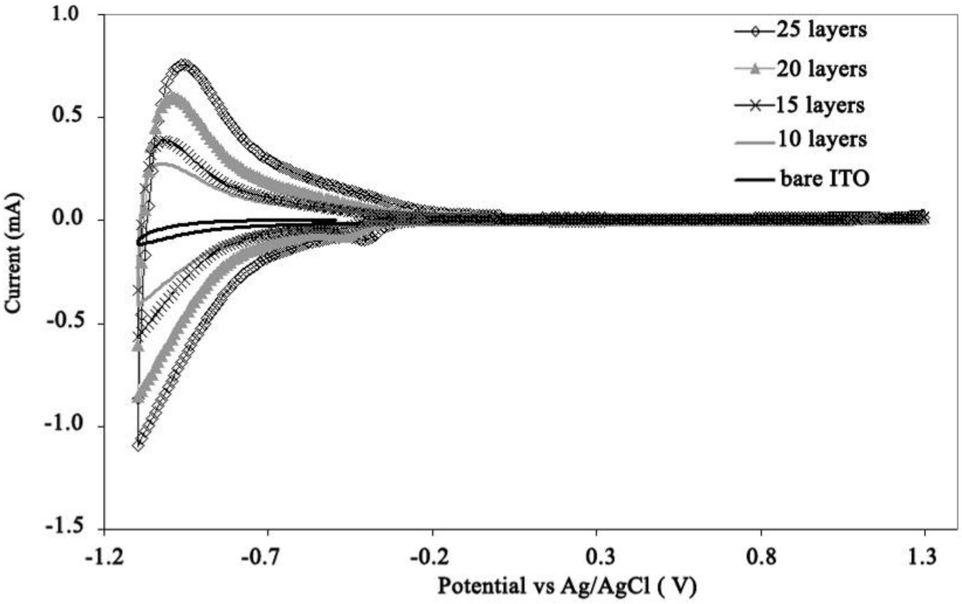

Figure 45 CV of TiO_2-SG electrodes in 0.5 M Na_2SO_4 (pH 6.3) recorded at different numbers of layers.

The cathodic and anodic currents of TiO_2-SG electrodes, which may account for the reduction/oxidation of Ti^{4+}/Ti^{3+} sites in the TiO_2 layer (Murakata *et al.*, 1999), increase with increasing numbers of layers. These results show that is attributed to the reduction of electroactive surface states of the TiO_2 film, namely Ti(IV) species, on the electrode surface in contact with the electrolyte (Ravichandran *et al.*, 1996 and Zhang *et al.*, 2004). It is well known that TiO_2 contains OH^- groups at the surface. Thus, the electroreduction process of TiO_2 film can be expressed as:

$$[Ti(OH)_2]^{2+} + H^+ + e^- \rightarrow [Ti(OH)]^{2+} + H_2O \qquad (24)$$

where $[Ti(OH)_2]^{2+}$ and $[Ti(OH)]^{2+}$ represent Ti(IV) and Ti(III) species in the TiO_2 film, respectively. This indicates that the faradaic current depends on the quantity of the hydroxylated site of TiO_2. For Ce-doepd TiO_2, it can be assumed that 2%Ce

TiO_2-SG with Ce(IV)/Ce(III) on the surface produced current from Ce(III) species according to the reduction of Ti(IV) (Li *et al.*, 2005):

$$\text{Ce(III)} + \text{Ti(IV)} \rightarrow \text{Ce (IV)} + \text{Ti(III)} \tag{25}$$

and oxidation of Ti(IV) produced the anodic current of 2%Ce TiO_2-SG. To a certain degree, the higher content of Ti(III) on the Ce-TiO_2 surface compared to that of TiO_2 would accelerate the interfacial charge transfer (Li *et al.*,2005) causing the high current. The maximum observed faradaic current of TiO_2-SG, 2%Ce TiO_2-SG and TiO_2-P25 are shown by the overlay voltammograms in Figure 46.

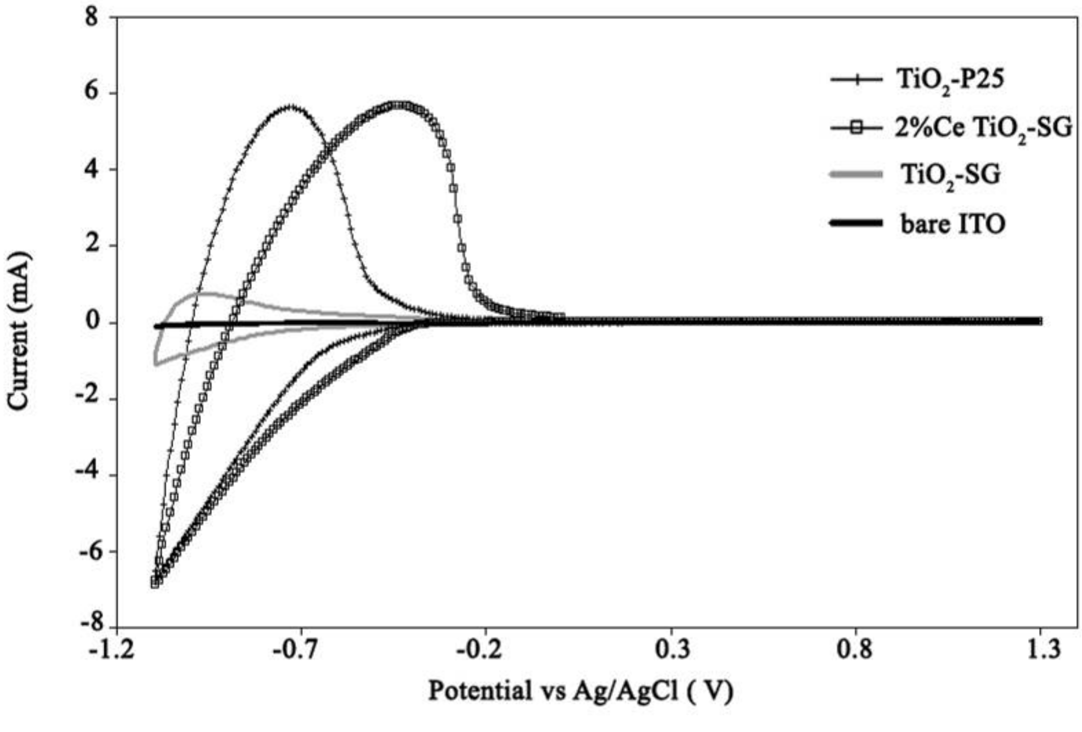

Figure 46 CVs of the different material TiO_2 electrodes in 0.5 M Na_2SO_4 at pH 6.3.

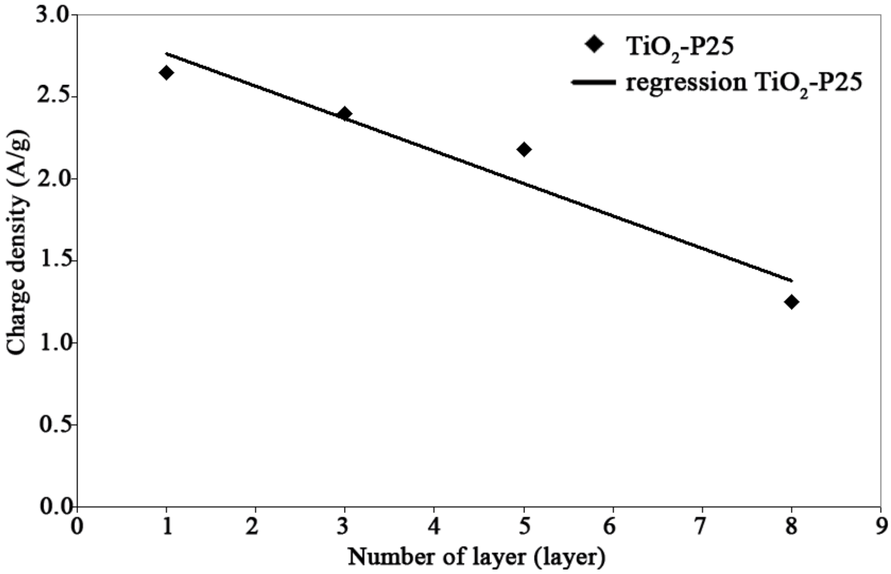

(b)

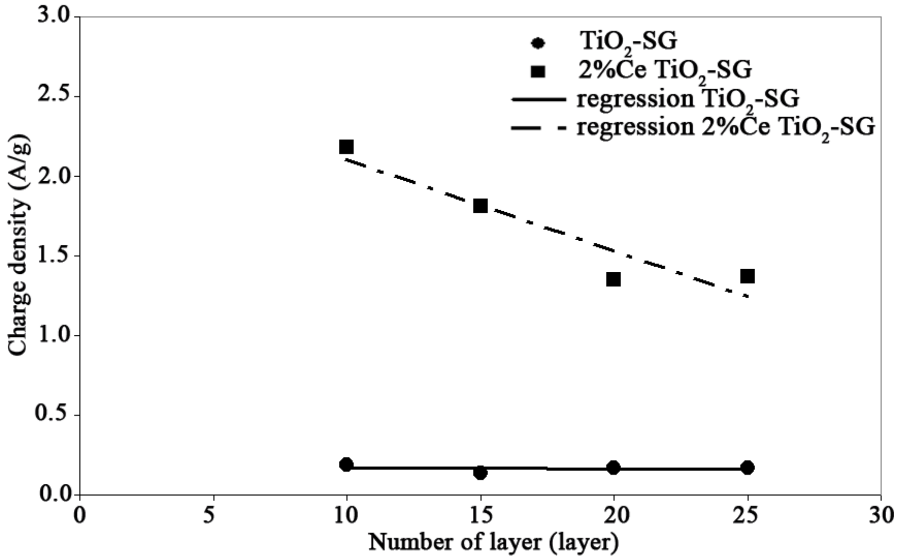

(a)

Figure 47 (a) anodic peak charge density as a function of the number of layers of TiO_2-SG and 2%Ce TiO_2-SG and (b) anodic peak charge density as a function of the number of layers of TiO_2-P25.

The current reveals the linearity as a function of the number of layers. Considerating, that the redox reaction takes place only at the hydroxylated surface site, it can derived that the inner surface area of the porous TiO_2 film is proportional to amount of deposited TiO_2. By the integration of i-v plots, charges of anodic branch can be calculated and taken to be proportional to the active redox sites per gram deposited TiO_2. For thicker films, there are small drops in charge density due to i) charge carrier diffusion migration limiting and ii) gradient in morphology. The doping by Ce has remarkable effects on the CV response comparing the different nanoporous TiO_2 film electrodes. The current "charge density" of 2%Ce TiO_2-SG film electrode is about 10 times the undoped TiO_2-SG film electrode, see Figure 47 (a), and is in the same region as the TiO_2-P25 electrode, see Figure 47 (b).

Alves *et al.* found that the voltammetric charge was a function of the CeO_2 content into $IrO_{0.3}Ti_{(0.7-x)}Ce_xO_2$ ternary metal oxide (Alves *et al.*, 1994). For CeO_2 content up to 30 mol%, the almost linearly increased charge with CeO_2 content reflects an increase of the effective surface area of the electrodes. The replacement of TiO_2 with CeO_2 can result in the formation of very fine crystallites because of the decrease in the probability of homogeneous crystal growth. Otherwise, the charge densities of 2%Ce TiO_2 and TiO_2-P25 at the similar weight of TiO_2 on ITO are similar. These indicate that the quantities of hydroxylated site related to the charge densities of both electrodes are very similar.

(b) pH of electrolyte solution

The effect of the pH of electrolyte was studied by the addition of 50 μL H_2SO_4 to the electrolyte solution (pH 2.9). It is noted that these voltammograms are markedly dependent upon the pH value, as shown in Figure 48. By comparison of Figure 46 and of Figure 48, the cathodic potential peak shifts in a positive direction with decreasing pH. The shift of cathodic peak can be explained by using the equation explaining the electroreduction process of TiO_2 film, see equation 24 in film thickness (a part of CV under dark condition). Under acidic condition, the concentration of proton increases which occurs easily the reduction reaction.

As is well-known, the changes in pH of the electrolyte solution displace the conduction band of TiO_2 upwards or downwards according to the expression: $E_{CB} = E_{CB}(pH0) - 0.059VpH$, where E_{CB} is conduction band potential (Bisquert *et al.* , 2008). In this figure, the shift is approximately 340 mV for TiO_2-SG and TiO_2-P25 electrodes and 290 mV for the 2%Ce TiO_2-SG electrode. These are not in good agreement with the predicted 59 mVpH unit^{-1}(i.e. 204 mV). However, these results correspond to the theory that the conduction band potential decreases with the decrease pH of the electrolyte solution.

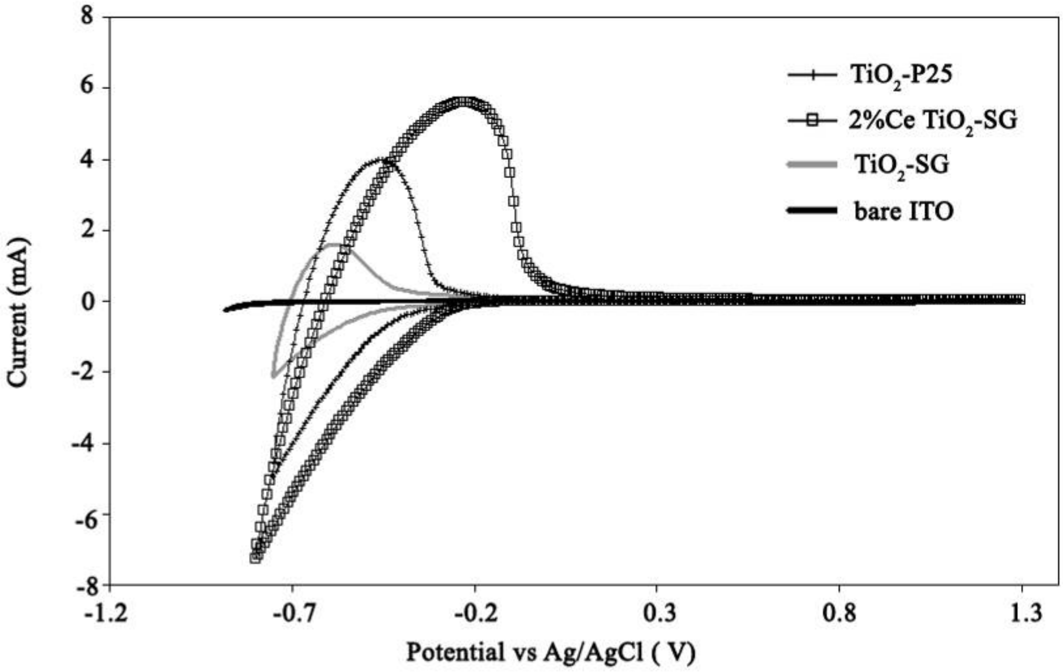

Figure 48 CVs for different material TiO_2 electrodes at pH 2.9.

4.1.2 Irradiation condition

(a) Film thickness

The photocurrents of the TiO_2-SG electrodes with different thicknesses were measured under chopped illumination at -0.4 to 1.2 V vs. Ag/AgCl and it was observed that faradaic current did not appear. The photocurrents of different thicknesses of the TiO_2-SG electrodes are shown in Figure 49 (a). The photocurrent increases with increasing thickness. The TiO_2-SG electrode with 20 layers shows a higher observed photocurrent than with 25 layers.

The nanoporous TiO_2 film electrodes are irradiated with energy exceeding the band gap of TiO_2. Excitation of electrons will lead to the generation of electron-hole pairs. The charge separation process of photoinduced electron-hole pairs occurs under an electric field in the space charge region. The photogenerated holes diffuse/migrate to the TiO_2 surface and may oxidize adsorbed water or surface hydroxylated groups, while the promoted electrons have to cross particle grain boundaries to be trapped at the TiO_2/ITO interface producing photocurrent, see Figure 50. An explanation for a thickness dependent photocurrent has been published (Hagfeldt and Gätzel, 1995 and Hagfeldt *et al.*, 1995). During illumination, the photoelectrons can create a gradient in the electrochemical potential between the particle and back contact. In this gradient, the electrons can transport through the interconnected particles to the back contact, where they are withdrawn as current (i.e. photocurrent). Thus, it is also clear that it will increase the probability of recombination with increasing film thickness, as the electron has, on average, to be transported across an increasing number of particles and grain boundaries.

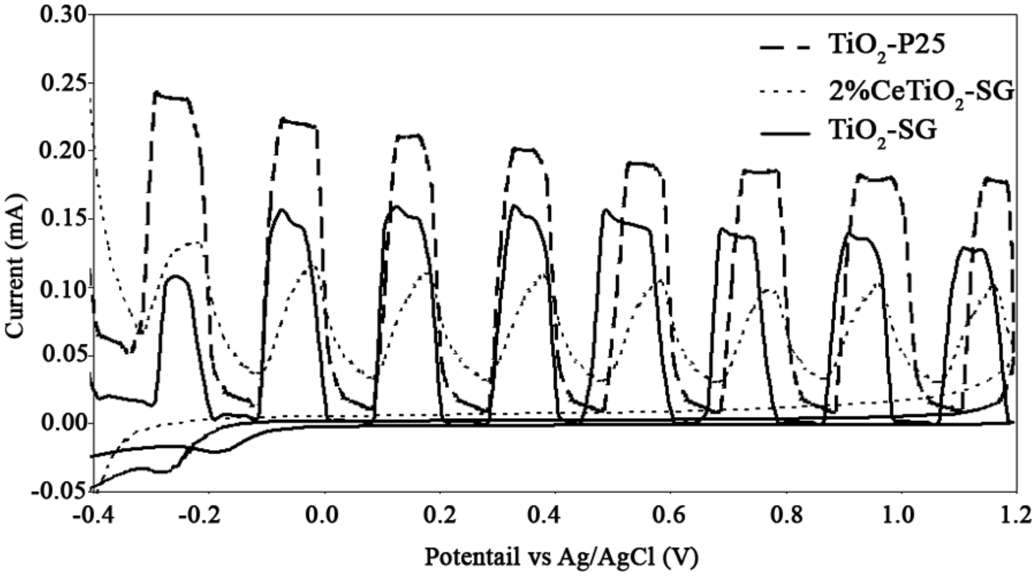

(b)

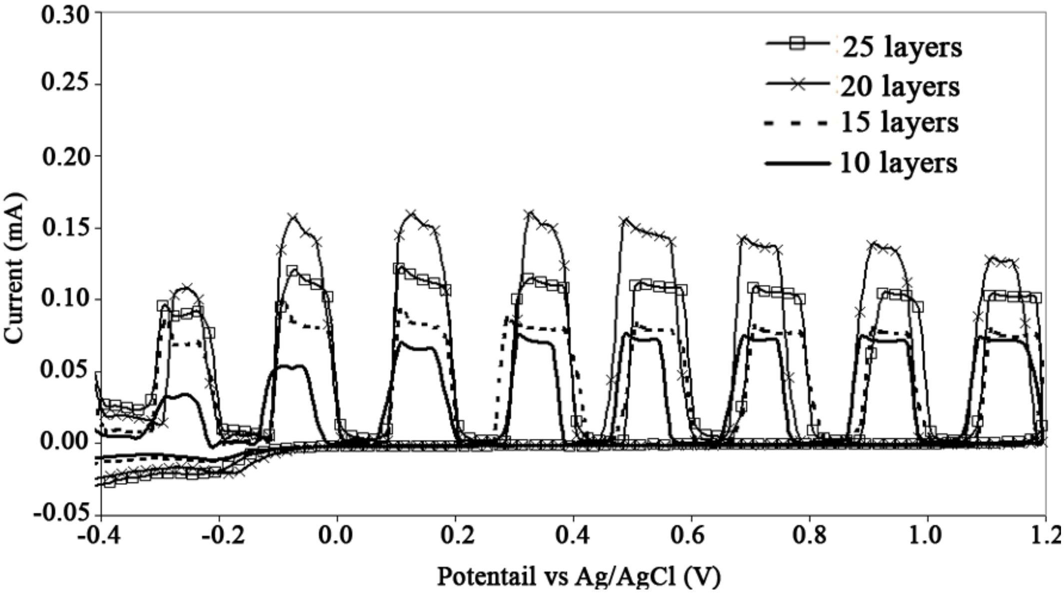

(a)

Figure 49 (a) The photocurrent of TiO_2-SG with different thicknesses and (b) The photocurrent of differential materials; TiO_2-SG, 2%Ce TiO_2-SG and TiO_2-P25.

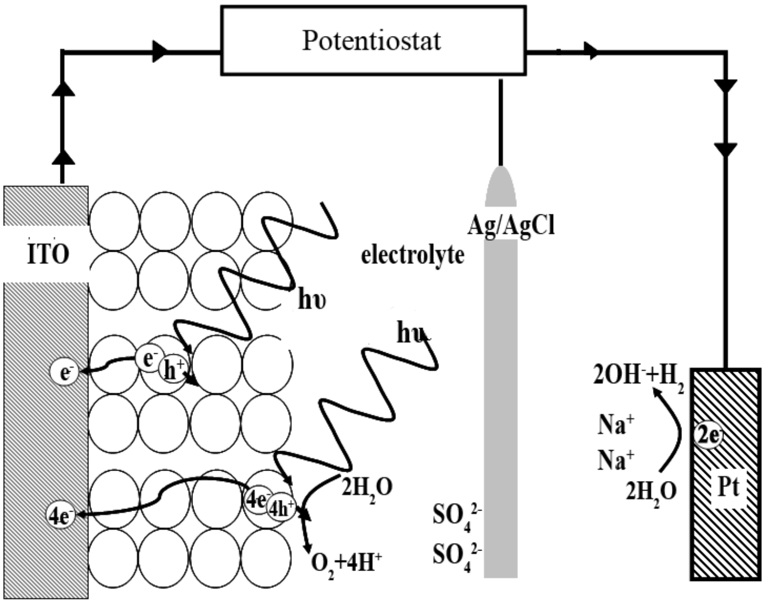

Figure 50 Schematic representation of proposed photoinduced processes generating photocurrent.

In this experiment, the thickest film (25 layers of TiO_2-SG electrode) may exceed the free diffusion length of the electrons and/or the penetration depth of light. Therefore, a loss of photocurrent might be due to the electron-hole recombination during diffusion/migration across the interconnected particle and grain boundaries to the ITO back contact. This phenomenon was found for all samples (TiO_2-SG, TiO_2-P25 and 2%Ce TiO_2-SG). For all TiO_2 film electrodes, a photocurrent maximum was observed, at 20 layers for TiO_2-SG, 15 layers for 2%CeTiO_2-SG and 5 layers for TiO_2-P25. Figure 49 (b) presents the overlay of CV photocurrents of different materials TiO_2 film electrodes at the obtained highest photocurrent.

For Ce doped electrode, it should also be noticed that the photocurrent of the 2%CeTiO_2-SG electrode was quite low with delay peaks consistently at every voltage, which can be attributed to an effective charge carrier trapping and recombination of photogenerated electron-hole pairs. The presence of metal ions in titania introduces new energy levels of the transition metal ions into the band gap of TiO_2 such as Ce which is located at about 1.5 eV below the conducting band of TiO_2 (Nagaveni *et al.*, 2004). These energy levels of metal ions act as electron or hole trapping centers depending on the energy level position of the conducting band and the valence band. Thus substituted Ce ions provide more trap sites for electrons acting as recombination centers.

The photon penetrated the bulk TiO_2 with deposited Ce (IV), generated electron-hole pairs. The Ce(IV) species captured electrons producing Ce(III). It has been reported that the cerium 4*f* level plays an important role in interfacial charge transfer and elimination of electron-hole recombination. The electrons trapped in Ce(IV)/Ce(III) site are subsequently transferred to the surrounding ions according to the equation(Li *et al.*, 2005):

$$Ce^{4+} + TiO_2\,(e^-_{CB}) \rightarrow Ce^{3+} + TiO_2 \qquad (26)$$

However, it was found that Ti (III) content increased with the increase Ce(III) and became recombination centers.

(b) Effect of photon flux

The photocurrent not only depends on the thickness of thin film but also on the photon flux (or intensity of the light source). The variation photon flux was performed by changing the distance between the light source and the prepared electrode (or working electrode). Figure 51 shows the overlay of anodic photocurrent of different photon flux to be a function of potential. The photocurrent increases with increasing the photon flux compared at a similar potential. These features can explain that higher intensities of light can penetrate much deeper and produce more charge carriers than a lower one.

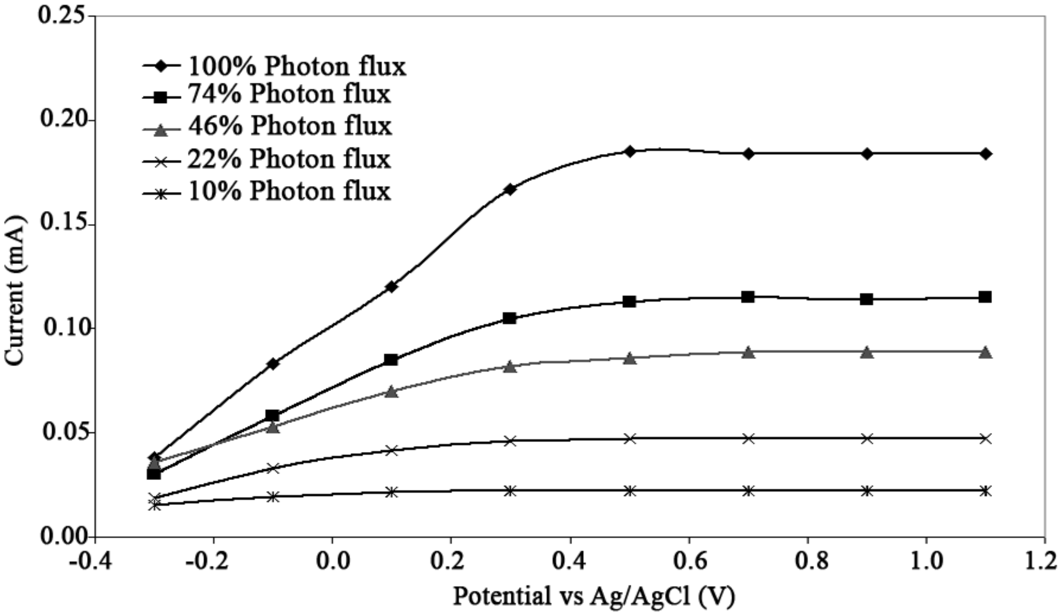

Figure 51 The photocurrent of 20 layers of TiO_2-SG electrode at different photon flux.

Moreover, the photocurrent flowing through the TiO_2 semiconductor consists of photogenerated carriers within the depletion layer and photogenerated carriers in bulk diffuse into the depletion layer (Butler, 1977 and Gärtner, 1959). The photocurrent depends on the carrier's density, the diffusion length of carriers, the flat band potential of the material, the wavelength of the incident light and the applied potential. At a similar photon flux, the photocurrent in the negative potential range increases with potential because the overall photocatalytic processes are controlled by the electron transport in the thin film electrode. Lindquist *et al.* derived an equation of relation of width of depletion layer (W) and the film thickness (d) for quantum efficiencies calculation i.e. $\phi = \frac{W}{d}$ (Lindquist *et al.*, 1983). According to the Gärtner-Bulter model, the quantum efficiency is the photocurrent, J, per incident light, Φ, ($\phi = J/q\Phi$). The width of the depletion layer is a function of voltage and impurities distribution across the junction ($W = W_0\sqrt{E - E_{fb}}$, where W_0 is the depletion layer width for a potential of 1 V across it, E is the applied relative to a reference electrode and E_{fb} is the flat band potential) (Butler, 1977). Considering at constant thickness of film electrode, the photocurrent increases with increasing the potential. These results correspond to the theoretical proposal that the photocurrent at negative potential increases with increasing the potential. At about 0.3 V vs. Ag/AgCl, the photocurrents of all different photon flux show almost constant photocurrent owing to the flat band reaching the potential of the material.

(c) Effect of methanol addition

The photocurrents of a 20 layers of TiO_2-SG electrode in 0.5 M Na_2SO_4 (pure electrolyte) and 0.5 M Na_2SO_4 with 2.5 M methanol addition are shown in Figure 52. The photocurrent of TiO_2 in a mixed 2.5 M methanol into an electrolyte solution is approximately 2 times more than in a pure electrolyte. The photocurrent of the semiconductor feature should be similar to the effect of photon flux that increases with potential until it reaches the flat band potential.

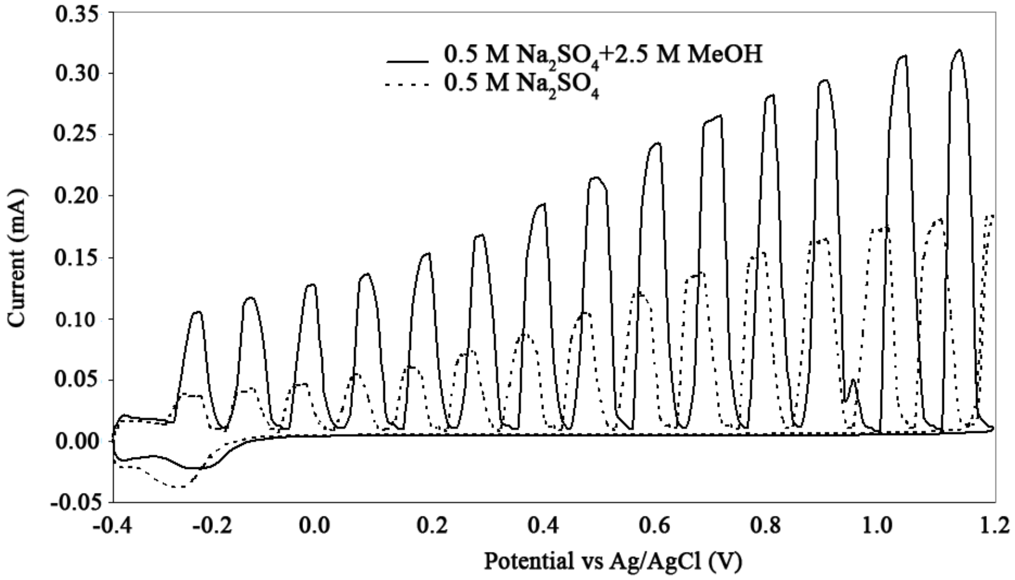

Figure 52 Photocurrent of 20 layers of TiO_2-SG electrode in pure electrolyte (0.5 M Na_2SO_4) and added 2.5 M methanol to pure electrolyte.

The behavior of a TiO_2-SG electrode changes dramatically in the presence of some hole scavengers, i.e. methanol in the electrolyte solution. This appears by increasing the photocurrent after addition of methanol to the pure electrolyte. It can be explained by the oxidation of the MeOH molecule. It may be initiated either by direct holes transfer (27) or by the reaction at the surface radicals, $Ti_s\text{-}O^{\bullet}$(28) (Solarsha *et al.*, 2006).

$$CH_3OH_{ads} + h^{+} \rightarrow {}^{\bullet}CH_2OH_{ads} + H_{aq}^{+} \quad (27)$$

$$CH_3OH + Ti_s\text{-}O^{\bullet} \rightarrow {}^{\bullet}CH_2OH + Ti_s\text{-}OH \quad (28)$$

In the α-H abstraction, in order to directly oxidize, methanol must be absorbed at the surface first while, in order to produce oxidative intermediate, it should be diffusion controlled. Wang *et al.* (2004) found that the indirect methanol oxidation depended on the ratio of water and methanol and the critical ratio between water and methanol was ca. 300 (0.15 M methanol in water). The direct oxidation is a dominant reaction in this experiment because of the lower water content (2.5 M methanol in pure electrolyte). These imply that methanol acts as a hole trapping center decreasing the electron-hole pair recombination.

4.2 Electrochemical impedance spectroscopy (EIS)

4.2.1 Dark condition

(a) Indium tin oxide (ITO), substrate

The absolute impedances and the phase angles of the impedance each as a function of the frequency, Bode plot, of non-calcined and calcined ITO (823K) at various applied potentials are shown in Figure 53 (a) and (b), respectively.

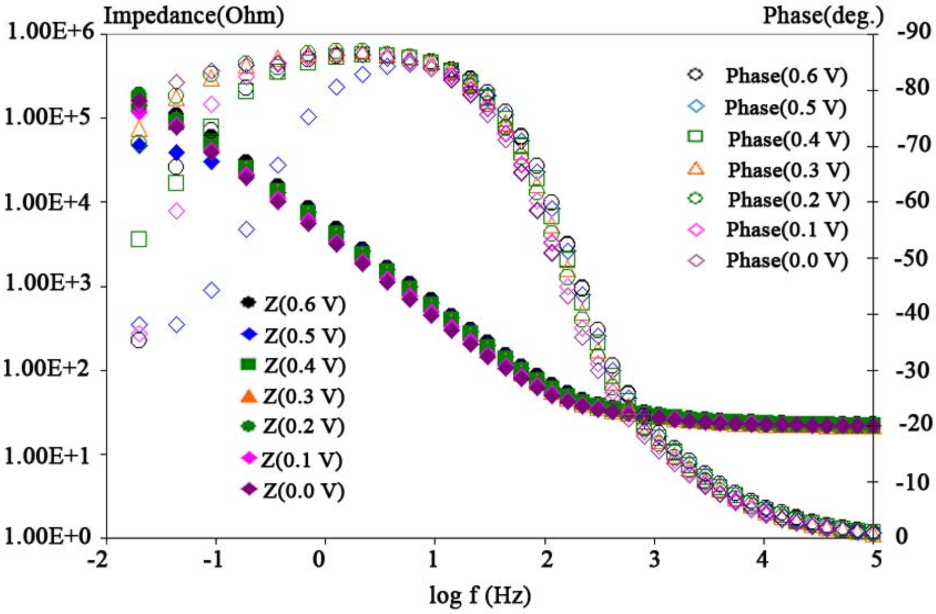

(b)

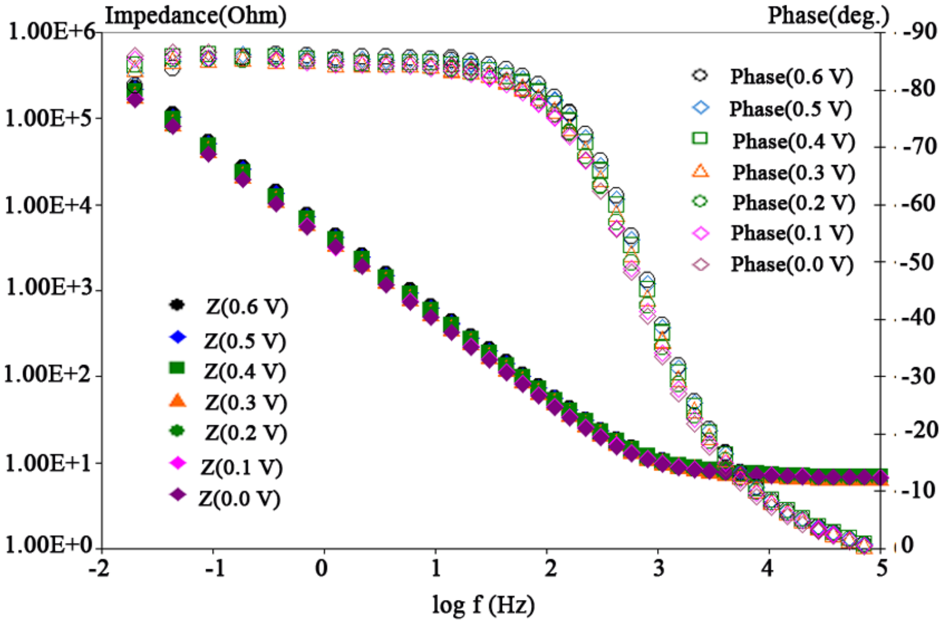

(a)

Figure 53 (a) The Bode plots of non-calcined ITO electrode and (b) The Bode plots of calcined ITO electrode (823 K) in the dark condition; filled symbol represents impedance and unfilled symbol represents phase angle.

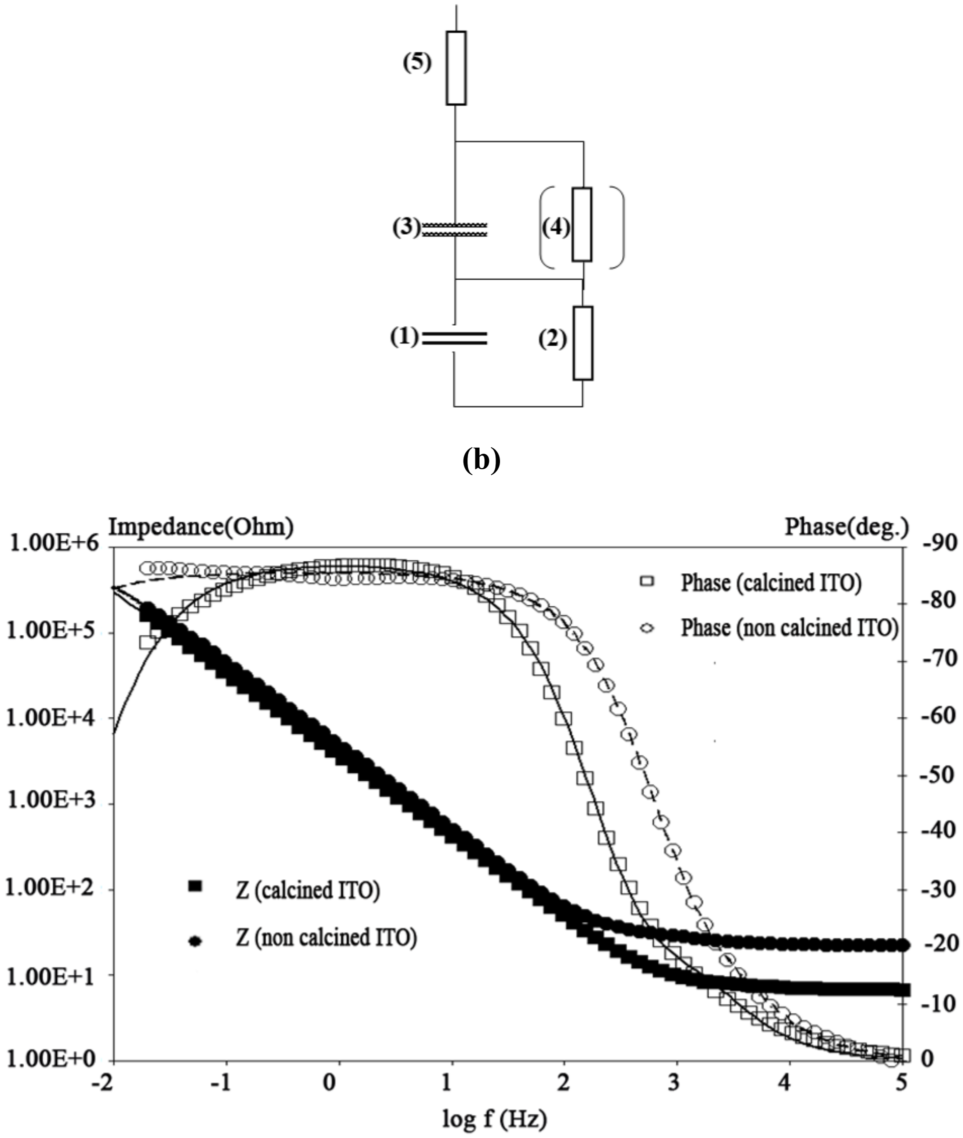

(b)

(a)

Figure 54 The simulation EIS data of non-calcined and calcined ITO electrodes (a); representing symbol as raw data and line as simulated data and (b) a proposed equivalent circuit of bare ITO; filled symbol represents impedance, unfilled symbol represents phase angle and line represents simulation data.

In this experiment, the frequency range was between 20mHz-100KHz. The Bode plots reveal two "time-constants". The first time-constant in the low frequency range (20 mHz to 10 Hz) shows the charge transfer across the ITO/electrolyte interface, and the second time-constant in the high frequency range (10 Hz to 100 KHz) reveals the impedance of ITO electrode. The total impedances of both electrodes are significantly different. The impedance of the calcined ITO electrode is smaller and the phase angle of the calcined ITO at lower frequency range bends more than a non-calcined one.

The interpretation of the EIS results should be derived from the equations governing the kinetics of the electrochemical reaction involved. Alternatively, a modeled electrochemical process presenting the network of electrical elements, called the equivalent circuit, is the other solution to explain the EIS results. The comparison of simulation data and experiment data shows in Figure 54 (a) and the equivalent circuit of bare ITO, Figure 54 (b) which was proposed in order to interpret EIS spectra. It is a combination of two RC circuits including an RC circuit of bulk ITO (element 1 and 2) and the other RC being an interfacial capacitance (3) and a charge transfer across ITO/electrolyte resistance (4). The bulk electrolyte resistance is element 5. The results of the fitting procedure using the proposed equivalent circuit of ITO electrode are shown in Table 10.

Table 10 The element values of non-calcined ITO and calcined ITO electrodes under dark condition using the equivalent circuit in Figure 54 (b); numbers in brackets are the significance of the elements and the error of the elements, respectively.

Condition (current)/ Elements	**Non-calcined ITO (-3.3423nA)**	**Calcined ITO (273.95nA)**
1. capacitance (uF)	45.06	16.03
	(0.03, 42.04)	(0.07, 27.89)
2. resistance (Ohm)	0.919	6.765
	(0.07, 5.80)	(0.17, 7.43)
3. interfacial capacitance (uF)	24.68	27.24
	(1.00, 1.28)	(1.00, 2,01)
α	947.5 m	970.6m
4. ITO/electrolyte resistance (Ohm)	13.89 x 10^6	699.4
	(0.01, 232.78)	(0.22, 32.75)
5. electrolyte resistance (Ohm)	6.885	22.44
	(1.00,3.25)	(1.00,2.40)

The elements 1 and 2 representing bulk ITO substrate of both fitting results of non calcined ITO and calcined ITO are significantly different. The ITO bulk may be defected by calcination at 823 K and shows a higher resistance (6.765 Ohm) and a lower capacitance (16.03 μF) compared to a non-calcined one (0.919 Ohm and 45.06 μF, respectively). In addition, the ITO/electrolyte resistance of the calcined ITO electrode (699.4 Ohm) was less than the non-calcined one (13.89 MOhm) because the defect of ITO surface increases the contact area of the ITO and electrolyte. It increases the charge transfer reaction across the ITO/ electrolyte interface. In contrast, the non-calcined ITO electrode, element 4 of the proposed equivalent circuit, can be neglected because it is a highly resistive element (13.89 MOhm). The current flows through the interfacial capacitance (element 3). These results indicate that the ITO surface was damaged by calcination and this will be important for the application and modification of the proposed circuit of the nanoporous TiO_2 film deposited on the ITO electrodes.

(b) Porous TiO_2-SG and 2%Ce TiO_2-SG film electrodes

The Bode plots of different nanoporous TiO_2-SG and 2%Ce TiO_2-SG film electrodes are shown in Figure 55. The impedances of all electrodes in the dark condition demonstrate high total impedances and a slightly bending phase angle. The Bode plots show the time constants corresponding to the impedance of the ITO bulk substrate, the impedance of the ITO/electrolyte interface, the impedance of the porous TiO_2/TiO_2 interface and the impedance of the porous TiO_2/electrolyte interface.

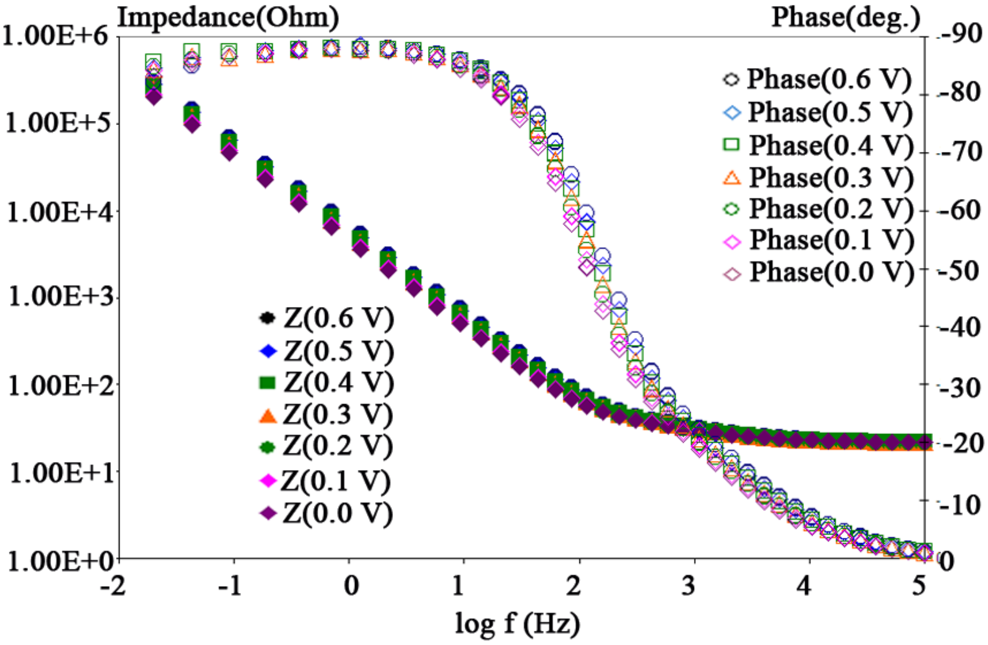

(b)

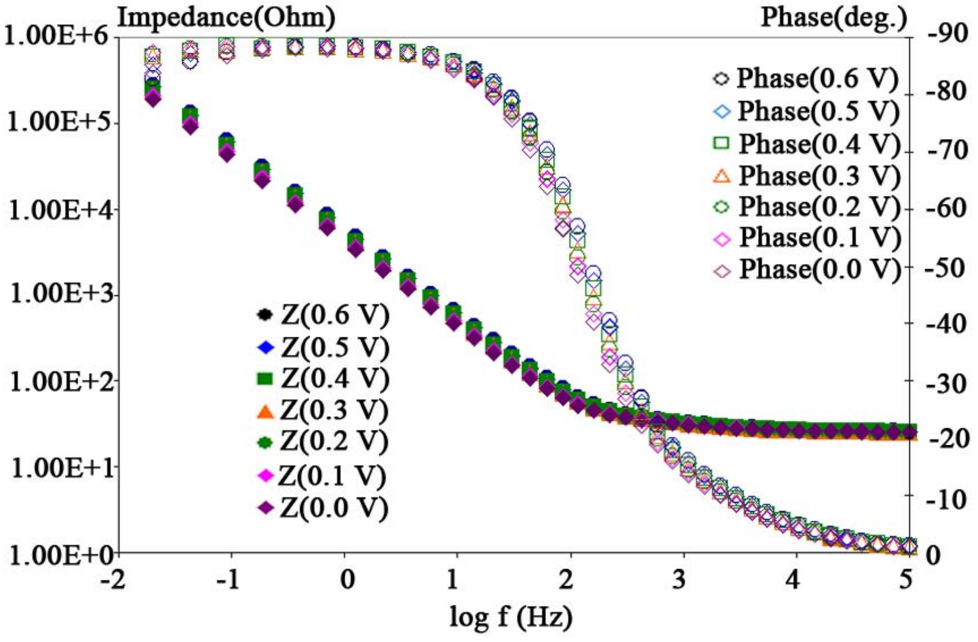

(a)

Figure 55 The Bode plots of different TiO_2 electrodes in the dark; (a) TiO_2-SG and (b) 2%Ce TiO_2-SG at various applied potentials; filled symbol represents impedance and unfilled symbol represents phase angle.

For the analysis of the EIS data, a porous electrode model based on the transmission line model has been employed [Figure 56 (a)]. The porous electrode model proposed by Göhr is implemented in the simulation and the evaluation program SIM in the Thales software (Zahner Elektrik, Germany) (Göhr, 1997 and Zahner manual). This model accounts for a porous electrode with homogeneous cylindrical uniform pores. Assuming that the porous TiO_2 film electrode is a random network of TiO_2 nanopaticles, one can employ this simplified model for the simulation procedure. The sum impedances of the porous layer may be expressed in terms of the macroscopic impedance elements consisting of the impedance elements of a porous TiO_2 layer/pores electrolyte interface (Zq), a porous TiO_2 layer of interconnected TiO_2 particles (Zs), a pore electrolyte (Zp), a porous TiO_2 layer/ITO layer interface (Zn) and a porous TiO_2 surface/bulk electrolyte interface (Zo), see Figure 56 (b). For the nanoporous TiO_2 electrodes, one can assume that the impedance of the outer porous TiO_2/bulk electrolyte interface (Zo) is very low compared to the impedance of the interior porous TiO_2/pore electrolyte interface (Zq) due to the small outer surface area compared to the interior surface area of the pore wall. Therefore, Zo can be dropped.

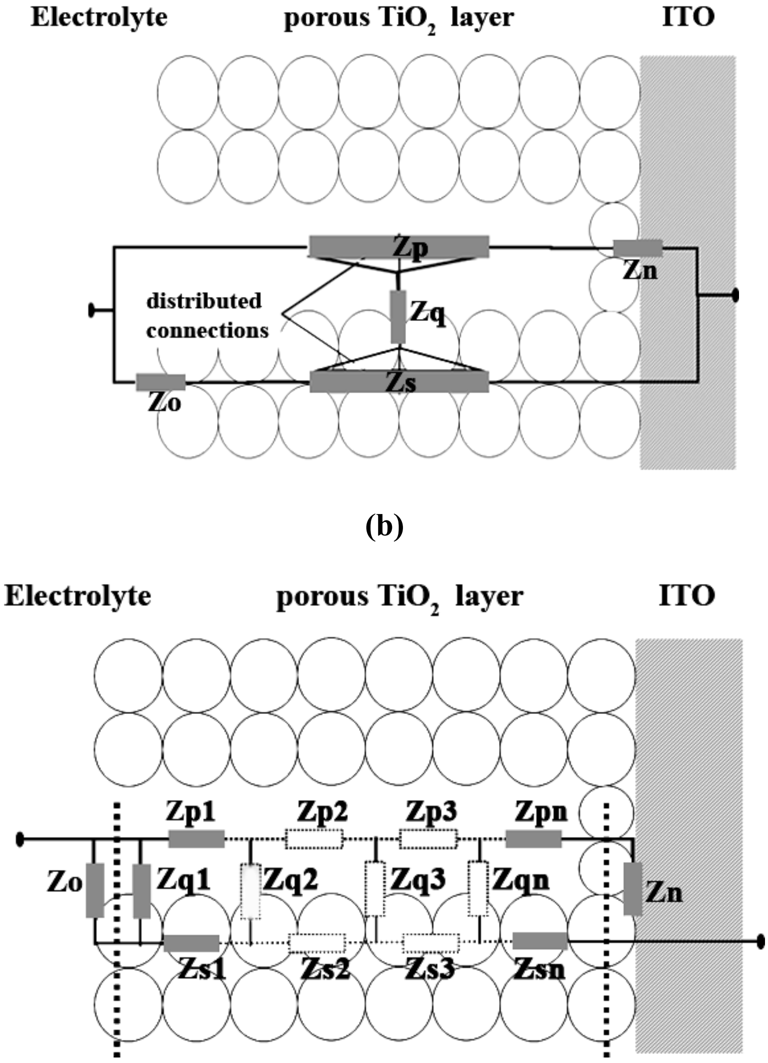

(a)

Figure 56 (a) Transmission line mode of a porous electrode and (b) The sum impedances of the porous layer.

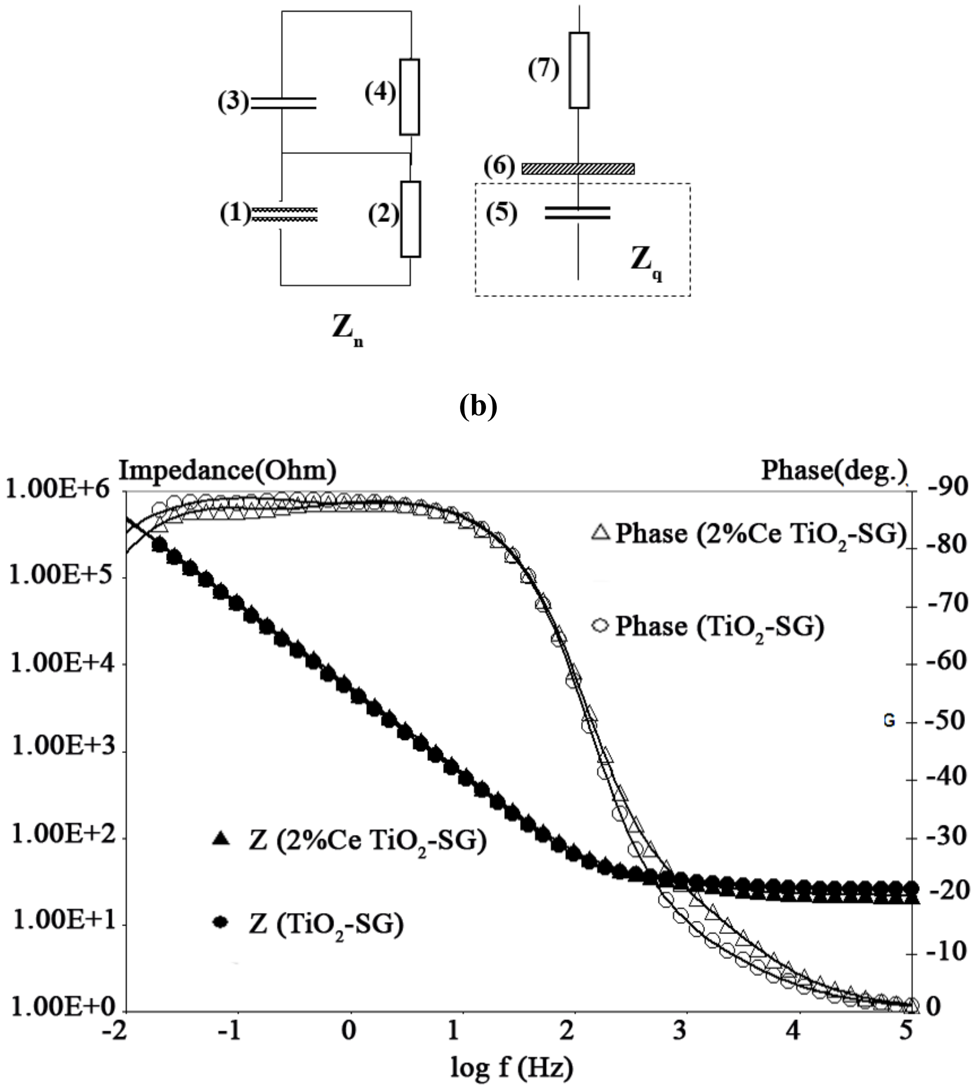

(b)

(a)

Figure 57 (a) EIS of different material nanoporous TiO_2-SG film electrodes at 0.3 V vs. Ag/AgCl; filled symbol represents impedance, unfilled symbol represents phase angle, line represents simulation data and (b) an equivalent circuit for the dark experiment.

From this simplification, the best fitting results were obtained by using the equivalent circuit for dark condition presented in Figure 57. It contains partial scheme in Figure 57 (b) on left-hand side for the interfacial impedance of porous TiO_2/ITO layers, Zn, and the other partial scheme in Figure 57 (b) on right-hand side for interfacial impedance of a porous TiO_2/pore electrolyte, Zq, which comprises of Zp, Zs (element 6) and impedance of bulk electrolyte, Ze (element 7). The results of ITO electrode in the dark showed that Zn comprised two RC circuits in serial connection. The first RC represents the conductive ITO bulk layer (element 1 and 2) and the second RC corresponds to the ITO/electrolyte interface at the bottom of the pore, taking into account the surface oxidation of the ITO layer by the thermal treatment (Poo-arporn, 2008) (elements 3 and 4). The impedance of the porous TiO_2/pore electrolyte interfaces (Zq) is described by only a capacitance (element 5). This element can be addressed to the capacitance of the space charge layer of the TiO_2 semiconductor material. The Helmholtz capacitance has not been considered under the experiment at the given depletion condition. Element 6 represents the network of the differential impedances, Zp and Zs (see Figure 56). By the simulation procedure, the integral pore electrolyte resistance (Zp_i, $i = 1, 2, 3, \ldots n$) and the integral solid bulk resistance, Zs_i, (i.e. resistance of the porous TiO_2 film consisting of the interconnected TiO_2 particles) can be determined. Finally, the impedance of bulk electrolyte is included as a pure ohmic resistance (element 7).

For comparing the undoped and doped TiO_2 electrodes, the results of the fitting procedure using the proposed equivalent circuit are represented in Table 11. The results of the impedance elements 1 to 4 for the interface pore ground electrolyte/ITO oxidation surface layer and ITO bulk material (Zn) are different for both materials, which may be explained by a different interface structure. Assuming different particle sizes and particle surface structure for the doped and undoped material, the total area of the pore ground will depend. The ITO surface oxidation during the calcination procedure can be affected by a different colloidal structure of the doped and undoped gels. A higher ratio of pore ground area to the area of the ITO surface protected by the TiO_2 particle should result in a decrease of the Zn. Comparing the fitting results for the pore electrolyte/TiO_2 interface (Zq) of the TiO_2-SG and 2%Ce TiO_2-SG, it should be mentioned that almost the same amount of TiO_2 material was deposited. The higher interfacial capacitance of the pore electrolyte/TiO_2 interface (element 5) for the 2%Ce TiO_2-SG can be explained by an increased doping concentration because of the Ce site within TiO_2 semiconductor and/or by a higher surface area. An increased surface area for the Ce-doped material is in accordance to the results of the CV characterization, see section 4.1.1 (a). The impedance for the TiO_2 layer (bulk material) of the 2%Ce TiO_2-SG material is significantly higher compared to the undoped material, see impedance element Zs in Table 11. This seems to be contradictory because the doping of material should lead to a higher conductivity and, therefore, to a smaller impedance. Zs is attributed to a porous TiO_2 layer consisting of an assembly of interconnected TiO_2 nanoparticles, so the effective conductivity of the porous film depends on the intrinsic conductivity of the TiO_2 particle, the geometry of the contact zone and the packing structure. On the other hand, the impedance of the sintered semiconductor particle network can be determined by discontinuities at the grain boundaries rather than by the intrinsic electronic properties. The impedance may depend mainly on the resistance of the grain boundaries.

Table 11 The elements value of different TiO_2-SG electrodes in the dark using the equivalent circuit in Figure 57 (b); the numbers in brackets are the significance of elements and the error of elements, respectively.

Material (current)/ Elements	**TiO_2-SG (38.75 nA)**	**2%Ce TiO_2-SG (51.16 nA)**
1. CPE (μF)	14.69	11.66
	(0.05, 5.65)	(0.10, 1.50)
A	698 m	740.8 m
2. resistance(Ohm)	11.14	16.94
	(0.15, 2.10)	(0.21, 1.41)
3. capacitance (μF)	30.53	28.07
	(0.99, 0.85)	(0.99, 1.06)
4. resistance (Ohm)	3.884×10^6	2.733×10^6
	(0.06, 20.55)	(0.09, 9.62)
5.capacitance (μF)	2.385	3.267
	(0.07, 21.51)	(0.10, 8.49)
6.porous impedance		
Z_p (Ohm)	8.896	7.592
	(0.35, 0.88)	(0.35, 1.50)
Z_s (Ohm)	240.6	524.5
	(0.03, 36.30)	(0.04, 21.93)
7.electrolyte resistance(Ohm)	16.42	14.01
	(0.64, 0.48)	(0.64, 0.81)

(c) Mott-Schottky plot of thin film electrodes

For the fitting EIS data of 20 layers of TiO_2-SG electrode with equivalent circuit in the dark condition [Figure 57 (b)], the calculated capacitances of TiO_2-SG depending on the potential are in range of 16.8 to 9.3 μF at 0.0 to 0.5 V vs. Ag/AgCl (see Table 12). The Mott-Schottky plot shows a straight line over a wide potential range, see Figure 58. The correlation coefficient for the linear regression was nearly unity for TiO_2-SG electrode. The flat band potential (intercepts of the Mott-Schottky plot) is about -0.2 V vs. Ag/AgCl at pH 6.3 obtained by extrapolation of a plot. The Mott-Schottky relation not only gives the flat band but also the donor density can be calculated. The donor density plays the influence on various (photo)electric properties of difference between bulk single crystals and porous nanostructure electrodes (van de Krol *et al.*, 1997). The donor density of film electrode is about 10^{17} cm^{-3} (van de Krol *et al.*, 1997 and Jongh, 1971).

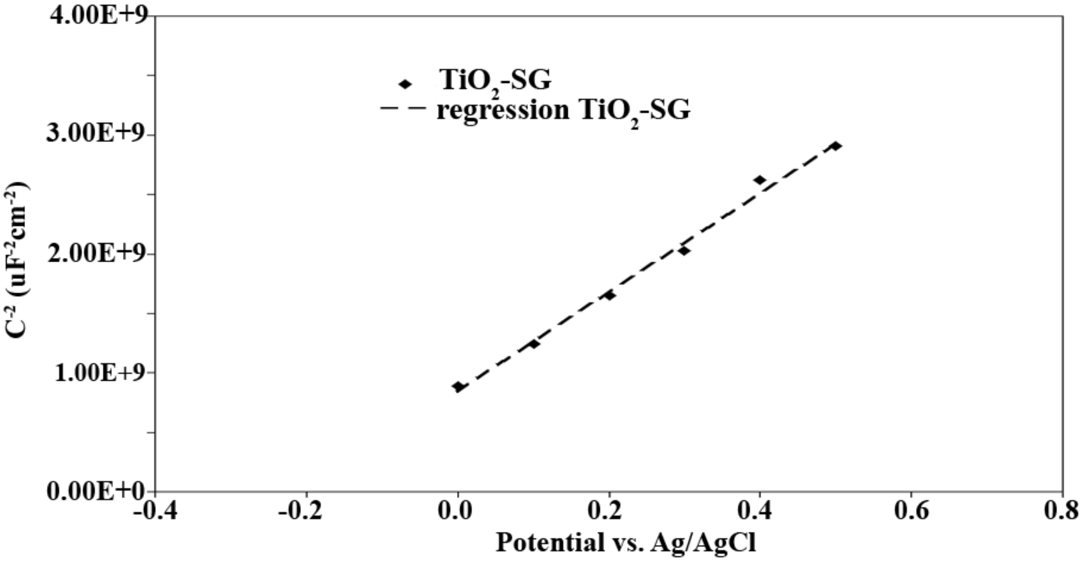

Figure 58 Mott-Schottky plot of 20 layers of TiO_2-SG film electrode.

Table 12 The elements value of TiO_2-SG electrodes under dark condition at various applied potential using the equivalent circuit in Figure 57 (b); the numbers in brackets are the significance of elements and the error of elements, respectively.

Potential (current) / Elements	**0.0 (-94.85 nA)**	**0.1 (98.89 nA)**	**0.2 (254.7 nA)**	**0.3 (396.9 nA)**	**0.4 (574.1 nA)**	**0.5 (848.9 nA)**
1. CPE (μF)	19.59	18.53	17.24	16.23	15.49	14.91
	(0.05, 12.91)	(0.05, 14.38)	(0.05, 14.58)	(0.05, 14.52)	(0.05, 16.56)	(0.05, 13.94)
α	562.3 m	559.3 m	562.4 m	567.2 m	570.2 m	574.6 m
2. resistance(Ohm)	13.09	13.05	12.71	12.64	12.57	12.77
	(0.12, 7.26)	(0.12, 7.03)	(0.12, 4.92)	(0.12, 4.64)	(0.13, 5.59)	(0.13, 4.68)
3. capacitance (μF)	36.00	33.22	30.58	28.21	26.13	24.4
	(0.96, 2.01)	(0.96, 1.92)	(0.96, 1.64)	(0.96, 1.91)	(0.96, 2.05)	(0.96, 2.16)
5. capacitance (μF)	16.8	14.17	12.32	11.10	9.765	9.272
	(0.30, 9.01)	(0.28, 9.57)	(0.27, 11.57)	(0.27, 11.44)	(0.26, 13.89)	(0.25, 10.54)
6.porous impedance						
Z_p (Ohm)	7.854	7.846	7.826	7.706	7.651	7.603
	(0.35, 3.64)	(0.35, 3.91)	(0.34, 3.60)	(0.34, 3.97)	(0.34, 2.60)	(0.34, 3.15)
Z_s (Ohm)	83.04	87.85	92.66	101.1	104.7	111.0
	(0.15, 22.60)	(0.14, 24.50)	(0.13, 25.71)	(0.13, 24.58)	(0.12, 27.08)	(0.12, 28.37)
7.electrolyte resistance(Ohm)	14.48	14.46	14.42	14.20	14.09	14.00
	(0.64, 1.97)	(0.64, 2.12)	(0.64, 1.95)	(0.63, 2.15)	(0.63, 1.41)	(0.63, 1.71)

(d) TiO_2-P25 particulate film electrode.

The Bode plots of different nanoporous TiO_2-P25 particulate film electrode are shown in Figure 59. The impedances of TiO_2-P25 electrode in the dark condition demonstrate high total impedances and a slightly bending phase angle.

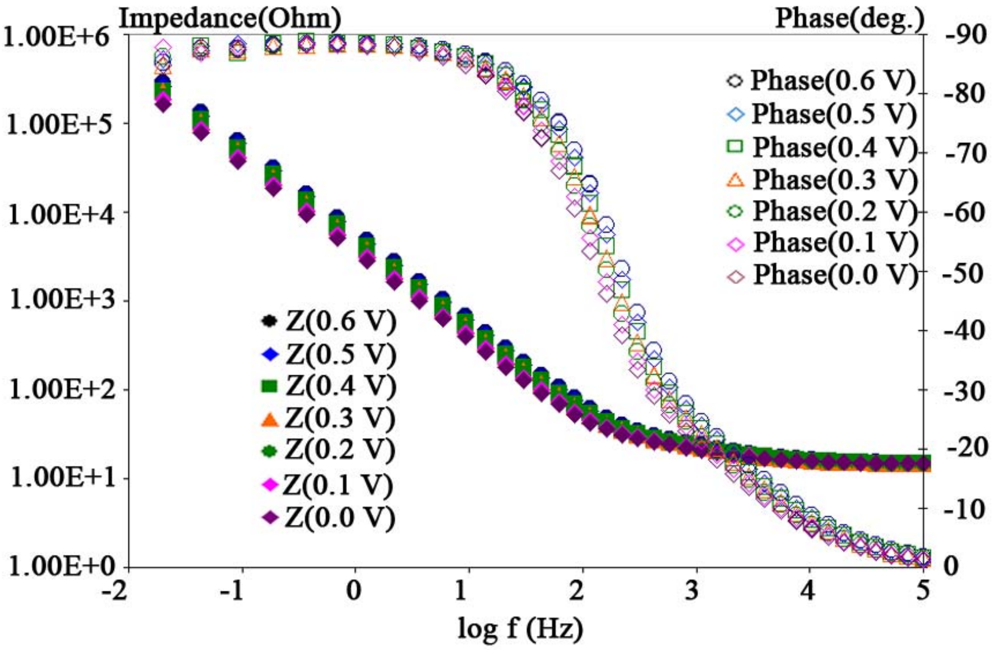

Figure 59 The Bode plots of TiO_2-P25 electrodes in the dark at various applied potential; filled symbol represents impedance and unfilled symbol represents phase angle.

The best fitting result of TiO_2-P25, see Figure 60, was obtained by using the equivalent circuit for dark condition presented in Figure 57 (b). The results of the fitting procedure using the proposed equivalent circuit are represented in Table 13. The results of the impedance elements 1 to 4 (Zn) are different comparing to TiO_2-SG and 2%Ce TiO_2-SG, which may be explained by a different morphology of TiO_2 deposited on ITO. The pore electrolyte/TiO_2 interface (Zq) of TiO_2-P25 electrode is almost similar comparing to 2%Ce TiO_2-SG. It can be explained by a doping concentration and/or by a higher surface area, corresponded to

CV in the dark of TiO_2 which is a high density charge [see 4.1.1 (a)]. The impedance for the TiO_2 layer (bulk material), Zs, is almost similar to TiO_2-SG (240.6 KOhm), see Table 13. The impedance of the sintered semiconductor particle network can be determined by discontinuities at the grain boundaries. This result implies that the resistance of the TiO_2-P25 grain boundaries is similarly to that of TiO_2-SG grain boundaries.

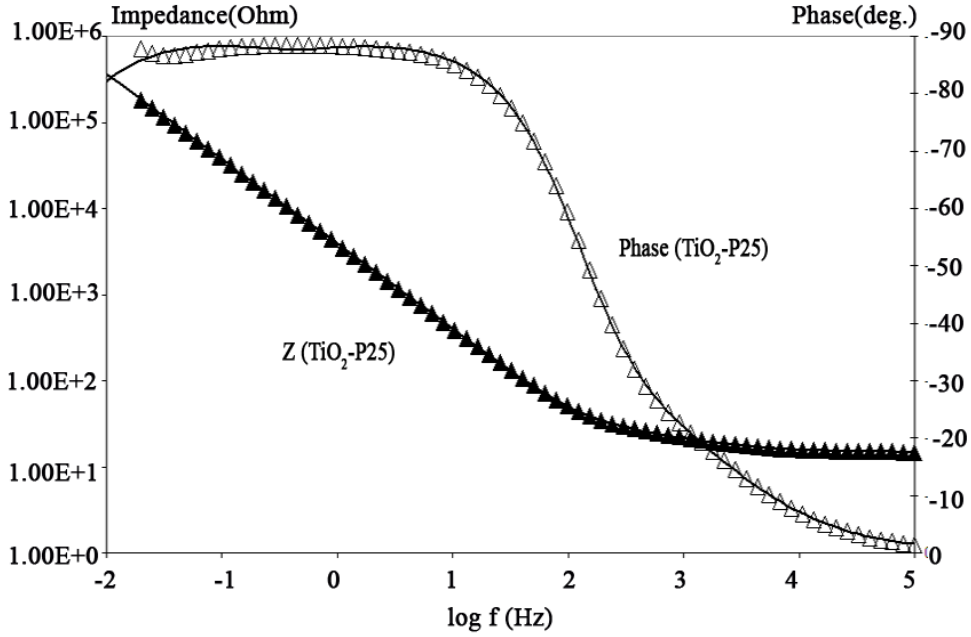

Figure 60 EIS of TiO_2-P25 film electrodes at 0.3 V vs. Ag/AgCl; filled symbol represents impedance, unfilled symbol represents phase angle, line represents simulation data.

Table 13 The elements value of different TiO_2-SG electrodes under dark condition at 0.3 V vs. Ag/AgCl using the equivalent circuit in Figure 57 (b); the numbers in brackets are the significance of elements and the error of elements, respectively.

Material (current)/ Elements	**TiO_2-P25 (99.75 nA)**	**TiO_2-SG (38.75 nA)**	**2%Ce TiO_2-SG (51.16 nA)**
1. CPE (μF)	19.06	14.69	11.66
	(0.07, 6.37)	(0.05, 5.65)	(0.10, 1.50)
	689 m	698 m	740.8 m
2.resistance (Ohm)	14.14	11.14	16.94
	(0.16, 5.43)	(0.15, 2.10)	(0.21, 1.41)
3.capacitance (μF)	38.33	30.53	28.07
	(0.99, 1.22)	(0.99, 0.85)	(0.99, 1.06)
4.resistance (Ohm)	$2.86x\ 10^6$	3.884×10^6	2.733×10^6
	(0.07, 38.32)	(0.06, 20.55)	(0.09, 9.62)
5.capacitance (μF)	3.079	2.385	3.267
	(0.07, 18.28)	(0.07, 21.51)	(0.10, 8.49)
6.porous impedance			
Z_p (Ohm)	7.769	8.896	7.592
	(0.35, 2.25)	(0.35, 0.88)	(0.35, 1.50)
Z_s (K Ohm)	251.1	240.6	524.5
	(0.03, 34.26)	(0.03, 36.30)	(0.04, 21.93)
7.electrolyte resistance(Ohm)	14.34	16.42	14.01
	(0.64, 1.22)	(0.64, 0.48)	(0.64, 0.81)

4.2.2 Irradiation condition

(a) Indium tin oxide (ITO), substrate

The overlay Bode plots of the calcined ITO electrode at various anodic potentials under irradiation are shown in Figure 61. The Bode plots are very similar compared with the results in the dark condition, see Figure 53 (b). These plots showed a time-constant in the low frequency range (20 mHz to 10 Hz) representing the charge transfer across the ITO/electrolyte interface and the other time-constant in the high frequency range (10 Hz to 100 KHz) revealing the impedance of the ITO electrode. The impedances of the calcined ITO electrode under irradiation were high and the phase angles at lower frequency range slightly bended.

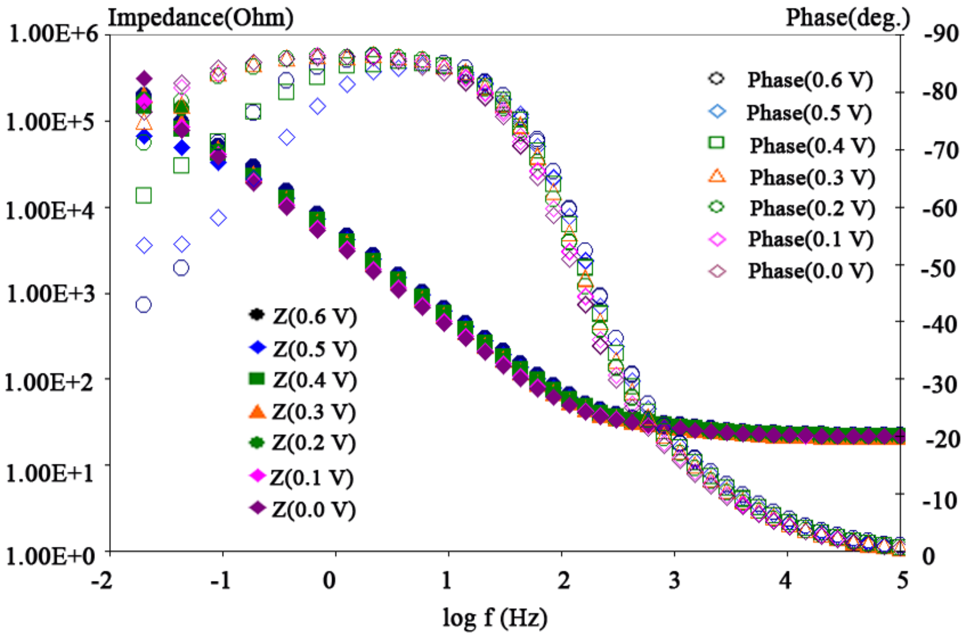

Figure 61 The Bode plots of calcined ITO electrodes under irradiation at various anodic potential; filled symbol represents impedance and unfilled symbol represents phase angle.

A simulation procedure of calcined ITO electrode was performed using the equivalent circuit for dark condition, see Figure 54 (b). The comparisons between simulation data and experimental data of the calcined ITO electrode, in dark condition and under irradiation, are shown in Figure 62. The best fitting results were observed. The results of the fitting procedure using the proposed equivalent circuit in the dark are shown in Table 14. According to the CV results, see section 4.1.1, the CV of bare ITO showed only the double layer charging. The photocurrent of the calcined ITO electrode at 0.3 V is 216.99 nA indicates no photoinduced processes at the ITO material. The photocurrent of porous TiO_2 electrodes deposited on the ITO substrate is produced only from the photoinduced processes of porous TiO_2 material.

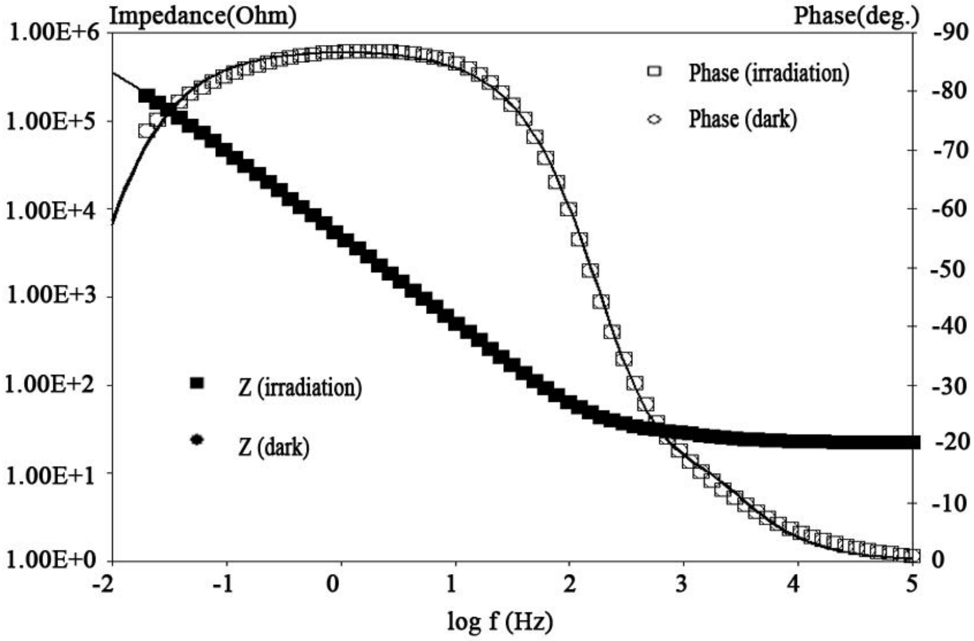

Figure 62 The simulation EIS data of the calcined ITO electrode in the dark condition and under irradiation; filled symbol represents impedance, unfilled symbol represents phase angle, line represents simulation data.

Table 14 The elements value of the calcined ITO electrode in the dark and under irradiation using the equivalent circuit in Figure 54 (b); the numbers in brackets are the significance of elements and the error of elements, respectively.

Condition [(photo)current]/ Elements	**Dark (273.95nA)**	**Irradiation (216.99nA)**
1. capacitance (μF)	16.03 (0.07, 27.89)	15.44 (0.07, 23.88)
2. resistance (Ohm)	6.765 (0.17, 7.43)	6.733 (0.17, 8.54)
3. interfacial capacitance (μF)	27.24 (1.00, 2,01)	27.9 (1.00, 0.98)
α	970.6m	970.9m
4. ITO/electrolyte resistance (Ohm)	699.4 (0.22, 32.75)	725.7 (0.22, 28.37)
5. electrolyte resistance (Ohm)	22.44 (1.00,2.40)	21.96 (1.00,2.16)

(b) Porous TiO_2-SG and 2%Ce TiO_2-SG film electrodes

Under irradiation, the charge carriers, being electrons and holes, are generated and subsequently the photogenerated electrons and holes are led to a responsible in photoelectrochemical current flow under applied potential called photocurrent. Figure 63 shows the overlay Bode plots of different TiO_2 film electrodes, TiO_2-SG and 2%Ce TiO_2-SG, under irradiation at various applied potentials. According to the photocurrent results, see section 4.1.2 (a), the photoinduced processes of porous TiO_2 material produce photocurrents leading to a significant decrease of the total impedance of the porous electrode in the frequency range below 10 Hz accompanied by a drop of the phase angle. The comparison of impedance of TiO_2-SG and 2%Ce TiO_2-SG electrodes is considered below.

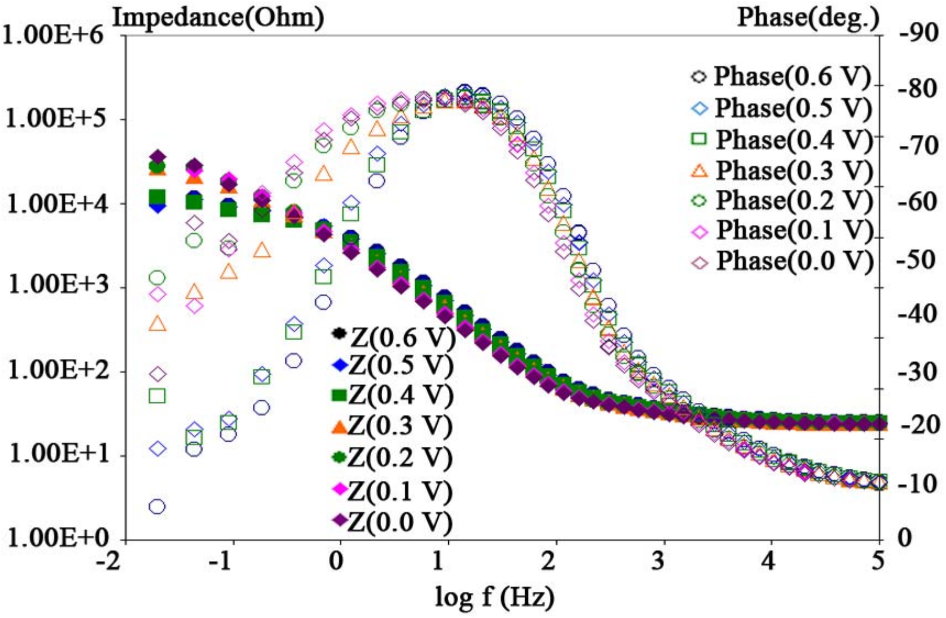

(b)

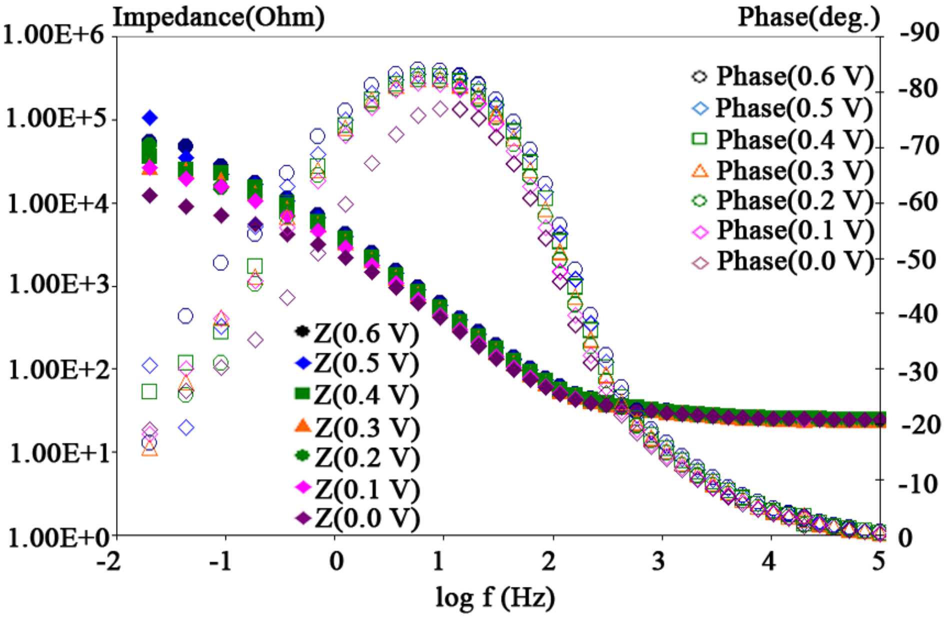

(a)

Figure 63 The Bode plots of different TiO_2 electrodes under irradiation; (a) TiO_2-SG and (b) 2%Ce TiO_2-SG at various applied potentials; filled symbol represents impedance and unfilled symbol represents phase angle.

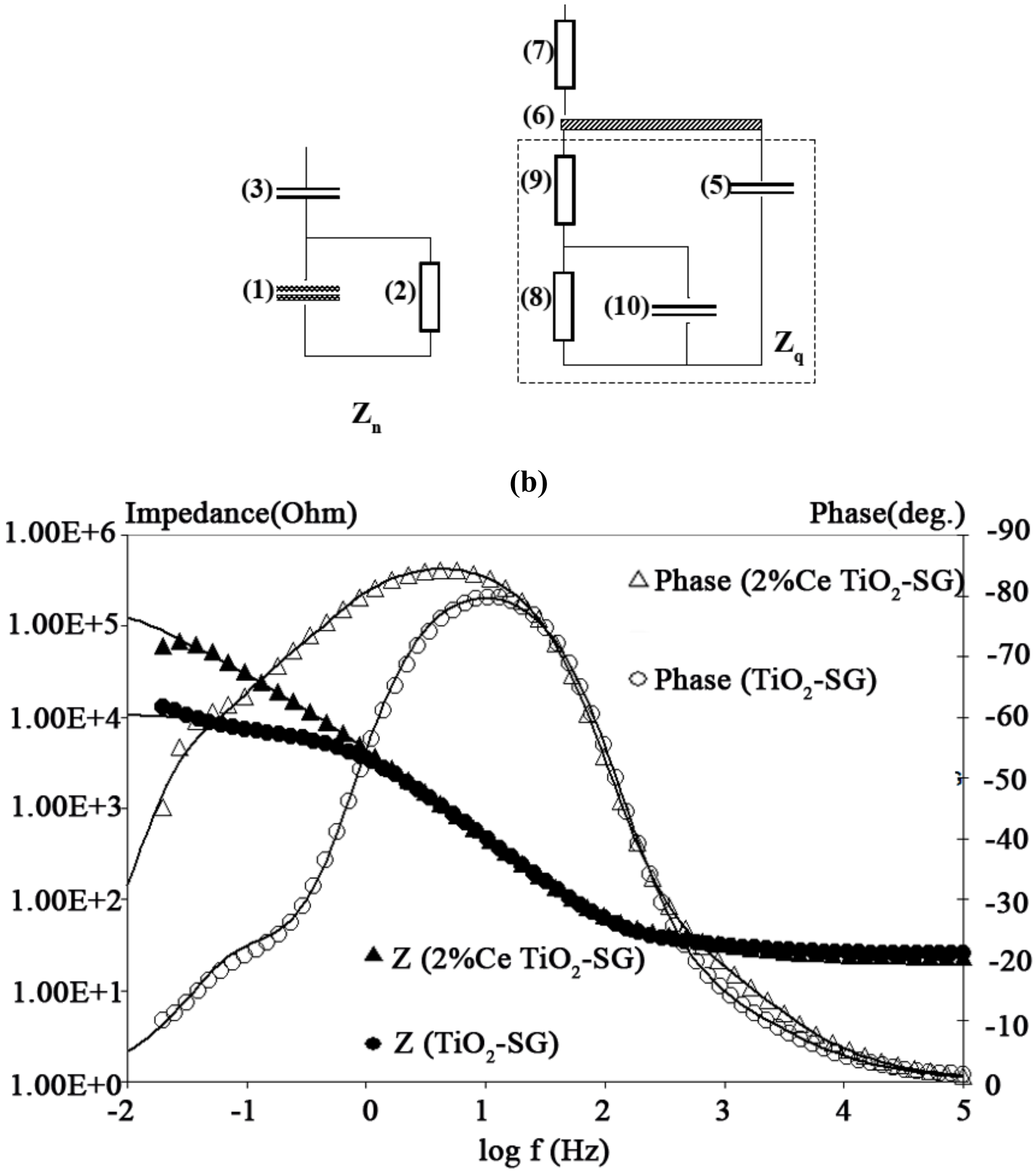

(b)

(a)

Figure 64 (a) EIS of different material nanoporous TiO_2-SG film electrodes at 0.3 V vs. Ag/AgCl; filled symbol represents impedance, unfilled symbol represents phase angle, line represents simulation data and (b) an equivalent circuit for electrodes under irradiation experiment.

The decreasing total impedance and drop of phase angle bending are more pronounced for the undoped TiO_2-SG electrode compared to 2%Ce TiO_2-SG material, see Figure 64 (a). The higher photoconductivity of the TiO_2-SG electrode was indicated by a smaller impedance and a high phase angle bending at the low frequency edge (10 Hz to 20 mHz, almost DC condition), that corresponds to the CV measurement which revealed a two times higher photocurrent for the undoped material. The EIS results were interpreted using a modified partial scheme of dark condition under consideration of the charge transfer and the recombination processes [Figure 64 (b)]. The partial equivalent circuit for Zn [Figure 64 (b) on the left-hand side] was modified because the impedance element 4 cannot be calculated after the implementation of additional elements for Zq [Figure 64 (b) on the right-hand side]. This element was eliminated i.e. the ITO/pore ground interface was fixed to be an insulating one. As a consequence, a charge transfer reaction at this interface was excluded and the observed current flow was only due to the photoinduced charge transfer at the TiO_2 semiconductor/electrolyte interface. Thus Zq was modified from the partial scheme of that for the dark condition [Figure 57(b)] by addition of elements considering the photoinduced reactions as follows: i) the heterogeneous charge transfer reaction at the porous TiO_2 layer/electrolyte interface ohmic resistance, element 8, ii) the accumulation of photoinduced charge carriers at the semiconductor surface by a capacitive element (element 10) parallel to the heterogeneous charge transfer reaction resistance and iii) the charge carrier recombination, represented by resistive element 9, which is a competition reaction to the heterogeneous charge transfer process.

In summary, Zq consists of two parallel paths, one for charging/discharging of the space charge layer (element 9 and 5) and one for faradaic photocurrent (element 8 and 10) related elements, i.e. the charge transfer and recombination resistance. Comparing the simulation results of dark and irradiation conditions, the elements for the interface ITO/pore ground (Zn, including element 1, 2 and 3), the pore electrolyte resistance (Zp) and the electrolyte resistance (element 7) remain almost constant (see Table 15). As expected, these elements are not affected by irradiation. The elements attributed to the photoinduced charge carrier flow are different for the TiO_2-SG and 2%Ce TiO_2-SG electrodes, under irradiation. It is noticeable that impedance element 8, 9 and Zs are significantly smaller for the

TiO_2-SG electrodes, revealing the higher photoactivity. For TiO_2-SG, which is a mixture phase of anatase and rutile (see section 3.2.1) the same as a commercial TiO_2-P25, it can be explain by the interconnection between anatase and rutile. It can be explained by the interconnection between anatase and rutile. The photogenerated holes transfer from the anatase to rutile while the photogenerated electrons are prevented under applied potential increasing the charge separation. This is in accordance with a higher rate constant for a heterogeneous charge transfer reaction, a smaller recombination rate and a higher conductivity for the bulk electrode material (network of TiO_2 particles).

Taking into account that almost the same mass of TiO_2 was deposited for TiO_2-SG and 2%Ce TiO_2-SG and assuming similar absorption characteristics, one may conclude that the Ce sites are acting as recombination centers for photoinduced charge carriers, see 4.1.2 (a). The other may be explained by the surface area of the material. The cerium doped TiO_2 film showed only the anatase phase (i.e. a low density phase) which is small contact area of each particle. These imply that high resistance.

Table 15 The elements value of different TiO_2-SG electrodes in the dark and under irradiation using the equivalent circuit in Figure 57 (b) and Figure 64 (b); the numbers in brackets are the significance of elements and the error of elements, respectively.

Dark condition			**Irradiation condition**		
Material (current)/ Elements	**TiO_2-SG (38.75 nA)**	**2%Ce TiO_2-SG (51.16 nA)**	**Material (photocurrent)/ Elements**	**TiO_2-SG (50.98 μA)**	**2%Ce TiO_2-SG (39.46 μA)**
1. CPE (μF)	14.69 (0.05, 5.65)	11.66 (0.10, 1.50)	1. CPE (μF)	14.52 (0.05, 10.74)	12.25 (0.09, 3.36)
α	698 m	740.8 m	A	755.8 m	756.5 m
2. resistance(Ohm)	11.14 (0.15, 2.10)	16.94 (0.21, 1.41)	2. resistance(Ohm)	9.504 (0.15, 4.37)	17.16 (0.21, 1.46)
3. capacitance (μF)	30.53 (0.99, 0.85)	28.07 (0.99, 1.06)	3. capacitance (μF)	30.61 (0.90, 1.23)	31.94 (0.95,0.80)
4. resistance (Ohm)	3.884 M (0.06, 20.55)	2.733 M (0.09, 9.62)			
5.capacitance (μF)	2.385 (0.07, 21.51)	3.267 (0.10, 8.49)	5. capacitance (μF)	45 (0.10, 24.31)	30.4 (0.13, 79.77)
6.porous impedance			6.porous impedance		
Z_p (Ohm)	8.896 (0.35, 0.88)	7.592 (0.35, 1.50)	Z_p (Ohm)	8.829 (0.35, 2.13)	8.198 (0.35, 0.71)
Z_s (Ohm)	240.6 (0.03, 36.30)	524.5 (0.04, 21.93)	Z_s (Ohm)	33.79 (0.49, 30.41)	146.4 (0.33,33.87)
7.electrolyte resistance(Ohm)	16.42 (0.64, 0.48)	14.01 (0.64, 0.81)	7.electrolyte resistance(Ohm)	16.49 (0.65, 1.14)	15.3 (0.65, 0.38)
			8. resistance (KOhm)	2.053 (0.20, 100.95)	100.8 (0.21, 28.45)
			9. resistance (KOhm)	1.231 (0.35, 6.08)	8.221 (0.03, 12.95)
			10. capacitance (mF)	1.582 (0.17, 13.46)	0.490 (0.19, 53.26)

(c) Film thickness

The thickness of the electrode is an important parameter relating to the diffusion length of charge carries. For a long diffusion length charge carriers, the recombination process may occur during the diffusion corresponding to CV results [section 4.1.2 (a)]. The Bode plots and simulation plots of different thickness TiO_2-SG electrodes under irradiation at 0.3 V vs. Ag/AgCl are shown in Figure 65. At the high frequency range (>10 Hz), the impedance of pore ground (Zn) is similar compared with the different thickness of TiO_2-SG electrodes. The significant difference of total impedances and bendings of phase angle are pronounced in the low frequency range (<10 Hz).

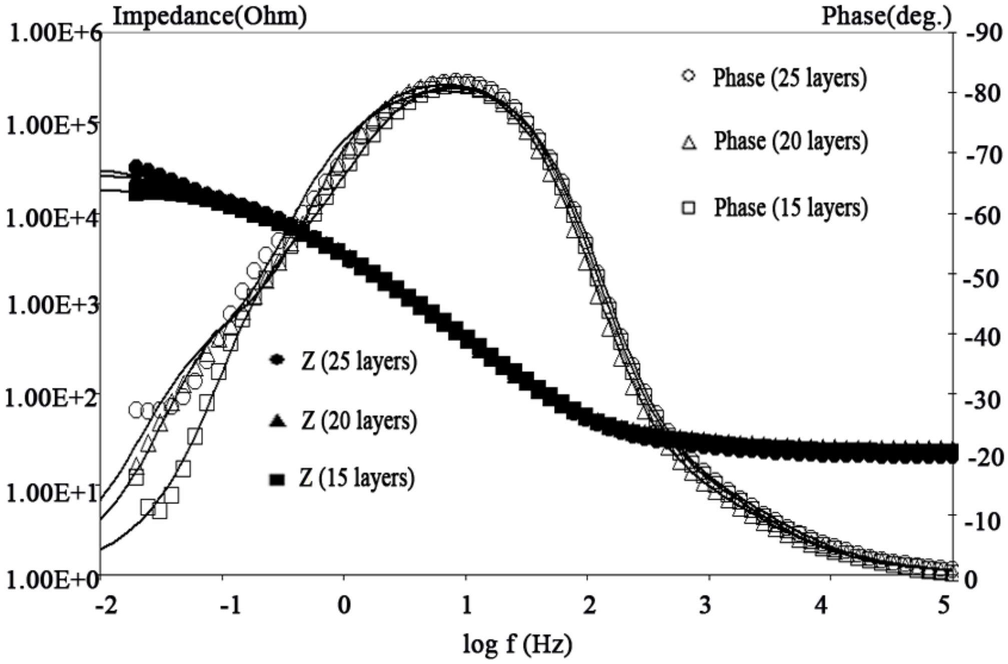

Figure 65 The Bode plots of different thickness nanoporous TiO_2-SG electrodes at 0.3 V vs. Ag/AgCl; filled symbol represents impedance and unfilled symbol represents phase angle and line represents simulation data.

The simulation procedure is performed using the proposed equivalent circuit for the irradiation probe without modification [Figure 64 (b)] and the fitting results are shown in Table 16. The elements corresponding to the impedance of pore ground (Zn) are closely constant. As expected, the ITO substrate was protected by porous TiO_2 material. These results indicate that the morphologies of the first layer of TiO_2 with different thickness are similar. These elements are independent on the thickness of TiO_2 material while the elements (element 5, 8, 9, 10 and Zs) representing the photoinduced processes depend on the thickness of the electrode.

Table 16 The elements value of different thickness TiO_2-SG electrodes under irradiation using the equivalent circuit in Figure 64 (b); the numbers in brackets are the significance of elements and the error of elements, respectively.

Number of layer (photocurrent) / Elements	**15 layers (40.55 μA)**	**20 layers (50.98 μA)**	**25 layers (42.04 μA)**
1. CPE (μF)	13.42 (0.06, 9.81)	14.52 (0.05, 10.74)	14.41 (0.06, 7.65)
α	805.2 m	755.8 m	784.3 m
2. resistance(Ohm)	9.18 (0.17, 6.98)	9.504 (0.15, 4.37)	9.132 (0.17, 5.23)
3. capacitance (μF)	29.43 (0.90, 3.30)	30.61 (0.90, 1.23)	31.08 (0.92, 2.16)
5. capacitance (μF)	151 (0.20, 21.40)	45 (0.10, 24.31)	112.8 (0.14, 30.78)
6.porous impedance			
Z_p (Ohm)	7.774 (0.35, 1.80)	8.829 (0.35, 2.13)	7.18 (0.35, 1.62)
Z_s (Ohm)	106.1 (0.48, 11.38)	33.79 (0.49, 30.41)	108.1 (0.48, 27.76)
7.electrolyte resistance(Ohm)	14.53 (0.65, 0.97)	16.49 (0.65, 1.14)	13.42 (0.65, 0.87)
8. resistance (KOhm)	12.74 (0.09, 109.54)	2.053 (0.20, 100.95)	11.19 (0.10, 78.21)
9. resistance (KOhm)	3.832 (0.24, 24.35)	1.231 (0.35, 6.08)	2.186 (0.18, 29.48)
10. capacitance (mF)	0.897 (0.21, 39.14)	1.582 (0.17, 13.46)	0.591 (0.24, 32.62)

Assuming the photon flux, the potential and wavelength of incident light are constant during the measurement, the photocurrents of the lowest thickness (15 layers) and the highest thickness (25 layers) are lower than a 20 layers TiO_2-SG electrode, see Table 16. The elements in an irradiated equivalent circuit of the lowest thickness can explain that the amount of TiO_2-SG deposited on ITO electrode relating to charge carrier density is less compared with a 20 layers of porous TiO_2-SG electrode since the photocurrent depends on the amount of deposited TiO_2. The resistive charge carrier and resistive recombination elements are higher than one. In contrast, the highest thickness has more TiO_2 but these elements are still higher than a 20 layer one. These show that the photocurrent not only depends on the amount of material, but also depends on the diffusion length of charge carriers to the back contact. These results can be explained by the quantum efficiencies and the penetration depth of light. The width of depletion layer constants is due to performance at constant potential (0.3 V vs. Ag/AgCl) and the constant incidence of light intensity. At the highest thickness, the penetration depth of the incidence of light is small resulting in not full absorption of light by the TiO_2 materials. Moreover, the diffusion length of the carrier is higher than the width of the depletion layer occurring the electron-hole recombination. Besides, during the diffusion, photogenerated electrons can be lost by transferring to reducible species in the electrolyte, which were penetrated into TiO_2 porous film (Jongh, 1971).

(d) Effect of photon flux

The effect of the photon flux was considered to achieve more information about the nature of possible rate determining processes, e.g. to be able to decouple the heterogeneous charge transfer and recombination processes by employing fitting procedure. Assuming the thickness of film electrode and potential are constant, Figure 66 shows the overlay Bode plots of a 20 layers TiO_2-SG electrode at the various percentage of photon flux, at 0.3 V vs. Ag/AgCl.

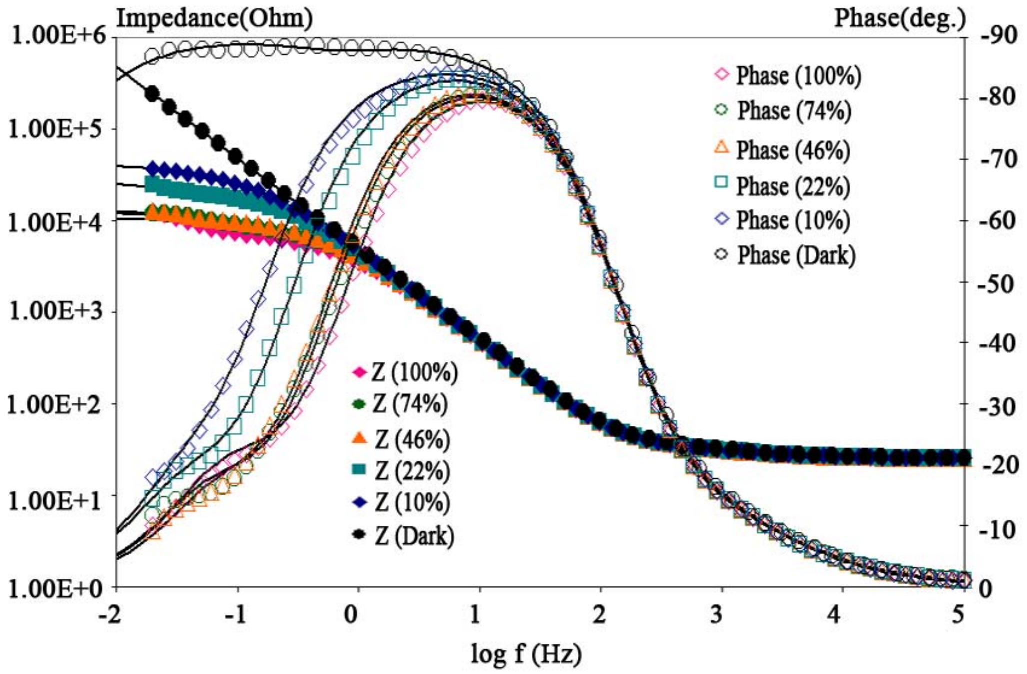

Figure 66 EIS of irradiated TiO_2-SG at various percentage of photon flux at 0.3 V vs. Ag/AgCl; filled symbol represents impedance and unfilled symbol represents phase angle and line represents simulation data.

The Bode plots of a TiO_2-SG electrode reveal the time-constant (below 10 Hz) according to increasing percentage of light. Considering the low frequency range relating to the photoinduced processes (about 10 Hz), the phase angle bends more with increasing the percentage of photon flux. The total impedances of different percentages of photon flux are significantly different. The 100% photon flux shows the lowest total impedance and the most bending phase angle.

The EIS data of a TiO_2-SG electrode were analyzed using the equivalent circuit for irradiated probes [Figure 64 (b)]. All impedance spectra obtained at different photon flux could be simulated with the same accuracy. The results of simulation procedure are listed in Table 17. Again, elements expected not to be affected by photoinduced processes [Zn (element 1 to 3), Zp and element 7 (bulk electrolyte resistance)] remain almost constant during variation of the photon flux. In contrast, element 8 considered as the heterogeneous charge transfer resistance and

Table 17 The elements value of TiO_2-SG electrodes under irradiation at various percentage of photon flux and 0.3V using the equivalent circuit in Figure 64 (b); the numbers in brackets are the significance of elements and the error of elements, respectively.

Percentage of photon flux (photocurrent) / Elements	**10% (12.13 μA)**	**22% (19.63 μA)**	**46% (38.30 μA)**	**74% (42.14 μA)**	**100 % (50.98 μA)**
1. CPE (μF)	14.86 (0.05, 10.12)	14.57 (0.05, 9.98)	14.13 (0.05, 9.47)	14.00 (0.05, 10.97)	14.52 (0.05, 10.74)
α	763.2 m	770.8 m	777.2 m	778 m	755.8 m
2. resistance (Ohm)	9.466 (0.15, 6.13)	9.383 (0.15, 4.28)	9.200 (0.15, 4.35)	9.190 (0.15, 5.32)	9.504 (0.15, 4.37)
3. capacitance (μF)	30.27 (0.95, 2.02)	30.67 (0.94, 1.53)	30.11 (0.91, 1.75)	29.91 (0.91, 1.84)	30.61 (0.90, 1.23)
5.capacitance (μF)	36.85 (0.10, 24.93)	34.34 (0.09, 35.53)	39.82 (0.11, 23.87)	41.08 (0.11, 26.52)	45 (0.10, 24.31)
6.porous impedance					
Z_p (Ohm)	8.901 (0.35, 1.69)	8.889 (0.35, 2.07)	8.864 (0.35, 2.53)	8.87 (0.35, 2.76)	8.829 (0.35, 2.13)
Z_s (Ohm)	123.7 (0.48, 7.18)	75.05 (0.48, 14.50)	36.6 (0.48, 8.33)	34.19 (0.48, 13.67)	33.79 (0.49, 30.41)
7.electrolyte resistance(Ohm)	16.64 (0.65, 0.90)	16.61 (0.65, 1.11)	16.56 (0.65, 1.36)	16.57 (0.65, 1.48)	16.49 (0.65, 1.14)
8. resistance (KOhm)	5.586 (0.06, 52.75)	4.401 (0.06, 53.19)	2.024 (0.15, 38.31)	2.237 (0.14, 34.06)	2.053 (0.20, 100.95)
9. resistance (KOhm)	7.416 (0.31, 7.42)	4.19 (0.35, 12.92)	2.183 (0.37, 8.86)	1.965 (0.37, 11.34)	1.231 (0.35, 6.08)
10. capacitance (mF)	0.969 (0.10, 33.25)	1.387 (0.13, 35.13)	1.66 (0.12, 27.75)	1.714 (0.13, 32.33)	1.582 (0.17, 13.46)

Zs resistance of the network nanoporous particles film decrease and are almost constant upon 46% of photon flux. These results can explain that light at a higher photon flux penetrated to a much greater depth producing more charge carriers and upon 46% photon flux reach the limitation of charge transfer reaction of this electrode. Considering the experimental procedure, the electrode was irradiated at front side and the variation photon flux change the distance between the irradiation source and the electrode. The space charge capacitance modestly increased with the increase in the photon flux while the element 10 as an accumulating charge carrier capacitance significantly increased. At the limitation charge transfer reaction, more charge carriers accumulate at the surface of the material and some of them accumulate in the space charge region. The element (9) representing the recombination reaction decreased with the intensity of photon. It can show that the lower intensity gives a smaller number of excited electrons and this gives a larger fraction of the electrons used to fill the recombination center.

4.3 Development of the experimental set up

4.3.1 Cyclic voltammetry (CV)

(a) TiO_2-P25 particulate film electrodes

The photon flux of the halogen cold lamp (250 W, KL 2500 LCD, Schott) and the halogen lamp (250W, 5025AF-S, Braun) are almost similar. The 5 layers of TiO_2-P25 electrode was used as a working electrode in the 0.5 M Na_2SO_4 electrolyte. The electrochemical set up I [Figure 67 (a)] and set up II [Figure 67 (b)] were used. Figure 68 (a) shows the similar overlay photocurrent of a TiO_2-P25 electrode.

(a) (b)

Figure 67 The electrochemical set up; (a) set up I and (b) set up II.

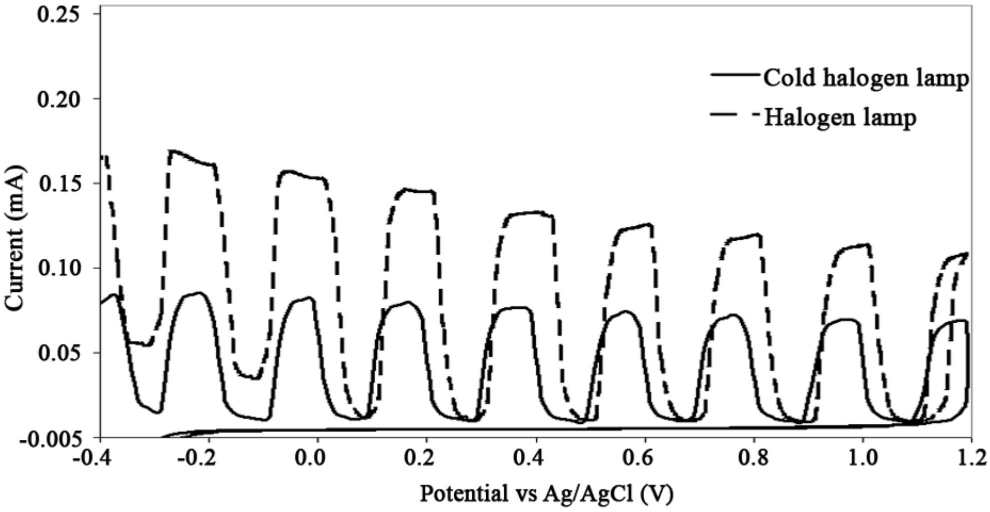

(b)

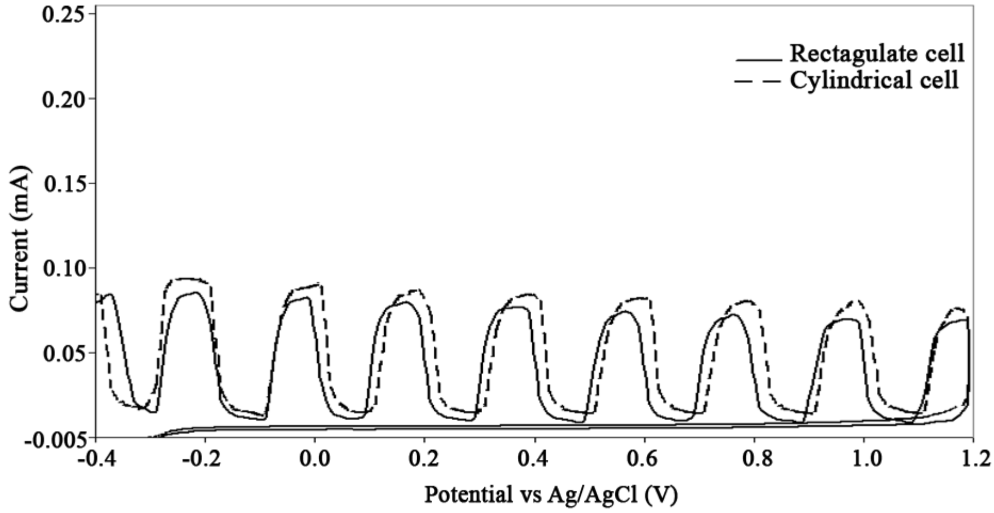

(a)

Figure 68 The photocurrent of a TiO_2-P25 electrode employing the different systems (a) comparing different electrochemical cells and (b) comparing different light sources.

The set up I was a cylindrical cell but the set up II was a rectangular cell. These results show that a shape of the electrochemical cell is not strong influence to enhance photocurrent. In contrast, the influence of light source shows significantly different photocurrent, see Figure 68 (b). The measurement of photocurrents was performed using the different light sources and the rectangular cell. The photocurrent using the old light source is about 1.5 times greater than one of using the new light source. It may effect the temperature during the operation, which can increase the rate of charge carrier diffusion. However, the halogen cold light source and the rectangular cell [set up II, Figure 67 (b)] were employed for the following experiments to reduce the effect of temperature and also to prevent the light scattering.

(b) TiO_2-SG film electrodes

The thin film semiconductor electrodes on transparent substrates can be illuminated from either side, and the following assignations are investigated: front side (EE, electrolyte/electrode interface), and back side (SE, substrate/electrode interface). From the well-known expression model, Gärtner-Bulter, considering front side illumination, the quantum efficiency relating to the photocurrent depends on the optical absorption coefficient, the diffusion length of the minority carriers (holes, in the case of n-doped semiconductor), and the depletion layers width (Lindquist *et al.*, 1983). In case of SE (substrate/electrode interface), the ITO absorption is considered. The photocurrent of a TiO_2-SG electrode studied the influence of illumination direction, including EE and SE illuminations (Figure 69). The results were very similar. This implies that the thickness of film is very thin. As far as the ITO absorption was concerned, the absorption of ITO was determined using the TiO_2 photodiode. The photovoltage decreases by about 10% of incident light when an ITO was inserted between the photodiode and the light source. Quartz is about 5 % of decreasing incident light indicating that the rectangular electrochemical cell made of quartz might absorb the same amount of incident light. These indicate that EE illumination (electrolyte/electrode interface) is better than SE illumination (substrate/electrode interface) because of the non losing of incident light by substrate absorption. More detail will be discussed in section 4.3.2 (i).

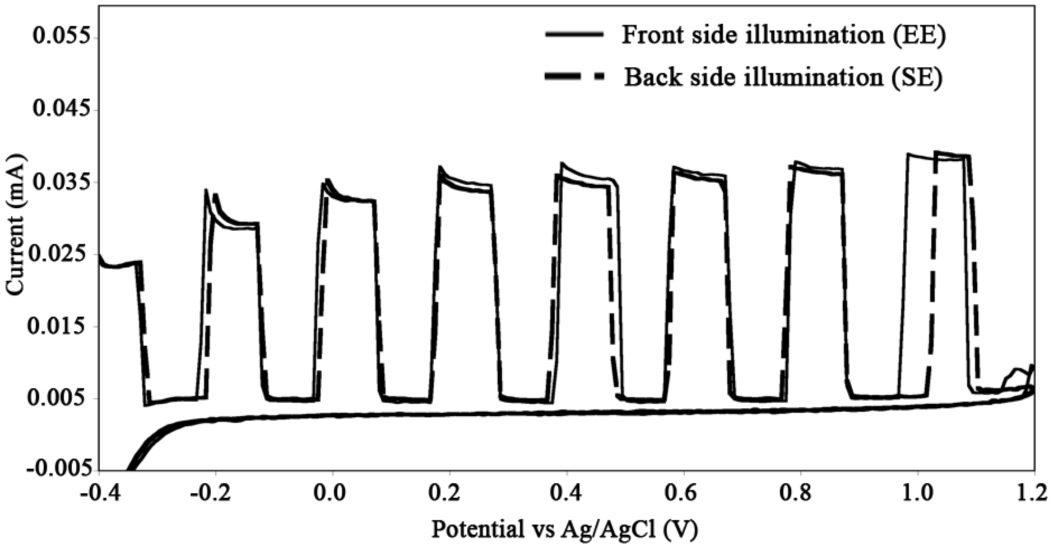

Figure 69 The photocurrent of a TiO_2-SG electrode for front and back side illuminations.

4.3.2 Electrochemical impedance spectroscopy (EIS)

(a) TiO_2-SG film eletrodes

(i) The direction of illumination

As shown in Figure 69, the photocurrents from both EE (EE, electrolyte/electrode interface) and SE (substrate/electrode interface) illuminations are similar. The simulation and experimental plots, Bode plots, of a TiO_2-SG electrode in the dark and under different side illuminations at 0.3V vs. Ag/AgCl, in 0.5 M Na_2SO_4 are shown in Figure 70.

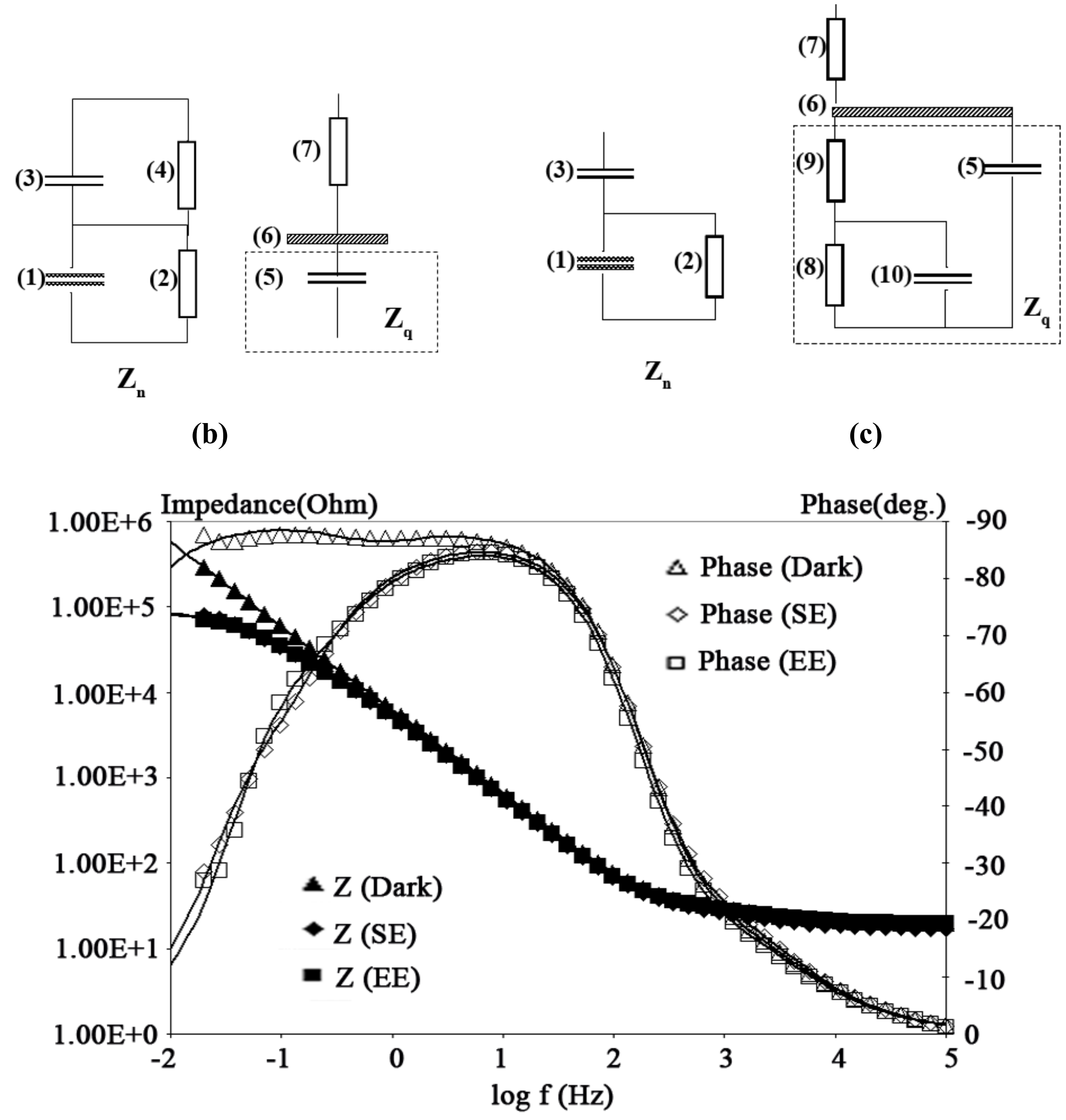

(b) (c)

(a)

Figure 70 (a) The Bode plots of different direction of illumination of a nanoporous TiO_2-SG electrode at 0.3 V vs. Ag/AgCl; filled symbol represents impedance and unfilled symbol represents phase angle and line represents simulation data, (b) the equivalent circuit for dark experiment and (c) the equivalent circuit for irradiation experiment.

As expected, the Bode plot of a TiO_2-SG electrode in the dark at 0.3V shows the high total impedance and the slightly bending phase angle comparing under irradiation. At below 10 Hz, the Bode plots of TiO_2-SG electrode under EE (EE, electrolyte/electrode interface) and SE (substrate/electrode interface) illuminations show similar plots. The total impedance decreases and the phase angle bends under irradiation. The simulation processes were performed using the dark equivalent circuit [Figure 70 (b)] for the dark condition and the irradiation equivalent circuit for the irradiation condition, including EE and SE illuminations [Figure 70 (c)] and the results of fitting process are listed in Table 18. The elements (element 1, 2, 3 and 7), relating to the impedance of the ITO bulk, of the TiO_2/ITO interface and the resistive electrolyte, are almost constant under dark and irradiation conditions. As discussed in section 4.2.2 (b), these elements are independent photoinduced processes. The element 4 representing the surface oxidation of ITO resistance is a high resistive element in the dark condition due to the thermal treatment. Under irradiation, this element could not be calculated and was fixed to an insulating element. The element 5 increases comparing the dark and the irradiation conditions. It may be some of the photogenerated heterogeneous charge carriers that can accumulate in the space charge region. For this photoinduced process, the resistive Zs element decreases. This suggests that the TiO_2 electrode becomes more conductive. Comparing the EE and SE illuminations, especially the elements relating to the photoinduced processes (element 8,9,10 and Zs) are different. The density of photogenerated charge carriers under the EE illumination decreases from the TiO_2/electrolyte towards the TiO_2/ITO interface while the concentration profile has the opposite trend for SE illumination. The charge transfer reaction of EE illumination is higher and the recombination reaction is smaller that that of SE illumination. These mean the charge transfer resistive element (element 8) of EE should be lower, and the recombination resistive element should be higher than of SE. The Zs, relating the resistive network TiO_2 particles, of EE illumination is lower than of SE illumination. Therefore, EE irradiation was performed in this experiment due to the ITO absorption and the high recombination resistive element (element 9) decreasing the recombination reaction.

Table 18 The element values of a TiO_2-SG electrodes under different direction of illumination at 0.3V vs. Ag/AgCl using the dark equivalent circuit in Figure 70 (b) and irradiation equivalent circuit in Figure 70 (c); the numbers in brackets are the significance of elements and the error of elements, respectively.

Condition (current) / Elements	**Dark (57.39 nA)**	**Condition (photocurrent) / Elements**	**Front (13.87 µA)**	**Back (14.23 µA)**
1. CPE (µF)	9.59 (0.09, 2.49)	1. CPE (µF)	9.70 (0.08, 4.94)	10.55 (0.09, 5.20)
α	728 m	A	744 m	750 m
2. resistance(Ohm)	13.95 (0.21, 1.97)	2. resistance(Ohm)	13.39 (0.21, 2.31)	12.96 (0.22, 3.31)
3. capacitance (µF)	23.84 (0.98, 0.89)	3. capacitance (µF)	25.51 (0.94, 0.85)	25.84 (0.95, 1.04)
4. resistance (Ohm)	4.17 M (0.07, 53.00)			
5.capacitance (µF)	3.47 (0.13, 15.71)	5. capacitance (µF)	27.01 (0.19, 9.63)	23.93 (0.14, 25.68)
6.porous impedance		6.porous impedance		
Z_p (Ohm)	6.83 (0.35, 1.56)	Z_p (Ohm)	6.80 (0.34, 1.80)	5.92 (0.34, 1.77)
Z_s (Ohm)	155.1 (0.05, 21.63)	Z_s (Ohm)	88.19 (0.29, 28.17)	98.82 (0.30, 17.56)
7.electrolyte resistance(Ohm)	12.57 (0.64, 0.85)	7.electrolyte resistance(Ohm)	12.71 (0.64, 0.96)	11.07 (0.64, 0.94)
		8. resistance (KOhm)	23.41 (0.12, 65.79)	31.84 (0.14, 23.35)
		9. resistance (KOhm)	31.02 (0.25, 32.26)	26.24 (0.20, 25.68)
		10. capacitance (µF)	48.99 (0.06, 31.73)	91.11 (0.13, 24.91)

(ii) Effect of applied potential

Usually, the photocurrent from TiO_2 disappears almost completely where a positive potential region to E_{fb} exists. The influence of applied potential was investigated by the variation of applied potentials of a TiO_2-SG electrode vs. an Ag/AgCl reference electrode in 0.5 M Na_2SO_4 assuming the photo incident intensity is constant during the measurement.

The simulation data and experimental data, Bode plots, of a TiO_2-SG electrode at various applied potentials under irradiation are shown in Figure 71 compared with the dark condition at 0.5V. The Bode plots show that the total impedance decreased and the phase angle bended more with increasing applied potential. The simulation processes were performed using the irradiation equivalent circuit [Figure 70 (c)] and the results of fitting process are shown in Table 19. As expected, all elements are not constant under the variation of applied potentials. The elements relating to the photoinduced processes are markedly different. The resistive elements representing the charge transfer and recombination processes decrease, while increasing the applied potential. The Zs also decreases under anodic potential. Where the three elements are the couple elements. The resistive recombination element (element 9) reaches the limitation about 0.3 V while the resistive charge transfer element slightly decreases. It can be explained, under high anodic potential, that the photogenerated electrons flows easily to the ITO (back contact) while photogenerated holes diffuse to the surface, see Figure 71 (b). This implies that the charge/discharge resistive element (element 8) should decrease and the charge accumulate element (element 10) should increase under high anodic potential corresponding to the fitting results (Table 19). Under easily photogenerated electrons flow, the recombination reaction might increase revealing by decrease of recombination resistive element (element 9).

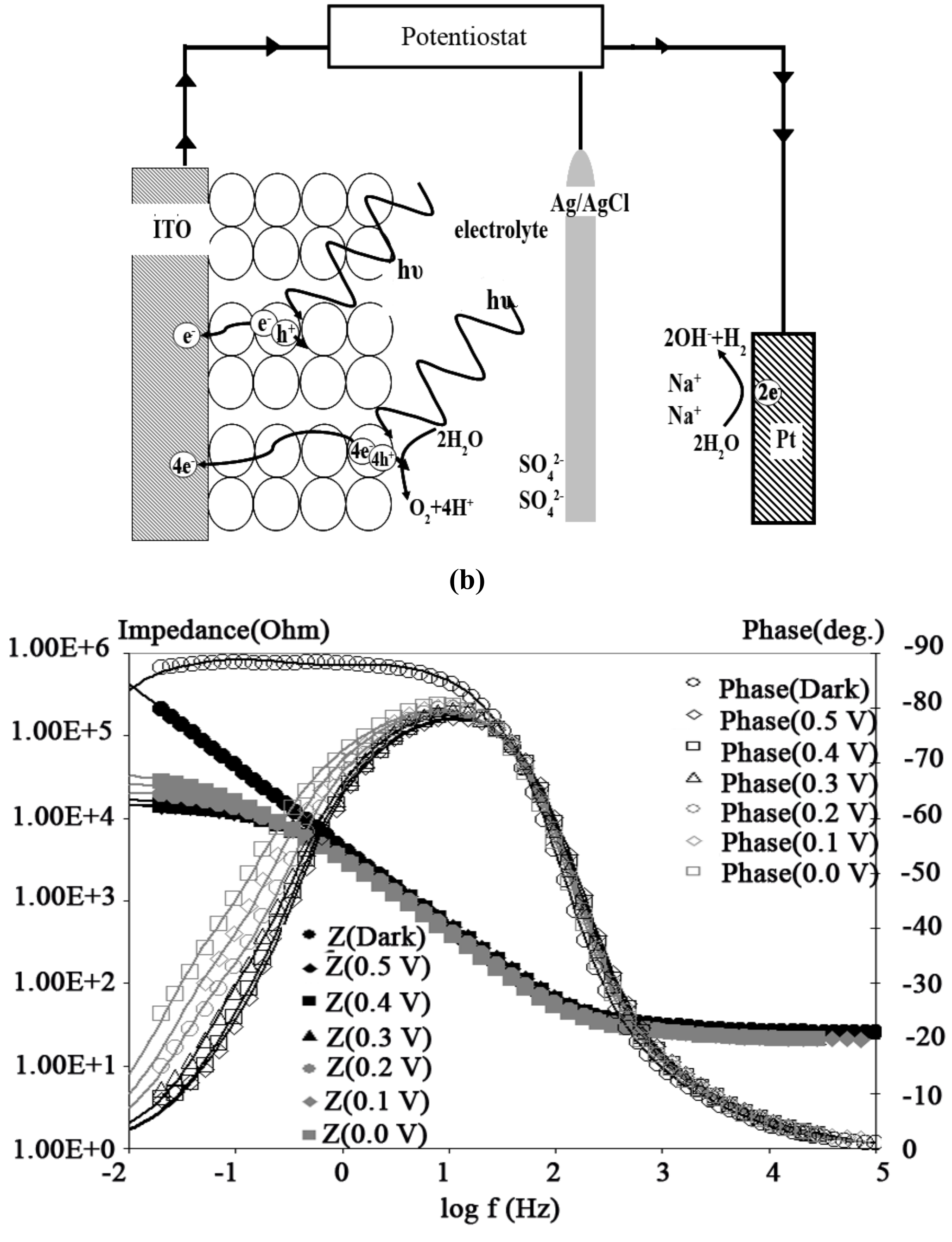

(b)

(a)

Figure 71 (a) The Bode plots of different applied potentials of a nanoporous TiO_2-SG electrode; filled symbol represents impedance and unfilled symbol represents phase angle and line represents simulation data and (b) Schematic of proposed photoinduced processes.

Table 19 The elements value of TiO_2-SG electrodes under irradiation at various applied potential using the equivalent circuit in Figure 70 (c); the numbers in brackets are the significance of elements and the error of elements, respectively.

Potential (photocurrent) / Elements	**0.0 (4.51uA)**	**0.1 (6.85uA)**	**0.2 (10.39uA)**	**0.3 (14.39uA)**	**0.4 (19.85uA)**	**0.5 (26.23uA)**
1. CPE (µF)	16.65	15.81	15.17	14.47	14.03	13.77
	(0.05, 10.03)	(0.05, 10.37)	(0.05, 10.56)	(0.05, 9.91)	(0.05, 10.40)	(0.05, 9.94)
α	737.4 m	744.9 m	749.8 m	745.2 m	708.6 m	692.3 m
2. resistance(Ohm)	8.801	8.796	8.817	9.004	9.489	9.937
	(0.16, 5.52)	(0.16, 4.36)	(0.16, 3.79)	(0.15, 3.34)	(0.15, 4.14)	(0.14, 2.80)
3. capacitance (µF)	35.32	33.14	31.3	29.54	27.67	26.1
	(0.89, 1.69)	(0.88, 2.02)	(0.88, 1.74)	(0.87, 1.40)	(0.87, 1.08)	(0.87, 0.44)
5. capacitance (µF)	190.2	161.3	139.8	122.4	113.6	106.8
	(0.24, 5.23)	(0.23, 7.70)	(0.21, 10.55)	(0.21, 9.70)	(0.22, 5.57)	(0.22, 5.78)
6.porous impedance						
Z_p (Ohm)	7.229	7.246	7.282	7.784	7.822	7.859
	(0.35, 5.36)	(0.35, 4.26)	(0.35, 3.93)	(0.35, 3.91)	(0.35, 3.66)	(0.35, 3.19)
Z_s (Ohm)	75.3	63.38	52.84	46.08	40.57	40.47
	(0.46, 5.61)	(0.47, 4.99)	(0.47, 2.63)	(0.48, 6.52)	(0.48, 9.15)	(0.48, 8.02)
7.electrolyte resistance(Ohm)	13.39	13.42	13.48	14.47	14.56	14.63
	(0.65, 2.89)	(0.65, 2.30)	(0.65, 2.12)	(0.65, 2.10)	(0.64, 1.97)	(0.64, 1.71)
8. resistance (KOhm)	8.487	6.036	4.343	2.742	1.659	1.589
	(0.09, 15.93)	(0.09, 22.32)	(0.13, 16.85)	(0.18, 17.27)	(0.14, 32.29)	(0.13, 29.74)
9. resistance (KOhm)	6.521	4.665	3.514	3.1	3.309	3.292
	(0.17, 31.60)	(0.20, 15.19)	(0.22, 10.12)	(0.27, 11.66)	(0.34, 12.97)	(0.34, 11.19)
10. capacitance (mF)	0.456	0.580	0.698	0.667	1.023	1.173
	(0.11, 15.85)	(0.13, 15.19)	(0.13, 16.85)	(0.11, 21.04)	(0.07, 9.57)	(0.07, 13.05)

(iii) Effect of methanol addition

The photocurrent can be enhanced by adding a more efficient hole scavenger, such as citrate, iodide, formic acid and methanol, to the pure electrolyte. Methanol was used as a model of hole scavenger, in this thesis. The addition of 2.5M methanol to 0.5M Na_2SO_4 increases the photocurrent by almost two times, comparing Table 20 and Table 21. The influence of the electrolyte solution was investigated to obtain more information about the processes relating to the elements in equivalent circuits. The simulation processes of a TiO_2-SG electrode were performed using the equivalent circuit for irradiation [Figure 70 (c)]. The results of simulation process are listed in Table 21 with the same accuracy. The plots of invert resistive elements (element 8, 9 and Zs) as a function of fraction of photon flux, comparing pure electrolyte (0.5M Na_2SO_4) and added methanol electrolyte, are shown in Figure 72. The heterogeneous charge transfer resistance of the added methanol solution is smaller than the one of the pure electrolyte (i.e. invert Rct of added methanol is higher than that of pure electrolyte). Until 0.58 fraction of photon flux, the element 8 of pure electrolyte is almost constant. This indicates that the heterogeneous charge transfer reaction of using pure electrolyte reaches a limitation of reaction while one using the added methanol electrolyte increases while increasing the fraction of photon flux. The methanol traps photogenerated holes at the surface while photogenerated electrons flow through the network of particles to the back contact producing more photocurrent. In contrast, in a pure electrolyte, a limitation of charge carriers transfer dominates the 0.58 fraction of photon flux. The recombination resistive element (element 9) decreases when increasing the fraction of photon flux both in a pure electrolyte and an added methanol electrolyte (i.e. invert Rrec of both electrolyte increases). Because Zs cannot decouple from element 8 and 9, the Zs represents the resistance of diffusion electron through the network of particles that consists of charge transfer and the recombination reaction. The feature of Zs is a combination of elements 8 and 9. Zs for an added methanol electrolyte show a linearity dependent fraction of the photon flux but in pure electrolyte, up to

0.58 fraction of photon flux, shows slightly increasing of resistance. These can explain why the photogenerated hole was trapped by methanol penetrating to the substrate while in pure electrolyte photogenerated electrons can be lost by a reducible species in the pure electrolyte.

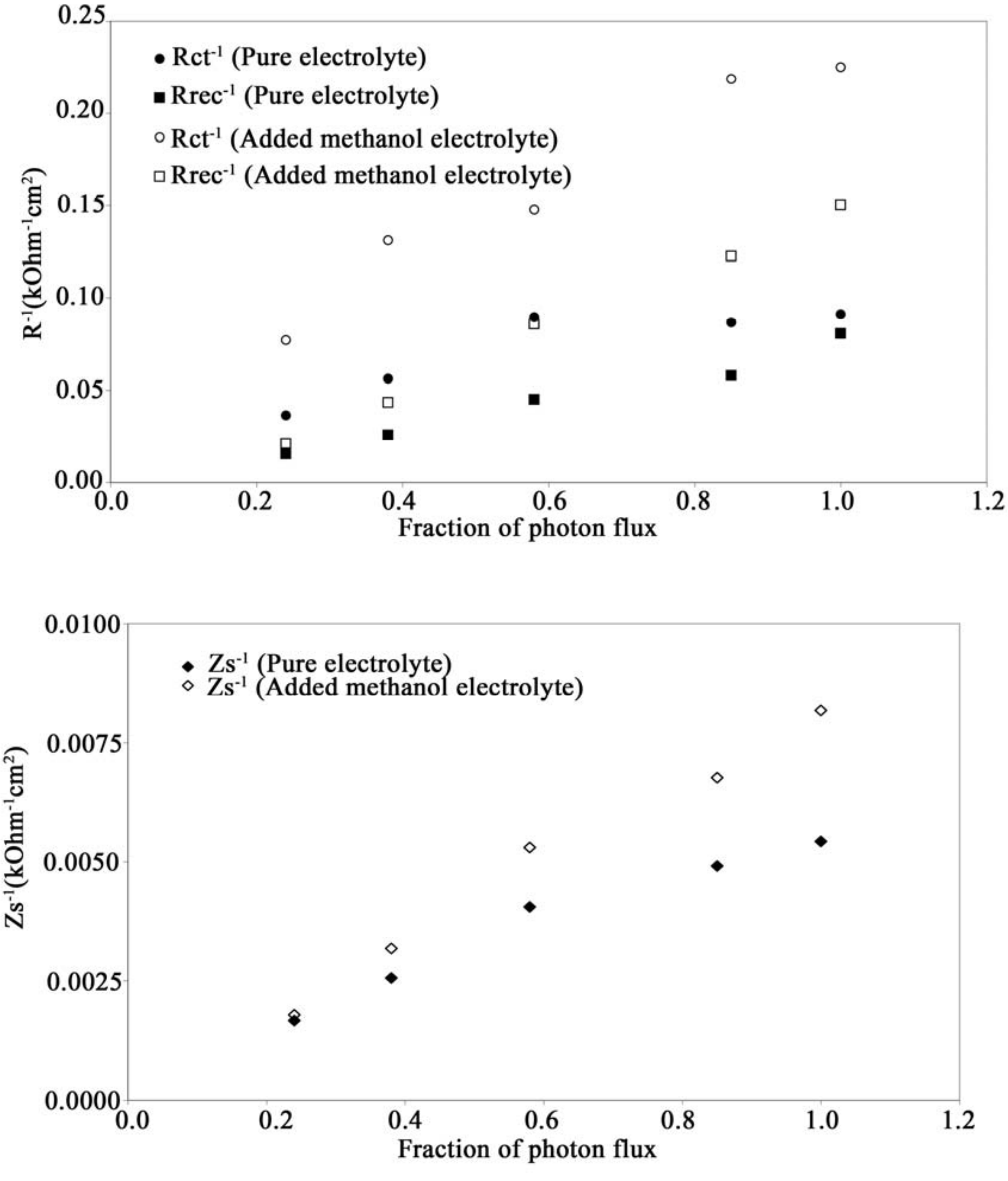

Figure 72 The inverse of resistances as a function of the fraction of photon flux using a pure electrolyte and an added methanol at 0.3 V vs. Ag/AgCl

Table 20 The elements value of 20 layers of TiO_2-SG electrodes under irradiation with different fraction of photon flux, pure electrolyte (0.5 M Na_2SO_4), at 0.3 V vs. Ag/AgCl using the equivalent circuit in Figure 70 (c); the numbers in brackets are the significance of elements and the error of elements, respectively.

Fraction of photon flux/ Element value	**0.24 (4.83uA)**	**0.38 (7.25uA)**	**0.58 (11.65uA)**	**0.85 (13.26uA)**	**1.00 (14.39uA)**
1. CPE (μF)	14.57	14.53	14.32	14.69	14.47
	(0.06, 8.50)	(0.06, 7.96)	(0.05, 9.53)	(0.05, 8.20)	(0.05, 9.91)
	709.3 m	730.8 m	736.6 m	737.9 m	745.2 m
2. resistance(Ohm)	9.839	9.555	9.386	9.365	9.004
	(0.16, 2.19)	(0.16, 2.46)	(0.16, 3.22)	(0.16, 3.39)	(0.15, 3.34)
3. capacitance (μF)	28.75	29.45	29.10	29.77	29.54
	(0.92, 0.80)	(0.90, 0.85)	(0.88, 1.03)	(0.88, 1.10)	(0.87, 1.40)
5. capacitance (μF)	121.0	136.0	132.9	126.7	122.4
	(0.23, 7.13)	(0.24, 4.67)	(0.23, 7.33)	(0.22, 6.38)	(0.21, 9.70)
6.porous impedance					
Z_p (Ohm)	7.209	7.266	7.254	7.234	7.784
	(0.35, 4.31)	(0.35, 4.24)	(0.35, 4.28)	(0.35, 4.02)	(0.35, 3.91)
Z_s (K Ohm)	149.5	97.79	61.1	50.91	46.08
	(0.46, 4.66)	(0.47, 3.20)	(0.47, 8.08)	(0.47, 3.31)	(0.48, 6.52)
7. electrolyte resistance(Ohm)	13.40	13.51	13.48	13.45	14.47
	(0.64, 2.32)	(0.64, 2.28)	(0.65, 2.30)	(0.65, 2.16)	(0.65, 2.10)
8. resistance (K Ohm)	6.838	4.443	2.794	2.882	2.742
	(0.06, 29.95)	(0.06, 29.21)	(0.07, 51.39)	(0.09, 22.35)	(0.18, 17.27)
9. resistance (K Ohm)	16.23	9.715	5.541	4.324	3.100
	(0.23, 9.25)	(0.29, 5.18)	(0.33, 11.75)	(0.31, 6.72)	(0.27, 11.66)
10. capacitance (mF)	0.640	0.730	1.092	1.14	0.667
	(0.06, 29.12)	(0.06, 28.60)	(0.07, 24.74)	(0.09, 16.44)	(0.11, 21.04)

Table 21 The elements value of 20 layers of TiO_2-SG electrodes under irradiation with different fraction of photon flux, added methanol electrolyte solution (0.5 M Na_2SO_4 with 2.5 M methanol), at 0.3 V vs. Ag/AgCl using the equivalent circuit in Figure 70 (c); the numbers in brackets are the significance of elements and the error of elements, respectively.

Fraction of photon flux/ Element value	**0.24 (8.55uA)**	**0.38 (14.06uA)**	**0.58 (22.63uA)**	**0.85 (27.27uA)**	**1.00 (30.81uA)**
1. CPE (μF)	25.41	23.87	23.07	22.73	21.72
	(0.03, 5.09)	(0.03, 20.17)	(0.03, 25.60)	(0.03, 15.96)	(0.03, 19.64)
	625.1 m	634.7 m	676.5 m	684.2 m	678.6 m
2. resistance(Ohm)	9.219	8.716	7.754	7.518	7.478
	(0.09, 4.36)	(0.09, 2.98)	(0.10, 1.77)	(0.10, 3.78)	(0.09, 5.21)
3. capacitance (μF)	32.17	32.22	32.34	31.83	31.82
	(0.90, 1.37)	(0.88, 0.99)	(0.85, 0.75)	(0.84, 0.83)	(0.82, 1.14)
5. capacitance (μF)	174.5	177.9	181.6	164.1	171.1
	(0.24, 7.32)	(0.24, 2.44)	(0.23, 3.95)	(0.22, 3.21)	(0.22, 6.06)
6.porous impedance					
Z_p (Ohm)	10.09	10.13	10.14	10.08	10.40
	(0.35, 4.61)	(0.35, 4.77)	(0.35, 4.93)	(0.35, 3.49)	(0.35, 5.74)
Z_s (K Ohm)	139.1	78.64	47.15	36.87	30.58
	(0.47, 13.27)	(0.48, 3.89)	(0.49, 21.13)	(0.49, 9.80)	(0.49, 2.05)
7. electrolyte resistance(Ohm)	18.79	18.86	18.87	18.76	19.36
	(0.65, 2.48)	(0.65, 2.56)	(0.65, 2.65)	(0.65, 1.88)	(0.65, 3.09)
8. resistance (K Ohm)	3.244	1.907	1.693	1.143	1.111
	(0.04, 58.51)	(0.06, 29.38)	(0.13, 79.00)	(0.16, 29.47)	(0.18, 5.56)
9. resistance (K Ohm)	11.75	5.764	2.912	2.042	1.665
	(0.26, 24.22)	(0.34, 5.53)	(0.31, 33.08)	(0.32, 15.08)	(0.30, 3.34)
10. capacitance (mF)	0.876	1.188	1.187	0.863	1.036
	(0.04, 73.75)	(0.05, 15.17)	(0.08, 35.03)	(0.07, 17.76)	(0.09, 18.21)

(b) TiO_2-P25 particulate film electrodes

The light source was replaced to decrease fluctuation. The impedance of TiO_2-P25 electrodes shows more noise signal in the low frequency range (below 10 Hz) representing the photoinduced processes [Figure 73 (a)]. The investigation of TiO_2-P25 impedance was studied by changing the setting parameters of IM6 software. The EIS measurement has several setting parameters, such as the DC potential, the AC amplitude, the AC frequency, the count of integration (Zahner manual). The overlay Bode plots of different setting parameters are shown in Figure 73 (b) and the setting parameters are listed in Table 22.

The photocurrents of all conditions are not significantly different (about 30 μA) and the low frequency range is the dominant investigation. The EIS of all conditions were measured at 0.6 V vs. Ag/AgCl. The condition A is the normal setting parameters for all impedance measurements for all EIS measurement. It was operated with 5 mV (AC potential amplitude), 1KHz (AC frequency) and 3, 7 (step per decade) and the frequency range was 20mHz-100KHz. The Bode plot of TiO_2-P25 with condition A markedly shows the noise signal in the low frequency range. This result lost the important data. The AC potential amplitude was considered to depress a noise signal. An AC potential amplitude of condition B was set at 10 mV, but it still showed the noise signal, see Figure 73 (b). This means the AC potential amplitude is not the main setting parameter for decreasing the noise signal. The AC frequency was modified to study the influent setting parameters. The condition C, D and E were the modified AC frequency, 100 Hz, 1K with 100mHz-100KHz frequency range, 5 KHz, respectively. The Bode plots of TiO_2-P25 with these conditions show similar to the modified AC potential amplitude results. These indicate that both AC potential and AC frequency have no effect on the EIS measurement of TiO_2-P25 particulate film electrode.

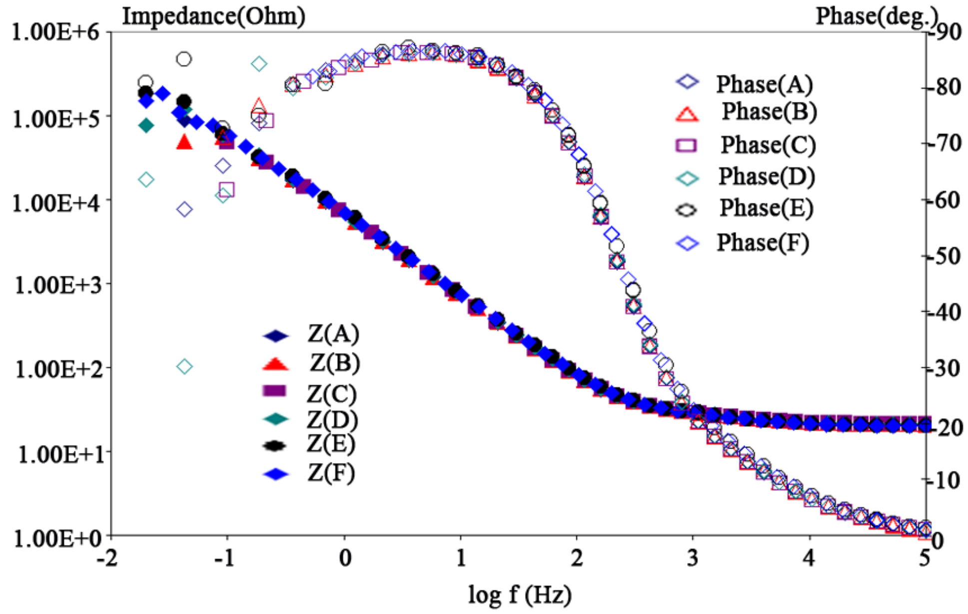

(b)

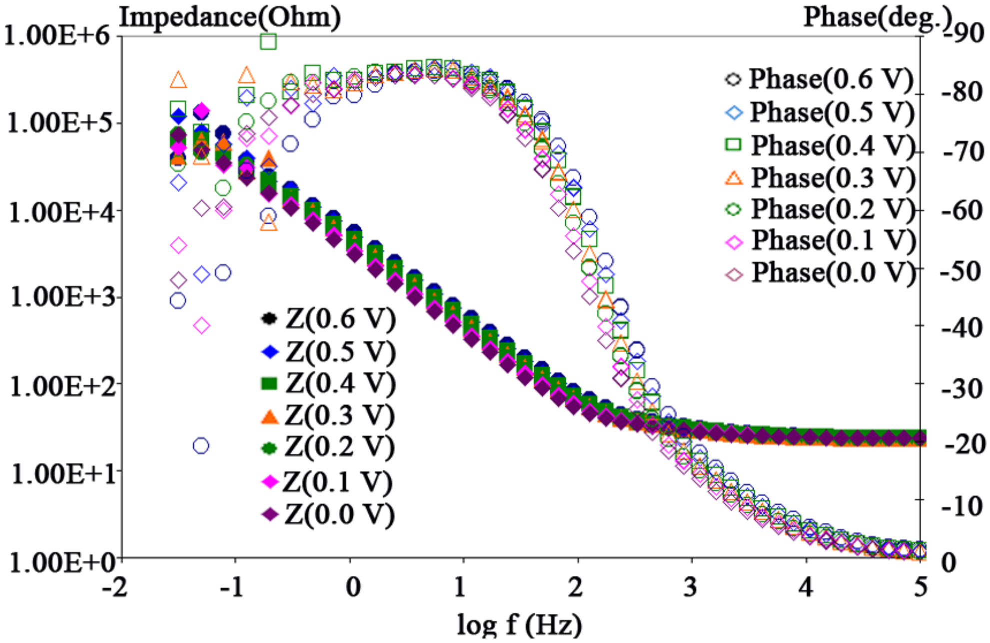

(a)

Figure 73 (a) The Bode plots of the TiO_2-P25 at various potential under irradiation and (b) The Bode plots of the different setting parameters EIS measurement of a TiO_2-P25 electrode at 0.6 V vs. Ag/AgCl; filled symbol represents impedance and unfilled symbol represents phase angle.

Table 22 The setting parameters of EIS measurements.

Condition	Photocurrent(μA)	AC potential amplitude(mV)	AC frequency (Hz)	Step per decade (<66 Hz, >66 Hz)
A	29.34	5	1K	3,7
B	27.98	10	1K	3,7
C	26.65	5	100	3,7
D	27.77	5	100m	3,7
E	30.65	5	5K	3,7
F	31.26	5	1K	5,7

The latest investigated setting parameter is the step per decade. The step per decade determines the frequency resolution of the measured impedance spectrum (Zahner manual). This resolution allows equidistant steps in the logarithmic frequency range. The measuring mode will be changed from AC coupled mode (>66 Hz) to the DC compensated mode (<66 Hz). The measuring time will become dominant below 66 Hz thus the splitting into two regions offers the possibility of optimize the two factor resolutions over measuring time and accuracy over measuring time. The two steps per decade parameters were set i.e. condition A, F, see Table 22. The Bode plots of them show the deceasing of the noise signal in the low frequency range. The best is the condition F showing a Bode plot without noise signal in the low frequency range. These indicate that the step per decade is the influent setting parameter for the impedance of TiO_2-P25 electrodes investigation. These can be explained by the higher step per decade (<66 Hz) increasing the time to reach a steady state of system.

CONCLUSION

The undoped TiO_2 and Ce doped TiO_2 powder were prepared by the sol-gel method with high water content (a high ratio of water to alkoxide precursor of 200:1) showing mixture phases of anatase and rutile, which were confirmed by XRD and EXAFS. The calculated percentages of anatase and rutile using the EXAFS technique corresponded to that of the XRD results.

Ce ions in the TiO_2 structure prevented the transformation of anatase to rutile, which was investigated by the XRD and EXAFS results indicating only the anatase phase. The EXAFS was used to observe the position of Ce ions in the TiO_2 structure. The substitution site and the interstitial site of Ce ions in TiO_2 structure were considered. The comparison of the simulation and experimental data concluded that Ce ions in TiO_2 are possibly in the interstitial position between the TiO_6 units in anatase.

Nanoporous TiO_2 and 2%Ce TiO_2 electrodes were prepared by the sol-gel dipping method, whereas TiO_2-P25 electrode was prepared by the suspension dropping method. Electrode cleaning methods, i.e. the conventional, chemical and oxygen plasma cleaning have been proved to have effects on the quality of film on electrodes as studied by SEM. The chemical cleaning was used for all preparations of TiO_2 film according to economic reasons. The undoped TiO_2 electrodes (TiO_2-SG and TiO_2-P25) showed mixture phases of anatase and rutile, whereas 2%Ce TiO_2-SG electrode showed only anatase. These confirmed that the incorporating Ce ions prevented the transformation of anatase to rutile. The TiO_2-P25 electrode showed agglomerated fine particles while the undoped and doped TiO_2-SG electrodes were relatively compact films according to the SEM results.

The cyclic voltammetries (CV) of the prepared nanoporous undoped TiO_2-SG and 2%Ce TiO_2-SG electrodes were studied in comparison with TiO_2-P25 electrodes both in the dark and under irradiation. The faradaic currents under the cathodic and the anodic polarization in the dark, linearly increasing with the number of layers, were ascribed to the redox of hydrated Ti(IV)/Ti(III) sites. The 2%Ce TiO_2 electrode showed a high anodic current density in the dark compared with that resulted from the TiO_2-SG electrode because of the additional content of Ti(III) on the Ce-doped TiO_2 surface which resulted from the reduction of Ti(IV) by Ce(III) on the surface. The photocurrent was studied in the potential range that faradaic current does not appear, so that the observed current was produced from the photoinduced process. The photocurrent maxima were observed at 20 layers of TiO_2-SG, 15 layers of 2%Ce TiO_2-SG and 5 layers of TiO_2-P25. Each number of layers did not result from the thickest films. It meant that free diffusion lengths of electrons play a role of charge transfer in the film electrode. The 2%Ce TiO_2-SG electrode produced the lowest photocurrent compared with that resulted from the undoped TiO_2-SG. It was concluded that on the 2%Ce TiO_2-SG film electrode, the Ti(III) content, which was increased according to the redox reaction of Ce(III)/Ti(IV) on the electrode film, produced electrons for the anodic current in addition to the electrons from the conduction band of TiO_2. However, in the environment of Ce(IV), the increased electrons could be recombined with cerium ions and limited the photocurrent density of the 2%Ce TiO_2-SG electrode.

The EIS results of the prepared nanoporous undoped TiO_2-SG and 2%Ce TiO_2-SG electrodes were simulated using a porous electrode model which is based on the transmission line model. The impedance corresponded to the porous TiO_2 layer/ pore electrolyte interface (Zq) representing the photoinduced processes impedance showed different values between the dark and irradiation experiments. It could have resulted from a space charge capacitance under the dark experiment. For the irradiation experiment, a resistive charge transfer element, an accumulate charge element and a resistive recombination element were added to Zq. The impedance of a porous TiO_2/ITO layer interface (Zn i.e. an independently photoinduced process impedance) was an RC representing the conductive ITO bulk layer in serial connection with an RC representing the ITO/electrolyte interface at the end of pore which responded to the surface oxidation of the ITO layer by thermal treatment.

From the simulation, it was concluded that in the photoinduced processes, especially the charge transfer and the recombination reactions were taken into account for the irradiated EIS experiments. Under irradiation, the overall impedance of the TiO_2-SG electrode showed smaller values to that of the 2%Ce TiO_2-SG electrode. The effective conductivity of material depended on the resistance of its grain boundaries. The lower impedances of TiO_2-SG from the EIS results meant the higher conductivity electrode, which could be explained in terms of fewer grain boundaries of the mixture phases of anatase and rutile. The charge transfer reaction was faster and the recombination reaction was slower. The higher impedances of 2%Ce TiO_2-SG film electrode corresponded to the lower conductivity. The major anatase phase of the 2%Ce TiO_2-SG film played a role in conductivity. The higher surface area of the anatase than the rutile causes the higher grain boundary, which increased the resistance between anatase TiO_2 particles. The high content of 2%cerium ions in TiO_2-SG film would also act as recombination centers.

The electrochemical set up, i.e. the light source and the electrochemical cell, was modified to investigate the proposed equivalent circuits. The potential dependence, the influence of photon flux and the effect of electrolyte solution were tested. The EIS results from the potential dependence showed the lower resistive charge transfers and higher resistive recombination elements with increasing the anodic potentials, which indicated the higher charge separation regions corresponding to the higher anodic polarizations. The influence of photon flux to the EIS results revealed that the charge transfer resistance decreased with the increasing photon flux implying a higher penetration depth of light. The recombination resistance also decreased with the increasing photon flux, which meant that more electron-hole recombination processes occurred. The depression of recombination was investigated using methanol as a hole scavenger. The photocurrent increased almost twice as that without the methanol addition, which resulted from the smaller charge transfer resistance. The increasing in photocurrent by a reducible species such as methanol was due to the penetration into the substrate, trapping the photogenerated holes and decreasing the recombination process.

LITERATURE CITED

Agarwal, P., M.E. Orazem and L.H. Garcia-Rubio. 1992. Measurement Models for Electrochemical Impedance Spectroscopy, I. Demonstration of Applicability. **The electrochemical Society, Inc.** 139(7): 1917-1927.

Alves, V.A., L.A. Da Silva, J.F.C. Boodts and S. Trasatti. 1994. Kinetic and Mechanism of Oxygen Evolution on IrO_2-Based Electrodes Contaning Ti and Ce Acidic Solutions. **Electrochem. Acta.** 39: 1585-1589.

Anonymous. **Application Note AC-1.** Princeton Applied Research. Available Source: http://www.princetonappliedresearch.com/products/appnotes.cfm.

______,. **Fundamental of Electrochemical impedance spectroscopy**. Available Source: http://www.gamry.com/App_Notes/EIS_Primer/EIS_Primer.htm.

Anthony R. W. 1999. **Basic Solid State Chemistry.** 2nd. John wiley & sons LTD. London.

Baiju, K.V., S. Shukla, K.S. Sandhya, J. James and K.G.K. Warrier. 2007. Photocatalytic Activity of Sol-Gel Derived Nanocrystalline Titania. **J.Phys.Chem.C.** 111: 7612-7622.

Bard, A.J. and L.R. Faulkner. 2001. Double-Layer Structure and Absorption, pp. 534-545. *In* **Electrochemical methods; Fundamentals and Applications**. John Wiley and Sons, Inc. New York.

Bare, S.R. XANES Measurements and Interpretation (script for EXAFS Data collection and analysis course, APS, July 26-29, 2005).

Bisquert, J., F. Fabregat-Santiago, I. Mora-Seró, G. Garcia-Belmonte, E.M. Barea and E. Palomares. 2008. A Review of Recent Results on Electrochemical Determination of the Density of Electronic States of Nanostructured Metal-Oxide Semiconductors and Organic Hole Conductors. **Inorg.Chimi.Acta**. 361: 684-698.

______, J., G. Garcia-Belmont, F. Fabregat-Santiago, N.-S. Ferriols, P. Bogdanoff and E.C. Pereira. 2000. Doubling Exponent Models for the Analysis of Porous Film Electrodes by Impedance: Relaxation of TiO_2 Nanoporous in Aqueous Solution. **J. Phys. Chem. B**. 104: 2287-2298.

Brinker, C.J., A.J. Hurd and K.J Ward. 1988. **Fundamentals of Sol-Gel Thin Film Formation, Ultrastructure Processing of Advanced Ceramics.** John Wiley&Sons. Canada.

Bulter, M.A. 1977. Photoelectrolysis and Physical Propoties of the Semiconducting Electrode WO_3. **J.Appl.Phys.** 48: 1914-1920.

Cahen, D., G. Hodes, M. Grätzel, J.F. Guillemoles and I. Riess. 2000. Nature of Photovoltaic Action in Dye-Sensitized Solar Cells. **J. Phys.Chem.B.** 104: 2053-2059.

Carp, O., C.L. Huisaman and A. Reller. 2004. Photoinduced Reactivity of Titanium Dioxide. **Progress Solid. State Chem.** 32: 33-177.

Choi, H.C., Y. M. Jung and S. B. Kim. 2005. Size Effects in the Raman Spectra of TiO_2 Nanoparticles. **Vibrational Spectroscopy.** 37: 33-38.

____, W., A. Termin and M.R. Hoffmann. 1994. The Role of Metal Ion Dopants in Quantum Sized TiO_2: Correlation Between Photoreactivity and Charge Carrier Recombination Dynamics. **J. Phys. Chem.** 98: 13669-13679.

Datye, A.K., G. Riegel, J.R. Bolton, M. Huang and M.R. Prairie. 1995. Microstructural Characterization of a Fumed Titanium Dioxide Photocatalyst. **J.Solid.Stat.Chem.** 115: 236-239.

Diebold, U. 2003. The Surface Science of Titanium Dioxide. **Surface Sci Reports**. 48: 53-229.

Douglas, A.S., F. J. Holler and S. R. Crouch. 2007. **Principles of Instrumental Analysis.** 6th. Tomson Brooks/Cole. USA.

Einaga, H., S. Futamura and T. Ibusuki. 2002. Heterogeneous Photocatalytic Oxidation of Bezene, Toluene, Cyclohexene and Cyclohexane in Humidified Air: Comparison of Decomposition Behavior on Photoirradiated TiO_2 Catalyst. **Appl. Catal. B.** 38: 215-225.

Fabregat-Santiago, F., I. Mora-Seró, G. Garcia-Belmonte and J. Bisquert. 2003. Cyclic Voltammetry Studies of Nanoporous Semiconductors, Capacitive and Reactive Properties of Nanocryatalline TiO_2 Electrodes in Aqueous Electrolyte. **J.Phys.Chem.** 107: 758-768.

Fang, J., X. Bi, D. Si, Z. Jiang and W. Huang. 2007. Spectroscopic Studies of Interfacial Sturctures of CeO_2-TiO_2 Mixed Oxides. **Appl.Surf. Sci.** 253: 8952-8961.

Fonda, E., D. Andreatte, P.E. Colavita and G. Vlaic. 1999. EXAFS Analysis of the L_3 edge of Ce in CeO_2. **J.Synchrotron Rad.** 6: 34-42.

Fujishima, A., T.N. Rao and D.A. Tryk. 2000. Titanium Dioxide Photocatalysis. **J. Photochem. Photobiol. C: Photochem Rev.** 1: 1-21.

Fujishima, A., X. Zhang and D.A. Tryk. 2008. TiO_2 Photocatalysis and Related Surface Phenomena. **Surf.Sci.Report**. 63: 515-582.

Gärther, W.W. 1959. Depletion-Layer Photoeffets in Semiconductors. **Phys.Rev.** 116 (1):84-87.

George, G.N. and I.J. Pickering. 1993. **EXAFSPAK - A Suite of Computer Programs for Analysis of X-ray Absorption Spectra**. Menlo Park. Canada.

Göhr, H. 1997. Impedance Modelling of Porous Elctrodes. **Electrochem. Appl.** 1: 2-3.

Gonzalez, R.D., T. Lopez and R. Gomez. 1997. Sol-Gel Preparation of Supported Metal Catalysts. **Catal. Today.** 35: 293-317.

Hagfeldt, A. and M. Grätzel. 1995. Light-Induced Rredox Reaction in Nanocrystalline Systems. **Chem. Rev.** 95: 49-68.

______,A., H. Lindeström, S. Södergren and S.E. Lindquist. 1995. Photoelectrochemical Studies of Colloidal TiO_2 Films: The Effect of Oxygen Studied by Photocurrent Transients. **J. Electroanal. Chem.** 381: 39-46.

He,C., D. Shu. Y. Xiong, X. Zhu and X. Li. 2006. Comparison of Catalytic Activity of Two Platinised TiO_2 Films Towards the Oxidation of Organic Pollutants. **Chemosphere.** 63: 183-191.

Hirano, K., E. Suzuki, A. Ishikawa, T. Moroi, H. Shiroishi and M. Kaneko. 2000. Sensitization of TiO_2 Particles by Dyes to Achieve H_2 Evolution by Visible Light. **J. Photochem. Photobio. A.** 136: 157-161.

Hsu. J.-P. and A. Nacu. 2003. On the Factors Influencing the Preparation of Nanosized Titania Sols. **Langmuir.** 19: 4448-4454.

Hu, Y., H.-L. Tsai and C.-L. Huang. 2003. Effect of Brookite Phase on the Anatase-Rutile Transition in Titania Nanoparticles. **J.Europ.Ceram.Soc.** 23: 691-696.

Jiang, D., H. Zhao, S. Zhang and R. John. 2003. Characterization of Photoelectrocatalytic Processes at Nanoprorous TiO_2 Film Electrodes: Photocatalytic Oxidation of Glucose. **J.Phys.Chem. B.** 107: 12774-12780.

______ , D., H. Zhao, S. Zhang and R. John. 2006. Comparison of Photocatalysis Degradatioin Kinetic Characteristics of Different Organic Compounds at Anatase TiO2 Nanoporous Film Electrodes. **J. Photochem.Photobio.A**. 177:253-260.

Jongh, P.E. 1999. **Photoelectrochemistry of Nanoporous Semiconductor Electrodes**. Ph.D. thesis, University of Utrecht.

Kanna , K. and S. Wongnawa. 2008. Mixed Amorphous and Nanocrystalline TiO_2 Powders Prepared by Sol-Gel Method:Characterization and Photocatalytic Study. **Mater.Chem. Phys.** 110: 166-175.

Kasanic, M.M. 1998. Photocatalytic Degradation of Oxalic Acid over TiO_2 Powder. **J. Photochem. Photobio. A. Chem.** 119: 119-122.

Kikkawa, H., B. O'Regan and M.A. Anderson. 1991. The Photoelectrochemical Properties of Nb-doped TiO_2 Semiconductor Ceramic Membrane. **J.Electroanal.Chem.** 309: 91-101.

Kim, H., J. Lee, C. Park and Y. Park. 2002. Surface Characterization of O_2-Plasma Treated Indium Tin Oxide (ITO) Anodes for Organic Light Emitting Device Applications. **J. Korea.Phys.Soc.** 41(3): 395-399.

Krause, S. 2003. Impedance methods, pp. 196-229. *In* A.J. Bard, M. Stratmann and P.R. Unwin, eds. **Encyclopedia of Electrochemistry Vol. 3: Instrumentation and Electroanalytical Chemistry.** Wiley VCH.

Lee, J.H. and Y.S. Yang. 2005. Effect of Hydrolysis Conditions on Morphology and Phase Content in the Crystalline TiO_2 Nanoparticles Synthesized from Aqueous $TiCl_4$ Solution by Precipitation. **Mater.Chem.Phys**. 93: 237-242.

Levie, R. de. 1963. On Porous Electrodes in Electrolyte Solutions. **Electrochemica Acta.** 8: 751-780.

Li F.B., X.Z Li, M.F. Hou, K.W. Cheah and W.C.H Choy. 2005. Enhanced Photocatalytic Activity of Ce^{3+}-TiO_2 for 2-mercaptobenzothiazole Degradation in Aqueous Suspension for Odour Control. **Appl. Catal. A: Gen.** 285: 181-189.

Li, G., C. Liu and Y. Liu. 2006. Different Effects of Cerium Ions Doping on Properties of Anatase and Rutile TiO_2. **Appl. Surface Sci**. 253: 2481-2486.

Li, Y., T.J. White and S.H. Lim. 2004. Low-temerature Synthesis and microstructural control of titania nano-particles. **J.Solid State Chem.** 177: 1372-1381.

Li,G. K.A. Gray. 2007. The Solid-Solid Interface:Exlaining the High and Unique Photocatalytic Reactivity of TiO_2-Based Nanocomposited Materials. **Chem.Phys.** 339:173-187.

Lindquist, S.-E., B. Finnström and L. Tegner. 1983. Photoelectrochemical Properties of Polycrystalline TiO_2 Thin Film Electrodes on Quartz Substrates. **J.Electrochem.Soc.** 130: 351-358.

Linsebigler, A.L., G. Lu and J.T. Yates. 1995. Photocatalysis on TiO_2 Surface: Principle, Mechanism and Selected Results. **Chem.Rev**. 95: 735-758.

Litter, M.I. 1999. Heterogeneous Photocatalysis Transition Metal Ions in Photocatalytic Systems. **Appl. Catal. B.** 23: 89-114.

Macdonald, D.D, E. Sikora and G. Engelhardt. 1997. **Electrochimica Acta.** 43 (1-2): 87-107.

Marci, G., M. Addamo, V. Auguglliaro, S. Coluccia, E. Garcia-López, V. Loddo, G. Martra, L. Palmisano and M. Schiavello. 2003. Photocatalytic Oxidation of Toluene on Irradiated TiO_2: Comparison of Degradation Performance in Humidified Air, in Water and in Water Containing a Zwitterionic Surfactant. **J.Photochem. Photobio. A Chem.** 160: 105-114.

Miller. J.B. and E.I. Ko. 1997. Control of Mixed Oxide Textural and Acidic Properties by the Sol-Gel Method. **Catal. Today.** 35: 269-292.

Mills. A. and S.L. Hunte. 1997. An Overview of Semiconductor Photocatalysis. **J. Photochem. Photobilo. A.** 108: 1-35.

Moon, J., C.Y. Yun, K.-W. Chung, M.-S. Kang and J. Yi. 2003. Photocatalytic Activation of TiO_2 under Visible Light using Acid Red 44. **Catal. Today.** 87: 77-86.

Murakara, T., K. Takekoshi and S. Sato. 1999. Electrochemical Properties of TiO_2 Coated ITO Electrodes Prepared by Sol-gel Method. **J.Chem.Eng.Japan**. 32: 825-829.

Nagaveni, K., M.S. Hegde and G. Madras. 2004. Stucture and Photocatalytic Activity of $Ti_{1-x}M_xO_{2\pm d}$ (M = W, V, Ce, Zr. Fe and Cu) Synthesized by Solution Combustion Method. **J. Phys. Chem. B.** 108: 20204-20212.

Nerendar Y. and G.L. Messing. 1997. Mechanisms of Phase Separation in Gel-based Synthesis of Multicomponent Metal Oxides. **Catal. Today.** 35: 247-268.

Ngamsinlapasathian, S., T. Sreethawong, Y. Suzuki and S. Yoshikawa. 2005. Single- and Double-Layered Mesoporous TiO_2/P25 TiO_2 Electrode for Dye-Sensitized Solar Cell. **Solar. Energ. Mater. Solar. Cells.** 86: 269-282.

Niemantsverdriet, J.W. 2000. **Spectroscopy in Catalysis.** 2nd. Wiley-VCH. Germany.

Niltharach, A., S. Kityakarn, R. Rattanakam, Y. Pooarporn, P. Songsiririttigul, S. Limpijumnong, A. Worayingyong. n.d. The Hydrolysis effect of the Sol-gel Preparation on Electronic Structure of TiO_2 and Ce/TiO_2 Photocatalysts. (manuscript in preparation).

Ohno, T., F. Tanigawa, K. Fujihara, S. Izumi and M. Matsumura. 1999. Photocatalytic Oxidation of Water by Visible Light Using Ruthenium-Doped Titanium Dioxide Powder. **J. Photochem. Photobio. A.** 127: 107-110.

Ohring, M. 1992. **The Materials Science of Thin Films.** Acasemic Press. London.

Oskam, A., R.L. Nellore. Penn and P.C. Searson. 2003. The Growth Kinetics of TiO_2 Nanoparticles From Titanium (IV) Alkoxide at High Water/Titanium Ratio. **J. Phys.Chem.B.** 107: 1734-1738.

Poo-arporn, Y. 2008. **Advance Oxidation Process (AOP) for the Degradation of Gaseous Sulfur Containing Compounds (Pollutants) using TiO_2 and Ce/TiO_2 Photocatalysts**. Ph.D. Thesis. Kasetsart University. Bangkok. Thailand.

Pulker, H.K. 1984. **Coating on Glass.** Elsevier Science Publisher.

Rajeshwar, K. 2002. Fundamentals of semiconductor electrochemistry and photoelectrochemistry, pp. 1-51. *In* A.J. Bard, M. Stratmann and S. Licht, eds. **Encyclopedia of Electrochemistry Vol. 6: Semiconductor Electrodes and Photoelectrochemistry.** Wiley VCH. Germany.

Ravichandran, C., M. Noel and P.N. Anantharaman. 1996. The pH-Dependence of Thermally-Coated Ti/TiO_2 Electrodes in the Absence and Presence of Nitrobenzene. **J. Appl. Electrochem.** 26: 195-201.

Rehr, J.J. and R.C. Albers. 2000. Theoretical Approaches to X-ray Absorption Fine Structure. **Rev.Mod.Phys.** 72: 621-654.

Ruiz-López, M.F. and A. Munoz-Páez. 1991. A Theoretical Study of the XANES Spectra of Rutile and Anatase. **J.Phys.Condens.Matter.** 3: 8981-8990.

Sakka, S. n.d. Sol-gel formation of bulk glasses, pp. 129-148. *In* S. Sakka, eds. **Handbook of Sol-Gel Science and Technology Vol.1: Sol-Gel Processing.** Kluwer Academic publishers. London.

Sayers. D.E. and E.A. Stern. 1971. New Technique for Inverstigating Noncrystalline Structures: Fourier Analysis of the Extended X-ray Absorption Fine Structure. **Phys.Rev.Lett.** 27: 1204-1207.

Schmidt, H. and M.Mennig. **Wet Coating Technologies for Glass**. Available Source: http://www.solgel.com.

Smith, M.F., W. Klysubun, S. Kityakarn, A. Worayingyong, S.B. Zhang, S.-H Wei, D. Onkaw, P. Songsiritthigul, S. Rujirawat and S. Limpijumnon. 2009. Determination of Phase Ratio in Polymorphic Meterials by X-ray Absorption Spectroscopy: The case of Anatase and Rutile Phase Mixture in TiO_2. **J.Appl.Phys.** 105 (024308): 1-4.

Sokmen, M., D.W. Allen, A.T. Hewson and M.R. Cleanch. 2001. Photocatalytic Oxidative Degradation of 2-methylthiophene in Suspensions of TiO_2: Identification of Intermediates and Degradation Pathways. **J. Photochem. Photobio. A. Chem.** 141: 63-67.

Solarsha, R., I. Rutkowska, R. Morand and J. Augustynski. 2006. Photoanodic Reaction Occurring at Nanostructured Titanium Dioxide Films. **Electrochemica Acta.** 51: 2230-2236.

Soloviev, R., C., T. Sanchez and A.V. Kanaev. 2001. Nucleation Stage in the Ti(OPr) Sol-Gel Process. **J.Phys.Chem.B.** 105: 4175-4180.

Spurr, R.A. and H. Mywers. 1975. Quantitative Analysis of Anatase-Rutile Mixtures with an X-ray Diffractometer. **Anal.Chem.** 29: 760-762.

Su, B., Y. Hong and C.-M. Tseng. 2004. Sol-Gel Preparation and Photocatalysis of Titanium Dioxide. **Catal Today.** 96: 119-126.

Sun, B. and G. S. Panagiotis. 2003. Interaction of Anatase and Rutile TiO_2 Particles in Aqueous Photooxidation. **Catal. Today.** 88: 49-59.

_____, V.V Alexandre and G.S. Panagiotis. 2003. Role of Platinum Deposited on TiO_2 in Phenol Photocatalytic Oxidation. **Langmuir.** 19: 3151-3156.

_____, D. 2005. **Effect of Water on the Electrochromic Properties of CeO_2-TiO_2, WO_3 and Nb_2O_5:Mo Sol-Gel Layers and Devices Prepared with Them.** Ph.D. Thesis. Universität des Saarlandes. Saarbrücken.

Tenderholt, A. B. Hedman and K.O. Hodgson. 2006. PySline: A Modern, Cross-platform Program for the Processing of Raw Averaged XAS Edge and EXAFS Data. SLAC-PUB-12219. **International Conference on X-ray Absorption Fine Structure (XAFS13) 13th.** SLAC-PUB. Stanford.

Thevenet, F., O. Guaitella, J.M. Herrmann, A. Rousseau and C. Guillard. 2005. Photocatalytic Degradation of Acetylene over Various Titanium Dioxide-Based Photocatalysts. **Appl. Catal. B.** 61: 58-68.

Tomkiewicz, M. 1990. Impedance Spectroscopy of Rectifying Semiconductor-Electrolyte Interface. **Electro.Chemica.Acta.** 35(10): 1631-1635.

Van de Krol, R., A. Goossens and J. Schoonman. 1997. Mott-Schottky Analysis of Nanometer-Scale Thin Film Anatase TiO_2. **J. Electrochem. Soc.** 144 (5): 1723-1727.

Vanmaekelbergh, D. and F. Cardon. 1986. Calculation of the Electrical Impedance Associated with the Surface Recombination of Free Carriers at an Illuminated Semiconductor/Electrolyte Interface. **J.Phys.D Apply.Phys.** 19: 643-656.

Vinodgopal, K., S. Hotchadani and P.V. Kamat. 1993. Electrochemically Assisted Photocatalysis.TiO_2 Particulate Film Electrodes for Photocatalytic Degradation of 4-Chlorophenol. **J.Phys.Chem.** 97: 9040-9044.

Vlachopoulos, N., J. Nissfolk, M. Möller, A. Briançon, D. Corr, C. Greave, N. Leyland, R. Mesmer, F. Pichot, M. Ryan, G. Boschloo and A. Hagfeldt. 2008. Electrochemical Aspects of Display Techmilogy Based on Nanostructured Titanium Dioxide with Attached Viologen Chromophores. **Electrochemica Acta.** 53: 4065-4071.

Wang, C.Y., H. Groenzin and M.J. Sultz. 2004. Direct Observation of Competitive Adsorption Between Methanol and Water on TiO_2: An in situ Sum-Frequency Generation Study. **J.Am.Chem.Soc.** 126: 8094-8095.

_____, J. 2000. **Analytical Electrochemistry.** 2nd. Wiley-VCH.

Watanabe, T., A. Fujishima and K. Honda. 1976. Photoelectrochemical Reactions at $SrTiO_2$ Single Crystal Electrode. **Bull. Chem. Soc. Jpn**. 49: 355-358.

Worayingyong, A., A. Nittharach and Y. Poo-arporn. 2004. A Comparative Study of Toluene Catalytic Oxidation over Cerium/TiO_2 (Anatase) and Vanadium/TiO_2 (Anatase) Catalysts. **Science Asia.** 30: 341-349.

Wrighton, M.S. 1979. Photoelectrochemical Conversion of Optical Energy to Electricity and Fuels. **Acc. Chem. Res.** 12: 303-310.

Wyckoff, R.W.G. 1948. **Crystal Structures**. Interscience. NewYork.

Xiao, J., T. Peng, R. Li, Z. Peng and C. Yan. 2006. Preparation, Phase Transformation and Photocatalytic Activites of Cerium-Doped Mesoporous Titania Nanoparticels. **J. Solid. State. Chem.** 179: 1161-1170.

Xie, Y. and C. Yuan. 2003. Visible Light Responsive Cerium Ion Modified Titania Sol and Nanocrystallites for X.3B Dye Photodegradetion. **Appl. Catal. B.** 46: 251-259.

Yamashita, H., M. Harada, J. Misaka, M. Takaeuchi, K. Ikeue and M. Anpo. 2002. Degradation of Propanol Diluted in Water under Visible Light Irradiation using Metal Ion-Implanted Titanium Dioxide Photocatalysts. **J. Photochem. Photobio. A.** 148: 257-261.

Yanqing, Z., S. Erwei, C. Zhizhan, L. Wenjun and H. Xingfang. 2001. Influence of Solution Concentration on the Hydrothermal Preparation of Titania Crystallites. **J. Mater.Chem.** 11: 1547-1551.

Yu, H.-F. and S.-M. Wang. 2000. Effects of Water Content and pH on Gel-Derived TiO_2-SiO_2. **J. Non-Crystal. Solids.** 261: 260-267.

_____, J., X. Zhao and Q. Zhao. 2001. Photocatalytic Activity of Nanometer TiO_2 Thin Films Prepared by the Sol-Gel Method. **Mater.Chem.Phys**. 69: 25-29.

_____, J.C., J. Yu, L. Zhang and W. Ho. 2002. Enhancing Effect of Water Content and Ultrasonic Irradiation on the Photocatalytic Activity of Nanosized TiO_2 Powder. **J. Photochem. Photobio. A.** 148: 263-271.

Zahner IM6 manual. Zahner –elektrik GmbH& Co. KG. Kronach. Germany.

Zhang, J., C. Yang, G. Chang, H. Zhu and M. Oyama. 2004. Voltammetric Behavior of TiO_2 Films on Graphite Electrodes Prepared by Liquid Phase Deposition. **Mater.Chem.Phys.** 88: 398-403.

APPENDICES

APPENDIX A

A1. Helmholtz layer

Helmholzlayer is an electrical double layer at the interface. It is two sheets of charge (opposite polarity), separated by a distance of molecular order, charge separation at the interface. Such a structure is equivalent to a parallel plate capacitor, which has relation between charge density, σ, and voltage drop,V, ($\sigma = \frac{\varepsilon\varepsilon_0}{d}V$). ε is dielectric constant of the medium and ε_0 is the permittivity of free space (Bard and Faulkner, 2001)

A2. Modification of prepave.keystroke file for EXAFS.

- A prepave.keystroke file was open by a text editor.
- The line with asterisks (e.g. ***absorpbing_element***) was changed to the appropriate information for data analysis (e.g. ***Ti***).
- The edited file was overwritten, i.e. prepave.keystroke.
- The command prompt was used to run PROCESS, i.e. C:..\...\>process/rec=prepave.keystroke.
- The .ave file should be ready and then PROCESS can be run avefile.ave.

A3. Simulation of anatase EXAFS spectrum

All processes could be referred to the FEFF7 manual but the researcher could do the following:

- The feff.inp was an input file that described the position of all atoms in the structure.
- The file feff.inp could be generated using ATOMS.

- ATOMS was saved to the folder which was the same as the data file.

<u>ATOMS file:</u>

```
title anatase TiO2
space i 41/a m d
rmax=6.0   a=3.7842   c=9.5146  core=Ti
atom
Ti    0.0   0.25  -0.125      Ti
O     0.0   0.25  0.083        O
```

- The data of the ATOMS file was changed (e.g. title, space group, rmax, lattice parameter and atom) and then a feff.inp file was generated (i.e. c:..\.....\>atoms)
- The feff.inp was opened and it showed:

```
         * This feff.inp file generated by ATOMS, version 2.42

         *  Space  group  i  41/a  m  d  is  commonly  referenced  with  alternative
origins.
         *  If  you  are  displeased  with  the  resulting  atom  list,  shift  all
atomic
         * coordinates in atom.inp by (0,.25,-.125) and run atoms again.

         * -- * -- * -- * -- * -- * -- * -- * -- * -- * -- * -- * -- * -- * --
         * total mu =     1695.0 cm^-1, delta mu =     1412.4 cm^-1
         * specific gravity =  3.895, cluster contains   79 atoms.
         * -- * -- * -- * -- * -- * -- * -- * -- * -- * -- * -- * -- * -- * --
         * mcmaster corrections:  0.00093 ang^2 and  0.165E-05 ang^4
         * -- * -- * -- * -- * -- * -- * -- * -- * -- * -- * -- * -- * -- * --

         TITLE   anatase TiO2

         HOLE 1   1.0     1=k edge, s0^2=1.0

         *         mphase,mpath,mfeff,mchi
         CONTROL   1      1     1     1
         PRINT     0      0     0     3

         RMAX     4.7059

         *CRITERIA     curved   plane
         *DEBYE        temp     debye-temp
         *NLEG         8
         *RMULTIPLIER  1.0

         POTENTIALS
         *   ipot   z  label
               0   22   Ti
               1    8   O
               2   22   Ti

         ATOMS
             0.0000     0.0000     0.0000  0   Ti               0.0000
```

```
     0.0000    -1.8921     0.3996  1   O               1.9338
     1.8921     0.0000    -0.3996  1   O               1.9338
    -1.8921     0.0000    -0.3996  1   O               1.9338
     0.0000     1.8921     0.3996  1   O               1.9338
     0.0000     0.0000    -1.9790  1   O               1.9790
     0.0000     0.0000     1.9790  1   O               1.9790
     0.0000    -1.8921     2.3787  2   Ti              3.0394
     1.8921     0.0000    -2.3786  2   Ti              3.0394
    -1.8921     0.0000    -2.3786  2   Ti              3.0394
     0.0000     1.8921     2.3787  2   Ti              3.0394
    -3.7842     0.0000     0.0000  2   Ti              3.7842
     0.0000    -3.7842     0.0000  2   Ti              3.7842
     0.0000     3.7842     0.0000  2   Ti              3.7842
     3.7842     0.0000     0.0000  2   Ti              3.7842
....
etc.
```

- The fourth number of PRINT line was changed to 3 or 4.
- The Debye line was changed to the temperature of measurement and the Debye temperature of solid (i.e. 530 K)
- The CRITERIA line, the number of paths were calculated, were changed to 14 (11) for anatase (rutile) and then saved to feff.inp
- Using command prompt, typed “feff7” and then typed “feff_hld7” (Note, the warning often shows that is something like: “R differs in path.dat and chi.dat” but there are no problems because the difference in R is very small.)
- The PATH.hld was ready. This file contains information about a theoretical EXAFS and can be ready by OPT. (Note, this file should be saved because it will be changed after using run OPT.) It is shown as following:

```
Za = Ti Edge=K F= x.xxxE+x  CPU= x xx:xx:xx.xx Time
1 Scale = 0.9 2 Data E0=0   3 Wave-1 Sig D=0 4 0 5 0
Component      ZBA=     ZBP=      NAT=   NPT=
 6 N=     7 R=        8 Sig^2=          9 E0=       10 E1=
```

PATHS.hld file:

```
   22.0    28     1    11111
    0.90000E+00 0.00000E+00 0.00000E+00 0.00000E+00 0.00000E+00
   010     1.00  1.00  5   5    01101
    0.39960E+01 0.19338E+01 0.79500E-02-0.10000E+02 0.00000E+00
   010     2.00  2.00  5   5    22221
    0.19980E+01 0.19790E+01 0.81200E-02-0.10000E+02 0.00000E+00
   020     3.00  3.00  5   5    22221
    0.39960E+01 0.30394E+01 0.50400E-02-0.10000E+02 0.00000E+00
   0210    4.00  4.00  5   5    22221
    0.79920E+01 0.34761E+01 0.66700E-02-0.10000E+02 0.00000E+00
   0210    5.00  5.00  5   5    22221
    0.79920E+01 0.34761E+01 0.66700E-02-0.10000E+02 0.00000E+00
```

```
   020     6.00  6.00  5   5    22221
    0.39960E+01 0.37842E+01 0.51900E-02-0.10000E+02 0.00000E+00
   0110    7.00  7.00  5   5    22221
    0.39960E+01 0.38259E+01 0.15390E-01-0.10000E+02 0.00000E+00
   0210    8.00  8.00  5   5    22221
    0.79920E+01 0.38259E+01 0.53700E-02-0.10000E+02 0.00000E+00
   010     9.00  9.00  5   5    22221
    0.79920E+01 0.38573E+01 0.10690E-01-0.10000E+02 0.00000E+00
   01010  10.00 10.00  5   5    22221
    0.39960E+01 0.38677E+01 0.15580E-01-0.10000E+02 0.00000E+00
   01010  11.00 11.00  5   5    22221
    0.39960E+01 0.38677E+01 0.31820E-01-0.10000E+02 0.00000E+00
   01210  12.00 12.00  5   5    22221
    0.39960E+01 0.38677E+01 0.61100E-02-0.10000E+02 0.00000E+00
   01010  14.00 14.00  5   5    22221
    0.19980E+01 0.39580E+01 0.31815E-02-0.10000E+02 0.00000E+00
…..
etc.
```

where

1. Scale	Overall scale factor $\mathbf{S_0^2}$-this should be about 0.9 for McKale and feff.
2. Data E0	Data E0 (k=0 point)shift in eV
3. Wave-1-Sig-D	Anharmonic Debye-Waller for component#1
4.	Not used
5.	Not used
6. N	Coordination Number
7. R	Absorpber-backscatterer distance in Å
8. Sig^2	Debye-Waller σ^2 value in Å^2
9. E0	Threshold E0 (k=0 point) shift in eV for the component.
10. E1	Not used

ZBA	Atomic number for backscatterer amplitude function
ZBP	Atomic number for backscatterer phase
NAT	Amplitude function type (1-6)
NPT	Phase shift function type (1-6) 1 = McKale curved wave theory 2 = parameterized 3 = generated by PROCESS with complex Fourier backtransforms of experimental data

4 = feff5 single scattering curved wave theory
5 = feff5 multiple scattering curved wave theory
6 = feff5 tables (for elements for hydrogen to americium)

- In command prompt, OPT was used to fitt data (c:..\.....\>opt. ***.ave PATHS.HLD) e.g."opt TiO2.ave PATHS.HLD"

Fitting processes for TiO_2 EXAFS

The EXFASPAK software not only was used to extract the EXAFS data from the raw data but also was applied to extract the structural information by using OPT (curve fitting, part of EXAFSPAK software). OPT can read only .ave and .fil file. The fitting processes following performance of a command prompt:

1 To type c:\\...\..\ OPT TiO2.ave PATHS.HLD ↵

TiO2.ave contains the data to be fitted and PATHS.HLD contains the theoretical structure information to be derived in the fit.

2 The main menu of OPT will appear as follows:

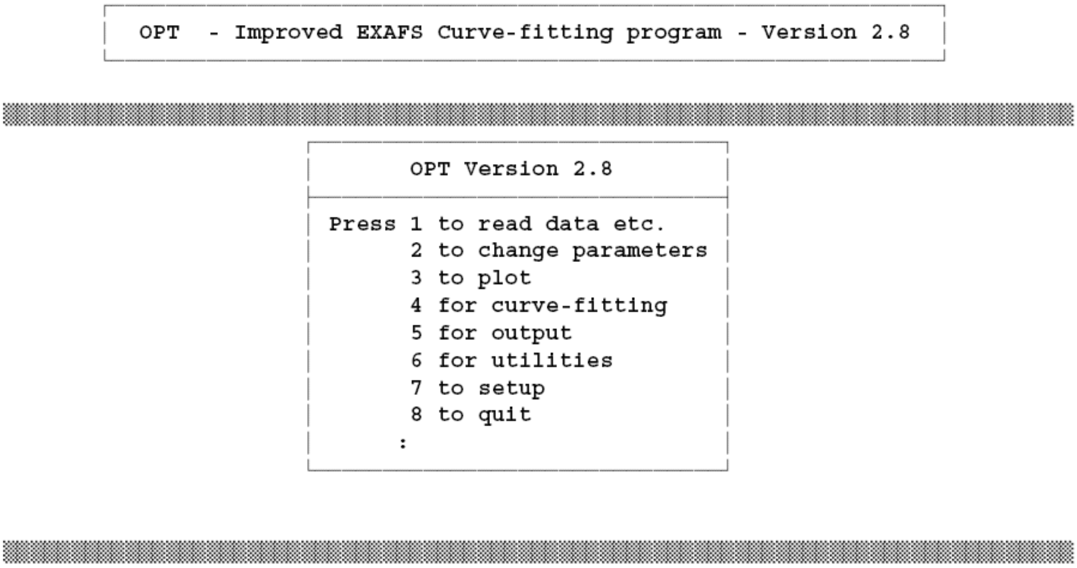

```
| OPT  - Improved EXAFS Curve-fitting program - Version 2.8 |

        OPT Version 2.8

Press 1 to read data etc.
      2 to change parameters
      3 to plot
      4 for curve-fitting
      5 for output
      6 for utilities
      7 to setup
      8 to quit
     :
```

3 Option 1 is selected to read a data and the dialog will appear as follows:

```
TiO2 xxx (Default value)Points in file, E0 = 4976.635
Enter k(min), k(max), Delta-k [1.00000, 14.00000, 0.0]: 1,11.6
Cannot read parameter file
Enter # component, power for k Weighthing [3, 3]:3
Enter edge (K, L1,…) [K]:
Enter 1 for smoothed data, 2 for raw data [2]:
Xxx points in data file, xxx points w/in range
```

The program then returns to main menu and option 2 should to be selected. The parameter edit screen will appear:

```
TiO2  k= 1 to 11.6 3 shells 4 Variables 0 Itern 0 F-evals
Za = Ti Edge=K F= x.xxxE+x  CPU= x xx:xx:xx.xx Time
1 Scale = 0.9 2 Data E0=0   3 Wave-1 Sig D=0 4 0 5 0
Component 010     ZBA=1.00  ZBP=8.00  NAT=5   NPT=5    10001
 N=4     R=1.9598 Sig^2=0.0862   E0=0
Component 010     ZBA=2.00  ZBP=2.00  NAT=5   NPT=5    12221
 N=2     R=2.034 Sig^2=0.1085   E0=0
Component 020     ZBA=3.00  ZBP=3.00  NAT=5   NPT=5    12221
 N=4     R=3.001 Sig^2=0.1091   E0=0
Component 0110     ZBA=4.00  ZBP=4.00  NAT=5   NPT=5    12221
 N=8     R=3.181 Sig^2=0.2120   E0=0
Component 0210     ZBA=7.00  ZBP=7.00  NAT=5   NPT=5    12221
 N=8     R=3.468 Sig^2=0.2314   E0=0
Component 0210     ZBA=8.00  ZBP=8.00  NAT=5   NPT=5    12221
 N=8     R=3.468 Sig^2=0.2314   E0=0
Component 020     ZBA=9.00  ZBP=9.00  NAT=5   NPT=5    12221
 N=4     R=3.776 Sig^2=0.6336   E0=0
Component 0110     ZBA=10.00  ZBP=10.00  NAT=5   NPT=5   12221
 N=4     R=3.8177 Sig^2=0.5591   E0=0
Component 0210     ZBA=11.00  ZBP=11.00  NAT=5   NPT=5   12221
 N=8     R=3.8177 Sig^2=0.1193   E0=0
...
```

```
...
...

PF1 = Exit, PF2 = Next page, PF3 = Fix/Float/Link, PF4 = More…
```

The R, N and Component should be fix in order to keep the correctly structure of TiO_2 (anatase and/or rutile).

Example PATHS.HLD of mixture phase of anatase and rutile.

The PATHS.HLD file for anatase and rutile ratio calculation was modified from PATHS.HLD of anatase and rutile ratio (50/50). It is shown as following:

PATHS.hld file:

```
22.0    28     1    11111
 0.90000E+00 0.00000E+00 0.00000E+00 0.00000E+00 0.00000E+00
010     1.00  1.00  5   5    01101
 0.20000E+01 0.19338E+01 0.79500E-02-0.10000E+02 0.00000E+00
010     2.00  2.00  5   5    22221
 0.10000E+01 0.19790E+01 0.81200E-02-0.10000E+02 0.00000E+00
020     3.00  3.00  5   5    22221
 0.20000E+01 0.30394E+01 0.50400E-02-0.10000E+02 0.00000E+00
0210    4.00  4.00  5   5    22221
 0.40000E+01 0.34761E+01 0.66700E-02-0.10000E+02 0.00000E+00
0210    5.00  5.00  5   5    22221
 0.40000E+01 0.34761E+01 0.66700E-02-0.10000E+02 0.00000E+00
020     6.00  6.00  5   5    22221
 0.20000E+01 0.37842E+01 0.51900E-02-0.10000E+02 0.00000E+00
0110    7.00  7.00  5   5    22221
 0.20000E+01 0.38259E+01 0.15390E-01-0.10000E+02 0.00000E+00
0210    8.00  8.00  5   5    22221
 0.40000E+01 0.38259E+01 0.53700E-02-0.10000E+02 0.00000E+00
010     9.00  9.00  5   5    22221
 0.40000E+01 0.38573E+01 0.10690E-01-0.10000E+02 0.00000E+00
01010  10.00 10.00  5   5    22221
 0.20000E+01 0.38677E+01 0.15580E-01-0.10000E+02 0.00000E+00
01010  11.00 11.00  5   5    22221
 0.20000E+01 0.38677E+01 0.31820E-01-0.10000E+02 0.00000E+00
01210  12.00 12.00  5   5    22221
 0.20000E+01 0.38677E+01 0.61100E-02-0.10000E+02 0.00000E+00
01010  14.00 14.00  5   5    22221
 0.10000E+01 0.39580E+01 0.31815E-02-0.10000E+02 0.00000E+00
xxxxx  14.00 14.00  5   5    22121
 0.50000E+00 0.39580E+01 0.31815E+02-0.10000E+02 0.00000E+00
xxxxx  21.00 21.00  5   5    31121
 0.50000E+00 0.19230E+01 0.87700E+02-0.10000E+02 0.00000E+00
010    21.00 21.00  5   5    21121
 0.20000E+01 0.19230E+01 0.87700E-02-0.10000E+02 0.00000E+00
```

```
010    22.00 22.00  5   5    22221
 0.10000E+01 0.20099E+01 0.91200E-02-0.10000E+02 0.00000E+00
020    23.00 23.00  5   5    22221
 0.10000E+01 0.29533E+01 0.55200E-02-0.10000E+02 0.00000E+00
0110   24.00 24.00  5   5    22221
 0.80000E+01 0.33573E+01 0.14220E-01-0.10000E+02 0.00000E+00
0210   25.00 25.00  5   5    22221
 0.40000E+01 0.33996E+01 0.73500E-02-0.10000E+02 0.00000E+00
010    26.00 26.00  5   5    22221
 0.20000E+01 0.34679E+01 0.11750E-01-0.10000E+02 0.00000E+00
020    27.00 27.00  5   5    22221
 0.40000E+01 0.35621E+01 0.57200E-02-0.10000E+02 0.00000E+00
010    28.00 28.00  5   5    22221
 0.20000E+01 0.35723E+01 0.11780E-01-0.10000E+02 0.00000E+00
0210   29.00 29.00  5   5    22221
 0.40000E+01 0.37474E+01 0.65400E-02-0.10000E+02 0.00000E+00
0210   30.00 30.00  5   5    22221
 0.40000E+01 0.37474E+01 0.65400E-02-0.10000E+02 0.00000E+00
0110   31.00 31.00  5   5    22221
 0.20000E+01 0.38460E+01 0.17190E-01-0.10000E+02 0.00000E+00
01010  32.00 32.00  5   5    22221
 0.20000E+01 0.38460E+01 0.17190E-01-0.10000E+02 0.00000E+00
01010  33.00 33.00  5   5    22221
```

At line 29-32 of PATHS.HLD file, they are the detail of anatase and rutile ratio in the TiO_2 powder, see following:

```
xxxxx  14.00 14.00  5   5    22121
 0.50000E+00  0.39580E+01  0.31815E+02-0.10000E+02  0.00000E+00

xxxxx  21.00 21.00  5   5    31121
 0.50000E+00 0.19230E+01 0.87700E+02-0.10000E+02 0.00000E+00
```

Then, OPT was used to fitt data (c:..\.....\>opt. ***.ave PATHS.HLD) e.g.“opt TiO2.ave PATHS.HLD”

Example: Simulation of Ce-for-Ti substitution EXAFS spectrum

- The file feff.inp can be generated using ATOMS based on anatase structure.
- The PATH.hld was generated by feff_hld7 in the same way as section 1.2.2 (i). it is shown as follows:

`PATHS.hld file:`

```
22.0    28     1    11111
 0.90000E+00 0.00000E+00 0.00000E+00 0.00000E+00 0.00000E+00
010     1.00  1.00  5   5    01101
```

```
 0.40000E-02 0.19338E+01 0.79500E-02-0.10000E+02 0.00000E+00
010      2.00  2.00  5   5    22221
 0.20000E-02 0.19790E+01 0.81200E-02-0.10000E+02 0.00000E+00
020      3.00  3.00  5   5    22221
 0.40000E-02 0.30394E+01 0.50400E-02-0.10000E+02 0.00000E+00
0210     4.00  4.00  5   5    22221
 0.80000E-02 0.34761E+01 0.66700E-02-0.10000E+02 0.00000E+00
0210     5.00  5.00  5   5    22221
 0.80000E-02 0.34761E+01 0.66700E-02-0.10000E+02 0.00000E+00
020      6.00  6.00  5   5    22221
 0.40000E-02 0.37842E+01 0.51900E-02-0.10000E+02 0.00000E+00
0110     7.00  7.00  5   5    22221
 0.40000E-02 0.38259E+01 0.15390E-01-0.10000E+02 0.00000E+00
0210     8.00  8.00  5   5    22221
 0.80000E-02 0.38259E+01 0.53700E-02-0.10000E+02 0.00000E+00
010      9.00  9.00  5   5    22221
 0.80000E-02 0.38573E+01 0.10690E-01-0.10000E+02 0.00000E+00
01010   10.00 10.00  5   5    22221
 0.40000E-02 0.38677E+01 0.15580E-01-0.10000E+02 0.00000E+00
01010   11.00 11.00  5   5    22221
 0.40000E-02 0.38677E+01 0.31820E-01-0.10000E+02 0.00000E+00
01210   12.00 12.00  5   5    22221
 0.40000E-02 0.38677E+01 0.61100E-02-0.10000E+02 0.00000E+00
01010   14.00 14.00  5   5    22221
 0.20000E-02 0.39580E+01 0.31815E-02-0.10000E+02 0.00000E+00
…
…
etc.
```

The PATHS.HLD of anatase phase was modified by substation Ce at the Ti location. The number of Ce atom can be calculated from equation (19). It is shown as follows:

PATHS.hld file:

```
58.0    16      4    11111
 0.30000E+01 0.00000E+00 0.00000E+00 0.00000E+00 0.00000E+00
010      1.00  1.00  5   5    10001
 0.40000E+01 0.20453E+01 0.98499E-02-0.27479E+02 0.00000E+00
010      2.00  2.00  5   5    12221
 0.20000E+01 0.20338E+01 0.51800E-02-0.27373E+02 0.00000E+00
020      3.00  3.00  5   5    12221
 0.30000E+01 0.30779E+01 0.14930E-01-0.27373E+02 0.00000E+00
030      4.00  4.00  5   5    12221
 0.10000E+01 0.30779E+01 0.10400E-02-0.27373E+02 0.00000E+00
020      5.00  5.00  5   5    12221
 0.40000E+01 0.38322E+01 0.14100E-01-0.27373E+02 0.00000E+00
0210     6.00  6.00  5   5    12221
 0.80000E+01 0.38744E+01 0.13430E-01-0.27373E+02 0.00000E+00
010      7.00  7.00  5   5    12221
 0.80000E+01 0.39062E+01 0.87399E-02-0.27373E+02 0.00000E+00
01010    8.00  8.00  5   5    12221
 0.40000E+01 0.39167E+01 0.67000E-03-0.27373E+02 0.00000E+00
01210    9.00  9.00  5   5    12221
 0.40000E+01 0.39167E+01 0.45600E-02-0.27373E+02 0.00000E+00
```

```
01010  10.00 10.00  5   5    12221
 0.20000E+01 0.40082E+01 0.50200E-02-0.27373E+02 0.00000E+00
010    11.00 11.00  5   5    12221
 0.80000E+01 0.43035E+01 0.17650E-01-0.27373E+02 0.00000E+00
010    12.00 12.00  5   5    12221
 0.80000E+01 0.43246E+01 0.16440E-01-0.27373E+02 0.00000E+00
0110   13.00 13.00  5   5    12221
 0.80000E+01 0.43895E+01 0.64500E-02-0.27373E+02 0.00000E+00
0110   14.00 14.00  5   5    12221
 0.16000E+02 0.45451E+01 0.52200E-02-0.27373E+02 0.00000E+00
020    15.00 15.00  5   5    12221
 0.70000E+01 0.49154E+01 0.13440E-01-0.27373E+02 0.00000E+00
020    16.00 16.00  5   5    12221
 0.80000E+01 0.55277E+01 0.12040E-01-0.27373E+02 0.00000E+00
```

The PATHS.HLD of anatase phase was modified by interstitial Ce in the anatase TiO_2. The number of Ce atom can be calculated from equation (20)It is shown as follows:

PATHS.hld file:

```
58.0    12      4    11111
 0.25000E+01 0.00000E+00 0.00000E+00 0.00000E+00 0.00000E+00
010     1.00  8.00  5   5    10001
 0.40000E+01 0.19401E+01 0.52600E-02-0.72296E+02 0.00000E+00
020     2.00  2.00  5   5    12221
 0.30000E+01 0.23303E+01 0.83300E-02-0.72296E+02 0.00000E+00
010     3.00  3.00  5   5    12221
 0.20000E+01 0.32129E+01 0.10200E-02-0.72296E+02 0.00000E+00
020     4.00  4.00  5   5    12221
 0.30000E+01 0.35148E+01 0.33900E-02-0.72296E+02 0.00000E+00
030     5.00  5.00  5   5    12221
 0.10000E+01 0.35148E+01 0.31400E-02-0.72296E+02 0.00000E+00
010     6.00  6.00  5   5    12221
 0.80000E+01 0.38487E+01 0.82800E-02-0.72296E+02 0.00000E+00
01010   7.00  7.00  5   5    12221
 0.40000E+01 0.44727E+01 0.15860E-01-0.72296E+02 0.00000E+00
010     8.00  8.00  5   5    12221
 0.80000E+01 0.49145E+01 0.17990E-01-0.72296E+02 0.00000E+00
0120    9.00  9.00  5   5    12221
 0.12000E+02 0.51226E+01 0.18120E-01-0.72296E+02 0.00000E+00
0110   10.00 10.00  5   5    12221
 0.16000E+02 0.51902E+01 0.20650E-01-0.72296E+02 0.00000E+00
010    11.00 11.00  5   5    12221
 0.80000E+01 0.54291E+01 0.19070E-01-0.72296E+02 0.00000E+00
020    12.00 12.00  5   5    12221
 0.80000E+01 0.56130E+01 0.17940E-01-0.72296E+02 0.00000E+00
```

Then, OPT was used to fitt data (c:..\.....\>opt. ***.ave PATHS.HLD) e.g.“opt 8CATL.ave PATHS.HLD”.

A4 PySpline

PySpile is a graphic, cross platform for processing raw averaged XAS and EXAFS data. It allows users to modify various parameters and see the effect on k^3-weight EXAFS and Fourier transform in real-time. It was modified by Stanford University and Stanford Synchrotron Radiation Laboratory (Tenderholt *et al.*, 2006)

Appendix A Table 1 Models and Impedance Elements.

Element	Description	Example	Symbol
Resistive Element	impedance of a homogeneous conductor	electrolyte resistance, charge transfer resistance	
Capacitive Element	model of an proper capacitor	plate capacitor, double layer, pseudo capacity at adsorption	
Young Element	model of a dielectric layer with an exponential gradient of conductance	films, coatings, passive layers of oxides, nitrides ...	
Constant Phase Element	model of a loss capacitor	fractal porous electrodes, surface layers with conductance gradients	
Inductive Element	classical inductance	piece of wire, coil, pseudo inductivity	
Warburg Diffusion Element	model of infinite one-dimensional diffusion in a semi-infinite space	bulk solution diffusion in absence of boundary effects such as convection	
Homogeneous Reaction Element	finite length diffusion limited by a bulk chemical reaction	product/educt redox system in solution	
Nernst Impedance Element	finite length diffusion with a constant concentration boundary	diffusion layers with convection, rotating electrodes, membranes	
Finite Diffusion Element	finite length diffusion with phase change boundary	membranes, intercalation of kations in a battery electrode	
Spherical Diffusion Element	spherical diffusion from local spots	pitting corrosion	
Porous Electrode	model of homogeneous pores	fuel cell cathode, battery electrodes, porous layers	

Source: http://www.zahner.de/sim/sim.htm

APPENDIX B

PRESENTATION

(Photo)Electrochemical Characterization of Nanoporous TiO_2 and Ce-doped TiO_2Electrodes

Sutasinee Kityakarn; Simone Robl; Yingyot Pooarporn; Michael Wörner; and Attera Worayingyong

Emil-Kirschbaum Kolloquium 2007, Universität Karlsruhe, Karlsruhe, Germany, 11 May 2007, entitled”(Poster)

Universität Karlsruhe (TH)

(Photo)Electrochemical Characterization of Nanoporous TiO_2 and Ce-doped TiO_2 Electrodes

Sutasinee Kityakarn[a,c]; Simone Robl[b]; Yingyot Pooarporn[a,c]; Michael Wörner[b]; and Attera Worayingyong[a]
[a] Department of Chemistry, Faculty of Science, Kasetsart University, Thailand
[b] Institut für Bio– und Lebensmitteltelteltechnik, Bereich IV: Molekulare Aufarbeitung von Bioprodukten, Universität Karlsruhe
[c] National Synchrotron Research Center, Thailand

Kasetsart University (KU)

Introduction

Photoelectrocatalysts have attracted attention in recent research, especially in the field of environmental purification technologies and solar energy conversion. TiO_2 is one of the most interesting ones, due to being non-photocorrosive and its non-toxic character combined with the ability to create highly reactive oxidative species, e.g. hydroxyl radicals. The processes occurring on TiO_2 electrode surfaces are discussed frequently. Electrochemical Techniques are agreed to be powerful methods to investigate charge transfer and recombination processes. The Electochemical Impedance Spectroscopy (EIS) is approved to be an excellent technique for (photo)electrochemical characterization of photocatalytical systems. In addition, the nanoparticulate TiO_2 film electrodes prepared by sol-gel method and the nanoparticulate P25 film electrodes prepared by particle suspension were also characterized by Cyclicvoltammetry (CV).

Experimental

Nanopaticulate P25 film electrodes were prepared by applying an aqueous suspension of P25 and methanol (4:1 v:v) on an ITO (Indium tin oxide)-coated glass plate (conductive substrate). The solvent was evaporated at 35°C during 2 hours. This process was repeated five times, followed by calcination at 450°C for 4 hours.

Titanium(IV)-bis(ethyl acetoacetato)-diisopropoxide was added drop-wise to acidic aqueous solution and stirred for 100 min at 85°C. A 2x2 cm^2 of an ITO-coated glass plate was dipped in the sol for a few minutes, withdrawn from the sol, and heated at 200°C for 10 min after this procedure was repeated several times to increase the thickness of the TiO_2 coating. Finally, the samples were calcined at 550°C for 4 hours to produce nanoporous TiO_2 film electrodes. Ce-doped TiO_2 film electrodes were prepared by a similar process, with cerium nitrate salt added to the acidic aqueous solution.

All prepared electrodes were characterized by employing CV and EIS.

Results and Discussion

The voltammetric response of bare and nanoporous TiO_2-coated ITO electrodes in 0.5 M Na_2SO_4 (pH 6.3) were investigated. The bare ITO electrode revealed only double layer charging (no faradaic reaction) in the potential range of 1.3 to -1.1 V, see Figure 1(a). Undoped TiO_2(sol-gel)-coated electrodes showed a cathodic reaction starting at about -0.4 V, depending on the number of layers (5, 10 and 15). The comparison of the CVs of P25 (5 layers), undoped TiO_2-coated (15 layers) and Ce-doped TiO_2-coated electrodes (15 layers) revealed significant differences in the cathodic potential range, see Figure 1(b).

The reaction can be understood if one assumes that the surface of TiO_2 is hydroxylated in water, possessing $[Ti(OH)_2]^{2+}$ sites. The reduction of hydrated Ti(IV) is proposed as follows[1]:

$$[Ti(OH)_2]^{2+} + H^+ + e^- \rightarrow [Ti(OH)]^{2+} + H_2O \qquad (1)$$

where $[Ti(OH)_2]^{2+}$ and $[Ti(OH)]^{2+}$ represent Ti(IV) and Ti(III) site on TiO_2 surface, respectively[1].

Therefore, from the CV results can be conducted that the method of TiO_2 film prepararion seems to have a strong influence on the reactivity in the dark.

The nanoporous TiO_2 film electrodes, immersed in aqueous electrolyte solution, were exposed to light with energy exceeding the band gap of TiO_2 leading to the generation of electron-hole pairs. The photogenerated holes diffuse/migrate to the TiO_2 surface of the particles and may oxidize adsorbed organic substrate while the promoted electrons have to cross particle grain boundaries to be trapped at the TiO_2/ITO interface. For Ce-doped TiO_2 film electrodes, there are two possibilities; (1) electrons in valence band of TiO_2 are excited into Ce *4f* levels and (2) electrons in the ground state of Ce_2O_3 are excited into Ce *4f* levels[3]. CVs of irradiated TiO_2 film electrodes showed that the photocurrent increases with the number of layers with exception of the thickest films (25 layers). The photocurrent maximum indicates that the thickness of layer reaches the free diffusion length of electrons. The probability for electron-hole recombination will depend on the distance between the photoexcited particle and the TiO_2/ITO interface. The photocurrent maximum was found for all samples. It depends on the method of film preparation and was observed for P25 (5 layers), undoped TiO_2-coated (20 layers) and Ce-doped TiO_2-coated electrodes (15 layers).

The impedance spectra of different TiO_2 film electrodes at -0.3 V in the dark and under irradiation are shown in Figure 4 (a) and (b). Two apparent time constants were found to be significant for irradiation experiments. Leng *et al.* proposed that the peak in the high frequency domain represents the space charge capacitance and the peak at low frequencies represents the interfacial capacitance[2]. For the fitting of our impedance data of the TiO_2/ITO composite electrodes, a model for porous electrodes was applied and modified, respectively. The overall impedance is a complex assemble of partial equivalent circuits of the semiconductor (TiO_2 particle)/pore interface (Z_q), of the TiO_2 coating (ensemble of interconnected particles) (Z_s), of the pores (interstitial electrolyte volume) (Z_p), of the ITO layer/porous TiO_2 particles interface (Z_n) and of the semiconductor surface(TiO_2)/bulk electrolyte interface (Z_0), see Figure 3. For the nanoporous TiO_2 film electrodes, the impedance of semiconductor surface/bulk electrolyte interface (Z_0) is small compared to the impedance of the pore electrolyte/pore wall interface and therefore can be neglected. The proposed "porous electrode model" consists of an impedance of the conductive ITO layer contacted with (pore)electrolyte and TiO_2 particles (Z_n), an impedance of the TiO_2/pore electrolyte interface (Z_q), together with Z_s and Z_p which are assembled to one interconnected impedance element (8), see Figure 4 (c and d). The impedance of Z_n is a serial combination of a capacitance and a parallel connection of a constant phase element (CPE) and a resistance. The impedance of Z_q is proposed to consist of the charge transfer resistance (4), the interfacial capacitance (5), the impedance element for the charge carrier recombination (6) and the space charge capacitance (7). The resistance of the bulk electrolyte is characterized by element (9), a pure ohmic resistance.

The charge transfer resistance decreases remarkably as expected when the electrode is exposed to light. The fitting of the EIS data of irradiated electrodes requires the implementation of a Warburg impedance (10) to the equivalent circuit, indicating that the diffusion of the charge carrier is limiting the measured photocurrent and not the heterogeneous charge transfer reaction.

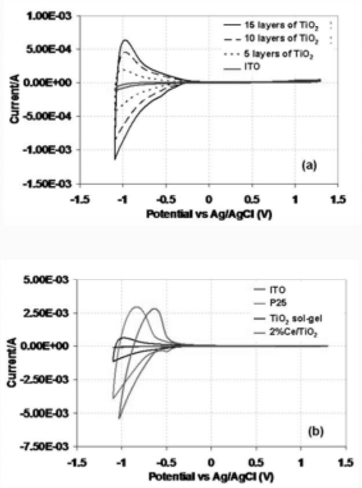

Figure 1. (a) CVs of TiO_2 film electrodes in 0.5 M Na_2SO_4, prepared by the sol-gel method in dependence of the film thickness (number of layers)
(b) CVs of different nanoporous TiO_2 film electrodes in 0.5 M Na_2SO_4, prepared by sol-gel method.

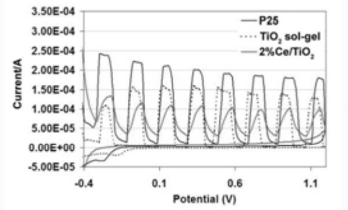

Figure 2. Photocurrent of different nanoporous TiO_2 film electrodes under chopped irradiation.

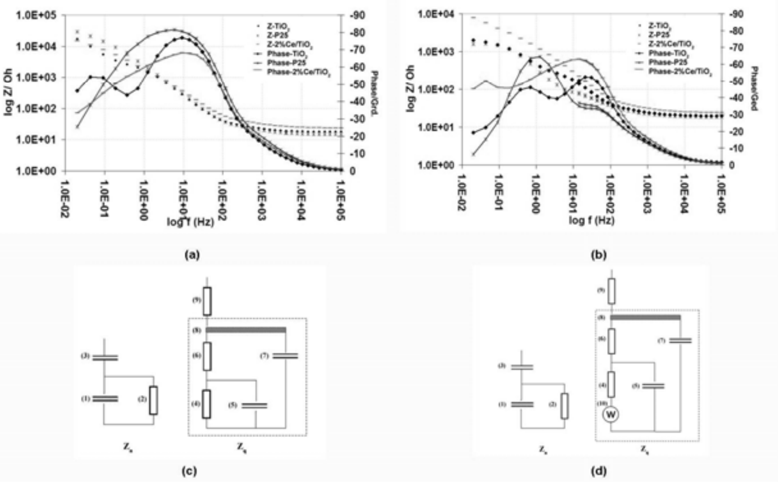

Figure 4. (a) EIS of different nanoporous TiO_2 film electrodes at -0.3V in the dark.
(b) EIS of different nanoporous TiO_2 film electrodes at -0.3V under irradiation.
(c) equivalent circuit for electrodes in the dark.
(d) equivalent circuit for electrodes under irradiation.

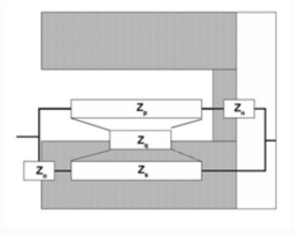

Figure 3. Model of porous electrodes employed for nanoporous TiO_2 film electrodes in EIS.

Acknowledgement

The authors acknowledge support from National Synchrotron Research Center, Thailand.

References

1. Zhang, J., Yang, C., Chang, G., Zhu, H. and Oyama, M., *Voltammetric behavior of TiO_2 films on graphite electrodes prepared by liquid phase deposition*, Mater.Chem.Phys., 88, 2004, p 398.
2. Leng, W.H., Zhang, Z., Zhang, J.Q. and Cao, C.N., *Investigation of the kinetics of a TiO_2 photoelectrocatalytic reaction involving charge transfer and recombination through surface states by electrochemical impedance spectroscopy*, J.Phys. Chem. B., 109, 2005, p 15008.
3. Li, F.B., Li, X.Z., Hou, M.F., Cheah, K.W. and Choy, W.C.H, *Enhanced photocatalytic activity of Ce^{+3}-TiO_2 for 2- mercaptobenzothiazole degradation in aqueous suspension for odour control*, Appl.Catal.A., 285, 2005, p 181.

PRESENTATION

Investigation of the Photoelectrochemical Properties of Nanoporous TiO_2 and Ce-doped TiO_2 Catalysts by Electrochemical Impedance Spectroscopy

Sutasinee Kityakarn; Yingyot Pooarporn; Simone Robl; Michael Wörner; and Attera Worayingyong

German-Thai Symposium on Nanoscience and Nanatechnology, Bang San, Chonburi, Thailand, 27-28 September 2007 (oral presentation)

OC-01

Investigation of Photoelectrochemical Properties of Nanoporous TiO_2 and Ce-doped TiO_2 Catalysts by Electrochemical Impedance Spectroscopy

Sutasinee Kityakarn,[1,3,C] ***Yingyot Pooarporn,***[1,3] ***Simone Robl,***[2] ***Michael Wörner,***[2] ***and Attera Worayingyong***[1]

[1] *Department of Chemistry, Faculty of Science, Kasetsart University, Bangkok 10900, Thailand*

[2] *Institut für Bio–und Lebensmitteltelteltechnik, Bereich IV: Molekulare Aufarbeitung von Bioprodukten, Engler-Bunte-Institut, Universität Karlsruhe,D-76131 Karlsruhe, Germany*

[3] *National Synchrotron Research Center, Nakhon-Ratchasima 30000, Thailand*

[C] To whom correspondence should be addressed. E-mail: kityakam@hotmail.com; **Fax**: 02-579-3955; **Tel.** 02-562-5555

Summary

TiO_2 and Ce-doped TiO_2 photocatalysts were prepared as nanoporous electrodes using sol-gel method. The (photo)electrochemical properties were investigated by Cyclic Voltammetry (CV) and Electrochemical Impedance Spectroscopy (EIS). The CV results showed that faradaic current under cathodic polarization (in the dark) increased with increasing number of layers ascribed to the reduction of hydrated Ti(IV) sites. The related onset potentials were shifted in anodic direction with decreasing pH. The EIS results revealed two time-constants under irradiation and were interpreted employing a porous electrode model. The proposed model was modified by consideration of the heterogeneous charge transfer and the charge recombination. The charge transfer resistance decreased remarkably as expected when the electrodes were exposed to light. An additional Warburg-like impedance was implemented to the equivalent circuit for irradiated electrodes indicating that the diffusion of charge carriers may limit the observed photocurrent.

Keywords : Photocatalyst, photoelectrochemistry, nanoporous TiO_2 electrodes.

LITERATURE CITED

1. Zhang, J., Yang, C., Chang, G., Zhu, H. and Oyama, M., "Voltammetric behavior of TiO_2 films on graphite electrodes prepared by liquid phase deposition. *Mater. Chem. Phys.*, 2004, **88**, 398-403.
2. Bisquert, J., Garcia-Belmonte, G., Fabregat-Santiago, F., Ferriols, N.-S., Bogdanoff, P. and Pereira, E.C., "Doubling exponent models for the analysis of porous film electrodes by impedance. Relaxation of TiO_2 Nanoporous in aqueous solution", *J. Phys. Chem. B*, 2000, **104**, 2287-2298.
3. Fujishima A., Rao, T. N.and Tryk, D. A., "Titanium dioxide photocatalysis", *J. Photochem. Photobiol. C: Photochem Rev.*, 2000, **1**, 1-21.
4. Leng, W. H., Zhang, Z., Zhang, J. Q. and Cao, C. N., "Investigation of the kinetics of a TiO_2 photoelectrocatlytic reaction involving charge transfer and recombination through surface states by electrochemical impedance spectroscopy", *J.Phys. Chem. B.*, 2005, **109**, 15008-15023.

PUBLICATION

Determination of Phase Ratio in Polymorphic Materials by X-ray Absorption Spectroscopy: The case of Anatase and Rutile Phase Mixture in TiO_2

M.F. Smith, W. Klysubun, S. Kityakarn, A. Worayingyong, S.B. Zhang, S.-H Wei, D. Onkaw, P. Songsiritthigul, S. Rujirawat and S. Limpijumnon

J. Appl.Phys., 105 (2009), 024308, pp. 1-4.

JOURNAL OF APPLIED PHYSICS **105**, 024308 (2009)

Determination of phase ratio in polymorphic materials by x-ray absorption spectroscopy: The case of anatase and rutile phase mixture in TiO_2

M. F. Smith,[1,a)] W. Klysubun,[1] S. Kityakarn,[2] A. Worayingyong,[2] S. B. Zhang,[3,b)]
S.-H. Wei,[3] D. Onkaw,[1,4] P. Songsiriritthigul,[1,4] S. Rujirawat,[1,4] and S. Limpijumnong[1,3,4,c)]
[1]*Synchrotron Light Research Institute, Nakhon Ratchasima 30000, Thailand*
[2]*Department of Chemistry, Kasetsart University, Bangkok 10900, Thailand*
[3]*National Renewable Energy Laboratory, Golden, Colorado 80401, USA*
[4]*School of Physics, Suranaree University of Technology , Nakhon Ratchasima 30000, Thailand*

(Received 3 October 2008; accepted 2 December 2008; published online 23 January 2009)

We demonstrate that x-ray absorption spectroscopy (XAS) can be used as an unconventional characterization technique to determine the proportions of different crystal phases in polymorphic samples. As an example, we show that ratios of anatase and rutile phases contained in the TiO_2 samples obtained by XAS are in agreement with conventional x-ray diffraction (XRD) measurements to within a few percent. We suggest that XAS measurement is a useful and reliable technique that can be applied to study the phase composition of highly disordered or nanoparticle polymorphic materials, where traditional XRD technique might be difficult. © *2009 American Institute of Physics.* [DOI: 10.1063/1.3065988]

I. INTRODUCTION

TiO_2 is a photocatalyst that is technologically important for air and water purification applications (for reviews, see Refs. 1 and 2). This is despite the fact that its absorption threshold is in the ultraviolet regime, which makes photoactivation by sunlight ineffective and large scale environmental applications difficult. Much broader applicability of TiO_2 could result from a successful attempt to enhance visible-light photocatalysis by narrowing its band gap via doping or change in crystal phase. Currently, it is still a great challenge to understand all factors that promote photocatalysis by TiO_2 and how its optoelectronic properties are affected by impurities and other conditions such as crystal phases.

Rutile and anatase are the most common phases of TiO_2 and coexist in most samples. The relative proportion of rutile and anatase affects photocatalysis of the samples.[2–7] Moreover, the effect of doping and native defects in the two phases can be very different because the electronic structures of rutile and anatase are different.[8–11] Therefore, it is important that the ratio of these two phases is known before other factors (such as doping) are considered. It is of interest to develop methods to determine this ratio, especially in impure samples, where the crystal quality might not necessarily be good, or in nanostructures that are the focus of much current TiO_2 research (see, e.g., Refs. 12–18). When single-phase domains are sufficiently large to satisfy the long-range nature of the diffraction, phase proportions can be determined accurately by conventional x-ray diffraction (XRD). However, XRD could become less accurate in systems with very small nanometer-sized crystals, in highly disordered systems, or in the systems with a large difference in grain size between anatase and rutile phases. Based on a rough estimation using Scherrer equation, which describe the relationship between the crystalline size and the broadening in XRD peaks, the main conventional XRD peaks of anatase and rutile would coalesce when the crystal grain reduces to around 10 nm. (The XRD peak width for 5 nm nanocrystalline anatase TiO_2 in Ref. 17 is shown to be clearly wider than the difference between anatase and rutile main peaks.) In addition, when anatase and rutile have different grain sizes, the XRD peaks would have different broadening factors, making the determination of relative peak intensity between the two phases difficult.

In this article, we demonstrate that extended x-ray absorption fine structure (EXAFS), which is the high energy region of the x-ray absorption spectroscopy (XAS),[19] can be applied to measure crystal phase proportions. Unlike XRD, which depends on the long-range periodicity of the crystal domains, EXAFS is sensitive to only a few neighbors of the absorbing atoms and does not require long-range order. Therefore, the approach presented here can be used effectively on highly disordered samples with nanoscale domains that can be difficult to characterize using conventional XRD measurements. Even for typical samples, our approach can be used instead of XRD or at least as an independent probe that can complement XRD.

II. THEORY AND METHODOLOGY

The determination of the ratio is done by comparing the Ti *K*-edge absorption, for samples with different anatase/rutile molar ratios, with simulation of EXAFS spectra based on the known anatase and rutile crystal structures.[20] In EXAFS experiments, an x ray excites a core electron (1*s* for *K*-edge absorption) to an empty state above the occupied

---

[a)] Present address: School of Physical Sciences, The University of Queensland, Brisbane QLD 4072, Australia.

[b)] Present address: Department of Physics, Rensselaer Polytechnic Institute, Troy, New York 12180.

[c)] Author to whom correspondence should be addressed. Also at Research Center in Computational and Theoretical Physics/ThEP Center, Suranaree University of Technology, Nakhon Ratchasima 30000, Thailand. Electronic mail: sukit@sut.ac.th.

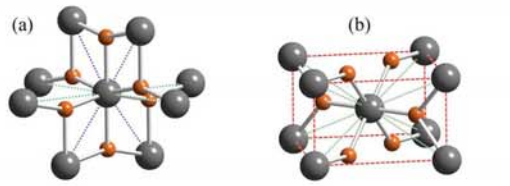

FIG. 1. (Color online) The arrangement of neighbors around the absorber Ti (in the middle) in (a) anatase and (b) rutile TiO_2. For rutile, the eight Ti atoms are equidistant but, for anatase, four Ti atoms (those sharing same basal plane in the figure) are farther than the other four by approximately 0.7 Å.

ground states, and the absorption $\mu(\omega)$ is measured as a function of photon frequency ω (see Refs. 19 and 21 for EXAFS reviews). EXAFS is concerned with oscillations in the spectrum that are known to contain information about the structure surrounding the absorbing atom. The EXAFS signal $\chi(\omega)$ is extracted by subtracting from the raw data the absorption by an isolated atom. We used the EXAFSPAK software package[22] to extract the EXAFS signal from the raw XAS measurements. These oscillations in the EXAFS result from the interaction between the excited electron and neighboring atoms. That is, the state of the excited electron at the absorber core may be described as a superposition of the wave functions of a free excited electron and the wave functions of an electron that has been backscattered from nearby atoms. The associated wave interference results in sine dependence of the EXAFS signal on the magnitude of the electron momentum $\hbar k=\sqrt{2m(\hbar\omega-E_0)}$ (E_0 is the energy of the absorption edge and m is electron mass) with the period of oscillation set by interatomic distances. According to the theory of multiple-scattering EXAFS analysis,[21] there is one sine component for every possible path that an electron may take whereby it leaves the absorber and, after being scattered by various neighbors, returns to the absorber. Thus actual spectra are composed of many mutually interfering paths.[23] However, in practice, only a cluster of atoms within roughly 5 Å of the absorber is considered because the probability of an electron to return from distant atoms quickly diminishes. This theory is well established and simulations are often reported to be in quantitative agreement with measurement.[21]

The approach proposed here is a relatively straightforward application of EXAFS analysis since we assume that the Ti absorber sees only a local environment that is either rutile or anatase TiO_2. Because both crystal structures are known, their molar ratio may be obtained by comparing the data to a weighted average of spectra simulated for rutile and anatase, with the weight used as a fitting parameter. Nevertheless, the environment of the Ti atom, especially up to the first nearest neighbors, is so similar for the two phases that an accurate determination of the volume ratio requires high-quality data and detailed multiple-scattering analysis.

The arrangement of neighbors around the absorber Ti in rutile and anatase is shown in Fig. 1. For both anatase and rutile, each Ti atom has six O nearest neighbors (actually two of the six are further away, but only by about 2.5%) and each O atom has three Ti nearest neighbors (one Ti is farther than the other two by 2.5%). Since the Ti–O bond lengths for both rutile and anatase are very similar, their respective EXAFS signals due to nearest-neighbor scattering are basically indistinguishable. The key structural difference is the fact that, in rutile, the Ti absorber has eight equidistant (next-nearest) Ti neighbors while, in anatase, the corresponding Ti neighbors are split into two groups of four. These next nearest neighbor Ti atoms are shown connecting to the absorber center using dotted lines in the Fig. 1. So, while the contributions of these eight scatterers always add constructively in rutile, they fall out of phase over certain ranges in k for anatase and the destructive interference removes would-be features from the anatase spectrum. More interestingly, such significant destructive interference would not occur if the EXAFS simulation includes only single-scattering paths. This is because direct scattering from the more distant group of Ti atoms in anatase is weak. However, if the simulation includes multiple-scattering paths in which oxygen nearest neighbors act as the centers to "focus" the back scattering electron, a more distant Ti atom can also play a crucial role. The focusing effect is strong in this particular case because the O atom locates only 0.4 Å off the line between the Ti absorber and Ti scatterer.

We use the FEFF7 package[24] to simulate the EXAFS spectra with the criteria for path selection taken to be the same for both structures. Atoms within a 5.5 Å radius from the Ti absorber are included in the cluster and 14 (11) most important single- and multiple-scattering paths for anatase (rutile) are kept. Debye–Waller factors were calculated using the correlated Debye model with a Debye temperature of 530 K estimated from nuclear resonance photon scattering measurements[9] (the EXAFS measurements were made at room temperature). Although this method of treating thermal vibration can lead to a small error, especially at high temperature, it has the advantage that no empirical parameters need to be introduced to fit the data.

III. RESULTS AND DISCUSSIONS

The simulated EXAFS signals for both rutile and anatase are shown in the main panel of Fig. 2(a) with the difference between the two shown using dots in the inset. To illustrate that the difference is almost exclusively coming from the difference in the geometry of a few neighbor Ti atoms, the difference in the signals that comes from a few key paths involving these atoms are calculated and shown in the inset using a solid curve. In rutile, these paths are single scattering paths from the ten closest Ti atoms, while in anatase they are single scattering from the eight nearest Ti atoms and multiple-scattering focusing paths. We can clearly see that the solid curve agrees very well with the dots, indicating that the difference between the EXAFS from the two phases is mainly driven by these next nearest neighbors. This analysis combining with the quality of fitting with the experiments (as will be seen next) indicates that EXAFS need only a rather short range cluster (less than 4 Å) to distinguish between the two phases. Therefore, it is applicable for very small nanoscale crystal where conventional XRD would have a difficulty in obtaining clear diffraction patterns due to limited crystal size.

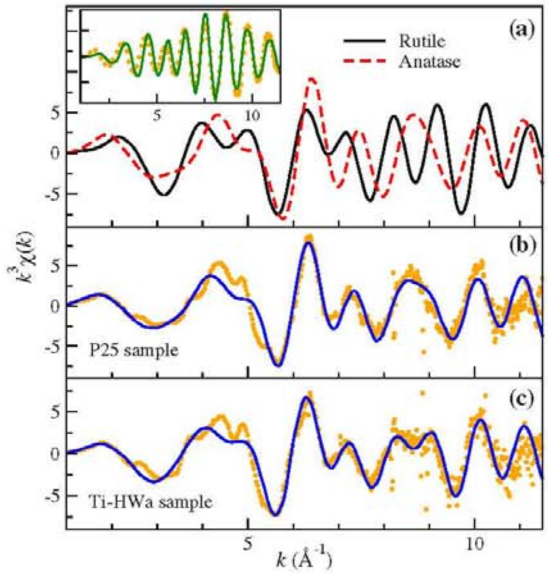

FIG. 2. (Color online) (a) Simulated k-weighted EXAFS spectra for pure rutile (solid curve) and anatase (dashed curve) TiO_2. Inset: dots show the difference between the two curves in the main panel. The solid curve is the part of the difference that comes from a few key scattering paths (described in text), which clearly dominate the total difference between the spectra of the two structures. In (b) and (c), comparisons between the simulated (solid curves) and measured k-weighted EXAFS signals (dots) are shown for P25 sample and Ti-HWa sample, respectively. The simulated curves are made using rutile/anatase ratio as the lone fitting parameter.

Having established the main qualitative difference between anatase and rutile EXAFS, we will fit the simulated spectra to a few cases of mixed rutile/anatase samples to demonstrate that the approach can give reliable composition ratios. The fit is done by generating the weighted sum of the two pure (anatase and rutile) signatures, i.e.,

$$S_{\text{av}}(k) = f_{\text{anatase}} S_{\text{anatase}}(k) + (1 - f_{\text{anatase}}) S_{\text{rutile}}(k), \tag{1}$$

where S_{anatase} and S_{rutile} are the simulated anatase and rutile EXAFS signatures [Fig. 2(a)] and f_{anatase} is the anatase fraction. f_{anatase} is allowed to vary between 1 (completely anatase) and 0 (completely rutile) until the best fit to each measured spectrum of mixed sample is obtained. If the EXAFS spectra of pure anatase and rutile were available, they can be used in the place of the simulated S_{anatase} and S_{rutile} on the right hand side of Eq. (1). The use of pure anatase and rutile spectra, if available, for S_{anatase} and S_{rutile} could potentially improve the fit quality (since it removes the small discrepancy between theory and experiment spectra). However, it can introduce additional error in the determination of the ratio if the standards are not completely pure anatase and rutile. Moreover, the use of simulated spectra may offer considerable advantages if one were to extend this technique to cases in which samples contained significant impurity concentrations or contributions from surface atoms. Under such circumstances, one could take advantage of the greater flexibility of simulations to obtain spectra for samples under a wide range of conditions. This would help trace the source of individual spectral features in the data, enhancing considerably the power of the technique.

TABLE I. Molar percentage of anatase (remainder is rutile) for several samples as determined from XRD and from EXAFS.

	Percentage of anatase	
Sample	XRD	EXAFS
Anatase	>99	94
P25	76	79
Ti-HWa	57	54
Ti-HWb	43	48

The samples used in this study include commercial anatase TiO_2, Degussa P25, and the samples prepared in-house using a sol-gel method,[25] labeled Ti-HWa and Ti-HWb. As references, the anatase/rutile molar ratios in these samples (shown in Table I) are estimated using the most intense peak in conventional XRD spectra of each phase (anatase and rutile) according to the method described in Ref. 26.

The XAS measurements are performed in the transmission mode at Beam Line No. 8 of the Siam Photon Laboratory, Synchrotron Light Research Institute, Thailand.[27] The x-ray beam is monochromatized using a Si (111) double-crystal monochromator and the EXAFSPAK package[22] was used to extract the EXAFS spectra from the raw absorption data. The number of fitting parameters was kept to a minimum: atomic coordinates were fixed at their known positions,[20] the overall constant (often called s_0^2 in the literature) was arbitrarily set to 0.9, and all Debye–Waller factors were determined using the correlated Debye model for both phases. A single parameter, the shift in the edge energy E_0 was determined from a fit between the pure anatase simulation and the commercial anatase sample and was (for other data) kept constant. Thus only the rutile/anatase ratio was adjusted to fit the data. From Figs. 2(b) and 2(c), we can see a good agreement between the data and these, nearly parameter-free simulations (the results for all the data were similar, as a representative, only the P25 and Ti-HWa samples are shown). From inspection of Figs. 2(a)–2(c), one sees more prominent rutile-derived features in those samples with a higher rutile/anatase ratio as determined by XRD (for example, the positive peak occurring at roughly 8.5 Å^{-1} appears split in the TiHWa data and rutile simulation, but not in the P25 data or anatase simulation). Note that, in the k region of 3.5–5.0 Å^{-1}, the measured spectra show the three-peak feature, which we can find the corresponding features in Fig. 2(a). However, due to a too large broadening (and possibly slight errors in the relative peak positions in the simulated spectra) the fitted spectra appear to contain fewer features in this region than the measured one. Quantitatively, the best-fit rutile/anatase molar ratio was compared with the values obtained from conventional XRD results (Table I). The success of the EXAFS determinations in roughly reproducing the results of the, more standard, XRD measurements suggests that EXAFS is a viable method for measuring phase composition of polycrystalline TiO_2. The advantage of EXAFS over XRD lies in the fact that EXAFS does not require a long-range ordering of the crystal. This makes it possible to apply the approach on highly disordered nanocrystalline samples where conventional XRD might not show clear diffraction peaks for analysis. However, for a small nanocrystal TiO_2, a considerable fraction of Ti atoms are at the surface. These surface Ti atoms have different coordination numbers, hence likely to provide different EXAFS signatures from those in bulk. Therefore, for the cases of small nanocrystals TiO_2, we propose that one might be able to improve the fit by simulating the EXAFS signature of surface Ti atoms, S_{surface}, in additional to the bulk Ti atoms and add the signature of the surface Ti atoms times its fraction to Eq. (1), i.e.,

$$S_{\text{av}}(k) = (1 - f_{\text{surface}})[f_{\text{anatase}}S_{\text{anatase}}(k) + (1 - f_{\text{anatase}})S_{\text{rutile}}(k)] + f_{\text{surface}}S_{\text{surface}}(k). \qquad (2)$$

The f_{surface} can be estimated from the grain size of the sample and fixed during the fit for f_{anatase}. Depending on the overall fitting quality, one might be able to fit for both f_{anatase} and f_{surface} and obtain both anatase/rutile ratio and the nanocrystal size simultaneously, if the crystal size is not known.

While our work has clearly shown that EXAFS is a viable method for measuring phase composition of polycrystalline TiO_2, further systematic experiments shall be carried out to confirm the reliability of the method. For instance, one could mix rutile/anatase TiO_2 powder at various known concentrations and use the method to determine the ratio. If such experiment can be carried out with varied TiO_2 powder size from regular size into the nanoscale region, it could further confirm that the EXAFS method is more suitable for nanocrystals. Moreover, this approach should work equally well to determine the phase ratios of other materials with polymorphs.

IV. CONCLUSION

In conclusion, we showed that combined experimental and computational EXAFS studies can determine rutile/anatase molar ratios of TiO_2 to within a few percent of conventional XRD determinations. This demonstrates that the EXAFS technique is a valuable tool in analysis of phase mixing in polymorphic materials, especially for disordered samples or nanocrystals that do not have sufficient long-range crystalline ordering for XRD measurements.

ACKNOWLEDGMENTS

This work was partially supported by the Commission on Higher Education (Program CHE-RES-RG "Theoretical Physics"). Work at NREL is supported by the U.S. DOE/BES and EERE (Grant No. DE-AC36-99GO10337). S.K. and A.W. acknowledge support from SLRI (Grant No. 1-2548/PS01).

[1] U. Diebold, Surf. Sci. Rep. **48**, 53 (2003).
[2] M. R. Hoffmann, S. T. Martin, W. Choi, and D. W. Bahnemann, Chem. Rev. (Washington, D.C.) **95**, 69 (1995).
[3] V. Collins-Martinez, A. L. Ortiz, and A. A. Elguezabal, Int. J. Chem. Reactor Eng. **5**, A92 (2007).
[4] S. Cheng, S.-J. Tsai, and Y.-F. Lee, Catal. Today **26**, 87 (1995).
[5] A. G. Agrios, K. A. Gray, and E. Weitz, Langmuir **19**, 1402 (2003).
[6] T. Ohno, K. Sarukawa, and M. Matsumura, J. Phys. Chem. B **105**, 2417 (2001).
[7] A. Sclafani and J. M. Herrmann, J. Phys. Chem. **100**, 13655 (1996).
[8] R. Asahi, Y. Taga, W. Mannstadt, and A. J. Freeman, Phys. Rev. B **61**, 7459 (2000).
[9] K. M. Glassford and J. R. Chelikowsky, Phys. Rev. B **46**, 1284 (1992).
[10] H. Tang, K. Prasad, R. Sanjines, P. E. Schmid, and F. Levy, J. Appl. Phys. **75**, 2042 (1994).
[11] S. Na-Phattalung, M. F. Smith, K. Kim, M.-H. Du, S.-H. Wei, S. B. Zhang, and S. Limpijumnong, Phys. Rev. B **73**, 125205 (2006).
[12] M. Fernandez-Garcia, C. Belver, J. C. Hanson, X. Wang, and J. A. Rodriguez, J. Am. Chem. Soc. **129**, 13604 (2007).
[13] J.-G. Li, M. Ikeda, R. Ye, Y. Moriyoshi, and T. Ishigaki, J. Phys. D **40**, 2348 (2007).
[14] P. Wen, H. Itoh, W. Tang, and Q. Feng, Langmuir **23**, 11782 (2007).
[15] T. Berger, O. Diwald, E. Knozinger, F. Napoli, M. Chiesa, and E. Giamello, Chem. Phys. **339**, 138 (2007).
[16] K.-P. Wang and H. Teng, Appl. Phys. Lett. **91**, 173102 (2007).
[17] J. Jiu, S. Isoda, M. Adachi, and F. Wang, J. Photochem. Photobiol., A **189**, 314 (2007).
[18] D. V. Bavykin, J. M. Friedrich, and F. C. Walsh, Adv. Mater. (Weinheim, Ger.) **18**, 2807 (2006).
[19] D. C. Koningsberger and R. Prins, *X-Ray Absorption: Principles, Applications, Techniques of EXAFS, SEXAFS and XANES* (Wiley, New York, 1988).
[20] R. W. G. Wyckoff, *Crystal Structures* (Interscience, New York, 1948).
[21] J. J. Rehr and R. C. Albers, Rev. Mod. Phys. **72**, 621 (2000).
[22] G. N. George and I. J. Pickering, EXAFSPAK–a suite of computer programs for analysis of x-ray absorption spectra, Menlo Park, CA, 1993.
[23] Further corrections, which account for smooth *k*-dependent factors that affect the phase and amplitude of the oscillation, are needed to obtain quantitatively accurate simulations of the spectra.
[24] S. I. Zabinsky, J. J. Rehr, A. Ankudinov, R. C. Albers, and M. J. Eller, Phys. Rev. B **52**, 2995 (1995).
[25] Y. Pooarporn, A. Worayingyong, M. Wörner, P. Songsiriritthigul, and A. M. Braun, Water Sci. Technol. **55**, 153 (2007).
[26] R. A. Spurr and H. Myers, Anal. Chem. **29**, 760 (1957).
[27] R. Apiwatwaja, S. Chunjarean, K. Hass, G. Hoyes, C. Kaewprasert, P. Klysubun, W. Klysubun, W. Pairsuwan, S. Rugmai, S. Rujirawat, N. Sanguansak, P. Songsiriritthigul, and H. Wiedemann, Solid State Phenom. **107**, 1 (2005).

CURRICULUM VITAE

Name : Sutasinee Kityakarn

Date of birth : September 1, 1979

Place of Birth : Uttaradit, Thailand

Education:

YEAR	INSTITUE	DEGREE
2002	ChaingMai Univ.	B. Sc. (Chemistry)
2004	Kasetsart Univ.	M. Sc. (Chemistry)

PUBLICATION:

- M.F. Smith, W. Klysubun, S. Kityakarn, A. Worayingyong, S.B. Zhang, S.-H Wei, D. Onkaw, P. Songsiritthigul, S. Rujirawat and S. Limpijumnong, Determination of Phase Ratio in Polymorphic Materails by X-ray Absorption Spectroscopy: The case of Anatase and Rutile Phase Mixture in TiO_2, **J. Appl.Phys.**, 105 (2009), 024308, 1-4.
- Attera Worayingyong, Praewpilin Kangvansura and Sutasinee Kityakarn, Sciff base complex sol-gel method for $LaCoO_3$ perovskite preparation with high adsorbed oxygen, **Colliods and Surfaces A**, 320 (2008), 123-129.
- Sutasinee Kityakarn, Michael Wörner, Attera Worayingyong, Yingyot Pooarporn and André Braun, (Photo)electrochemical studies of nanoporous TiO_2 and Ce-doped TiO_2 Film Electrodes Prepared by Sol-gel Method in Comparison with Nanoparticulated TiO_2-P25 electrodes (submitted for Electrochemica Acta).
- Yingyot Pooarporn, Anwaraporn Nittharach, Sutasinee Kityakarn, Prayoon Songsiririttigul, Attera Worayingyong, Michael Wörner and André Braun, Thiophene Photocatalytic Oxidation over TiO_2 and Ce/TiO_2 Photocatalysts: *in-situ* DRIFTS and XPS studies (submitted for publication)
- Anwaraporn Nitharach, Sutasinee Kityakarn, Ramida Rattanakam, Yingyot Pooarporn, Prayoon Songsiririttigul, Sukit Limpijumnong, Attera Worayingyong, The hydrolysis effect of the sol-gel preparation on electronic structures of TiO_2 and Ce/TiO_2 photocatalysts (submitted for publication).

SCHOLARSHIP : Graduate Scholarship, Synchrotron Light Research Institute, Thailand during 2005-2009